論文 / 著書情報
Article / Book Information

題目(和文)	LHC-ATLAS検出器における重心系エネルギー13 TeV陽子陽子衝突データによるぼやけた二次崩壊点を用いた長寿命超対称性粒子の探索
Title(English)	Search for long-lived supersymmetric particles using fuzzy displaced vertices in pp collision at $\sqrt{s}$ = 13 TeV with the LHC-ATLAS detector
著者(和文)	潮田理沙
Author(English)	Risa Ushioda
出典(和文)	学位:博士(理学), 学位授与機関:東京工業大学, 報告番号:甲第12826号, 授与年月日:2024年9月20日, 学位の種別:課程博士, 審査員:陣内 修,中村 隆司,関口 仁子,宗宮 健太郎,須山 輝明
Citation(English)	Degree:Doctor (Science), Conferring organization: Tokyo Institute of Technology, Report number:甲第12826号, Conferred date:2024/9/20, Degree Type:Course doctor, Examiner:,,,,
学位種別(和文)	博士論文
Type(English)	Doctoral Thesis

Ph.D Thesis

Search for long-lived supersymmetric particles using fuzzy displaced vertices in pp collision at $\sqrt{s} = 13$ TeV with the LHC-ATLAS detector

Risa Ushioda
Tokyo Institute of Technology, Department of Physics
Jinnouchi Lab.

August 23, 2024

Abstract

The Standard Model (SM) accurately predicts most of the experimental results from particle physics. However, there are several problems that the SM cannot explain, such as the existence of dark matter and the fine tuning problem of the Higgs boson mass. Many theories beyond the SM are proposed to solve such problems. One of the most famous and comprehensive models is the Supersymmetry (SUSY).

Among many SUSY models, this thesis focuses on a model called bino-wino co-annihilation scenario, which is motivated by dark matter relic density. In this model, the second lightest neutralino $\tilde{\chi}_2^0$ can have a decay length measurable by the collider experiments. This thesis presents the search for the pair production of the second lightest neutoralino $\tilde{\chi}_2^0$ and the lightest chargino $\tilde{\chi}_1^\pm$ in such model using 137 fb^{-1} of proton-proton (pp) collision at $\sqrt{s} = 13$ TeV collected by the LHC-ATLAS detector. The target process:

$$pp \to \tilde{\chi}_2^0 + \tilde{\chi}_1^\pm,\ \tilde{\chi}_1^\pm \to \tilde{\chi}_1^0 + W^*(\to ff'),\ \tilde{\chi}_2^0 \to \tilde{\chi}_1^0 + h^*(\to b\bar{b})$$

is searched using an unconventional signature. Suppose $\tilde{\chi}_2^0$ has a lifetime of an order of $\mathcal{O}(10^{-2})$-$\mathcal{O}(1)$ ns. In this case, it makes a secondary vertex away from the pp collision point with high track multiplicity and invariant mass. Such a signature called the displaced vertex (DV) helps identify the heavy neutral long-lived particle (LLP), which is not included in the SM.

The standard method for reconstructing DVs used in ATLAS cannot efficiently reconstruct them when the LLP decay includes b-quarks. A new method for DV reconstruction has been developed to solve this fatal drawback to this search. Using this new algorithm, the efficiency with which signal events have DVs with high track multiplicity and an invariant mass increased by a factor of 2–6. The first analysis using DVs reconstructed by the new method was performed. The signal region (SR) was required to have a missing transverse momentum larger than 150 GeV and at least one DV reconstructed by the new method with five or more tracks and an invariant mass larger than 10 GeV. The SM processes may have DVs that pass the selections for the SR by experimental effects. The number of background events in the SR was estimated by a new estimation method using the correlations between the DV and the other variables. After validating the validity of the estimation, the data in the SR were unblinded. Three events were observed, while the estimated number of background events was 0.81 ± 0.49. The upper limits were set based on the results. The $\tilde{\chi}_2^0$ mass up to 650 GeV is excluded at 95% confidence level for the case when $\tilde{\chi}_2^0$ lifetime is 0.03 ns, and the mass splitting between $\tilde{\chi}_2^0$ and $\tilde{\chi}_1^0$ is 50 GeV. This search gives the first exclusion limit in the LHC experiments for the target model.

Contents

1 Introduction **1**

2 Theoretical background **3**

2.1 The Standard Model . . . 3

2.1.1 Elementary particles and interactions . . . 3

2.1.2 Problems in the SM . . . 5

2.2 Supersymmetry . . . 7

2.2.1 The Minimal Supersymmetric Standard Model . . . 7

2.2.2 Supersymmetry breaking . . . 8

2.2.3 Target scenario . . . 9

2.3 Search strategy . . . 15

3 LHC and ATLAS experiment **18**

3.1 LHC . . . 18

3.1.1 Overview . . . 18

3.1.2 LHC in Run 2 . . . 19

3.2 ATLAS Detector . . . 21

3.2.1 Magnet system . . . 22

3.2.2 Inner detector . . . 24

3.2.3 Calorimaters . . . 28

3.2.4 Muon detector . . . 28

3.2.5 Trigger system . . . 28

3.2.6 $E_{\mathrm{T}}^{\mathrm{miss}}$ trigger . . . 31

4 Data and simulation samples **34**

4.1 Data samples . . . 34

4.2 Simulation samples . . . 35

4.2.1 Event generation . . . 35

4.2.2 Detector simulation . . . 38

5 Physics object reconstruction **39**
5.1 Track . . . 39
5.1.1 Inside-out tracking . . . 42
5.1.2 Outside-in tracking . . . 43
5.2 Large radius tracking . . . 43
5.3 Primary vertex (PV) . . . 46
5.4 Jet . . . 47
5.4.1 Calo jet . . . 47
5.4.2 Track jet . . . 49
5.5 Electron and Photons . . . 49
5.6 Muon . . . 49
5.7 Overlap removal . . . 50
5.8 Missing transverse momentum ($E_{\mathrm{T}}^{\mathrm{miss}}$) . . . 50

6 Displaced vertex reconstruction **52**
6.1 Standard displaced vertex . . . 52
6.1.1 Form two-track seed vertices . . . 52
6.1.2 Form multi-track vertex . . . 53
6.1.3 Track attachment . . . 54
6.2 Special displaced vertex . . . 54
6.2.1 Machine learning for seed track pair selection . . . 56
6.2.2 Form two-track seed vertices . . . 56
6.2.3 Multi-track vertex reconstruction . . . 58
6.3 Displaced vertex reconstruction performance . . . 60
6.3.1 Signal DV reconstruction efficiency . . . 60
6.3.2 Features of reconstructed signal DVs . . . 60
6.3.3 Background DV rate . . . 62

7 Event selection **68**
7.1 Trigger and filter . . . 68
7.1.1 DRAW filter . . . 68
7.1.2 SUSY15 filter . . . 70
7.2 Event cleaning . . . 70
7.3 PV selection . . . 71
7.4 Offline $E_{\mathrm{T}}^{\mathrm{miss}}$ selection . . . 71
7.5 Non-collision background veto . . . 71
7.6 Dead Tile module veto . . . 73
7.7 DV selection . . . 73
7.7.1 Baseline DV selection . . . 77
7.7.2 DV-track selection . . . 78

7.7.3 Signal DV selection . . . 84
7.8 Signal selection efficiency . . . 85

8 Background estimation **89**
8.1 Background component . . . 89
8.2 Background estimation strategy . . . 90
8.2.1 Variables correlated with DVs . . . 92
8.2.2 Background estimation procedure . . . 96
8.3 Uncertainty of background estimation . . . 98
8.4 Validation . . . 100
8.4.1 Inside material region . . . 100
8.4.2 Low number of seed region . . . 100
8.4.3 Low track multiplicity/low mass region . . . 102

9 Systematic uncertainties **105**
9.1 Uncertainties on tracking efficiency . . . 105
9.2 Uncertainties on $E_{\mathrm{T}}^{\mathrm{miss}}$ trigger efficiency . . . 107
9.3 Uncertainty on offline $E_{\mathrm{T}}^{\mathrm{miss}}$ . . . 109
9.4 Luminosity . . . 110
9.5 Theoretical uncertainties . . . 110

10 Results **111**
10.1 Expected signal events . . . 111
10.2 Observed events . . . 111

11 Interpretation and discussion **117**
11.1 Statistical analysis . . . 117
11.2 Interpretation on bino-wino model . . . 120
11.2.1 Limit setting . . . 120
11.2.2 Discussion on observed events . . . 121
11.3 Possible future improvements . . . 124

12 Conclusion **129**

Acknowledgments **133**

Acronyms

The following acronyms are often used in this thesis.

pp	proton-proton.
BDT	Boosted decision tree.
CL	Confidence level.
DM	Dark matter.
DV	Displaced vertex.
EW	Electroweak.
IBL	Insertable B-layer.
ID	Inner detector.
ISR	Initial state radiation.
LHC	Large Hadron Collider.
LLP	Long-lived particle.
LSP	Lightest SUSY particle.
MC	Monte Carlo.
MET ($E_{\mathrm{T}}^{\mathrm{miss}}$)	Missing transverse momentum.
MTR	$E_{\mathrm{T}}^{\mathrm{miss}}$-triggered region.
MSSM	Minimal Supersymmetric Standard Model.
NCB	Non-collision background.
Pixel	Pixel detector.
PDF	Parton distribution function.
PTR	Photon-triggered region.
PV	Primary vertex.
SCT	Semiconductor tracker.
SM	Standard Model.
SR	Signal region.
SUSY	Supersymmetry.
TRT	Transition radiation tracker.
QCD	Quantum chromodynamic.
VR	Validation region.

Chapter 1

Introduction

Particle physics has revealed the origin of the matter and the interactions between them. The Standard Model [1, 2, 3, 4] is a powerful theory explaining the nature of the elementary particles and how they interact via strong, weak, and electromagnetic forces. It accurately predicts most of the experimental results from particle physics. The verification of the Standard Model was finally completed by the discovery of the Higgs boson using the Large Hadron Collider (LHC) by the ATLAS and CMS experiments in 2012 [5, 6]. On the other hand, many astronomical observations, for example, galaxy rotation curves [7, 8, 9], gravitational lensing [10] and Bullet cluster [11], indicate that there is unknown massive object called "dark matter" in Universe. According to the recent measurements from the cosmological microwave background [12], the matter we know composes only approximately 16% of the matter in the Universe [1)].

Many theories beyond the Standard Model have been proposed to explain the existence of dark matter and other problems in the Standard Model. Out of many theories, one comprehensive scenario is the supersymmetry (SUSY). Despite the LHC experiments have been searching vigorously for the SUSY since the beginning of the LHC operation in 2009, there have been no signs of it. However, it is still early to say that we have exhaustively searched all the regions of parameter space that are explorable with the LHC. The signs of the SUSY may be hidden in somewhere more challenging parameter space.

The work presented in this thesis targets the search for long-lived SUSY particles decaying in the ATLAS detector. Since the ATLAS detector is not designed to search for long-lived particles, this search is challenging and requires special techniques to reconstruct specific signatures called displaced vertices. A displaced vertex can be reconstructed when a long-lived neutral particle decays into multiple charged particles after traveling a sizable distance ($\gtrsim$ 4 mm) in the detector. Since the Standard Model does not have a long-lived heavy particle, a displaced vertex with high track multiplicity and high invariant mass is a powerful discriminant that suppresses the background events. Several SUSY scenarios contain SUSY particles that give such signatures. This thesis presents the search for long-lived SUSY particles in the bino-wino co-annihilation scenario [13, 14] with the ATLAS detector using the LHC Run 2 dataset. This scenario is interesting from the point of view of dark matter. However, it is particularly challenging to search because the objects in the final state are soft due to small mass splitting between the lightest and the next lightest SUSY particles. I developed a new algorithm to reconstruct displaced vertices to

[1)] In terms of the total energy in the Universe, this only accounts for 5%.

enable this search. I also contributed to most of the analysis steps, including event selection, background estimation, systematic uncertainty on the signal events, and interpretation of the results.

This thesis begins with the motivation of the SUSY and clarification of the target model in Chapter 2. Chapter 3 introduces an overview of the experimental setup: the LHC and the ATLAS detector. Chapter 4 explains the actual data and simulated samples used for this analysis. Chapters 5 and 6 describe the methods and performances of the object reconstructions. Chapters 7 and 8 detail the selection criteria for the signal region, which is used to evaluate the signal's existence, and the estimation of the Standard Model background events that pass the criteria. Chapter 9 describes the systematic uncertainties of the signal events, which affects the sensitivity. Chapter 10 shows the results, and Chapters 11 gives their interpretation. Finally, Chapter 12 concludes this thesis.

Chapter 2

Theoretical background

This chapter describes the overview of the Standard Model (SM), and the suprsymmetry (SUSY), one of the most attractive and comprehensive extensions of the SM. A detailed description of the SUSY model, on which this thesis focus, is also provided. In this thesis, particle mass and energy are usually expressed in natural units where the speed of light c and the reduced Planck constant $\bar{h}$ are set to 1.

2.1 The Standard Model

The SM of particle physics is a quantum filed theory which explains all elemental particles and the interactions between them. Most experimental observations and measurements in the particle physics agree with the predictions from the SM with a great accuracy. The SM has been established in 1970s. It composes Glashow-Weinberg-Salam theory [1, 2, 3], which describes electromagnetic and weak interactions, and Quantum cayromodynamics (QCD) [4], which describes strong interactions. These theories are based on $SU(3)_C \otimes SU(2)_L \otimes U(1)_Y$ gauge symmetry, where C, L, and Y are the color charge, weak isospin, and hyperchage, respectively. A famous form of the SM Lagrangian is written as:

$$\mathcal{L}_{\mathrm{SM}} = -\frac{1}{4}F_{\mu\nu}F^{\mu\nu} + i\bar{\psi}\not{D}\psi + \psi_i y_{ij}\psi_j\phi + |D_\mu\phi|^2 - V(\phi). \tag{2.1}$$

The first term is the product of the field strength tensor $F_{\mu\nu}$ of the gauge field (photon, W, Z, and gluon). The second term describes the interaction between fermions and gauge fields. The field ψ describes fermion, and $\not{D}$ is the covariant derivative, featuring all the gauge bosons except their self-interactions. The third term describes how fermions couple to the Higgs field ϕ and obtain their mass. y_{ij} is the matrix of Yukawa coupling, representing the coupling parameters to the Higgs field. The fourth term describes how gauge bosons couple to the Higgs field. The last term is the Higgs potential $V(\phi)$. Unlike other fields, this potential does not have a minimum at zero, but has different minima. This is caused by the spontaneous symmetry breaking.

2.1.1 Elementary particles and interactions

Elementary particles in the SM include the ferminos (quarks and leptons) and the bosons (gauge bosons and Higgs boson). Figure 2.1 shows the summary of the SM particles.

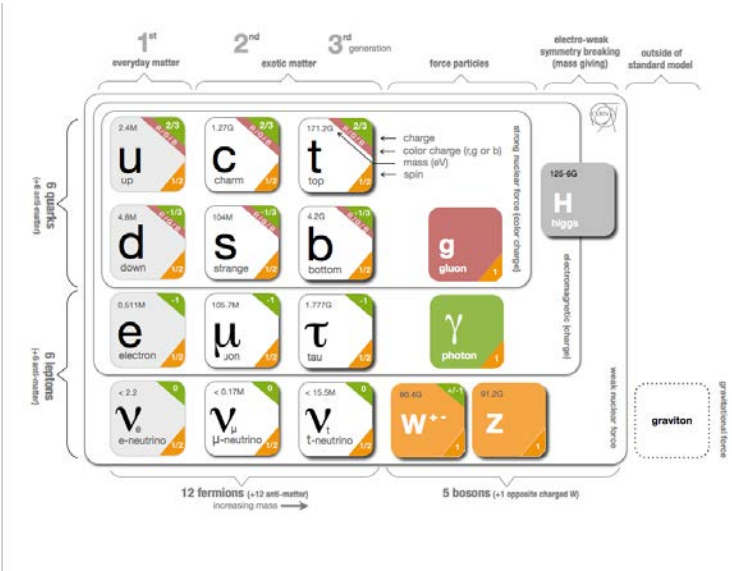

Figure 2.1: Elementary particles in the SM [15]. Graviton is not included in the SM.

Fermions have spin 1/2 and consist matters. Fermions that participate in the strong interaction are called quarks. There are six quarks, and they are further categorized into up-type (+2/3) and down-type (−1/3) by their electronic charge. Fermions that do not participate in the strong interaction are called leptons. There are six leptons, and three of them are electorically neutral, called "neutrinos." Neutrinos are assumed to be massless in the SM. Both quarks and leptons have three generations. The mass of the quarks and charged leptons increases with each generation. Fermions have two eigenstates of left-handed and right-handed chiralities. Since neutrinos are assumed to be massless, only left-handed neutrinos are considered.

Gauge bosons have spin 1 and mediate the fundamental interactions between elementary particles. Photon (γ) mediates the electromagnetic interaction. W-bosons ($W^{\pm}$) and Z-boson (Z^0) carry the charged and neutral current in weak interaction, respectively. Gluons mediate the strong interaction between color-charged elementary particles.

The Higgs boson has spin 0. The Higgs filed feeds masses to elementary particles by the Higgs-Englert-Brout mechanism, and the Higgs boson is the excited state of the Higgs filed.

The massless electroweak gauge bosons $W^i (i = 1, 2, 3)$ and B acquire masses after spontaneous symmetry breaking. The mass eigenstates of gauge bosons are written as follows:

$$W^{\pm} = \frac{1}{\sqrt{2}}(W^1 \mp iW^2), \tag{2.2}$$

$$\begin{pmatrix} Z \\ \gamma \end{pmatrix} = \begin{pmatrix} \cos\theta_W & -\sin\theta_W \\ \sin\theta_W & \cos\theta_W \end{pmatrix} \begin{pmatrix} W^3 \\ B \end{pmatrix}. \tag{2.3}$$

Here, θ_W is called Weinberg angle defined by the coupling constants g_W, g_B.

$$\tan\theta_W = g_B/g_W. \tag{2.4}$$

2.1.2 Problems in the SM

Fine tuning problem

The Higgs boson was discovered in 2012 [5, 6], and its mass was measured as approximately 125 GeV. The SM Higgs filed is a complex scalar H, and its potential can be written as follows:

$$V = \mu^2|H|^2 + \lambda|H|^4. \tag{2.5}$$

When $\lambda > 0$ and $\mu^2 < 0$, the potential takes the minimum at the vacuum expectation value given with:

$$\langle H \rangle = \sqrt{-\frac{\mu^2}{2\lambda}} = \frac{v_0}{\sqrt{2}}, \tag{2.6}$$

where v_0 is known to be approximately 246 GeV from measurements of the properties of weak interactions. The mass of the Higgs boson m_H is given as:

$$m_H = \sqrt{-2\mu^2} = v_0\sqrt{2\lambda}. \tag{2.7}$$

When the $m_H = 125$ GeV, we obtain $\lambda = 0.13$ and $\mu^2 = -(89\text{ GeV})^2$ under the assumption that the SM is correct as an effective field theory. The m_H^2 receives quantum corrections from the virtual effects of particles or other phenomenon that couple to H. Figure 2.2 shows the correction to the Higgs mass from one-loop by a fermion with mass m_f. This correction is given by:

$$\Delta m_H^2 = -\frac{|\lambda_f|^2}{8\pi^2}\Lambda^2 + O(\ln\Lambda), \tag{2.8}$$

where λ_f is the Yukawa coupling and Λ is a cutoff energy scale up to which the SM is valid (Planck scale). Each lepton and quark in the SM can make the correction represented by Equation 2.8. The major correction is given by the top quark with $\lambda_f \simeq 0.94$. Therefore, the observed Higgs mass is expressed as:

$$m_H^2 \simeq m_{H,\text{bare}}^2 - \frac{|0.94|^2}{8\pi^2}\Lambda^2 + ..., \tag{2.9}$$

where $m_{H,\text{bare}}$ is the bare Higgs mass. Since the Planck scale is $O(10^{19})$ GeV, then this quantum correction to m_H^2 is more than 30 orders of magnitudes larger than the required value of m_H^2. If we do not assume any additional mechanism, the squared bare Higgs mass is required to be the same as the correction with more than 30 digits of precision to achieve the observed Higgs mass. This unnaturally huge cancellation is called the "fine tuning problem."

Dark matter

Astrophysical and cosmological observations suggest that some unknown matter, which has gravitational interaction, exists in the universe. An example is the galaxy rotation curves [7, 8, 9]. The rotational velocity, which is the orbital velocity of visible stars and gas in the galaxy as a function of the radial distance, r, between the center of the galaxy and the orbital object was measured. The rotational velocity

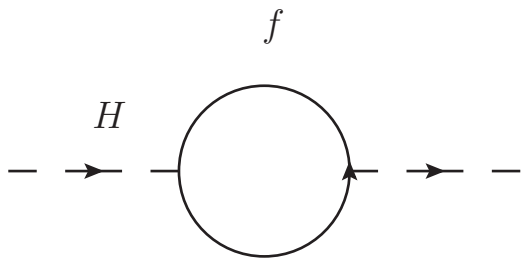

Figure 2.2: One-loop correction to the m_H from a fermion f.

is expected to be proportional to $1/\sqrt{r}$ if only visible objects were assumed to exist. However, the measured velocity was approximately constant in the region with large r. This means that there are invisible massive objects in the garaxy and such an object is called "dark matter (DM)."

The measurements of the gravitational lensing [10] is another evidence showing the existence of DM. The gravitational lensing is a phenomena in which the path of light is bent by the gravity of massive objects between a light source and the observer, distorting the shape of the image of the light source. The measured gravitational lensing of the galaxies could not be explained by the mass predicted from the spectrum of emitted light, implying the invisible mass sources. Not only the gravitational lensing from a single cluster of galaxies but also from two colliding clusters of galaxies strongly supports the existence of DM [11]. The two clusters of galaxies have moved ahead of their respective plasma cloud. If there was no DM, their gravitational distribution would move along the dominant visible matter component, which is the X-ray plasma. If the mass was dominated by DM, the mass distribution would trace that component, which was expected to be spatially consistent with the center of each galaxy cluster. The estimated mass distribution of them based on the measurement of gravitational lensing supported the latter hypothesis. The recent cosmic microwave background (CMB) measurement reported that the baryon density Ω_b and the dark matter density Ω_c of Universe are [12]:

$$\Omega_b h^2 = 0.0224 \pm 0.0001 \Rightarrow \Omega_b \simeq 5\%, \tag{2.10}$$

$$\Omega_c h^2 = 0.120 \pm 0.001 \Rightarrow \Omega_c \simeq 26\%, \tag{2.11}$$

where h is the scaling factor for Hubble constant, measured as 0.674 [12].

There are several types of DM. If DM is assumed to be composed of elementary particles, they should have the following properties to explain the observations:

- They do not have electromagnetic and strong interactions
- They are stable
- They have a finite mass and then interact though the gravitational interaction

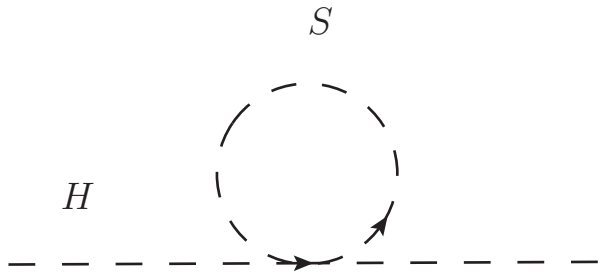

Figure 2.3: One-loop correction to the m_H from a scalar particle S.

2.2 Supersymmetry

A supersymmetry (SUSY) is a symmetry relating boson and fermion. An operator Q that generates the transformation from a formionic (bosonic) into a bosonic (fermionic) state are introduced as follows:

$$Q\,|\text{Fermion}\rangle = |\text{Boson}\rangle\,,\ Q\,|\text{Boson}\rangle = |\text{Fermion}\rangle\,, \tag{2.12}$$

Since the angular momentum must be invariant in Equation 2.12, the operator Q is fermionic.

The SUSY gives a solution to the fine-tuning problem. A scalar particle coupled to the Higgs boson gives a correction to the Higgs mass via the diagram in Figure 2.3. This correction is given by:

$$\Delta m_H^2 = \frac{\lambda_S}{16\pi^2}\Lambda^2 + O(\ln\Lambda) \tag{2.13}$$

Therefore, if every SM fermion is accompanied by two scalar partners with $\lambda_S = |\lambda_f|^2$, the quadratic terms are nearly cancelled out.

2.2.1 The Minimal Supersymmetric Standard Model

In the minimal extension of the SM, called the Minimal Supersymmetric Standard Model (MSSM), each elementary particle must have a superpartner with spin difference of 1/2. More detail is described in Ref. [16].

The superpartners of the SM fermions are called "sfermions", denoted by $\tilde{f}$. Each SM fermion has two scalar partners, one for left-handed and the other for the right-handed fermion.

Although the SM contains one Higgs doublet, two Higgs doublets, denoted (H_u^+, H_u^0) and (H_d^0, H_d^-), are introduced in the case of the MSSM. These two doublets have eight degrees of freedom. Three of them are used for $W^\pm, Z^0$ masses, and the remaining five of them give five mass eignestates, two CP even neutral Higgs bosons (h^0 and H^0), one CP odd neutral Higgs boson (A^0) and two charged Higgs bosons ($H^\pm$). Their superpartoners are called "higgsinos", and denoted by $\tilde{H}_u^-, \tilde{H}_u^0$ and $\tilde{H}_d^-, \tilde{H}_d^0$.

The superpartners of the SM vector bosons are referred to as "gauginos." The gluon superpartner is called "gluino" ($\tilde{g}$) and electroweak gauge boson partners are called "winos" ($\tilde{W}^\pm$ and $\tilde{W}^0$) and "bino" ($\tilde{B}$). The SM W^3 and B gauge eigenstates form mass eigenstates Z^0 and γ after electroweak symmetry braking. The corresponding mass eigenstates of neutral wino and bino are called "zino" and "photino." Tables 2.1 and 2.2 summarize all the SUSY and SM particles included in the MSSM.

Table 2.1: Fermions, Higgs bosons, and their super partners of the MSSM [17].

Names		spin 0	spin 1/2	$SU(3)_C$, $SU(2)_L$, $U(1)_Y$
squarks, quarks (×3 families)	Q	$(\tilde{u}_L, \tilde{d}_L)$	(u_L, d_L)	$(\mathbf{3}, \mathbf{2}, 1/6)$
	$\bar{u}$	$\tilde{u}_R^*$	$u_R^\dagger$	$(\bar{\mathbf{3}}, \mathbf{1}, -2/3)$
	$\bar{d}$	$\tilde{d}_R^*$	$d_R^\dagger$	$(\bar{\mathbf{3}}, \mathbf{1}, 1/3)$
sleptons, leptons (×3 families)	L	$(\tilde{\nu}, \tilde{e}_L)$	(ν, e_L)	$(\mathbf{1}, \mathbf{2}, -1/2)$
	$\bar{e}$	$\tilde{e}_R^*$	$e_R^\dagger$	$(\mathbf{1}, \mathbf{1}, 1)$
Higgs, higgsinos	H_u	(H_u^+, H_u^0)	$(\tilde{H}_u^+, \tilde{H}_u^0)$	$(\mathbf{1}, \mathbf{2}, +1/2)$
	H_d	(H_d^0, H_d^-)	$(\tilde{H}_d^0, \tilde{H}_d^-)$	$(\mathbf{1}, \mathbf{2}, -1/2)$

Table 2.2: Gauge bosons and their super partners of the MSSM [17].

Names	spin 1/2	spin 1	$SU(3)_C$, $SU(2)_L$, $U(1)_Y$
gluino, gluon	$\tilde{g}$	g	$(\mathbf{8}, \mathbf{1}, 0)$
winos, W bosons	$\tilde{W}^\pm$ $\tilde{W}^0$	$W^\pm$ W^0	$(\mathbf{1}, \mathbf{3}, 0)$
bino, B boson	$\tilde{B}^0$	B^0	$(\mathbf{1}, \mathbf{1}, 0)$

To explain the fact that the lepton number and baryon number violating processes have not been seen experimentally, a new symmetry called "R-parity" [18] is introduced in the MSSM:

$$R = (-1)^{3(B-L)+2S}, \tag{2.14}$$

where B, L and S are the baryon number, the lepton number and the spin, respectively. Equation 2.14 shows that all the SM particles have R-parity of 1, while all the SUSY particles have R-parity of -1. Under R-parity conservation, the SUSY particles are always produced in pairs and their decay products include an odd number of SUSY particles. Therefore, the lightest SUSY particle (LSP) must be stable and become a possible candidate for DM.

2.2.2 Supersymmetry breaking

Since any SUSY particles have not been observed, the supersymmetry must be a broken symmetry. These breaking terms should be "soft" to prevent divergence in the Higgs mass. It means that the Lagrangian of MSSM can be divided into two components:

$$\mathcal{L}_{\text{MSSM}} = \mathcal{L}_{\text{SUSY}} + \mathcal{L}_{\text{soft}}, \tag{2.15}$$

where $\mathcal{L}_{\text{SUSY}}$ is SUSY conserving part, and $\mathcal{L}_{\text{soft}}$ is the SUSY breaking part which has only mass terms and coupling parameters with positive mass dimension [1)]. The soft SUSY breaking terms in MSSM are

[1)] The non-supersymmetric correction to the squared Higgs mass needs to be vanished in the $m_{\text{soft}} \to 0$ limit, where m_{soft} is the mass scale associated with the soft term, in order to keep the cancellations to the Higgs mass intact.

expressed as:

$$\begin{aligned}\mathcal{L}_{\text{soft}}^{\text{MSSM}} = &-\frac{1}{2}(M_3\tilde{g}\tilde{g} + M_2\tilde{W}\tilde{W} + M_1\tilde{B}\tilde{B} + c.c.) \\ &- (\tilde{u}\mathbf{a_u}\tilde{Q}H_u - \tilde{\bar{d}}\mathbf{a_d}\tilde{Q}H_d - \tilde{\bar{e}}\mathbf{a_e}\tilde{L}H_d + c.c.) \\ &- \tilde{Q}^\dagger\mathbf{m_Q^2}\tilde{Q} - \tilde{L}^\dagger\mathbf{m_L^2}\tilde{L} - \tilde{u}\mathbf{m_{\bar{u}}^2}\tilde{\bar{u}}^\dagger - \tilde{\bar{d}}\mathbf{m_{\bar{d}}^2}\tilde{\bar{d}}^\dagger - \tilde{\bar{e}}\mathbf{m_{\bar{e}}^2}\tilde{\bar{e}}^\dagger \\ &- m_{H_u}^2 H_u^* H_u - m_{H_d}^2 H_d^* H_d - (bH_u H_d + c.c.),\end{aligned} \tag{2.16}$$

where M_1, M_2 and M_3 are the bino, wino, and gluino mass terms. $\mathbf{a}_i$ $(i = u, d, e)$ is a complex 3×3 matrix in generation space with dimension of mass, which is in one-to-one correspondence with the Yukawa couplings of the superpotential. $\mathbf{m}_i^2$ $(i = Q, L, \bar{u}, \bar{d}, \bar{e})$ is a squark or slepton mass term described as a complex 3×3 matrix in generation space. $m_{H_u}^2$, $m_{H_d}^2$, and b are the squared-mass terms and contribute to the Higgs potential. In total, 105 additional masses, phases, and mixing angles are included in the MSSM.

The neutral gauginos and higgsinos mix and form four mass eigensitates called "neutralinos" $\tilde{\chi}_i^0$ $(i = 1, 2, 3, 4)$ because they have the same quantum numbers. The index i is labeled in ascending order with mass. In the same way, charged gauginos and higgsinos form two mass eigenstates called "charginos" $\tilde{\chi}_i^\pm$ $(i = 1, 2)$. The neutralino mass matrix which describes this mixing is written as [17]:

$$\mathcal{M}_{\tilde{\chi}^0} = \begin{pmatrix} M_1 & 0 & -m_Z \sin\theta_W \cos\beta & m_Z \sin\theta_W \sin\beta \\ 0 & M_2 & m_Z \cos\theta_W \cos\beta & -m_Z \cos\theta_W \sin\beta \\ -m_Z \sin\theta_W \cos\beta & m_Z \cos\theta_W \cos\beta & 0 & -\mu \\ m_Z \sin\theta_W \sin\beta & -m_Z \cos\theta_W \sin\beta & -\mu & 0 \end{pmatrix}, \tag{2.17}$$

where θ_W is the Weinberg angle and β is a parameter defined by the ratio of two vacuum expectation values:

$$\tan\beta = \frac{\langle H_u^0 \rangle}{\langle H_d^0 \rangle}. \tag{2.18}$$

$$\mathcal{M}_{\tilde{\chi}^\pm} = \begin{pmatrix} \mathbf{0} & \boldsymbol{X}^{\boldsymbol{T}} \\ \boldsymbol{X} & \mathbf{0} \end{pmatrix}, \text{ with } \boldsymbol{X} = \begin{pmatrix} M_2 & \sqrt{2} m_W \sin\beta \\ \sqrt{2} m_W \sin\beta & \mu \end{pmatrix}. \tag{2.19}$$

2.2.3 Target scenario

The lightest neutralino is an attractive candidate of DM under R-parity conservation in the MSSM. In the early universe, SUSY particles existed in thermal equilibrium with the SM particles. As the universe cooled and expended, the production cross-section of the heavy SUSY particles was suppressed, and they annihilated or decayed to the LSPs. Since some of LSPs annihilated to the SM particles, a mechanism to suppress the annihilation is necessary in order to explain the dark matter relic density. If there are other SUSY particles slightly heavier than the LSP, they existed in thermal equilibrium with the LSP.

Figure 2.4 shows a result of phenomenological MSSM (pMSSM) scan indicating which type of LSP is favored. It assumes several experimental constraints to reduce the number of parameters included in the

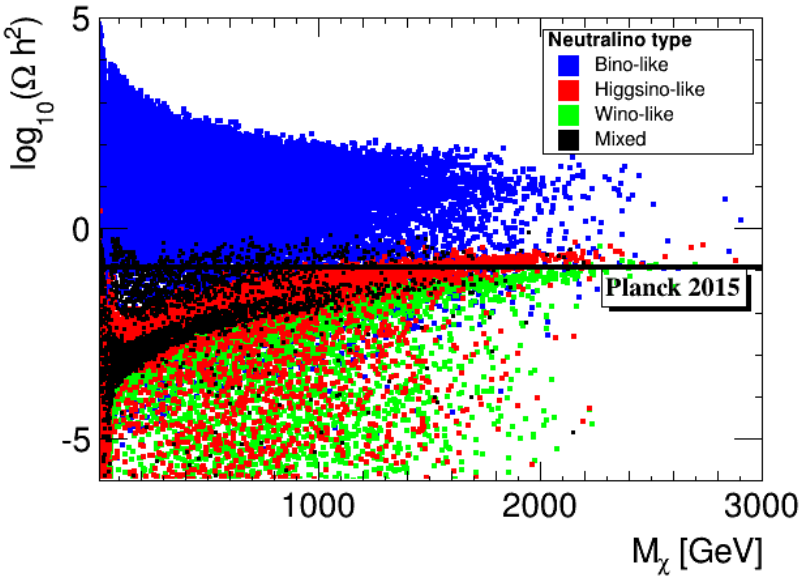

Figure 2.4: DM relic density depending on the LSP type [19]. 'Mixed' means the case where DM is composed of any combination of bino, higgsiono, and wino.

MSSM. Generally, the DM relic density estimated from the bino-like DM is higher than the observation, because of its small self-annihilation cross section. However, if there is another SUSY particle with mass close to the bino, the observed DM relic density can be well explained by the co-annihilation mechanism. This thesis focuses on the co-annihilation of the bino and wino. Figure 2.5 shows the mass spectrum of this scenario. $\tilde{\chi}_1^0$ becomes bino-like, $\tilde{\chi}_2^0$ and $\tilde{\chi}_1^\pm$ become wino-like. $\tilde{\chi}_3^0$, $\tilde{\chi}_4^0$, and $\tilde{\chi}_2^\pm$ are higgsino-like and much heavier than $\tilde{\chi}_1^0$, $\tilde{\chi}_2^0$, and $\tilde{\chi}_1^\pm$. We assume that sfermion mass scale is similar to or larger than the higgsino mass, and then their contributions to the $\tilde{\chi}_2^0$ or $\tilde{\chi}_1^\pm$ decay are negligible. In this case, the predicted DM relic density is reduced by the co-annihilation shown in Figure 2.6.

In order to avoid overproduction of DM, M_2 must be close to the M_1. Figure 2.7 shows the region that explain the observed DM relic density as a function of bino mass and mass difference between the bino and wino. We focus on the case when the ΔM is $\mathcal{O}(10)$ GeV, which well explain the observed DM relic density.

Gaugino lifetime and decay mode

The decay rate of the winos to the bino LSP depends on the Higgsino mass, refered to μ. A wino-like $\tilde{\chi}_1^\pm$ decays into a bino-like $\tilde{\chi}_1^0$ and a pair of fermions via off-shell W-boson exchange as shown in Figure 2.8. This decay is caused by the bino-wino mixing and typically immediate. On the other hand, decay of the wino-like $\tilde{\chi}_2^0$ is not always rapid. Since ΔM is assumed to be smaller than the Z-boson mass, the $\tilde{\chi}_2^0$ can decay into a $\tilde{\chi}_1^0$ and a pair of fermions. It occurs through the off-shell Z or Higgs boson exchange as shown in Figure 2.9. $\tilde{\chi}_2^0$'s decay widths into a pair of fermions $f\bar{f}$ via Higgs boson Γ_f^h, and the one via

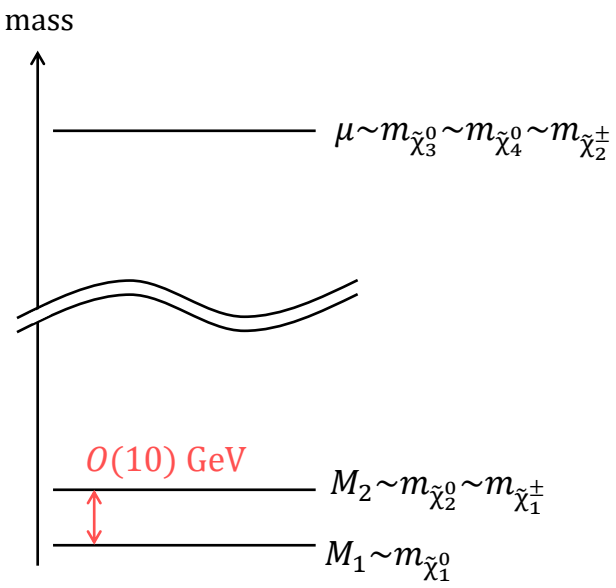

Figure 2.5: Mass spectrum of gauginos in bino-wino co-annihilation scenario.

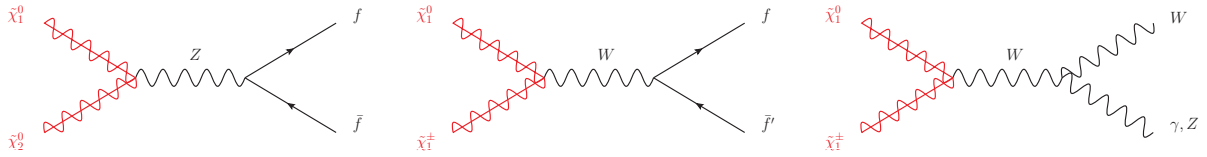

Figure 2.6: Contributions to the co-annihilation of dark matter $\tilde{\chi}_1^0$ LSPs with slightly heavier $\tilde{\chi}_2^0$ and $\tilde{\chi}_1^\pm$.

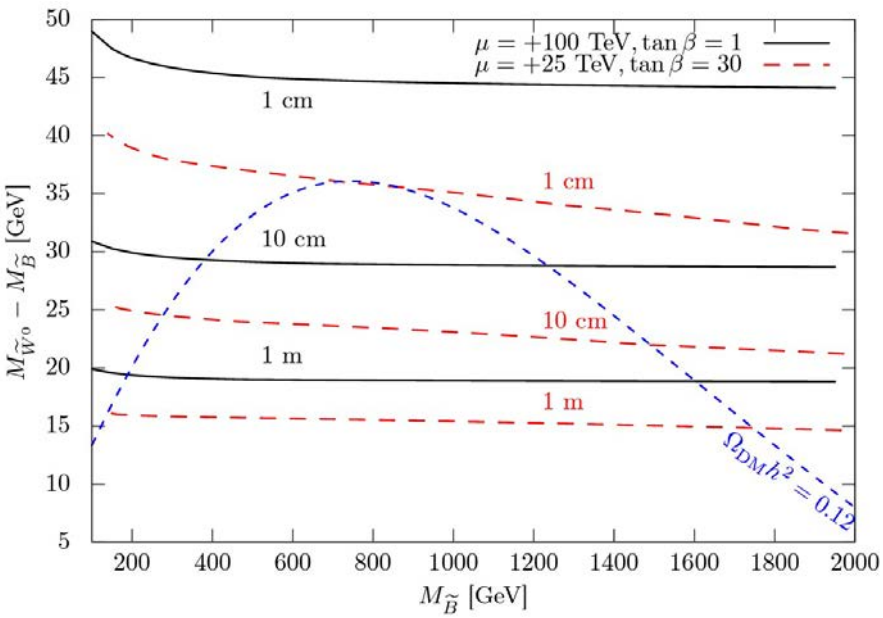

Figure 2.7: The relation between the DM relic density (blue dashed line) and bino mass ($M_{\tilde{B}^0}$) and mass difference between bino and wino ($M_{\tilde{W}^0} - M_{\tilde{B}^0}$) [14]. The black and red lines show the decay length of $\tilde{W}^0$ with fixed μ and $\tan\beta$. Equation 2.23 is an approximation of the formula used to calculate these decay lengths.

Z-boson Γ_f^Z are given by [13]:

$$\Gamma_f^h(\tilde{\chi}_2^0 \to f\bar{f}\tilde{\chi}_1^0) \simeq \frac{4\alpha^2}{15\pi}\frac{(\Delta M)^5}{m_h^4}\frac{s_{2\beta}^2}{s_{2W}^2}\frac{m_f^2}{\mu^2}, \tag{2.20}$$

$$\Gamma_f^Z(\tilde{\chi}_2^0 \to f\bar{f}\tilde{\chi}_1^0) \simeq \frac{\alpha^2}{20\pi}k_Z^f\frac{c_{2\beta}^2}{s_{2W}^2}\frac{(\Delta M)^5}{\mu^4}, \tag{2.21}$$

where $s_{2\beta} = \sin 2\beta$, $c_{2\beta} = \cos 2\beta$, $s_{2W} = \sin 2\theta_W$, and $c_{2W} = \cos 2\theta_W$. k_Z^f is given by [13]:

$$k_Z^f = (2I_3 - 4Qs_W^2)^2 + (2I_3)^2, \tag{2.22}$$

where I_3 and Q are the isospin and the electric charge of the fermion f. k_Z^f for each type of fermion is obtained as follows:

$$u : 1.16$$
$$b : 1.49$$
$$e : 1.01$$
$$\nu : 2$$

As Equations 2.20 and 2.21 show, the Z-boson mediated decay is suppressed by a factor of $\cos^2 2\beta|\mu|^{-4}$, while the Higgs boson mediated decay is suppressed by a factor of $\sin^2 2\beta|\mu|^{-2}$. Figures 2.10 show the total decay width (Γ_{tot}), Higgs mediated decay width (Γ_h), and Z-boson mediated decay width (Γ_Z)

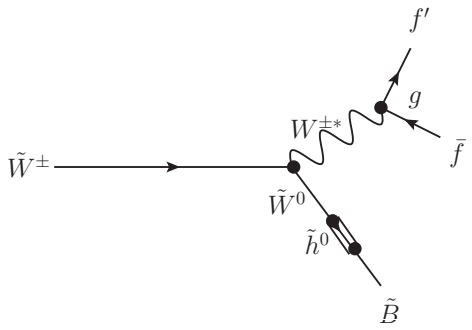

Figure 2.8: Diagrams contributing to $\tilde{W}^{\pm} \to f' \bar{f}\ \tilde{B}^0$. The coupling is proportional to $g/|\mu|$.

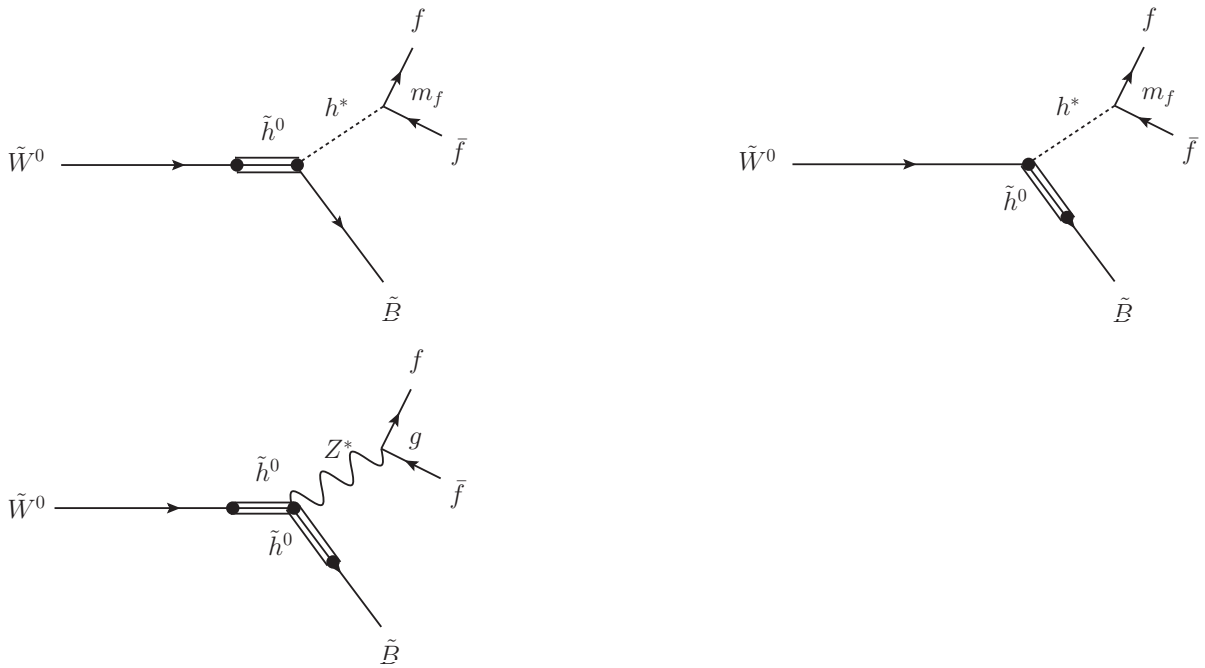

Figure 2.9: Diagrams contributing to $\tilde{W}^0 \to f \bar{f}\ \tilde{B}^0$. The coupling of $\tilde{W}^0 - \tilde{B}^0 - h^*$ is proportional to $m_f/|\mu|$ and the coupling of $\tilde{W}^0 - \tilde{B}^0 - Z^*$ is proportional to $g/|\mu|^2$. While Higgs mediated decay needs a $\tilde{h}^0$-$\tilde{W}^0$ or $\tilde{h}^0$-$\tilde{B}^0$ mixing, Z boson mediated decay needs both $\tilde{h}^0$-$\tilde{W}^0$ mixing and $\tilde{h}^0$-$\tilde{B}^0$ mixing.

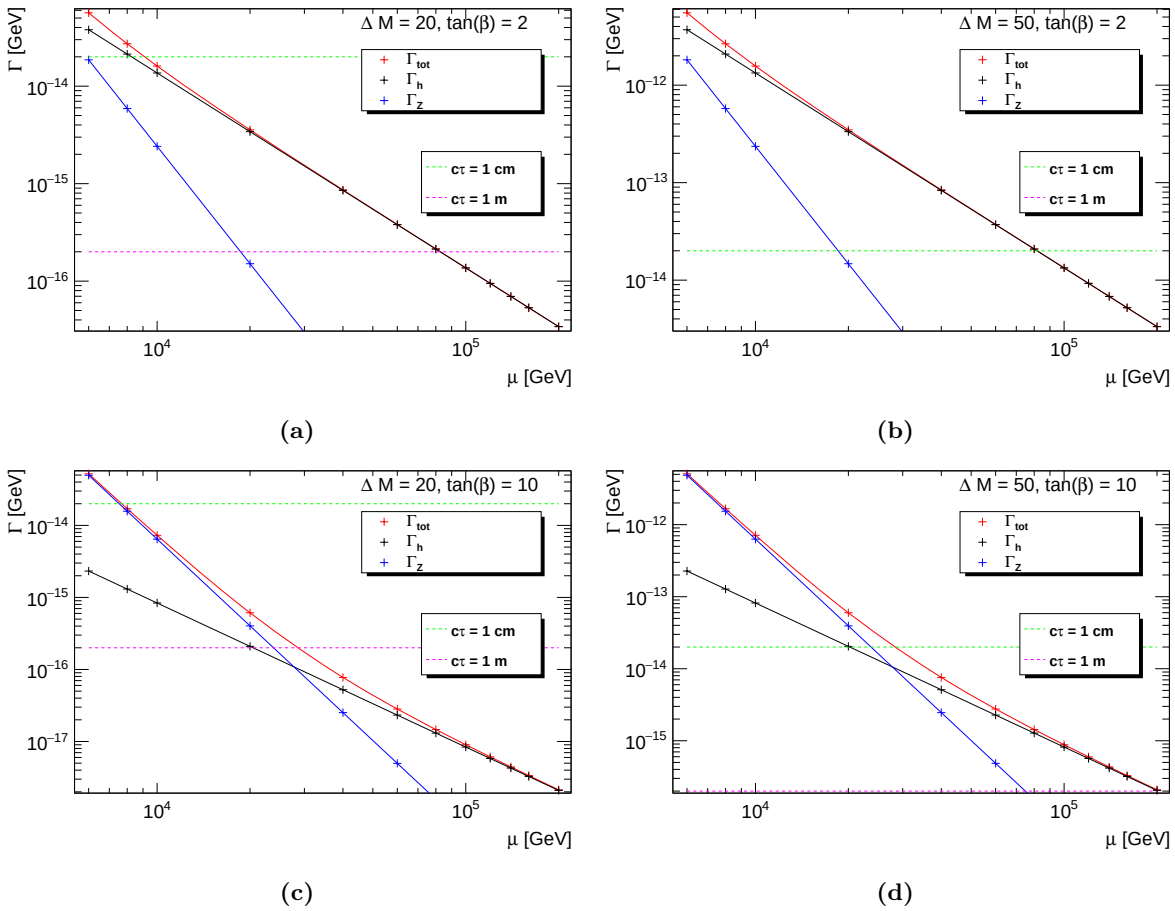

Figure 2.10: The decay width of $\tilde{\chi}_2^0$ as a function of μ with $\Delta M = 20$, 50 GeV and $\tan\beta = 2$, 10. The black line, red line, and blue lines show the total, Higgs boson mediated, and Z-boson mediated decay width. The range between around the green and pink lines corresponds the lifetime where the decay would occur in the ATLAS inner detector. The structure of the ATLAS detector is described in Chapter 3.

calculated from Equations 2.20, 2.21, and 2.22. Z-boson mediated decay becomes dominant when $|\mu|$ is relatively small and $\tan\beta$ is large, while Higgs boson mediated decay becomes dominant when $|\mu|$ is large and $\tan\beta$ is small.

Previous searches

As discussed in Section 2.2.3, the decay length and mode of the $\tilde{\chi}_2^0$ varies depending on the unknown parameters. The region with $\tilde{\chi}_1^\pm/\tilde{\chi}_2^0$ mass bellow around 100 GeV has been excluded by the results from the LEP II experiments [20]. Those searches use a photon by the initial state radiation (ISR) in $\tilde{\chi}_1^+\tilde{\chi}_1^-$ pair production or decay products from $\tilde{\chi}_1^\pm$, and they are independent from $\tilde{\chi}_2^0$'s decay mode and lifetime. Recently, the $\tilde{\chi}_1^\pm\tilde{\chi}_2^0$ pair production in the scenario where $\tilde{\chi}_2^0$ promptly decays via off-shell Z-boson is being actively searched in the collider experiments. Figure 2.11 shows the exclusion limit from previous ATLAS analyses [21]. For example, the region with $\tilde{\chi}_2^0$ mass up to around 250 GeV has been excluded when ΔM is 30 GeV. This exclusion limit was set assuming that the $\tilde{\chi}_2^0$ is prompt and decay via off-shell

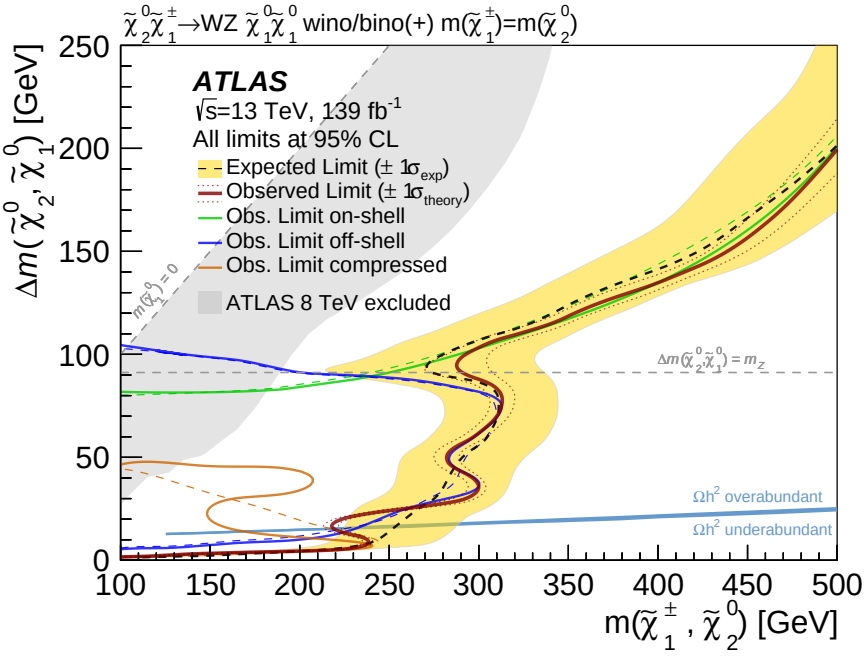

Figure 2.11: Current exclusion limits obtained for the WZ-mediated models in the bino-wino co-annihilation scenario by the ATLAS Experiment [21].

Z-boson with 100%. Scenarios other than this decay feature have not been explored with collider after LEP II experiments. Therefore, this thesis focuses on the case where $\tilde{\chi}_2^0$ is long-lived and decays via Higgs boson emission, which has not been searched enough despite the interest from the DM's point of view.

When the Higgs mediated decay is dominant, the $\tilde{\chi}_2^0$ decay length is approximated as the following formula [13]:

$$c\tau_{\tilde{\chi}_2^0} \simeq 1\ \text{cm} \times \left(\frac{\mu}{10^2\ \text{TeV}}\right)^2 \left(\frac{50\ \text{GeV}}{\Delta M}\right)^5 \left(\frac{1}{\sin 2\beta}\right)^2. \tag{2.23}$$

2.3 Search strategy

A search for pair production of $\tilde{\chi}_1^\pm\tilde{\chi}_2^0$ under bino-wino co-annihilation scenario in proton-proton (pp) collision at the Large Hadron Collider is presented in this thesis. Figures 2.12 shows the Feynman diagram of the target signal event. In this thesis, the mass of all SUSY particles other than $\tilde{\chi}_1^0$, $\tilde{\chi}_2^0$, and $\tilde{\chi}_1^\pm$ are assumed to be decoupled so that they do not affect the production cross-section or the branching ratio of $\tilde{\chi}_1^0$, $\tilde{\chi}_2^0$, and $\tilde{\chi}_1^\pm$. Since mass of gauginos satisfy $M_1 \lesssim M_2 \ll |\mu|$, wino-dominated $\tilde{\chi}_2^0$ and $\tilde{\chi}_1^\pm$, and bino-dominated $\tilde{\chi}_1^0$ are obtained. The mass of $\tilde{\chi}_2^0$ and $\tilde{\chi}_1^\pm$ is assumed to be equal. The $\tilde{\chi}_1^\pm$ is assumed to decay promptly, while the $\tilde{\chi}_2^0$ is assumed to have a lifetime of $\mathcal{O}(10^{-2})$-$\mathcal{O}(10)$ ns. Figure 2.13 shows the topology of the signal event with a hadron jet by ISR. The ISR jet is not required but it enhances the missing transverse momentum and makes the signal events more likely to be triggered. The production cross-section is calculated for pure wino $\tilde{\chi}_1^\pm\tilde{\chi}_2^0$ production, which is shown in Figure 2.14.

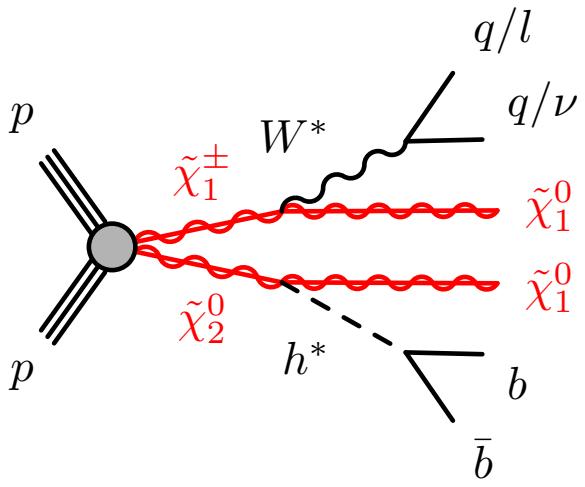

Figure 2.12: Diagram of the pair production of electrowikinos $\tilde{\chi}_2^0\tilde{\chi}_1^{\pm}$ decaying to $\tilde{\chi}_1^0$ via off-shell W-boson and Higgs boson. The off-shell Higgs decays into any pair of fermions with a mass less than itself. In the case of ΔM of a few tens of GeV, which is the target of this thesis, the dominant decay mode is the b-quark pair.

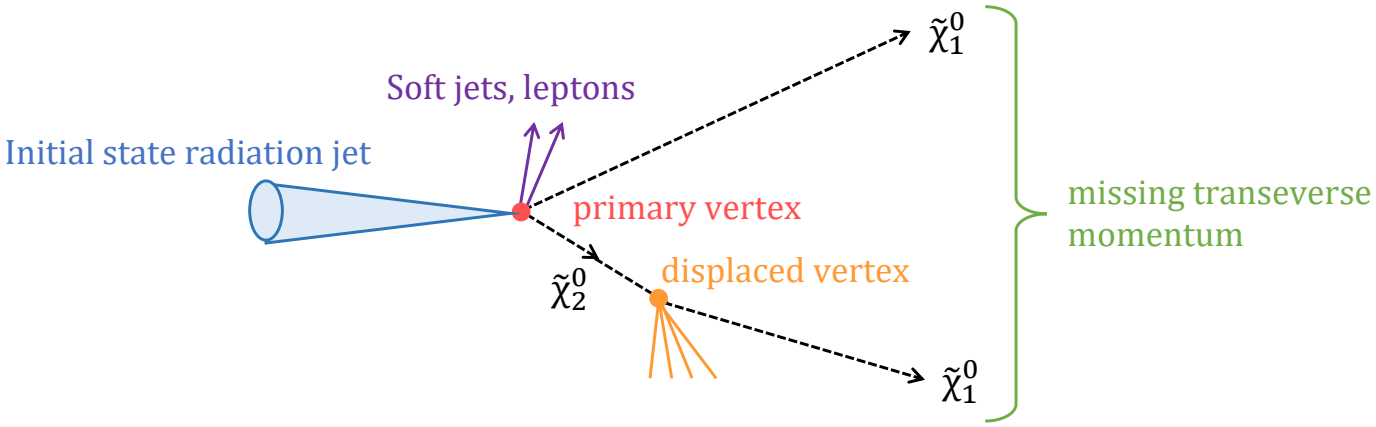

Figure 2.13: Topology of the signal event with an ISR jet.

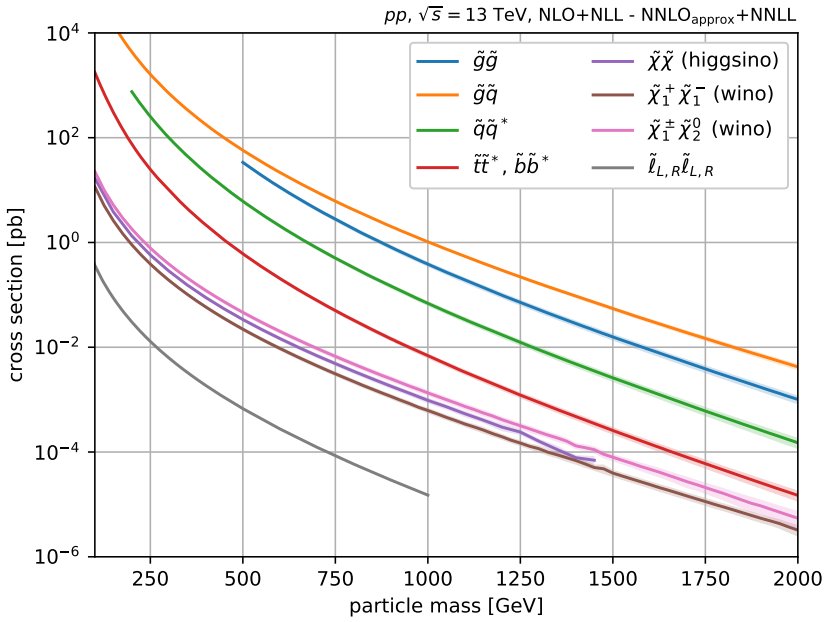

Figure 2.14: Production cross-section of SUSY particles [22]. The cross section of the signal event is calculated based on the pink line.

Chapter 3

LHC and ATLAS experiment

This analysis uses the data collected by the LHC-ATLAS experiment. This chapter gives an overview of the Large Hadron Collider (LHC) [23] and the ATLAS detector [24].

3.1 LHC

3.1.1 Overview

The LHC is a particle accelerator and collider composed of two rings with a 26.7 km circumference. It is located 100 m underground and contributed by the European Organization for Nuclear Research (CERN). It has been operated with the center-of-mass energy of 7 TeV and 8 TeV in Run 1 (2010-2012), 13 TeV in Run 2 (2015-2018), and 13.6 TeV in Run 3 (2022-). Groups of 10^{11} protons, called "bunches", are accelerated by the electromagnetic fields built from coils of electric cables. Several types of superconducting magnets are used in the LHC to bend and focus the proton bunches. Proton bunches are bent by dipole magnets, are squeezed by quadrupole magnets, and collide. Table 3.1 shows the LHC design parameters.

Figure 3.1 shows the structure of a series of accelerators. Proton beams are accelerated by four accelerators and injected into the LHC. First, protons are obtained by ionizing the electrons of hydrogen atoms. Then, the first linear accelerator (LINAC2) accelerates the protons up to 50 MeV and injects them into the Proton Synchrotron Booster (Booster). Protons are accelerated up to 1.4 GeV by the booster, up to 25 GeV by the Proton Synchrotron (PS), up to 450 GeV by the Super Proton Synchrotron (SPS),

Table 3.1: LHC design parameters [23].

Ring circumference	26.7 km
Center-of-mass energy	14 TeV
Instantaneous luminosity	1×10^{34} cm^{-2}s^{-1}
Number of protons per bunch	1.15×10^{11}
Number of bunches in the ring	2808
Collision time interval	25 ns

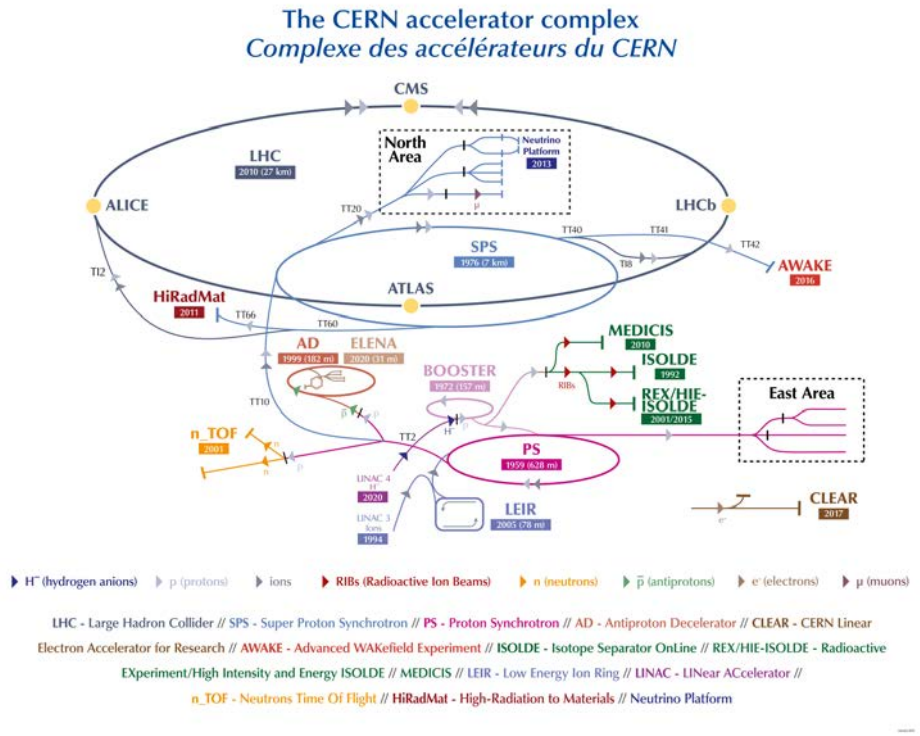

Figure 3.1: Accelerator complex at CERN [25].

and finally up to 7 TeV by the LHC.

The rate that events of interest occurs (N_{events}) is expressed in the following formula:

$$\frac{dN_{\text{events}}}{dt} = \mathcal{L}\sigma(\sqrt{s}), \tag{3.1}$$

where $\mathcal{L}$ is the instantaneous luminosity of the beam and $\sigma(\sqrt{s})$ is the cross-section of the event with center-of-mass energy of $\sqrt{s}$. The instantaneous luminosity in the pp collision at the LHC is expressed as:

$$\mathcal{L} = \frac{f_{\text{crossing}} N_{\text{bunch}}^2}{4\pi\sigma_x\sigma_y} \tag{3.2}$$

$$\simeq \frac{f_{\text{crossing}} N_{\text{bunch}}^2}{4\epsilon\beta^*}, \tag{3.3}$$

where σ_x and σ_y are the size of beam in x and y respectively, f_{crossing} is the collision frequency, N_{bunch} is the number of protons in a bunch. ϵ is a parameter called emittance, showing the property of the beam. If ϵ is small, it means that the variance of the position and axis of the particles in the beam is small. β^* is the beta function defined as $\beta = \pi\sigma_x\sigma_y/\epsilon$ at the interaction point.

3.1.2 LHC in Run 2

In Run 2, the LHC was operated with performance exceeding its design value. Table 3.2 summarizes the LHC parameters used in each year.

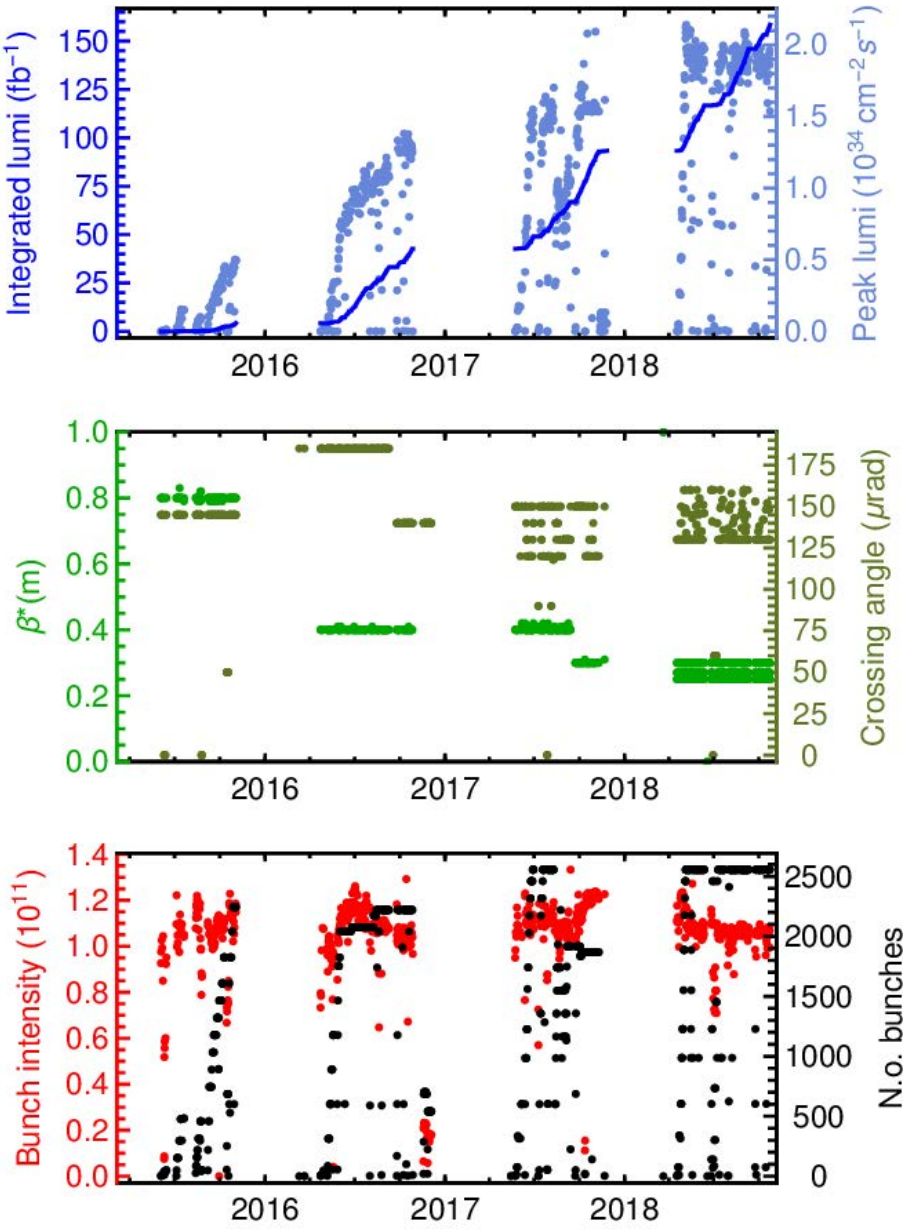

Figure 3.2: The integrated and peak luminosity (top), the β^* and beam crossing angle (middle), and the bunch luminosity and the number of bunches (bottom) during Run 2 [27].

Table 3.2: The LHC operational parameters in each year of Run 2 [26]. These values are representative of the best LHC performance during the normal operation period.

	2015	2016	2017	2018
Peak instantaneous luminosity ($\times 10^{34}$) [$\mathrm{cm^{-2}s^{-1}}$]	0.5	1.3	1.6	1.9
Typical number of protons per bunch ($\times 10^{11}$)	1.1	1.1	1.1/1.2	1.1
Maximum number of bunches in the ring	2232	2208	2544/1909	2544
The collision time interval [ns]	25	25	25	25
Peak number of pp collisions per bunch crossing	16	41	41/60	55
Total delivered integrated luminosity [$\mathrm{fb^{-1}}$]	4.0	39.0	50.6	63.8

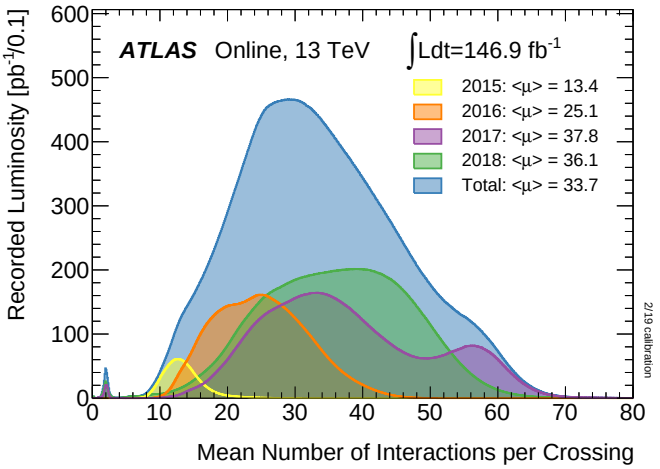

Figure 3.3: The number of pp interactions per bunch crossing in 2015-2018 [28].

The instantaneous luminosity larger than the design value was achieved. Figure 3.2 shows the time evolution of the LHC parameters. As the instantaneous luminosity increases, the number of pp interactions per bunch crossing increases. When one pp collision of interest occurs, multiple pp collisions that produce soft QCD interactions occur in behind simultaneously. Those pp collisions are called pileups. Figure 3.3 shows the number of pp collisions per bunch crossing each year.

3.2 ATLAS Detector

The ATLAS is a general-purpose detector located at "Point 1," one of the LHC's pp collision points. Figure 3.4 shows the overview of the ATLAS detector. It consists of the inner detector, the calorimeter, the muon detector, and a magnet system. It has a cylindrical shape of 25 m diameter and 44 m length and consists of several kinds of sub-detectors. The total weight is 7,000 tons. As shown in Figure 3.5, the ATLAS uses the right-handed coordinate. The direction along the beam is defined as the z-axis, and the plane perpendicular to the beam is defined as the x-y plane. The positive side of the z-axis is called the "A-side", and the negative side is called the "C-side." The cylindrical coordinates use $R(=\sqrt{x^2+y^2})$ for the radial direction, $\phi(-\pi < \phi < \pi)$ measured around the z-axis as azimuth angle, $\theta(0 < \theta < \pi)$ measures

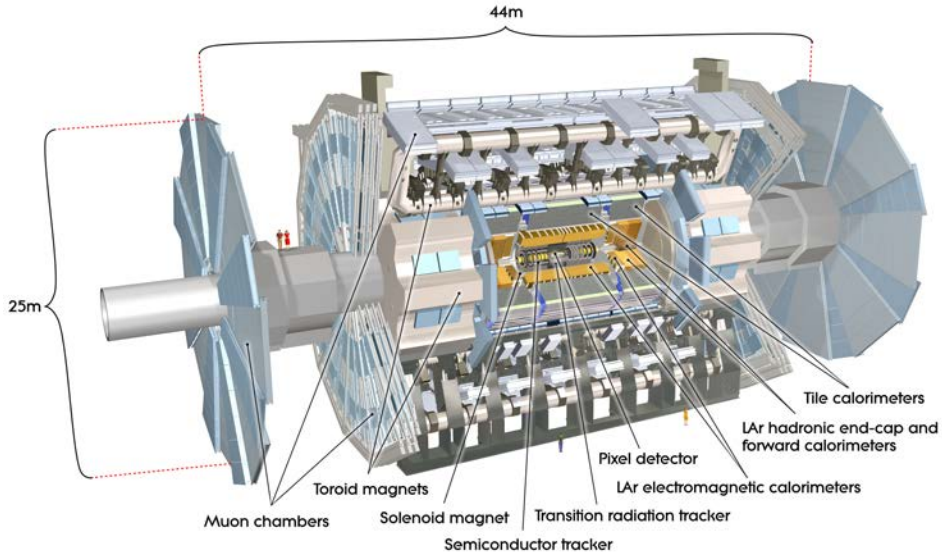

Figure 3.4: Overview of the ATLAS detector [29]. It consists of the inner detector, calorimeters, muon detector, and magnet system.

against the z-axis as polar angle. The pseudo-rapidity is defined as:

$$\eta \equiv -\ln\left[\tan\left(\frac{\theta}{2}\right)\right]. \tag{3.4}$$

It is often used instead of θ because the η between two objects is a Lorentz-invariant value.

Since incoming partons have momenta almost parallel to the z-direction, the momentum of particles produced at collision is expected to be zero in the transverse plane perpendicular to the z-axis. When the sum of the transverse momentum of the detected particles is not zero, it suggests that the final state contains particles that ATLAS cannot detect, such as neutrinos or unknown particles. Therefore, transverse momentum $p_{\mathrm{T}}(=\sqrt{p_x^2+p_y^2})$ and transverse energy $E_T(=\sqrt{E_x^2+E_y^2})$ are important parameters. Distance between two physics objects are often expressed as $\Delta R(=\sqrt{\Delta\eta^2+\Delta\phi^2})$, where $\Delta\eta$ and $\Delta\phi$ are the difference between their η and the difference between their ϕ, respectively.

3.2.1 Magnet system

The ATLAS magnet system consists of a central solenoid and three toroidal magnets, as shown in Figure 3.6. The central solenoid has a 2.5 m diameter and 5.8 m length, located between the inner detector and the calorimeter. It provides a uniform 2 T axial magnetic field to the inner detector to bend the trajectory of the charged particle in the ϕ direction, as shown in Figure 3.7a. The toroidal magnets consist of one barrel toroid and two endcap toroids. They are located inside the muon detector, providing the magnetic field in the ϕ direction to bent muon trajectory in θ direction, as shown in Figure 3.7b. The barrel toroid has a 25.3 m length and 20.1 m outer diameter, and the maximum magnetic field is 3.9 T. The endcap toroids have a 5 m length and 10.7 m outer diameter, and the maximum magnetic field is 4.1 T.

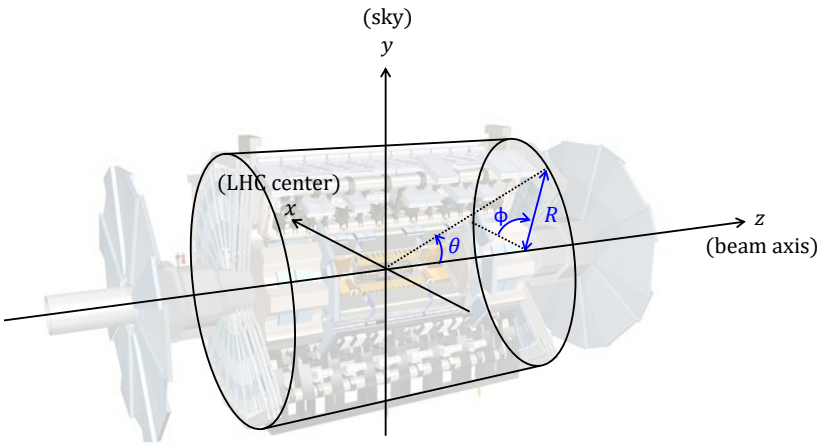

Figure 3.5: ATLAS coordinate system.

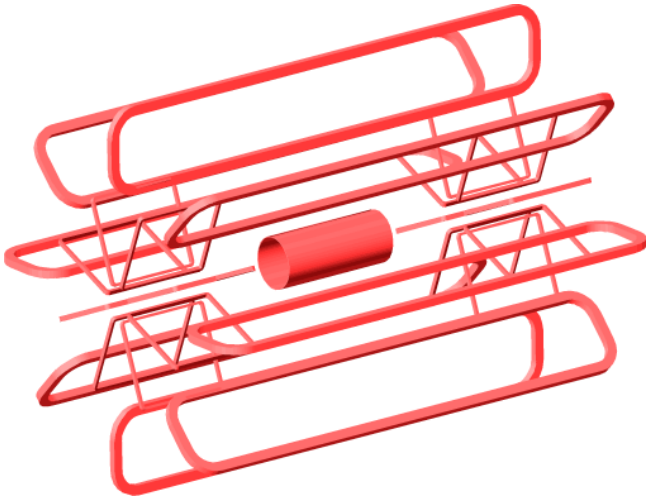

Figure 3.6: Illustration of the ATLAS magnet system [30]. The inner cylinder shows the solenoid, and the outer rings show the toroids.

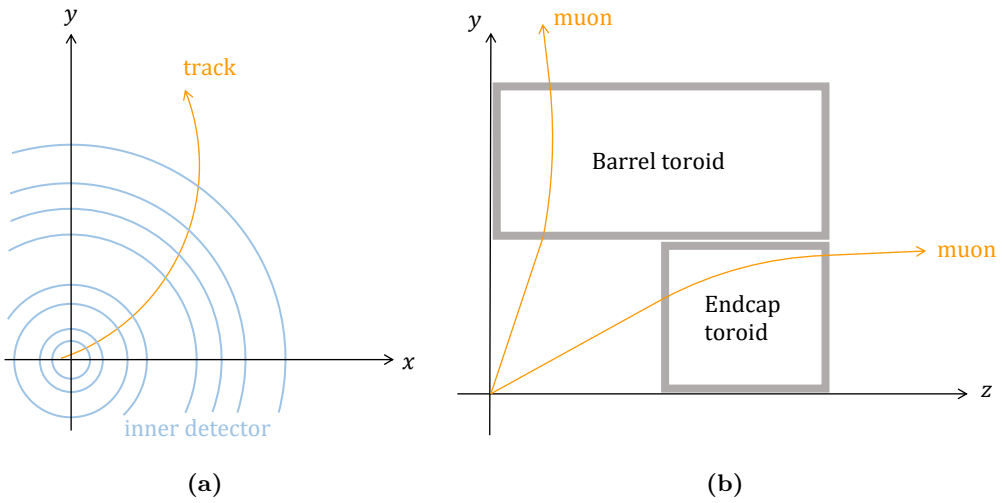

Figure 3.7: Particle trajectories. (a)Charged particles passing through the inner detector. (b)Muon passing through the toroidal magnet region.

3.2.2 Inner detector

The inner detector (ID) reconstructs charged particle tracks. It is surrounded by the central solenoid. When a charged particle goes through the ID, its trajectory is bent by the magnetic field. The track of the charged particle is reconstructed using the energy deposits detected on the ID layers (called "hits"), and particle momentum is calculated by its curvature. In addition, the production and decay positions of the particles are reconstructed using ID tracks called vertices. It consists of three subdetectors: Pixel detector (Pixel), Semiconductor Tracker (SCT), and Transition Radiation Tracker (TRT). Figure 3.8 shows the layout of the ID, and Figure 3.9 shows the R-z cross-sectional view of the ID.

The Pixel and SCT are semiconductor detectors. They are composed of modules with silicon sensors. When a charged particle passes through the sensor's depletion region, a large number of electron-hole pairs are generated. The electric field in the depletion region causes the generated electrons to move to the positive electrode and the holes to move to the negative electrode. The charged particle can be detected by reading it out as an electrical signal.

Pixel

Pixel is the innermost sub-detector in the ATLAS detector, made of pixelated silicon semiconductor detectors. It comprises four cylindrical barrel layers and three disk endcap layers for each side. The barrel layers are named Insertable B-Layer (IBL), B-Layer, Layer-1, and Layer-2 from inside. IBL was newly installed in 2014 to retain the tracking performance under high-luminosity environments from Run 2 [33, 34]. Table 3.3 shows the ATLAS Pixel structure.

Two types of silicon sensors are used in the IBL: n^+-in-n planer sensor and 3D sensor. A planar sensor is one in which the electrodes are placed horizontally relative to the sensor surface. In the case of n^+-in-n type, the electrodes made from n^+-type semiconductor are implanted in the bulk made from n-type semiconductor. The depletion region extends from the p-n junction on the back surface of the

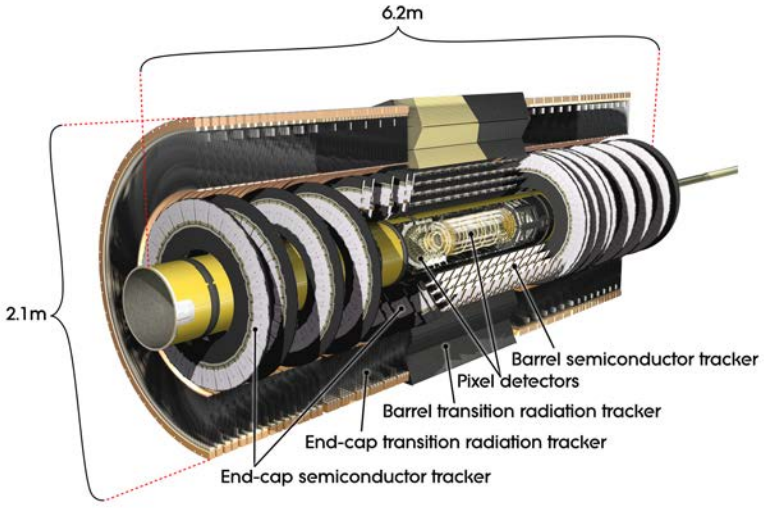

Figure 3.8: Cut-away view of the inner detector [31].

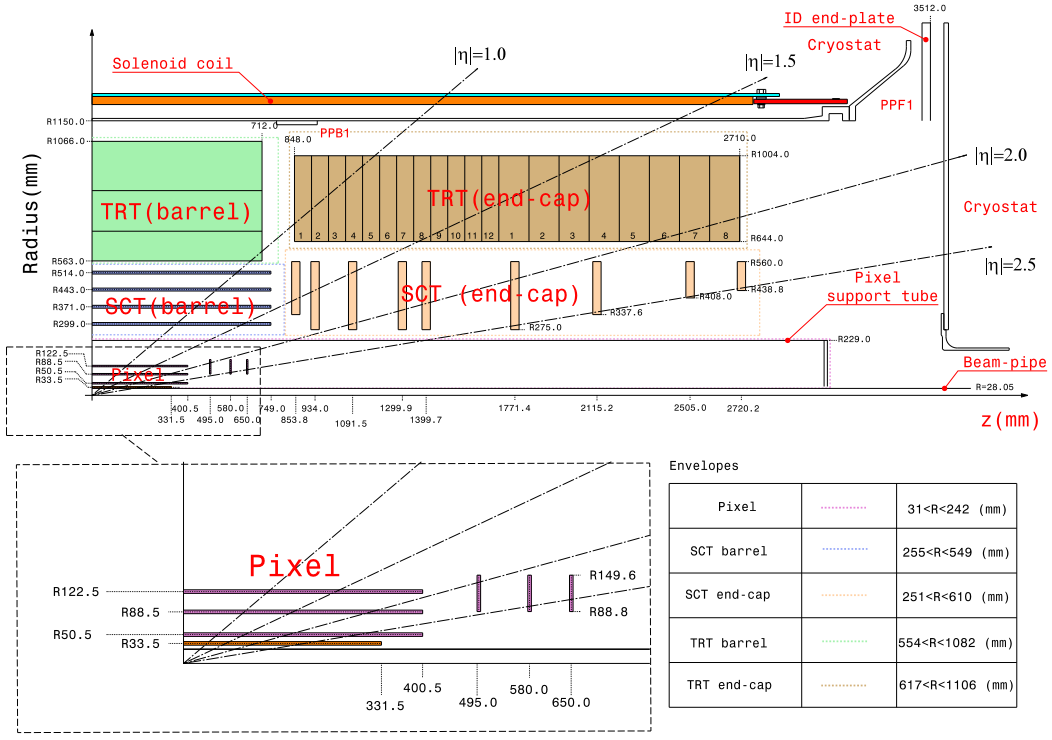

Figure 3.9: *R-z* cross-sectional view of the inner detector. The upper part shows 1/4 of the inner detector, and the bottom shows a zoomed view of the Pixel detector [32].

Table 3.3: Layout of the Pixel detector [34, 36].

	Radius [mm]	Length [mm]	staves/sectors	Modules	Pixels ($\times 10^6$)
IBL	$\langle R \rangle = 33.25$	$\|z\| < 332$	14	224	6.02
B-Layer	$\langle R \rangle = 50.5$	$\|z\| < 400.5$	22	286	13.2
Layer1	$\langle R \rangle = 88.5$	$\|z\| < 400.5$	38	494	22.8
Layer2	$\langle R \rangle = 122.5$	$\|z\| < 400.5$	52	676	31.2
Disk1	$88.8 < R < 149.6$	$\langle z \rangle = 495$	8×2	48×2	4.4
Disk2	$88.8 < R < 149.6$	$\langle z \rangle = 580$	8×2	48×2	4.4
Disk3	$88.8 < R < 149.6$	$\langle z \rangle = 650$	8×2	48×2	4.4

sensor toward the electrode. The 3D sensor is a new technology, and ATLAS is the first experiment to use it in high-energy experiments. A 3D sensor is one in which the electrodes are arranged perpendicular to the sensor surface. An n^+-type and a p^+-type electrode are vertically arranged on the bulk of a p-type semiconductor. Depletion is achieved by applying a voltage between the electrodes. Since the distance between the electrodes is short, the depletion voltage can be reduced, resulting in a high radiation tolerance. Other layers are composed only of the planer sensors. The module size is 4.08×1.68 cm^2 on the IBL planner sensors, 2.04×1.68 cm^2 on the IBL 3D sensors, and 6.08×1.64 cm^2 on the other layers. Pixel size is 50×250 μm^2 on the IBL and 50×400 μm^2 on the other layers. The thicknesses of the pixels are 200 μm for the IBL planner sensors, 230 μm for the IBL 3D sensors, and 250 μm for the other layers. The position resolution is 12 (8.5) μm in the transverse plane and 66 (47) μm in the z-direction in Pixel (IBL).

The total number of readout channels in Pixel is 90 million, which corresponds to approximately 90% of ATLAS readout channels. The signal from each pixel is measured as the time-over-threshold (ToT), the time the signal pulse is above a certain threshold, as shown in Figure 3.10. Since the pulse shape can be approximated as a triangle, the ToT is proportional to the charge of the signal. When a charged particle passes through the sensor, the charge is typically collected from multiple pixels. Groups of neighboring pixels that detect signals called clusters are found using a connected component analysis [35]. The position where a charged particle passes is estimated by taking the average of the pixel positions weighted by the collected charge, as shown in Figure 3.11.

SCT

The second innermost sub-detector is the SCT, made of microstrip silicon modules. It consists of four barrel layers and nine endcap layers for each side. Table 3.4 shows the SCT structure. An SCT module comprises a pair of two strip sensors tilted by 40 mrad, enabling 3D measurement of charged particle tracks. The p-in-p planer sensor is used. The sensor size is 63.56×63.96 mm^2, and the thickness is 285 μm. An SCT sensor has 768 strips with an 80 μm pitch. The position resolution is 16 μm in the transverse plane and 580 μm in the longitudinal direction. The total number of readout channels in SCT is 6.3 million.

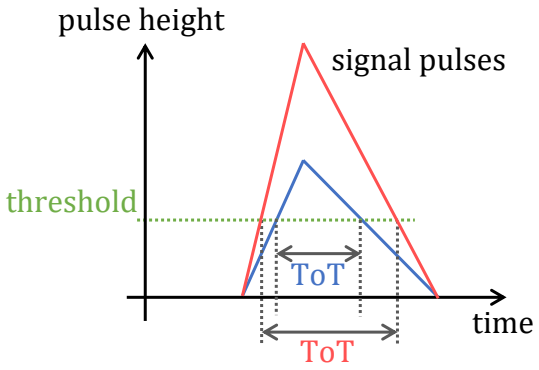

Figure 3.10: ToT. It becomes larger proportional to the signal pulse height.

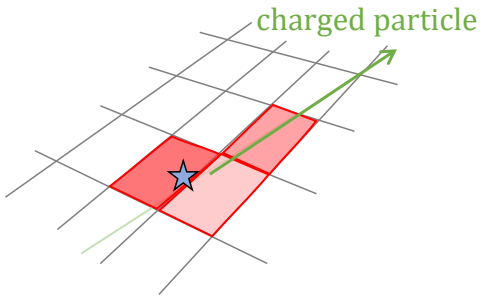

Figure 3.11: Pixel cluster. The red shade shows the magnitude of charge collected by each pixel. The average pixel position weighted by the collected charge shown by a star is assumed to be the position where the charged particle passes.

Table 3.4: Layout of the SCT [37].

	Radius [mm]	Length [mm]	layers	Modules	channels ($\times 10^6$)
SCT barrel	$299 < R < 514$	$\|z\| < 749$	4	2112	3.2
SCT endcap	$275 < R < 560$	$839 < \|z\| < 2735$	9×2	1976	3.0

TRT

TRT is the outermost subdetector in the ID, composed of approximately 350,000 straw-shaped drift tubes. The TRT barrel is located from 563 mm $< R <$ 1066 mm from the beam line, and the endcap covers 848 mm$< |z| <$ 1066 mm. The barrel region contains 52,544 straw tubes of 1.5 m length parallel to the beam line. There are 122,880 straw tubes in the endcap region. The tubes are located outward from the beam line. A tube with a 4 mm diameter, made from Kapton, plays the role of anode. In the center of the tube, there is a gold-plated tungsten wire. It is the cathode, and a 1.5 kV voltage is applied. A gas mixture of xenon, carbon dioxide, and oxygen is sealed inside the tube. Electrons generated by the ionization are drifted toward the wire. The position where charged particles pass through is determined by the arrival time of the electron. The position resolution is 170 μm per straw.

3.2.3 Calorimaters

The ATLAS calorimeters are located outside the central solenoid. There are two types of calorimeters in the ATLAS: electromagnetic and hadron calorimeters, as shown in Figure 3.12. The electromagnetic calorimeter mainly measures the energy of the electrons and photons using electromagnetic showers. The hadron calorimeter measures the energy of the hadron jet using hadron showers. The electromagnetic calorimeter is a sampling calorimeter with liquid argon as active materials and lead as absorbers. The barrel region of the electromagnetic calorimeter covers $|\eta| < 1.475$ and $1.5 < |\eta| < 3.2$, respectively. The hadron calorimeter is also a sampling calorimeter, composed of the Tile calorimeter, the Hadronic endcap calorimeter, and the forward calorimeter. The Tile calorimeter uses tiled plastic scintillators as active materials and iron as absorbers, covering $|\eta| < 1.7$. The Hadronic endcap calorimeter uses copper liquid argon as active materials and copper as absorbers, covering $1.5 < |\eta| < 3.2$. The forward calorimeter uses liquid argon as active materials and copper or tungsten as absorbers, covering $3.1 < |\eta| < 4.9$.

3.2.4 Muon detector

The muon detector, shown in Figure 3.13, is located at the outermost position in the ATLAS detector since muons do not interact strongly and are less likely to emit bremsstrahlung than electrons. It has multiple layers, each measuring the position where the muon passes. Muon tracks are reconstructed from the hit position of each layer, and muon momentum is measured by its curvature bent by the toroidal magnetic field. There are four components: Monitored Drift Tubes (MDT), Cathode Strip Chambers (CSC), Resistive Plate Chambers (RPC), and Thin Gap Chambers (TGC). The barrel region ($|\eta| < 1.05$) consists of MDT and RPC, and the endcap region ($1.05 < |\eta| < 2.7$) consists of CSC and TGC. The MDT and CSC have excellent position resolution and precisely measure muon momenta. The RPC and TGC provide a fast response and are used as triggers.

3.2.5 Trigger system

Most pp collision events are inelastic QCD events, which are not interesting for the ATLAS experiment. Figure 3.14 shows the predicted and measured cross-sections of various SM processes in the LHC. The

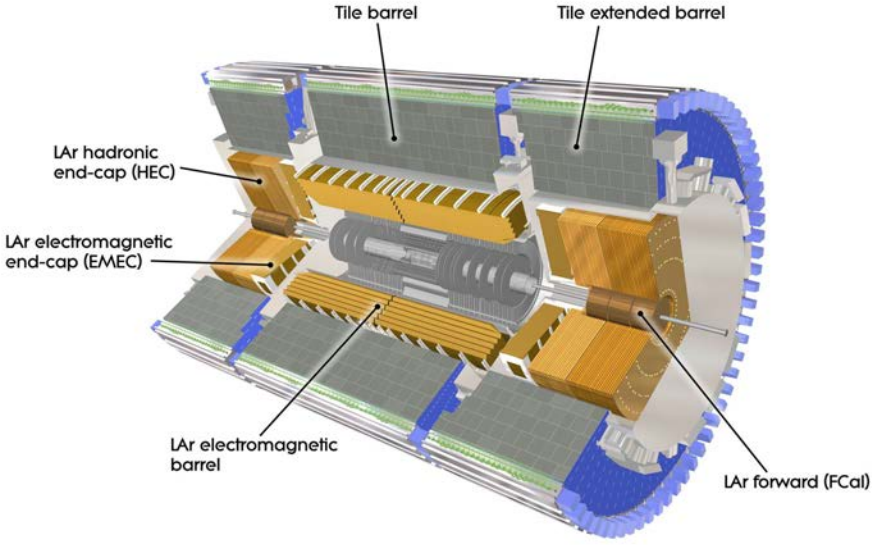

Figure 3.12: Cut-away view of the ATLAS calorimeter [38]. The electromagnetic calorimeter, which measures electron and photon energies, is located inside, and the hadron calorimeter, which measures quark and gluon jet energies, is located outside.

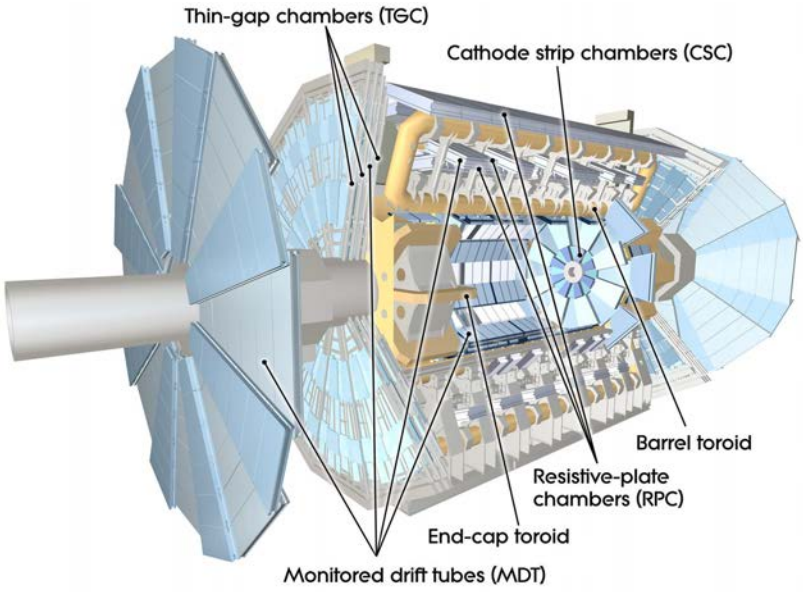

Figure 3.13: Cut-away view of the ATLAS muon detector [39]. The barrel region consists of MDT and RPC, and the endcap region consists of CSC and TGC.

ATLAS data acquisition system cannot record all collision events at 40 MHz. Therefore, the ATLAS uses a trigger system to select only interesting events, such as the electroweak process, top quark or Higgs boson productions, and new physics. Those processes usually contain the high p_{T} objects such as hardon jets, photons, and leptons, or large missing energy.

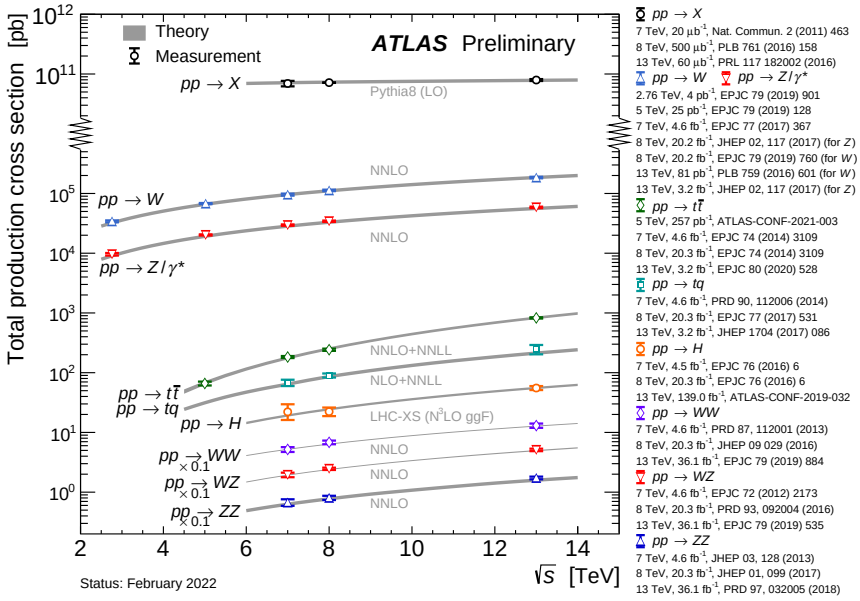

Figure 3.14: Predicted and measured cross-sections of the SM processes in pp collision in the LHC [40]. Each line shows a theoretical prediction of the cross-section of each process, and each point shows the measurement by ATLAS.

Figure 3.15 shows the overview of the trigger and data acquisition system used in ATLAS. The pp collisions events occurring with 40 MHz are reduced to 100 kHz in the hardware-based level-1 (L1) trigger and to about 1 kHz in the software-based high-level trigger (HLT).

The L1 trigger is a hardware-based trigger that uses fast custom-made electronics. It can select events by considering event-level quantities, object multiplicity, and topological requirements. It uses information from the calorimeter and muon detectors with reduced granularity and processes it with a latency of less than 2.5 μs. There are three kinds of L1 triggers: L1 calorimeter trigger (L1Calo) [41], L1 muon trigger (L1Muon) [42], and L1 topological trigger (L1Topo) [43]. The L1Calo takes signals from the electromagnetic and hadron calorimeters as input, identifies electron, photon, τ-lepton, and jet candidates, and calculates the global sum of missing transverse momentum ($E_{\mathrm{T}}^{\mathrm{miss}}$). The L1Muon identifies muon candidates by using hits from RPCs and TGCs. The L1Topo receives each trigger object identified by the L1Calo and L1Muon as input and makes trigger decisions based on the angular and energy information in the event.

In addition to taking the role of the first selection, the L1 trigger also identifies the Region of interest (RoI) in η and ϕ within the detector to be further investigated by the HLT.

If an event passes the L1 trigger, data are read out from the other sub-detectors and sent to the HLT, further reducing the number of events. Full-granularity calorimeter information, precise measurements on

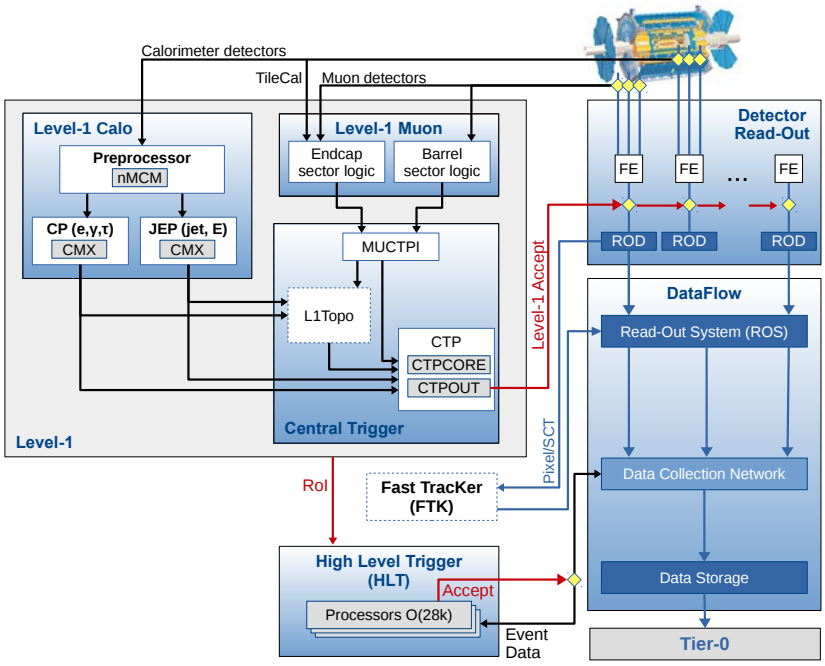

Figure 3.15: The ATLAS trigger system [44]. The L1 trigger is formed by the Central Trigger Processor (CTP), which receives input from the calorimeter and muon detectors. The events that pass the L1 trigger are then buffered in the Readout System (ROS) and processed by the HLT. The events that pass the HLT are transferred to the data storage.

the muon detector, and tracking information from the ID are available at the HLT stage. Precise object reconstruction, similar to offline reconstruction, is typically carried out only within the RoI. The selection of object candidates is performed at each step to reduce the time the HLT needs to reconstruct the events and make a trigger decision. The processing time of the HLT is 0.2 s per event on average. A prescale can be applied to control the rate of accepted events. If the prescale is n, it means that $1/n$ of the events passing that trigger are randomly accepted.

Events triggered by the HLT are sent to the data storage for an offline process.

3.2.6 $E_{\mathrm{T}}^{\mathrm{miss}}$ trigger

This section describes the algorithms and performance of the $E_{\mathrm{T}}^{\mathrm{miss}}$ trigger. This analysis uses the $E_{\mathrm{T}}^{\mathrm{miss}}$ for triggering because the target events include $\tilde{\chi}_1^0$ in the final states, which are not directly detected in the ATLAS detector and measured as $\boldsymbol{E}_{\mathrm{T}}^{\mathrm{miss}}$, the vector whose magnitude is $E_{\mathrm{T}}^{\mathrm{miss}}$.

At the L1 trigger level, the $\boldsymbol{E}_{\mathrm{T}}^{\mathrm{miss}}$ is calculated from the calorimeter cells. The analog sum of signals

from the calorimeter, which forms projective towers, is digitized, with the granularity of $\Delta\eta \times \Delta\phi = 0.1 \times 0.1$ in the central region and larger or less regular in other regions which are coarser than the calorimeter full-granularity. After applying noise thresholds, the towers are summed up into larger projective towers called "jet element" with an approximate granularity of $\Delta\eta \times \Delta\phi = 0.2 \times 0.2$. $\boldsymbol{E}_{\mathrm{T}}^{\mathrm{miss}}$ is then computed by summing up the x, y component of jet elements as follows:

$$E_x^{\mathrm{miss}} = -\sum_i E_i \sin\theta_i \cos\phi_i, \tag{3.5}$$

$$E_y^{\mathrm{miss}} = -\sum_i E_i \sin\theta_i \sin\phi_i, \tag{3.6}$$

where E_i, θ_i, and ϕ_i are the i-th tower's energy deposit, polar angle, and azimuthal angle, respectively. If the $E_{\mathrm{T}}^{\mathrm{miss}}$ calculated at the L1 trigger stage is larger than a given threshold, the event is transferred to the HLT.

At the level of HLT, $\boldsymbol{E}_{\mathrm{T}}^{\mathrm{miss}}$ is recalculated by one or more of the following algorithms [45]. The event is sent to the data storage if the $E_{\mathrm{T}}^{\mathrm{miss}}$ calculated at the HLT stage is larger than a certain threshold. Sometimes, different HLT $E_{\mathrm{T}}^{\mathrm{miss}}$ algorithms are combined by requiring more than one algorithm to indicate that the event has a large $E_{\mathrm{T}}^{\mathrm{miss}}$. This combination allows the removal of events whose $E_{\mathrm{T}}^{\mathrm{miss}}$ exceed a threshold due to the impact of the tail of $E_{\mathrm{T}}^{\mathrm{miss}}$ resolution, which depends on the algorithm.

- Trigger using calorimeter cell signals (`cell`)

  The most straightforward HLT $E_{\mathrm{T}}^{\mathrm{miss}}$ algorithm, `cell`, calculates the $\boldsymbol{E}_{\mathrm{T}}^{\mathrm{miss}}$ from a sum of complete sets of calorimeter cells without calibrations or pileup corrections. To reduce the noise effects, only cells with energy deposits significantly larger than the noise are included in the calculation.

- Trigger using topo-clusters of calorimeter cells (`tc_lcw`)

  The topological cluster ("topo-clusters") [46] is defined as the cluster that is created by merging topologically connected calorimeter cells. The algorithm identifies the seed cell with an energy deposit significantly greater than the noise level and forms an energy cluster by collecting its neighboring cells iteratively. The topo-clusters' energy is corrected depending on the type of energy deposit. These calibrated topo-clusters are directly used in $\boldsymbol{E}_{\mathrm{T}}^{\mathrm{miss}}$ calculation in the `tc_lcw` algorithm.

- Trigger using jets (`mht`)

  In most events of interest, jets are the primary visible component. The `mht` algorithm determines $\boldsymbol{E}_{\mathrm{T}}^{\mathrm{miss}}$ from the negative vector sum of the momentum of the calibrated HLT jets. The HLT jets are reconstructed from the calibrated topo-clusters using the FastJet tool kit and calibrated similarly for the offline analysis mentioned in Section 5.4.1.

- Trigger implementing local pileup suppression (`pufit`)

  The `pufit` algorithm includes the pileup effect correction on the high-$E_{\mathrm{T}}^{\mathrm{miss}}$ signals. The topo-clusters used in the second algorithm are used as inputs. The pileup contribution is estimated by a fitting to low-$E_{\mathrm{T}}^{\mathrm{miss}}$ signals and subtracted to determine the $\boldsymbol{E}_{\mathrm{T}}^{\mathrm{miss}}$.

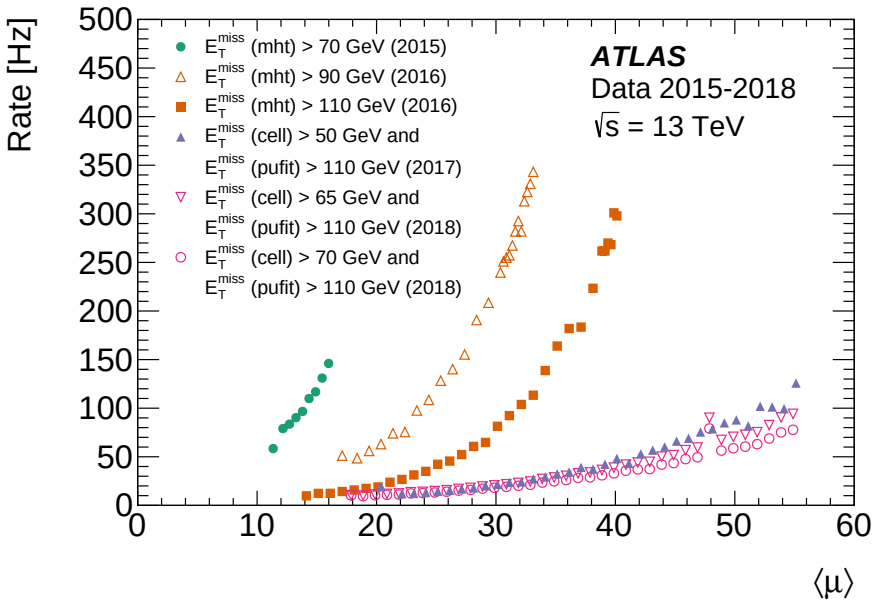

Figure 3.16: Rates of various HLTs as a function of $\langle\mu\rangle$ in each year [47].

Figure 3.16 shows the rates for various HLT algorithms year-by-year as a function of an average number of pileups $\langle\mu\rangle$. Since pileup events worsen the $E_{\mathrm{T}}^{\mathrm{miss}}$ resolution, the trigger rates increase more rapidly than linearly. `pufit`-based algorithm mitigates this effect significantly.

This chapter explained the LHC, which produces the physics processes we target, and the ATLAS detector, which detects the signals from particles produced at collisions. The technique for reconstructing physical objects from the detected signals is described in Chapters 5 and 6.

Chapter 4

Data and simulation samples

This chapter describes the details of the data and simulation samples used in this analysis.

4.1 Data samples

This analysis uses the data of the pp collision at $\sqrt{s} = 13$ TeV recorded by the ATLAS detector in Run 2. The LHC delivered the collision data to the ATLAS with the integrated luminosity of 156 fb^{-1} in total. Due to detector problems, the ATLAS detector did not record some of the collision data delivered by the LHC. Online monitoring of the detector was performed during data-taking to minimize such data loss. The ATLAS recorded 147 fb^{-1} data in Run 2. In addition to online monitoring, continuous assessment of data quality after data collection, called offline monitoring, has been conducted to ensure high-quality data. At this stage, the data are judged as "good" or "bad." The data taken under bad detector conditions are flagged as bad. In the Pixel detector case, for example, if the fraction of disabled modules on a layer is greater than 30%, the data were flagged as bad in Run 2. Figure 4.1 shows the fraction of data flagged as bad in each sub-detector during Run 2. The good and bad flags are assigned to each luminosity block [48] of each run and summarized in a list called Good Runs List (GRL) [48]. A luminosity block is a unit of data-taking, corresponding to approximately one minute. In Run 2, 140.07 ± 1.17 fb^{-1} data are assessed as good for physics analysis. Table 4.1 shows the integrated luminosity assessed as good for physics each year. Figure 4.2 shows the time evolution of integrated luminosity delivered by the LHC, recorded by the ATLAS, and good data used for physics analyses.

Triggers control which collision events are recorded. The used trigger in this analysis is detailed in Section 7.1.1. Since no trigger suitable for this analysis is included in the DRAW filter, which is used

Table 4.1: Summary of the integrated luminosity and uncertainties assessed as good for physics. [26]. Data taken in 2015 are not used for this analysis as mentioned later.

year	2015	2016	2017	2018	Total
Integrated luminosity [fb^{-1}]	3.24	33.40	44.63	58.79	140.07
Total uncertainty [fb^{-1}]	0.04	0.30	0.50	0.64	1.17

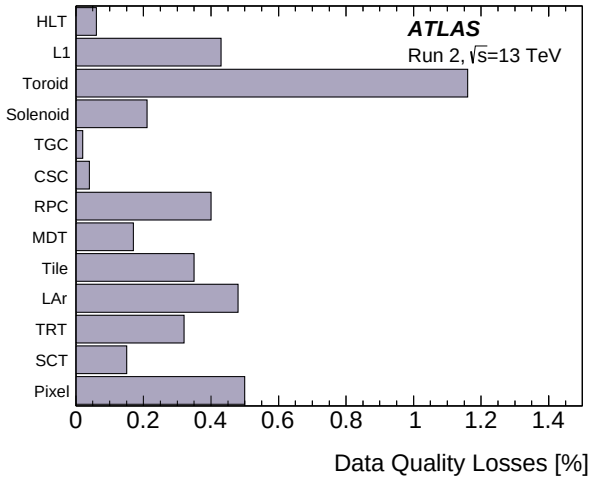

Figure 4.1: Fraction of data flagged as bad in each sub-detector [49].

to select events processed with special reconstruction for LLP searches, only the data with 137 fb^{-1} of integrated luminosity taken from 2016 to 2018 are used for this analysis. The DRAW filter is explained in Section 7.1.1.

4.2 Simulation samples

This analysis uses simulated samples made by the Monte Carlo (MC) method to study the signal and background event characteristics and estimate the number of signal events. The event generator calculates all possible Feynman diagrams for a specific physics process. The schematic of the event generation is shown in Figure 4.3. The MC simulates the interactions between the particles generated by the event generator and the detector materials to make the simulated data equivalent to the real data. After that, the same reconstruction software used for the real collision data described in Chapters 5 and 6 is processed.

4.2.1 Event generation

The pp collision is modeled by factorization. The main idea is to separate the soft-QCD process from the hard-scatter process so that perturbative quantum field theory can be applied to calculate the QCD hard-scatter part while adding constraints from other experiments to the soft-QCD part. The energy scale at the boundary between the perturbative QCD and the soft QCD part is called factorizatoin scale μ_F. The cross-section of a physics processes $pp \to X$ can be written as follows [50]:

$$\sigma_{pp\to X} = \sum_{ab} \int dx_1 dx_2 f_a(x_1, \mu_F^2) f_b(x_2, \mu_F^2) \hat{\sigma}_{ab\to X}(x_1 p_1, x_2 p_2, \mu_F^2, \mu_R^2, \alpha(\mu_R^2)), \tag{4.1}$$

where $f_{a(b)}(x_{1(2)}, \mu_F^2)$ is the parton distribution function (PDF) of the partons $a, b(= q, \bar{q}, g)$ in the proton 1(2) and $\hat{\sigma}_{ab\to X}$ is the cross-section of the physics process $ab \to X$. The PDF represents the probability that the fraction of momentum of a parton becomes x out of the proton's momentum at the energy scale μ_F.

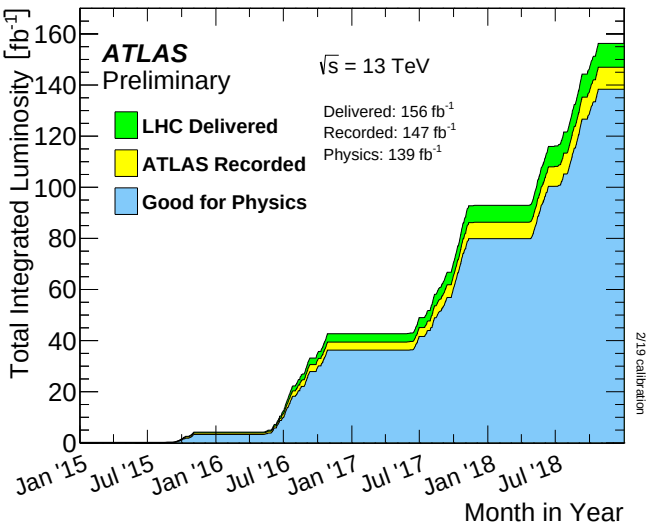

Figure 4.2: Total integrated luminosity delivered by the LHC ('LHC delivered'), recorded by ATLAS ('ATLAS recorded') and available for physics analyses ('Good for physics') in 2015-2018 [28]. The integrated luminosity of "Good for physics" is 139 fb^{-1} in this figure but has been re-calculated as 140 fb^{-1} [26].

The cross-section of the hard-scatter part can be obtained by the QCD and the electroweak theory using the fraction of momentum of the partons (x_1p_1 and x_2p_2), the QCD coupling constant α_S at the renormalization scale μ_R, and μ_F. The matrix element with a fixed order is calculated, and then the parton shower method complements additional parton emission using the probability of parton splitting. Finally, colored particles are evolved into colorless hadrons, a process called hadronization.

The configuration of event generation in this analysis is detailed below. The matrix element for the wino-like $\tilde{\chi}_1^{\pm}\tilde{\chi}_2^0$ pair production is calculated at leading order accuracy using MG5_aMC@NLO2.6.1 [51] with the NNPDF23LO [52] PDF set and at most two extra partons. $\tilde{\chi}_1^{\pm}$ and $\tilde{\chi}_2^0$ are decayed with Madspin [53]. The branching ratios for $\tilde{\chi}_2^0 \to \tilde{\chi}_1^0 h^*$, $\tilde{\chi}_1^{\pm} \to \tilde{\chi}_1^0 W^*$ are fixed to 100%. The theoretical calculation of the branching ratio of Higgs boson with various masses is shown in Figure 4.4. Since the mass of the off-shell Higgs boson in this model is considered to be $\mathcal{O}(10)$ GeV, $h^* \to b\bar{b}$ are fixed to 100%. The events are then interfaced with PYTHIA 8.212 [54] for modeling of Parton shower, hadronization, and underlying event with A14 set of tuned parameter [55]. The signal cross-sections for bino-wino pair production are calculated at next-leading order plus next-to-leading-log accuracy. In this analysis, $\tilde{\chi}_2^0$ mass ($m_{\tilde{\chi}_2^0}$), the mass splitting between $\tilde{\chi}_2^0$ and $\tilde{\chi}_1^0$ ($\Delta M(\tilde{\chi}_2^0, \tilde{\chi}_1^0)$), and $\tilde{\chi}_2^0$ lifetime ($\tau_{\tilde{\chi}_2^0}$) are set to 200-1100 GeV, 20-50 GeV, and $O(0.01) - O(1)$ ns, respectively.

The SM processes with a large $E_{\mathrm{T}}^{\mathrm{miss}}$ may become signal-like and contaminate the signal region defined in Chapter 7. As the representative of those SM "background events", the MC sample of $Z \to \nu\bar{\nu}$ + jets process shown in Figure 4.5 is made. They are used to study the background components and determine the signal region selection criteria. This sample is generated using SHERPA 2.2.11 [57]. Matrix elements are calculated up to two partons at the next-to-leading order and four partons at the leading order. They are interfaced with the SHERPA parton shower with NNPDF3.0NNLO parton distribution set [58] and A14 set of tuned parameters.

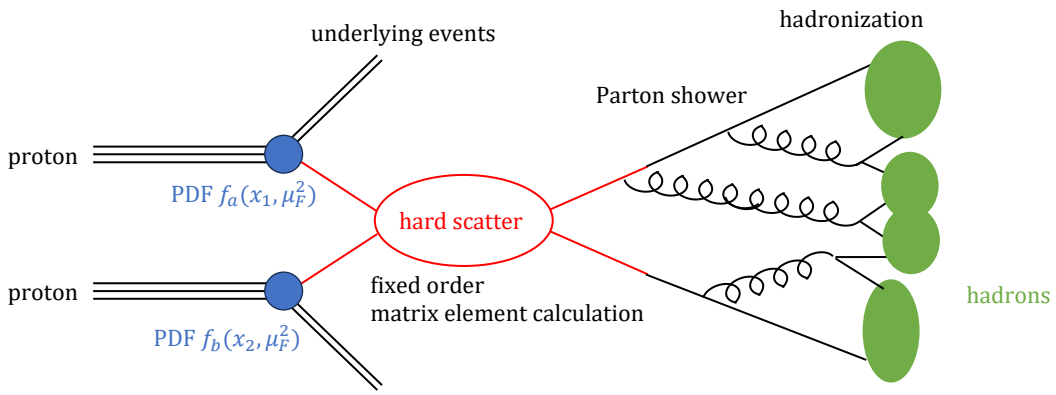

Figure 4.3: Schematics of the event generation process.

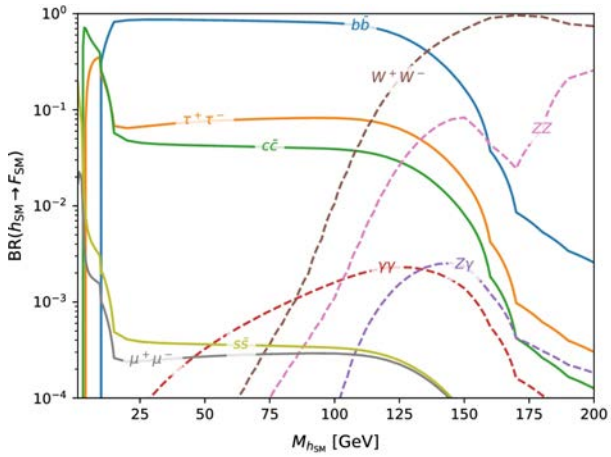

Figure 4.4: Theoretical calculation of the branching ratio of Higgs boson with various mass [56].

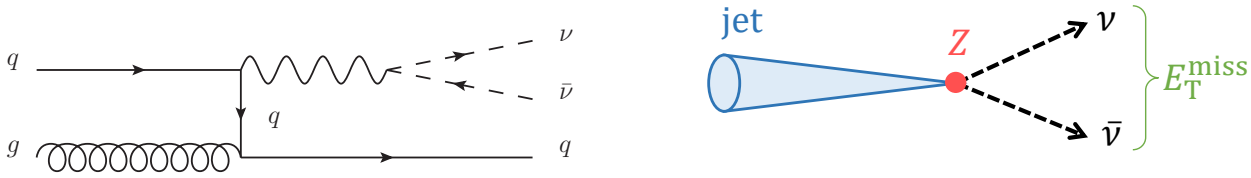

Figure 4.5: Feynman diagram (left) and event topology (right) of $Z \to \nu\bar{\nu}$ + jets event.

In addition, the MC sample of $Z \to \mu^+\mu^-$ + jets process is used to estimate the signal uncertainty by the trigger efficiency, as described in Section 9.2. This sample is generated with the same conditions as $Z \to \nu\bar{\nu}$ + jets samples.

When a hard scatter pp collision occurs, multiple additional pileup collisions occur simultaneously. Those events are generated using soft QCD processes of Pythia 8.186 with A3 tune [59] and the MSTW2008LO parton distribution function set [16]. They are overlaid onto each simulated hard scatter event so that the number of pileup distributions matches the one observed in the data, as shown in Figure 3.3.

4.2.2 Detector simulation

The interaction between the particles generated by the event generator and the detector materials is simulated by the ATLAS simulation framework [60] based on GEANT4 simulation [61].

The long-lived particle generated by the generator would decay in the detector material. However, the event generator does not know anything about the detector material nor magnetic field inside the detector. On the other hand, the GEANT4 can not simulate the complex decays such as b-hadrons, τ lepton, or BSM particles decays. To correctly simulate the decay of the long-lived particle in the detector, a list of all particles, both themselves and their daughter particles, is made. The particles in the list are propagated to GEANT4, and GEANT4 simulates their decay according to the list. In the case of long-lived $\tilde{\chi}_2^0$, we do not need to consider the material interaction and magnetic field because $\tilde{\chi}_2^0$ has only weak interaction. The GEANT4 just needs to simulate the decay at the decay position based on the information propagated from the event generator.

Chapter 5

Physics object reconstruction

This chapter describes the standard reconstruction of the physics objects used in ATLAS.

The signal event is characterized by a primary vertex (PV), which is the position where pp collision occurs, a displaced vertex (DV), which is the position where the LLP decays, and missing transverse momentum ($E_{\mathrm{T}}^{\mathrm{miss}}$ or MET) created by the LSPs. Therefore, those three objects are required to be included in the signal region events. However, many other objects are also used indirectly. Figure 5.1 shows the relation between objects. Tracks reconstructed in the ID are used to reconstruct vertices (PVs and DVs) and other objects by combining with the information of other sub-detectors, as described in Section 5.4 to 5.6, and Chapter 6. A single object is sometimes reconstructed as two or more different types of object. This ambiguity is solved by the "overlap removal" procedure, as described in Section 5.7. Jets, photons, electrons, and muons are not required to be included in the signal region but are used to calculate $E_{\mathrm{T}}^{\mathrm{miss}}$, which is used to select the signal region events, as described in Section 5.8. A lepton is included in the final state of the signal events when the off-shell W-boson originating from $\tilde{\chi}_1^{\pm}$ decays leptonically. However, leptons are not required for this analysis to be less strongly dependent on the W-boson mode.

Jets are also used to remove events with a large fake $E_{\mathrm{T}}^{\mathrm{miss}}$; When the event has a jet satisfying certain conditions, the event is excluded. It is detailed in Section 7.5. Moreover, jets are used to estimate the number of background events in the signal region. It is detailed in Chapter 8.

Photons are also used for DV veto; DVs reconstructed around photons are removed to suppress background DVs originating from photon conversion. It is explained in Section 7.7.1.

Table 5.1 briefly shows how each object is used in this analysis. DVs are reconstructed using specific methods after the reconstruction of these standard objects. They are described in Chapter 6.

5.1 Track

Charged particles are produced at the beam collision point and pass through the detector, depositing the energies on the detector segments. Their tracks are reconstructed by connecting the hit points. A magnetic field bends their directions. When a charged particle with a unit charge and the transverse

Table 5.1: Usage of each object in this analysis.

Object	Usage in this analysis
Track	Reconstruction of primary and displaced vertices
	Reconstruction of jets, muons, and electrons
	Missing transverse momentum calculation
Primary vertex	Event selection
Jet	Non-collision background veto
	Overlap removal
	Missing transverse momentum calculation
	Background estimation
Photon	Event selection for control region
	DV veto around photons
	Overlap removal
	Missing momentum transverse calculation
Electron	Overlap removal
	$E_{\mathrm{T}}^{\mathrm{miss}}$ reconstruction
Muon	Overlap removal
	Missing momentum transverse calculation
Missing transverse momentum	Event selection
Displaced vertex	Event selection (detailed in Chapter 6)

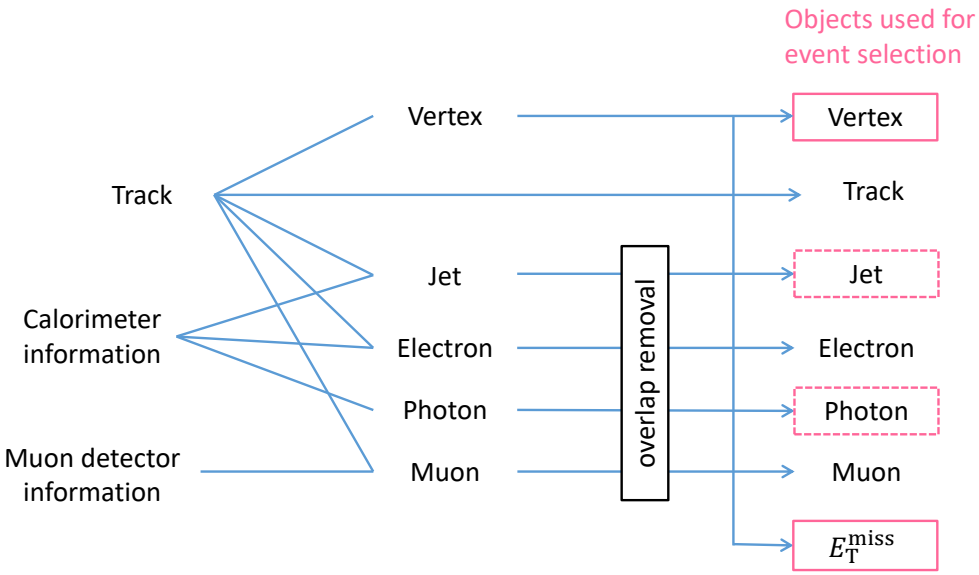

Figure 5.1: Relation between the objects. Objects in boxes on the right are used in the signal region selection. Events are not required to have jets, but events with jets satisfying certain criteria are excluded. Furthermore, events are not required to have photons, but DVs are required to be away from photons.

Table 5.2: Description of the track parameters.

Parameter	Description
q/p	The ratio of the track charge divided by the magnitude of the momentum
ϕ	The azimuthal angle of the track momentum in the x-y plane, defined from $-\pi$ to π
θ	The polar angle of the track momentum in the beam direction, defined from 0 to π
d_0	The transverse impact parameter
z_0	The longitudinal impact parameter

momentum p_{T} goes through the magnetic field B, the curvature radius R is given as follows:

$$p_{\mathrm{T}}[\mathrm{GeV}/c] = 0.3 \times B[\mathrm{T}] \times R[\mathrm{m}] \tag{5.1}$$

Tracks are described with five track parameters listed in Table 5.2 at the "perigee", the point of closest approach of the track to the beamline in x-y plane. Figure 5.2 schematically shows their definition.

The standard tracks, which originate from the beam collision point, are reconstructed by two algorithms in ATLAS, Inside-out and outside-in tracking, as described in [62, 63]. After these two track reconstructions, a special tracking algorithm reconstructs tracks that do not originate from the collision points.

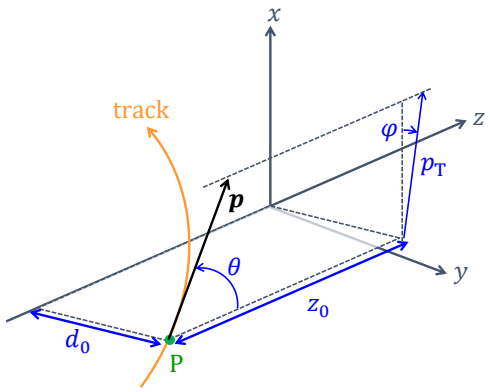

Figure 5.2: Schematic of the track parameters at the perigee (P).

5.1.1 Inside-out tracking

The primary track finding algorithm in the ATLAS is the inside-out strategy. It starts with seeding in the silicon detectors (Pixel and SCT) and then performs a hit finding in the outer detector (TRT). There are four steps as follows:

1. Formation of space-points

   As the first step, three-dimensional representations of detector measurements, called "space-points," are created. The clusters of silicon hits on the Pixel and SCT are created by finding connected cells. They are transformed into three-dimensional space-points using the position information of the clusters on the detector surfaces and the position of the detector.

2. Track finding

   Figure 5.3 shows the schematic of the track finding procedure. The track candidate search starts from consecutive space-points. Track seeds are first built from three consecutive space-points (Figure 5.3(a)). Pixel-only, SCT-only, or mixed seed are being considered. The initial cuts, such as the requirements of momenta and impact parameters, are applied to reduce the number of seed candidates. Once the track seed passes the initial cuts, further associated hits are searched by a road window search through the seed direction to build a track candidate (Figure 5.3(b)). An algorithm based on a combinatorial Kalman filter [64] judges if the hits within the road window are to be added to the track candidate and performs the refitting (Figure 5.3(c)). Track candidates within the silicon detector are completed at this point (Figure 5.3(d)).

3. Ambiguity solving

   Track candidates include many fake tracks and overlapping tracks with shared hits. Ambiguity solving is carried out to eliminate those tracks. In order to reject such track candidates, they are ranked by the order of the score corresponding to the likelihood. Before scoring the track candidates, their fitting are modified based on the refined geometry information with the material details, and

the χ^2 of the fit divided by the number of degrees of freedom (reduced χ^2) is obtained for each track. Both reduced χ^2 and track scoring are used to classify the tracks. Generally, a track candidate with a relatively more number of associated hits obtains a better score. A track receives a penalty when it has missing hits on the track trajectory, i.e., a track hole. The hits on different sub-detectors are weighted with different scores. Pixel hits are highly weighted because the position resolution is more precise than SCT's. Figure 5.4 illustrates an example of track characteristics to be resolved in the SCT barrels. When a track candidate has a shared hit with other track candidates, the shared hit is assigned to the track with a higher score, and the fitting of the track with a lower score is modified by removing the shared hits. After iterating this procedure, only the tracks with scores higher than a specific threshold are stored.

4. TRT extension

   Tracks that pass the ambiguity solving are further extended into the TRT measurements. Coordinates of the TRT hits are expressed in $R-\phi$ in the barrel and $R-z$ in the endcap region. Then, a linear fit is performed to estimate whether the TRT hit is compatible with the silicon tracks. If the original score is higher than after the TRT extension, the original one is stored.

5.1.2 Outside-in tracking

The inside-out tracking cannot reconstruct tracks coming from the long-lived particle decaying outside of the silicon detector, such as K_s^0 or from photon conversion. Outside-in tracking is performed to reconstruct such tracks. A standard Hough transform mechanism identifies the TRT track segments. Finally, the TRT segments are extended back to the silicon detector to find the small track segments that have not been used in the inside-out tracking.

5.2 Large radius tracking

Tracks from the LLP decay tend to have large impact parameters. Due to the constraint on the impact parameters, standard tracking is inefficient for reconstructing those tracks. To improve the reconstruction efficiency for those tracks, a re-tracking, called large radius tracking [65], is performed after the standard tracking. This re-tracking follows the same strategy as the inside-out tracking but uses only the hits that are not used for the inside-out tracking nor outside-in tracking. The selection of the impact parameters and the number of silicon hits are relaxed, as summarized in Table 5.3. Figure 5.5 shows the track reconstruction efficiency with and without large radius tracking. Tracking efficiency is defined as the number of true LLP decays with at least two reconstructed true charged particles over the number of true LLP decays that are within $r_{\text{decay}} < 300$ mm, $|z_{\text{decay}}| < 300$ mm, where r_{decay} and z_{decay} are r and z coordinates of the LLP decay position, and that include at least two true charged particles with $p_{\text{T}} > 1$ GeV and $|\eta| < 2.5$.

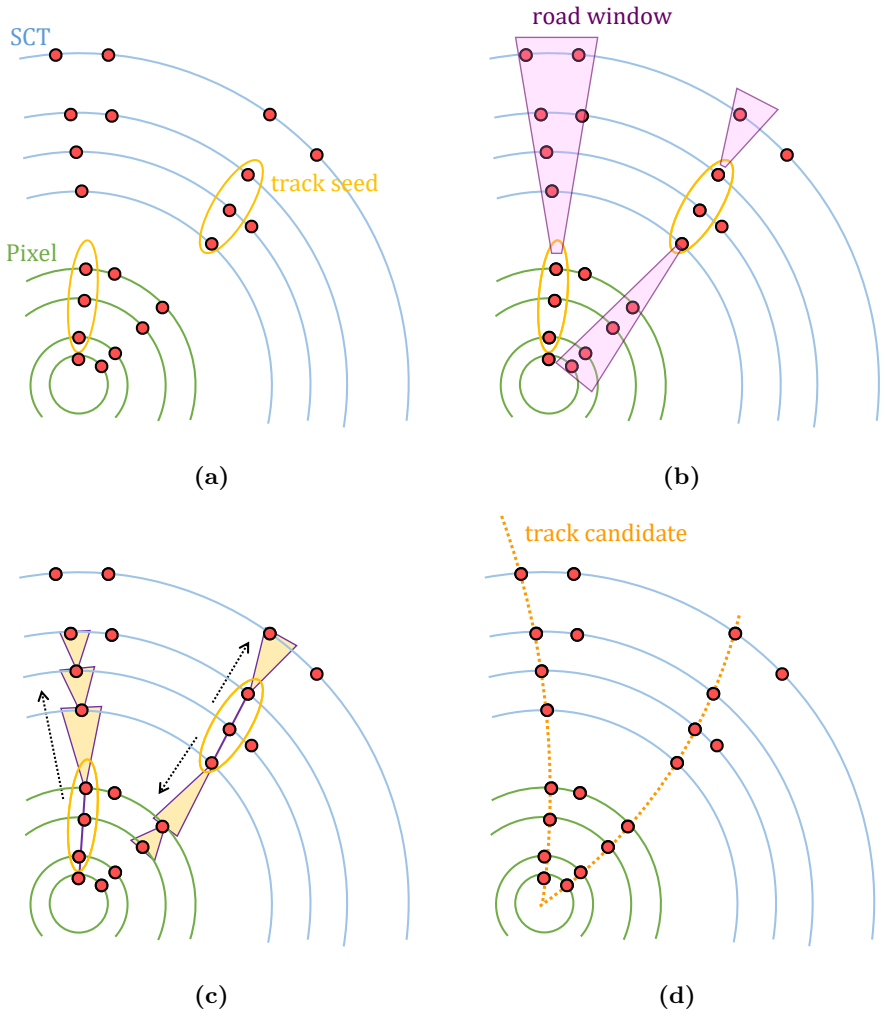

Figure 5.3: Schematic figure of track finding procedure. (a)Track seeds are build from three consecutive space-points. (b)The road window is set by the direction of the seed. (c)The hits in the window are judged to be added by a combinatorial Kalman filter. (d)Reconstructed track candidates.

Table 5.3: Track selections used for the standard tracking and large radius tracking [65].

	Standard	Large radius
Maximum d_0 [mm]	10	300
Maximum z_0 [mm]	250	1500
Maximum $\|\eta\|$	2.7	5
Maximum shared silicon modules	1	2
Minimum shared silicon hits	6	5
Minimum silicon hits	7	7

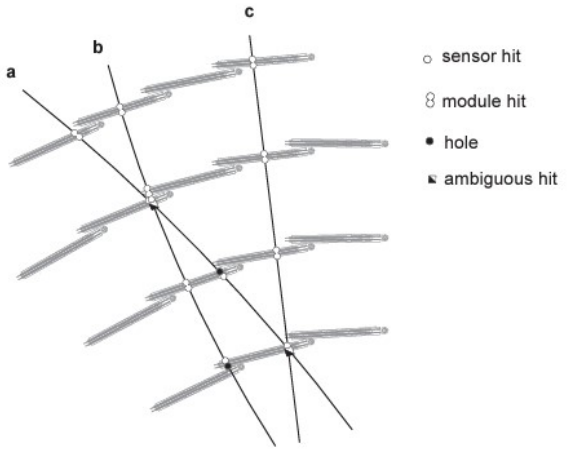

Figure 5.4: Simple example of the ambiguity solving process, illustrated in the SCT barre region [63]. Track candidates **a**, **b**, and **c** have been reconstructed at the stage of the track finding but have several shared hits (ambiguous hits). In this example, a module hit representing measurements on both sides of an SCT module obtains a relatively higher score than two sensor hits representing single measurements only on one side of the module. Hits in an overlapping region for track **b** receive particularly a high score, while holes on tracks give a penalty to the track score.

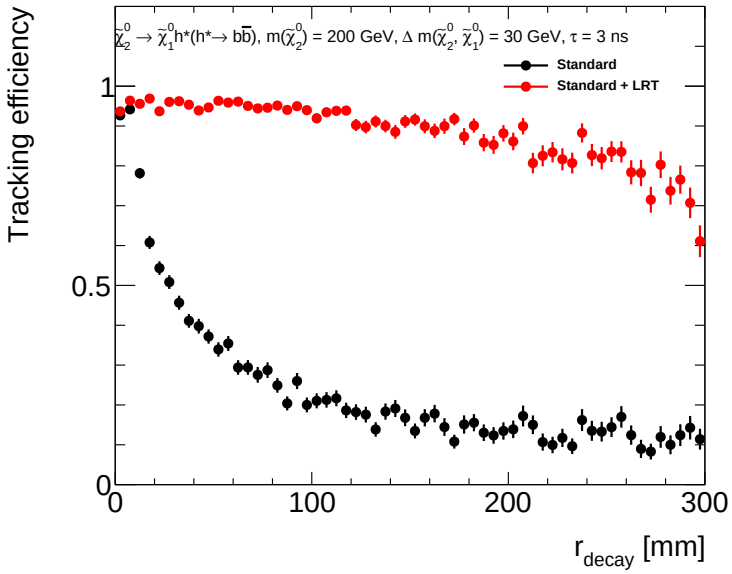

Figure 5.5: Track reconstruction efficiency with and without large radius tracking (LRT) as a function of the LLP decay radius (r_{decay}) for signal MC sample ($m_{\tilde{\chi}_2^0}$ = 200 GeV, $\Delta M(\tilde{\chi}_2^0, \tilde{\chi}_1^0)$ = 30 GeV, $\tau_{\tilde{\chi}_2^0}$ = 3 ns). The r_{decay} shown here is target range of the LLP decay of this search, which corresponds to inside the innermost SCT layer.

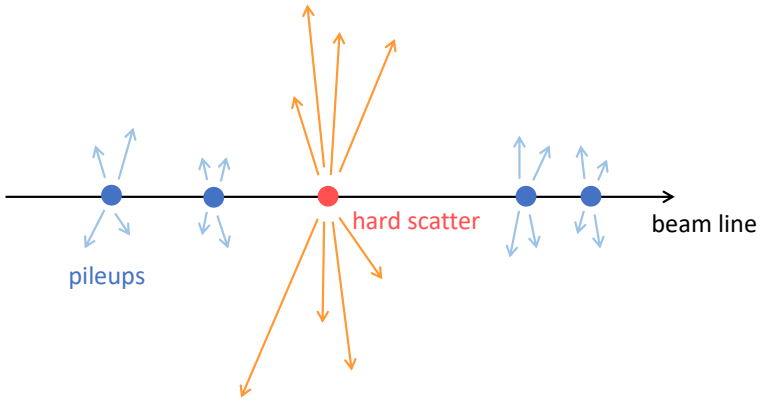

Figure 5.6: Hard scatter vertex and pileup vertices.

5.3 Primary vertex (PV)

PVs are reconstructed using the vertex finding and vertex fitting algorithms [66]. PV reconstruction uses all standard tracks that satisfy the following criteria to maintain a low rate of fake tracks and to avoid using the tracks originating from the secondary vertices [67]:

- $p_{\mathrm{T}} > 400$ MeV, $|d_0| < 4$ mm, $\sigma(d_0) < 5$ mm, $\sigma(z_0) < 10$ mm
- SCT hits ≥ 4, silicon hits ≥ 9, pixel holes $= 0$
- if $|\eta| \geq 1.65$, silicon hits ≥ 11, SCT holes ≤ 1
- IBL hits + B-Layer hits ≥ 1
- A maximum of one shared pixel hit or two shared SCT hits

Here, $\sigma(d_0)$ and $\sigma(z_0)$ are the uncertainties of d_0 and z_0.

After applying the track selection, PVs are reconstructed in the following steps:

1. A seed position of the vertex is determined. The transverse position is set to the beam line. The z-coordinate is determined as the mode of z_0 with respect to the beam line.
2. The best vertex position is estimated. The vertex fit is iteratively processed, and in each iteration, the weight of the less compatible tracks is removed, and the vertex position is recalculated.
3. Tracks incompatible with the vertex are removed after the vertex position is determined.
4. The procedure is repeated with the tracks not already used to fit vertices to create another vertex.

In Run 2, PVs of an order of ten are reconstructed per bunch crossing, but only one can usually create the event of interest. This PV, called the "hard scatter" vertex, is identified by choosing the one with the highest sum of p_{T} square of associated tracks ($\Sigma {p_{\mathrm{T}}}^2$). PVs other than the hard scatter vertex are called "pileup" vertices, as shown in Figure 5.6.

5.4 Jet

This analysis uses two kinds of jets reconstructed by different algorithms: calo jets and track jets. In this analysis, calo jets are used to eliminate the non-collision background events. The detail is described in Section 7.5. Track jets are used in the background estimation, as detailed in Chapter 8.

5.4.1 Calo jet

Calo jets are reconstructed from topo-clusters using anti-k_{T} algorithm [68]. The calorimeter cell energy is measured at the EM scale, corresponding to the energy deposit by electromagnetic interaction. The anti-k_{T} algorithm introduce the distance between cluster i and j ($d_{i,j}$) and the distance between cluster i and the beam axis ($d_{i,B}$) defined as follows:

$$d_{i,j} = \min(k_{ti}^{-2}, k_{tj}^{-2}) \frac{\Delta R_{ij}^2}{D^2}, \tag{5.2}$$

$$d_{i,B} = k_{ti}^{-2}, \tag{5.3}$$

where $\Delta R_{ij}^2 = (\eta_i - \eta_j)^2 + (\phi_i - \phi_j)^2$, k_{ti}, $\eta_{i(j)}$ and $\phi_{i,j}$ are the transverse momentum, pseudorapidity and azimuthal angle of particle $i(j)$, respectively. D is the jet-cone radius fixed to 0.4 in most ATLAS analyses. If $d_{i,j}$ is the smallest among all combinations of clusters and smaller than $d_{i,B}$, clusters i and j are merged. If $d_{i,B}$ is smaller than $d_{i,j}$, cluster i is defined as a jet and removed from the list of clusters. This procedure is repeated until no clusters are left in the list.

The energy of reconstructed jets is calibrated. Jet energy scale (JES) calibration corrects the jet energy from reconstructed to the particle level. The reconstructed and particle-level truth energy ratio is calculated using MC samples, depending on the η and truth energy. The absolute JES is calibrated using the mean of the ratio obtained by the Gaussian fitting. Figure 5.7(a) shows the uncertainty of the JES as a function of jet p_{T}. The jet energy resolution (JER) is measured using dijet events, where the p_{T} of the two leading jets are balanced using derivation from exact balance [69]. Figure 5.7(b) shows the JER and its uncertainty as a function of jet p_{T} obtained from data and dijet MC samples. The JER in MC tends to be overestimated, and this non-closure between data and MC is considered a systematic uncertainty.

Tracks reconstructed in ID are associated with the calorimeter jets. There are two association methods: ΔR matching and ghost association [71]. In the ΔR matching, tracks are associated with the jets based on the ΔR between the jet and the track. Threshold of the ΔR depends on the jet p_{T}. In the ghost association, ID tracks are extracted into the calorimeter and treated as particles with infinitely low p_{T} by scaling down their p_{T}. They are added as inputs of the jet reconstruction algorithm. Since tracks are treated as infinitely soft particles, they do not affect the jet reconstruction in the calorimeter. However, it is possible to identify which tracks were clustered into which jets after the jet reconstruction algorithm.

In this thesis, "jets" usually means calo jets. They are required to have $p_{\mathrm{T}} > 20$ GeV and $|\eta| < 4.5$.

Jets from the pileup PVs degrade the resolution of the missing transverse momentum. In order to reduce those effects, a jet vertex tagger [72] is applied to the jets with $|\eta| < 2.4$ and $p_{\mathrm{T}} < 60$ GeV. It classifies the jets from the hard scatter PV and the pileup PV using two variables showing the fraction of contribution of the hard scatter PV-originated tracks. Those variables are calculated using information

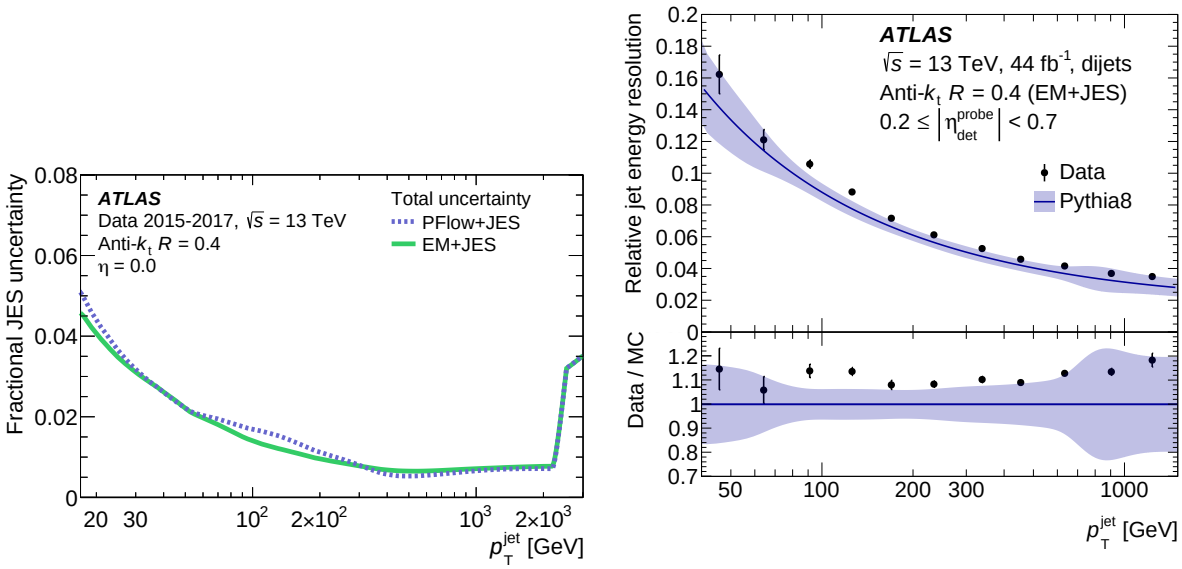

(a) **(b)**

Figure 5.7: (a) Fractional JES systematic uncertainty as a function of jet p_{T} [70]. The green line labeled 'EM+JES' is the JES uncertainty for the jets used in this analysis. (b) Relative JER as a function of jet p_{T} [69].

on tracks that are ghost-associated with jets. For jets with $2.5 < |\eta| < 4.5$ and $p_{\mathrm{T}} < 60$ GeV, a forward jet vertex tagger [73] is applied. Those jets do not have track information because it is out of the ID's coverage. Therefore, a forward jet vertex tagger classifies the jets from the pileup PVs using a method totally different from the jet vertex tagger. Most pileup jets are produced in pairs. Due to transverse momentum conservation, the jet pairs have opposite directions in the transverse plane. Each jet with $2.5 < |\eta| < 4.5$ and $p_{\mathrm{T}} < 60$ GeV is matched to a jet with $|\eta| < 2.5$ classified as a pileup jet by the jet vertex tagger so that their transverse momentum is balanced. Jets with $2.5 < |\eta| < 4.5$ and $p_{\mathrm{T}} < 60$ GeV that do not match any pileup jets with $|\eta| < 2.5$ are classified to originate from the hard scatter PV.

Only jets classified to originate from the hard scatter PV by jet vertex tagger or forward jet vertex tagger are used to calculate the missing transverse momentum.

Jets containing b-quarks (b-jets) are identified using the characteristics of the lifetime of b-hadrons. It uses information on tracks associated with jets by ΔR matching. Impact parameter-based algorithms [74] use the impact parameters of the tracks associated with the jets. Discriminants to tag b-jets are built from the log-likelihood ratios in which the probability density function of the impact parameter significance ($d_0/\sigma(d_0)$ and $z_0/\sigma(z_0)$) of b- and light jets are obtained from MC simulation. The vertex-based algorithm [74] uses the tracks associated with jets to reconstruct the secondary vertex. b-jets are tagged based on the distance between the PV and the reconstructed secondary vertex. The decay chain-based algorithm [75] uses the topology of the decays of b- and c-hadrons. A Kalman filter finds a common line of b-hadron, c-hadron, and PV. Several variables, such as flight length significances, are used for discriminating b- and light jets. Outputs from these different algorithms are combined with kinematic variables using a deep neural network called *DL1* [76]. This analysis uses the working point at 77% b-jet tagging efficiency.

5.4.2 Track jet

Track jets are reconstructed from ID tracks with an anti-k_{T} algorithm. All tracks that have $p_{\mathrm{T}} > 1$ GeV and $|d_0| < 2$ mm and pass *Loose* criteria are used. All tracks are associated with one PV as the following steps to find track jets:

1. Tracks are associated with a PV if their longitudinal impact parameter with respect to the PV meets $|z_0/\sigma(z_0)| < 3$.
2. Any remaining tracks not associated with any PVs are associated with a PV if their longitudinal impact parameter with respect to the PV meets $|z_0| < 0.5$ mm.
3. If a single track is associated with multiple PVs, the PV with the highest $\Sigma {p_{\mathrm{T}}}^2$ is chosen to associate with.

After this association, tracks associated with the same PV are clustered into a track jet. In this analysis, track jets with $p_{\mathrm{T}} > 10$ GeV are used in the background estimation.

5.5 Electron and Photons

Electrons and photons are reconstructed from the energy deposit in the cell of the electromagnetic calorimeter using a cluster-size algorithm to form clusters [77]. An electron candidate is identified as a cluster matching an ID track. If it matches an ID track, it is refitted considering energy from bremsstrahlung photons. Clusters without a matching ID track become unconverted-photon candidates. Clusters become converted-photon candidates if their matched ID tracks form a conversion vertex in the following ways. Two-track conversion vertices are reconstructed from two tracks with opposite charges that form a vertex whose invariant mass is consistent with that of a massless particle. Single-track conversion vertices are essentially tracks without hits in the IBL. Tracks used to form conversion vertices must have a high probability of being electrons determined by the TRT [78].

After reconstruction, likelihood-based selection using shower shape in the electromagnetic calorimeter and track properties are applied to the electron candidate to identify genuine electrons while rejecting a significant fraction of fake electrons. On the other hand, prompt photons are identified using several cut-based selection criteria using the shower shape variables in the electromagnetic calorimeter.

In this analysis, electrons are required to have $p_{\mathrm{T}} > 10$ GeV and $|\eta| < 2.47$ and to satisfy the *LooseAndBLayerLH* identification criteria [79]. Photons are required to have $p_{\mathrm{T}} > 25$ GeV and $|\eta| < 2.37$ and to satisfy the *Tight* identification criteria [80].

5.6 Muon

Muon candidates are reconstructed by combining the tracks reconstructed independently in the ID and the muon detector. After reconstruction, muons are identified using the number of hits in the ID and muon detector, track fit properties, and variables testing the compatibility of the individual measurement in the ID and muon detector.

In this analysis, muons are required to have $p_{\mathrm{T}} > 10$ GeV and $|\eta| < 2.7$ and to satisfy the *Medium* identification criteria [81].

5.7 Overlap removal

Since muons, electrons, photons, and jets are reconstructed by independent algorithms, a single particle may be reconstructed as different physics objects simultaneously. An overlap removal is performed to avoid such overlaps. This overlap removal procedure is not applied to the track jets. The overlap removal is separated into the following steps:

1. Muon-electron: Electrons are removed if they have a shared ID track with a muon.
2. Electron-jet: Jets are removed if they have an electron within $\Delta R < 0.2$ to reject jets originating from calorimeter showers made by an electron. Subsequently, electrons are removed if they have remaining jets within $\Delta R < 0.4$ to reject electrons originating from hadronic decays.
3. Muon-jet: Jets with less than three associated tracks are removed if any of their ghost-associated tracks match a muon or they have a muon within $\Delta R < 0.2$. Subsequently, muons are removed if they have a remaining jet within $\Delta R < 0.2$ in order to reject muons originating from hadronic decays.
4. Lepton-photon: Photons are removed if they have an electron or a muon within $\Delta R < 0.4$.
5. Photon-jet: Jets are removed if they have a photon within $\Delta R < 0.4$.

5.8 Missing transverse momentum ($E_{\mathrm{T}}^{\mathrm{miss}}$)

$E_{\mathrm{T}}^{\mathrm{miss}}$ is a crucial variable representing the sum of transverse momentum made by undetectable non-interacting particles such as neutrinos. The missing transverse momentum is reconstructed from the components $p_{x(y)}^{\mathrm{miss}}$, given by:

$$p_{x(y)}^{\mathrm{miss}} = -\Sigma p_{x(y)}^{\mathrm{jet}} - \Sigma p_{x(y)}^{e} - \Sigma p_{x(y)}^{\mu} - \Sigma p_{x(y)}^{\gamma} - \Sigma p_{x(y)}^{\text{soft term}}, \tag{5.4}$$

where $\Sigma p_{x(y)}^{\mathrm{jet}}$, $\Sigma p_{x(y)}^{e}$, $\Sigma p_{x(y)}^{\mu}$ and $\Sigma p_{x(y)}^{\gamma}$ are the sum of $x(y)$ component of the transverse momentum of calo-jets, electrons, muons, and photons, respectively. The soft term $\Sigma p_{x(y)}^{\text{soft term}}$ is calculated from tracks that are associated with the hard-scatter PV and are not associated with any other objects. $E_{\mathrm{T}}^{\mathrm{miss}}$ and its direction $\phi_{\mathrm{T}}^{\mathrm{miss}}$ are calculated as:

$$\boldsymbol{E}_{\mathrm{T}}^{\mathrm{miss}} = (E_x^{\mathrm{miss}}, E_y^{\mathrm{miss}}), \tag{5.5}$$

$$E_{\mathrm{T}}^{\mathrm{miss}} = |\boldsymbol{E}_{\mathrm{T}}^{\mathrm{miss}}|, \tag{5.6}$$

$$\phi_{\mathrm{T}}^{\mathrm{miss}} = \arctan(E_x^{\mathrm{miss}}/E_y^{\mathrm{miss}}). \tag{5.7}$$

It is represented as:

$$\boldsymbol{E}_{\mathrm{T}}^{\mathrm{miss}} = -\Sigma \boldsymbol{p}_{\mathrm{T}}^{\mathrm{jet}} - \Sigma \boldsymbol{p}_{\mathrm{T}}^{e} - \Sigma \boldsymbol{p}_{\mathrm{T}}^{\mu} - \Sigma \boldsymbol{p}_{\mathrm{T}}^{\gamma} - \Sigma \boldsymbol{p}_{\mathrm{T}}^{\text{soft term}}. \tag{5.8}$$

DVs are not included in the $E_{\mathrm{T}}^{\mathrm{miss}}$ calculation based on the following discussions. First, including the DVs in the $E_{\mathrm{T}}^{\mathrm{miss}}$ calculation may cause a mis-measurement of the $E_{\mathrm{T}}^{\mathrm{miss}}$ in the SM background events. A hadron produced at the hard scatter PV is reconstructed as a jet that passes the jet vertex tagger and is included in the $E_{\mathrm{T}}^{\mathrm{miss}}$ calculation. Tracks in such a jet sometimes form a DV. In this case, the $\boldsymbol{p_{\mathrm{T}}}$ of a single hadron is double-counted, and the $E_{\mathrm{T}}^{\mathrm{miss}}$ is mismeasured if the DV is included in the $E_{\mathrm{T}}^{\mathrm{miss}}$ calculation. Most of the background events from the SM do not have a real $E_{\mathrm{T}}^{\mathrm{miss}}$. Mis-measurement of the $E_{\mathrm{T}}^{\mathrm{miss}}$ may give them a large reconstructed $E_{\mathrm{T}}^{\mathrm{miss}}$, increasing the number of signal-like background events. $E_{\mathrm{T}}^{\mathrm{miss}}$ that include DVs in its calculation affects signal events differently. The b-hadrons originating from the decay of the $\tilde{\chi}_2^0$ in the signal events are not often included in the $E_{\mathrm{T}}^{\mathrm{miss}}$ calculation since their momentum may be too small to be reconstituted as jets, or even if they were reconstituted, they may not be classified to originate from the hard scatter PV by jet vertex tagger. Therefore, including DV in the $E_{\mathrm{T}}^{\mathrm{miss}}$ calculation will not result in the mis-measurement of $E_{\mathrm{T}}^{\mathrm{miss}}$ in most cases. However, removing DV from the $E_{\mathrm{T}}^{\mathrm{miss}}$ calculation slightly enhances the $E_{\mathrm{T}}^{\mathrm{miss}}$ in the signal events, increasing signal selection efficiency. This is because the $E_{\mathrm{T}}^{\mathrm{miss}}$ of signal events is made from two $\tilde{\chi}_1^0$s in the final state when DVs are included in the $E_{\mathrm{T}}^{\mathrm{miss}}$ calculation, while the $E_{\mathrm{T}}^{\mathrm{miss}}$ is made from $\tilde{\chi}_1^0$ of the final state and the intermediate $\tilde{\chi}_2^0$ when DVs are not included in the $E_{\mathrm{T}}^{\mathrm{miss}}$.

Chapter 6

Displaced vertex reconstruction

This chapter describes how to reconstruct LLP's decay points, called the displaced vertices (DVs).

6.1 Standard displaced vertex

The ATLAS has a standard dedicated displaced vertex reconstruction algorithm [82] for LLP search. It has three steps:

1. Form two-track seed vertices
2. Form multi-track vertex
3. Track attachment

The following subsections describe each step.

6.1.1 Form two-track seed vertices

The algorithm starts with forming the intersections of pairs of tracks, called "seed" vertices. Before forming the seed vertices, the track pre-selection is applied to reject low-quality tracks that contain many fake tracks. The pre-selection conditions are as follows:

- Track $p_{\mathrm{T}} > 1$ GeV.
- Track is not associated with any primary vertices.
- If the track does not have any hits in the Pixel, it must have at least six hits in the SCT.
- If the track has fewer than two hits in the Pixel, it must have at least one hit in the TRT.
- If the track p_{T} is lower than 20 GeV, it must have at least seven hits in the SCT. In addition, if the track $|\eta|$ is smaller than 1.7, it must have at least 20 hits in the TRT.
- At least one of the tracks must have $|d_0| > 2$ mm.

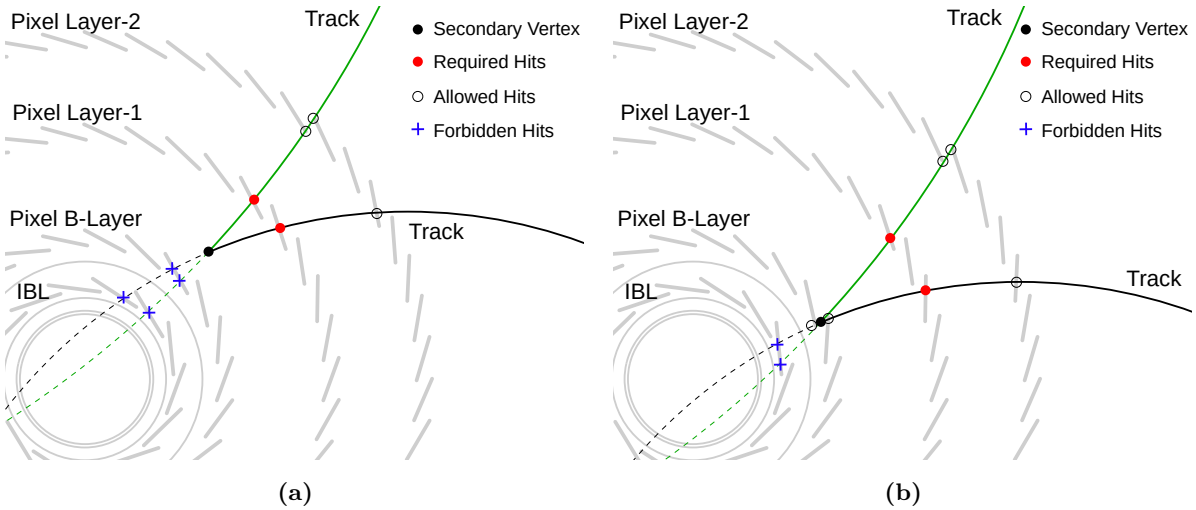

Figure 6.1: Schematics of the hit pattern consistency used for secondary vertices [82]. (a) A vertex is reconstructed between B-Layer and Layer-1. The tracks must not have any hits on the IBL nor B-Layer, the layers inner than the radial vertex position, and must have a hit on the Layer-1, the closest layer outside the vertex position. (b) A vertex is reconstructed close to and inside B-Layer. The tracks must not have any hits on the IBL but are allowed to have a hit on the B-Layer and must have a hit on the Layer-1.

The seed vertices are formed by the VKalVrt fitting algorithm [83] from pairs of the pre-selected tracks. The "hit-pattern consistency" is then checked for both tracks composing the seed vertices. Figure 6.1 is an example of the hit-pattern consistency. The concept is that tracks composing the seed vertices must have hits on the layers outer than the vertex position and must not have hits on the layers inner than the vertex position. If both tracks satisfy this consistency, the seed vertices are retained.

6.1.2 Form multi-track vertex

At the stage of two-track seed vertex forming, a single track may constructs different seed vertices. Multi-track vertex forming starts with extracting a group of fully compatible tracks (i.e., every single track does not create multiple vertices) using the incompatibility graph method [84]. Vertex fitting is performed again using each extracted track group to reconstruct vertices that are independent of each other.

Next, vertices close to each other are merged into a single vertex to avoid the split of a single LLP decay. The vertex merging is performed in ascending order of the number of the pre-selected tracks that construct the vertex. Each combination of two vertices is judged to be merged. First, if the positions of the two vertices are within 10σ, where σ is the uncertainty on the difference of between the two vertex positions calculated from the covariance matrices of two vertex fits, whether they are possible to be merged. The vertex with the lower number of tracks of the two is denoted "LMV," and the one with the higher number of tracks is denoted "HMV". Whether to merge the two vertices or not is determined by the following tests:

- The LMV position is recalculated by vertex fitting using the HMV position as the initial value. If the HMV position and the updated LMV position are within 10σ, LMV and LMV are merged. The

vertex position after merging is calculated by fitting using all tracks from LMV and HMV.

- The tracks constructing the HMV are associated one by one with the LMV, and the LMV position is recalculated by vertex fitting using the HMV position as the initial value. It is repeated for all HMV tracks. If any of these recalculated vertex positions and the HMV position are within 10σ, they are merged, and the vertex position after merging is recalculated using all tracks from both vertices.
- A vertex fitting is performed using all tracks constructing the LMV and HMV with the HMV position as the initial value. If the recalculated vertex position and the HMV position are within 10σ, they are merged, and the vertex position after merging is recalculated using all tracks from both vertices.

6.1.3 Track attachment

As the final step, tracks that do not satisfy the seed track selection criteria are associated with the reconstructed vertices to improve the vertex kinematics (e.g., track multiplicity and invariant mass). The requirements for those tracks are as follows:

- $p_{\mathrm{T}} > 1$ GeV
- d_0-significance w.r.t DV < 5
- z_0-significance w.r.t DV < 5

The final vertex fitting is performed after the track attachment. The vertex invariant mass is calculated, assuming all tracks have pion mass.

6.2 Special displaced vertex

As shown in Section 6.1, the standard displaced vertex reconstruction algorithm assumes that all the tracks originate from the same point. In the target signal event, however, LLP decay contains b-hadrons, and not all tracks intersect at one point due to b-hadrons' lifetime, as shown in Figure 6.2. In such cases, the standard method is inefficient in reconstructing DVs. Moreover, due to small mass-splitting between the LLP and the LSP, the reconstructed track multiplicity and invariant mass that is reconstructed from all the reconstructed particles is not always large, as shown in Figure 6.3. For this thesis, a special reconstruction method has been developed to efficiently reconstruct such soft and not "point-like" LLP decay points. It has mainly two steps:

1. Form two-track seed vertices
2. Form multi-track vertex

The following subsections describe the machine learning used in the special method first, and each step of the method subsequently.

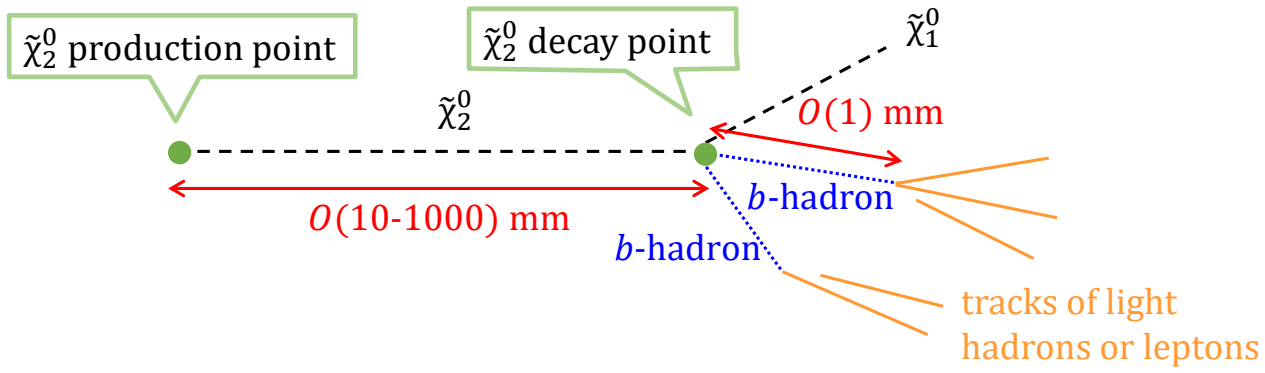

Figure 6.2: Sketch of the $\tilde{\chi}_2^0$ decay in the target event. $\tilde{\chi}_2^0$ decays to $\tilde{\chi}_1^0$ and a pair of b-quarks, forming b-hadrons. B-hadrons decay into lighter hadrons and leptons after flying a few mm.

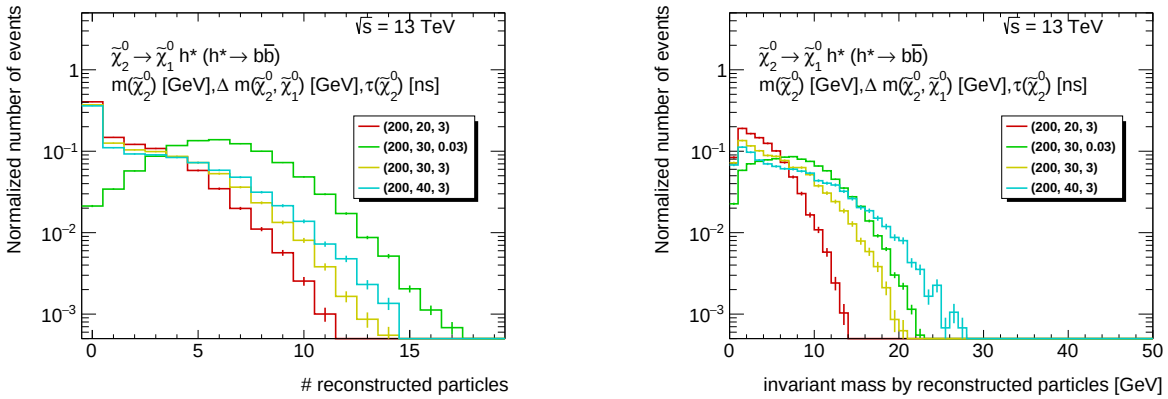

Figure 6.3: The number of reconstructed particles originating from $\tilde{\chi}_2^0$ and the invariant mass reconstructed by all the reconstructed particles originating from $\tilde{\chi}_2^0$. Only the events with at least two reconstructed events are included in the left figure.

Table 6.1: Dataset information used for training to develop the special DV reconstruction method. The sample labeled as "signal-long / signal-middle / signal-short" and "background" are used to learn the characteristics of track pairs of the signal events with long / middle / short lifetime and background events.

Process	category	$\tilde{\chi}_2^0$ mass [GeV]	$\tilde{\chi}_2^0$ lifetime [ns]	$\Delta m(\tilde{\chi}_1^0, \tilde{\chi}_2^0)[GeV]$
$pp \to \tilde{\chi}_2^0\tilde{\chi}_1^\pm, \tilde{\chi}_2^0 \to \tilde{\chi}_1^0 h^*, h^* \to b\bar{b}$	signal-long	300-500	1	30
$pp \to \tilde{\chi}_2^0\tilde{\chi}_1^\pm, \tilde{\chi}_2^0 \to \tilde{\chi}_1^0 h^*, h^* \to b\bar{b}$	signal-middle	300-500	0.1	30
$pp \to \tilde{\chi}_2^0\tilde{\chi}_1^\pm, \tilde{\chi}_2^0 \to \tilde{\chi}_1^0 h^*, h^* \to b\bar{b}$	signal-short	300-500	0.01	30
Data, Run 364292	background	-	-	-

6.2.1 Machine learning for seed track pair selection

The special DV reconstruction algorithm uses machine learning to select signal-like track pairs efficiently with less computation. In order to cover a wide range of possible lifetimes, bino-wino MC samples with three different lifetimes (notated as "short", "middle", and "long") are used as signal sample datasets, and some data is used as a background sample dataset for training. Table 6.1 summarizes the information from the dataset used.

Signal track pair samples and background track pairs samples used for training are chosen as follows:

- Signal: Two tracks originating from the LLP decay with the smallest ΔR in the event are chosen using the events in signal-long, signal-middle, or signal-short dataset.
- Background: Two tracks randomly selected in the same event are chosen using the events in the background dataset.

The motivation for using BDT for track-pair selection is to select signal-like track pairs that are likely to form a seed among all combinations of track pairs. Signal training samples mimic the signal track pairs that are likely to form a seed. Background training sample mimics any combination of track pairs. The training was done by Boosted decision tree (BDT) algorithm in TMVA [85]. The variables listed in Table 6.2 are used for classification.

6.2.2 Form two-track seed vertices

Similar to the standard DV method, it starts with forming the two-track seed vertices. However, the way of selecting track pairs used to form seeds is different. Figure 6.4 summarizes the procedure.

First, as a track level, all tracks are required to pass the following "pre-selection" criteria:

- $p_{\mathrm{T}} > 1$ GeV
- Not associated with any PVs
- The number of silicon hits ≥ 2

Second, all track pairs are judged if they are signal-like based on the BDT scores. Three scores with different target lifetimes (s_{short}, s_{middle} and s_{long}), where the training was done as 6.2.1 mentions, are

Table 6.2: Variables used to classify the signal-like tarck pairs and random-like track pairs. The superscript indicates the index of the track (1 or 2). The first seven variables are for tracks #1 and #2, there are 18 variables in total.

Variables	Note
η^1, η^2	
d_0^1, d_0^2	
$S(d_0)^1, S(d_0)^2$	$S(d_0)$: d_0-significance
z_0^1, z_0^2	
$z_0^1 - z_{\mathrm{PV}}, z_0^2 - z_{\mathrm{PV}}$	z_{PV}: z position of the primary vertex
$S(z_0)^1, S(z_0)^2$	$S(z_0)$: z_0-significance
innermost hit category of track #1 and track #2	0: IBL, 1: B-Layer, 2: Layer-1 or Layer-2, 3: SCT
$\Delta\eta$ between track #1 and track #2	
$\Delta\phi$ between track #1 and track #2	
$({p_{\mathrm{T}}}^1 - {p_{\mathrm{T}}}^2)/({p_{\mathrm{T}}}^1 + {p_{\mathrm{T}}}^2)$	
difference of the innermost hit category	

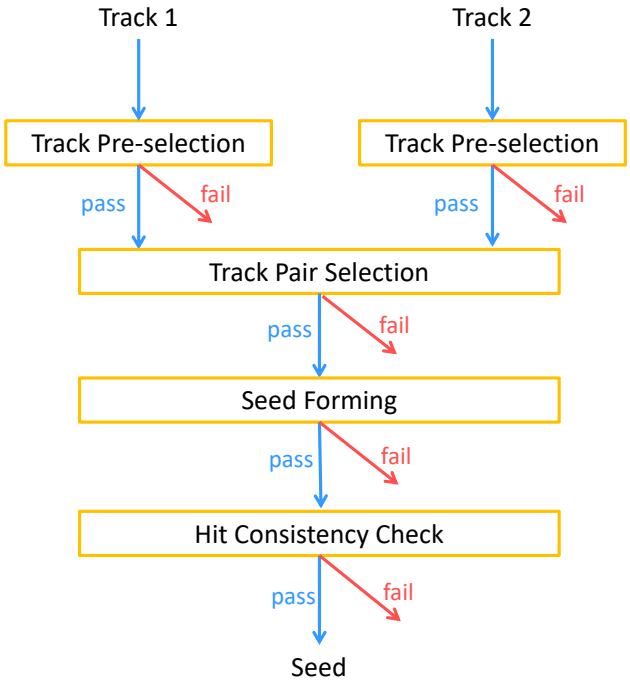

Figure 6.4: Schematic diagram of two-track seed vertex reconstruction in the special method.

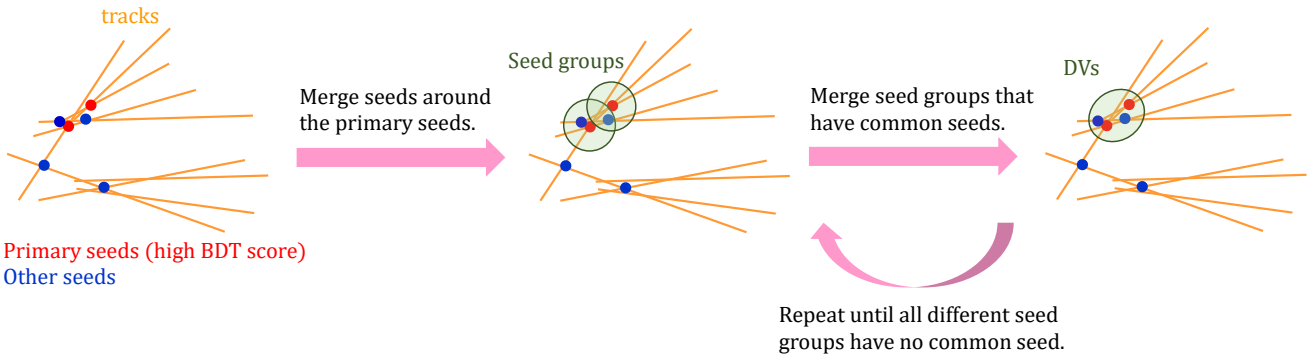

Figure 6.5: The way of multi-track vertex reconstruction in the special method.

calculated for all track pairs. When at least one of them is higher than -0.05, the track pair is used to form two-track seed vertices. The same fitting algorithm and hit-consistency check are performed as Section 6.1.1.

6.2.3 Multi-track vertex reconstruction

At this step, two steps of seed merging are performed as summarized in Figure 6.5.

All two-track seeds have three BDT scores showing if they are signal-like, which are used in the previous step. If $s_{\text{middle}} > 0.15$ or $s_{\text{long}} > 0.15$, the seed is defined as "primary seeds." s_{short} is not used to select primary seeds. Seeds around a primary seed are merged into a seed group. When the x, y, z position difference from a primary seed are all smaller than 1 mm(3 mm/5 mm) and $r_{\text{seed}} < 23.5$ mm(23.5 mm $\leq r_{\text{seed}} <$ 33.5 mm/33.5 mm $\leq r_{\text{seed}}$), respectively, the seed is a candidate to be merged. Those seeds are called "substitute seeds." If the primary seed and the substitute seed meet the following criterion, the substitute seed is merged into the primary seed:

$$\sum {p_{\text{T}}}^{\text{prim}} + \sum {p_{\text{T}}}^{\text{sub}} > 3.0 \times (\phi_{\text{max}} - \pi/2) + 4.0, \tag{6.1}$$

where $\sum {p_{\text{T}}}^{\text{prim}}$ and $\sum {p_{\text{T}}}^{\text{sub}}$ are the sum of the p_{T} of two tracks included in the primary seed and the substitute seed respectively, and ϕ_{max} is the maximum angle between the tracks included in the primary seed and the substitute seed, as explained in Figure 6.6. As Figure 6.7 shows, the condition Equation 6.1 prevents merging large amounts of background seeds, especially those inside the beam pipe, while keeping merging signal seeds. This seed merging process is performed for all primary seeds with the order of BDT score.

As the final step, all seed groups with common seeds are merged. This seed group merging step is repeated until all different seed groups do not have any common seeds with other seeds. The final remaining seed groups are defined as a DV. At this point, the vertex kinematics are calculated. The vertex mass is calculated similarly as the standard DV, as described in Section 6.1. The vertex position is defined as the average position of the seeds included in the DV. The variance and covariance of the seeds' positions, which indicate the vertex position uncertainties, are also calculated. Two-track seeds that have not merged with any other seeds are removed.

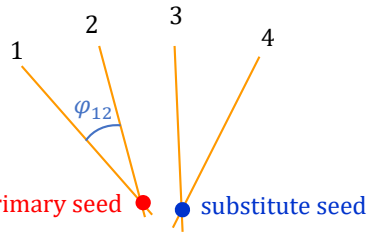

$$\sum p_{\mathrm{T}}^{\mathrm{prim}} = p_{\mathrm{T}}^{1} + p_{\mathrm{T}}^{2}$$
$$\sum p_{\mathrm{T}}^{\mathrm{subs}} = p_{\mathrm{T}}^{3} + p_{\mathrm{T}}^{4}$$
$$\varphi_{\mathrm{max}} = \max(\varphi_{12},\ \varphi_{13}, \varphi_{14}, \varphi_{23}, \varphi_{24}, \varphi_{34})$$

Figure 6.6: Definitions of variables $\sum p_{\mathrm{T}}{}^{\mathrm{prim}}$, $\sum p_{\mathrm{T}}{}^{\mathrm{sub}}$, and ϕ_{max}, which are used for seed merging.

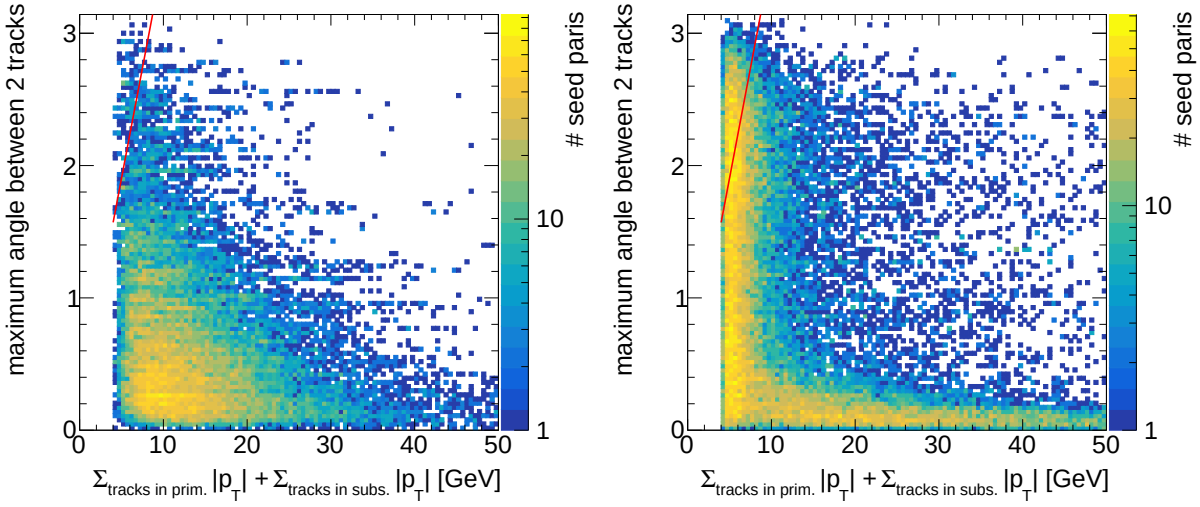

Figure 6.7: Correlation between the primary seeds and substitute seeds inside the beam pipe in the signal MC (left) and data (right). The bino-wino signal sample with $m_{\tilde{\chi}_2^0} = 200$ GeV, $\Delta M(\tilde{\chi}_2^0, \tilde{\chi}_1^0) = 30$ GeV, $\tau_{\tilde{\chi}_2^0} = 0.03$ ns is used. The pairs of primary and substitute seeds above the red line are not merged.

6.3 Displaced vertex reconstruction performance

This section compares the performance of the standard and special reconstruction.

6.3.1 Signal DV reconstruction efficiency

Figure 6.8 shows the DV reconstruction efficiency as a function of the LLP decay radial position (r_{decay}) for bino-wino signal events. It is defined as follows:

$$\begin{aligned}&\text{DV reconstruction efficiency}\\ &= \frac{\text{Number of reconstructed DVs matching with LLP}}{\text{Number of LLPs with at least two reconstructed charged particles}}.\end{aligned} \tag{6.2}$$

The definition of "DV matching with LLP" is as follows:

- The DV has at least one track originating from a descendant particle of the LLP
- The scalar p_{T} sum of tracks originating from a descendant particle of the LLP is larger than 0.5 of the scalar p_{T} sum of all tracks

The second condition is applied to assure the purity of the DV. Since the special DVs with only two tracks have been removed at the end of the vertex reconstruction algorithm, reconstructed DVs with at least three tracks are counted here to make a fair comparison. In each case and at each LLP decay position, the DV reconstruction efficiency of the special reconstruction is higher than that of the standard one, up to approximately 1.5 times.

6.3.2 Features of reconstructed signal DVs

Figure 6.9 is an example of a signal event display in x-y plane with a DV reconstructed by the standard and the special DV method in the same event. In this event, the DV is reconstructed using both methods, but the special method reconstructs the DV with more tracks than the standard one. Figures 6.10 and 6.11 show the distribution of the number of tracks and invariant mass of the signal DVs reconstructed by the standard and special DV methods. The number of tracks and the invariant mass are calculated using only the tracks originating from the LLP. The DVs reconstructed by the special method tend to have a larger number of tracks and a higher invariant mass. For example, the number of special DVs with more than four tracks and invariant mass higher than 10 GeV is 2 to 6 times larger than that of standard DVs.

As the consistency check, the performance is also compared using other signal models, the long-lived gluino ($\tilde{g}$) decaying to the $\tilde{\chi}_2^0$ and light quarks, as shown in Figure 6.12. Since the LLP decay does not contain b-quarks, it is expected that the standard and special method have a similar performance. Figure 6.13 shows the distribution of the number of tracks and invariant mass of the signal DVs in the gluino model with the mass splitting between the $\tilde{g}$ and $\tilde{\chi}_1^0$ ($DletaM(\tilde{g}, \tilde{\chi}_1^0)$) is 30 GeV, which is a similar value to the bino-wino case. The number of DVs reconstructed by the standard and special methods with a high number of tracks and invariant mass does not have a large difference unlike the bino-wino model case as expected. From this comparison, it can be said that the special method reconstructs the point-like

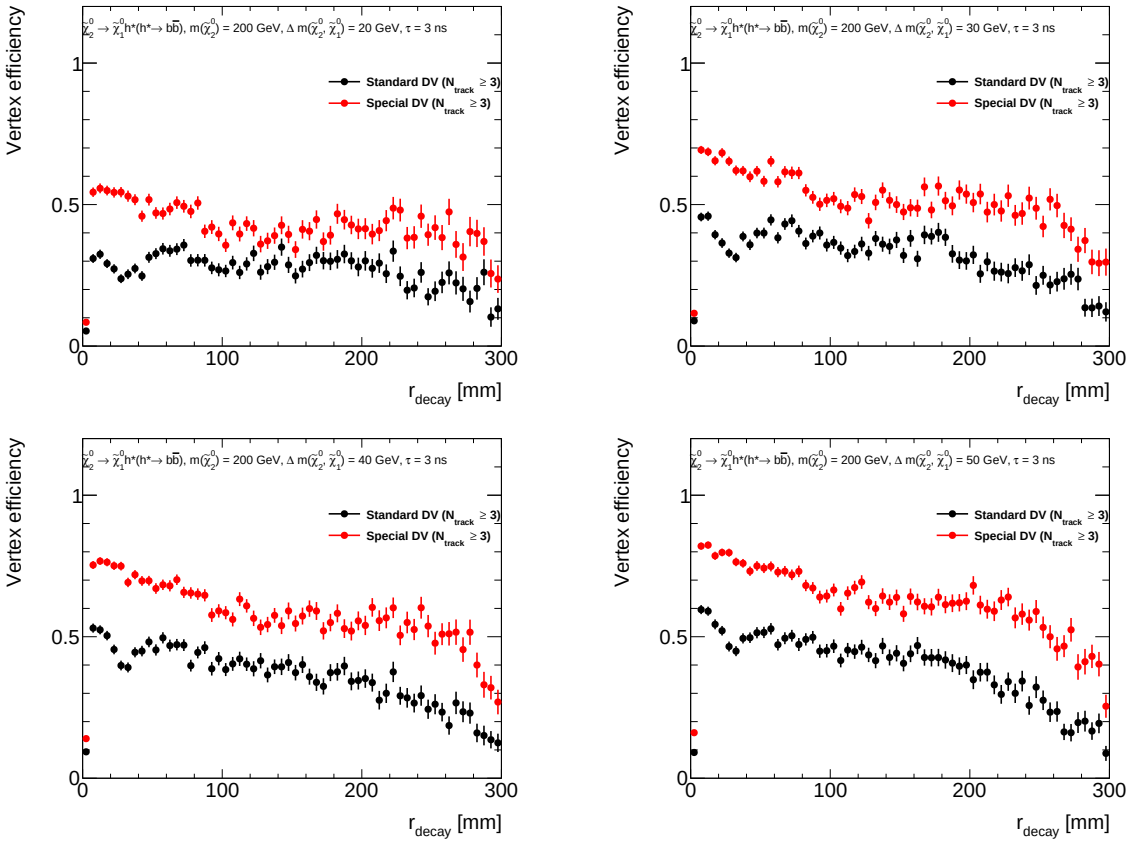

Figure 6.8: DV reconstruction efficiency of standard (black) and special (red) DV method as a function of the LLP decay position. The signal events in the bino-wino model with $m_{\tilde{\chi}_2^0} = 200$ GeV and $\tau_{\tilde{\chi}_2^0} = 3$ ns are used. Reconstructed DVs are required to have at least three tracks here because special DVs with only two tracks have been removed.

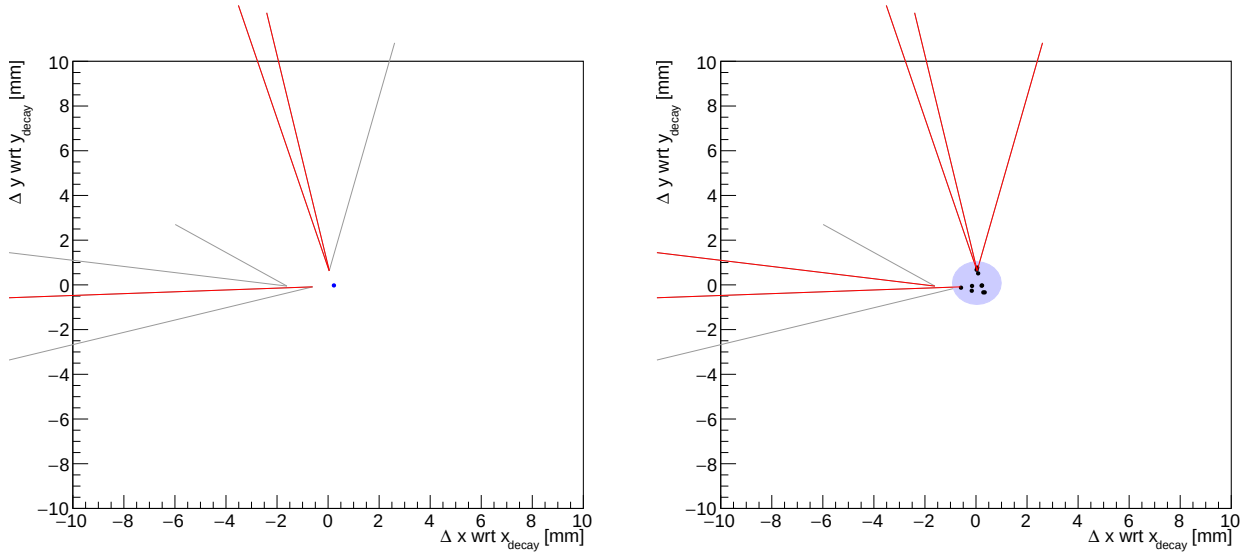

Figure 6.9: Comparison of a signal DV reconstructed by the standard (left) and the special method (right) in the same event. The origin is the signal LLP decay point. Gray lines and red lines show the tracks associated and not associated with the DV, respectively. The blue point in the left figure is the DV reconstructed by the standard method. In the right figure, black points show the two-track seed vertices belonging to the DV, and the blue circle is five times the size of the DV reconstructed by the special method, where the size is defined as the standard deviation of the two-track seed positions included in it.

LLP decay, which are the target of the standard method, with the similar performance as the standard method.

6.3.3 Background DV rate

Figure 6.14 shows the radial position of the DVs reconstructed by the standard and special reconstructed methods in one run taken in one run from 2018 with an integrated luminosity of 6.7 pb^{-1}. The peaks around 20, 30, 50, 90, and 120 mm correspond to the beam pipe and Pixel layers. The special method reconstructs more DVs in the small radial region. It is expected to be caused by removing the requirements that at least one of the tracks must have $|d_0| > 2$ mm in the seed forming step, which is used in the standard method. In these DVs, there are a lot of DVs originated from the b-hadron decays, which include a large track multiplicity. Rejecting such background DVs while keeping DVs from signal events becomes a challenge when using this special method.

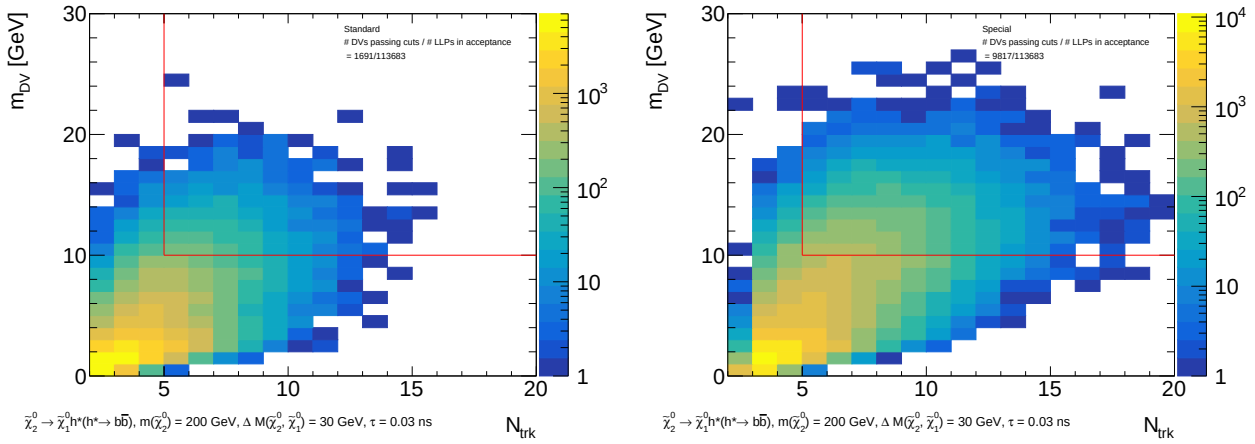

(a) Standard DV, $\tau_{\tilde{\chi}_2^0} = 0.03$ ns

(b) Special DV, $\tau_{\tilde{\chi}_2^0} = 0.03$ ns

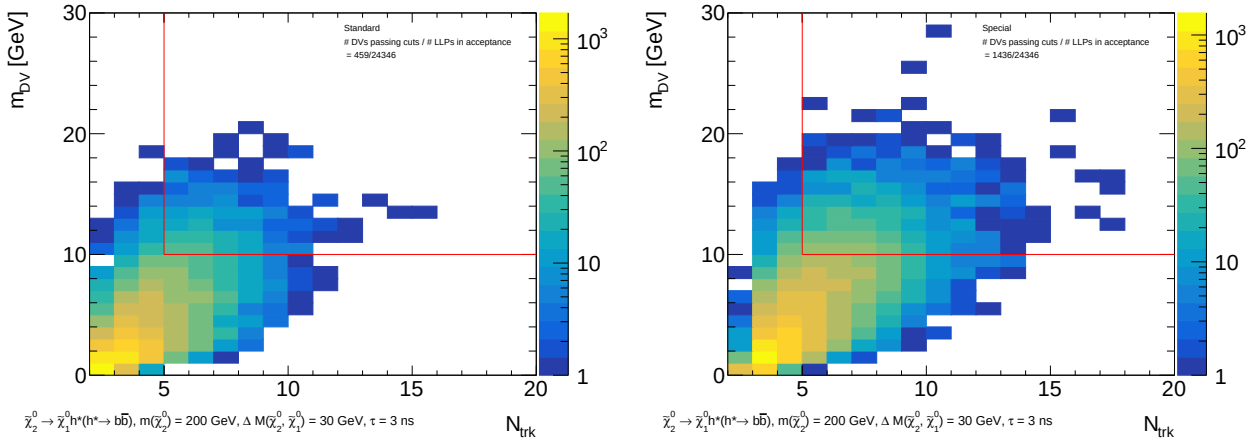

(c) Standard DV, $\tau_{\tilde{\chi}_2^0} = 3$ ns

(d) Special DV, $\tau_{\tilde{\chi}_2^0} = 3$ ns

Figure 6.10: Number of tracks and invariant mass of the signal DVs reconstructed by the standard method (left) and special method (right). Only the tracks originating from the LLP are counted. The bino-wino signal events with $m_{\tilde{\chi}_2^0} = 200$ GeV and $\Delta M(\tilde{\chi}_2^0, \tilde{\chi}_1^0) = 30$ GeV are used. "DV passing the cut" shows the number of DVs that meet the cuts shown in the red line.

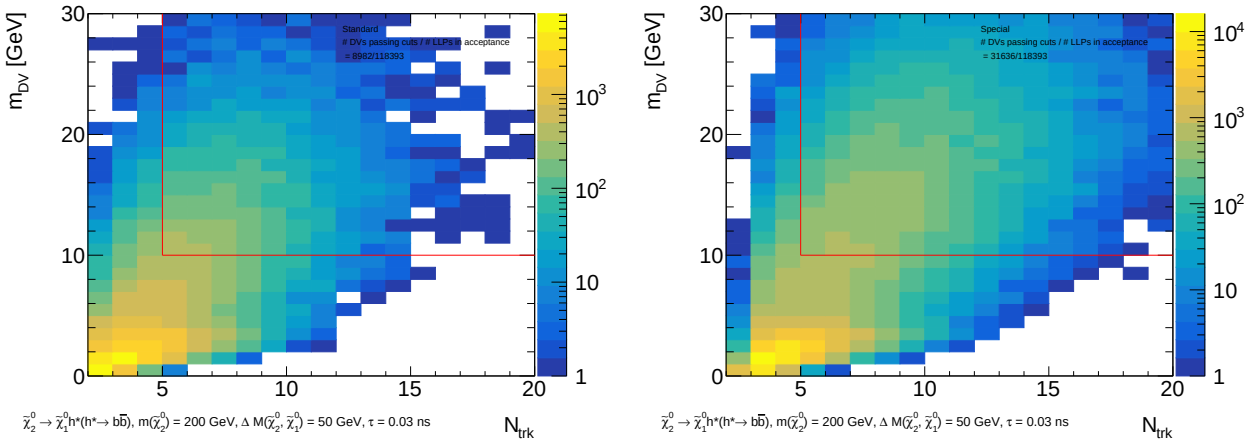

(a) Standard DV, $\tau_{\tilde{\chi}_2^0} = 0.03$ ns

(b) Special DV, $\tau_{\tilde{\chi}_2^0} = 0.03$ ns

(c) Standard DV, $\tau_{\tilde{\chi}_2^0} = 3$ ns

(d) Special DV, $\tau_{\tilde{\chi}_2^0} = 3$ ns

Figure 6.11: Number of tracks and invariant mass of the signal DVs reconstructed by the standard method (left) and special method (right). The bino-wino signal events with $m_{\tilde{\chi}_2^0} = 200$ GeV and $\Delta M(\tilde{\chi}_2^0, \tilde{\chi}_1^0) = 50$ GeV are used. "DV passing the cut" shows the number of DVs that meet the cuts shown in the red line.

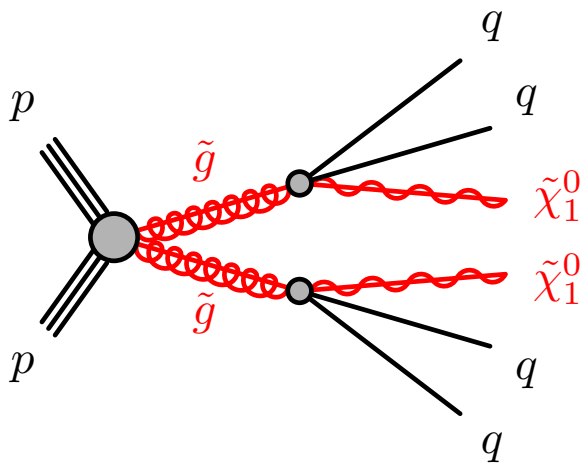

Figure 6.12: Feynman diagram of pair production of $\tilde{g}$ decaying to the $\tilde{\chi}_1^0$ and light quarks (q). In this case, $\tilde{g}$ becomes long-lived.

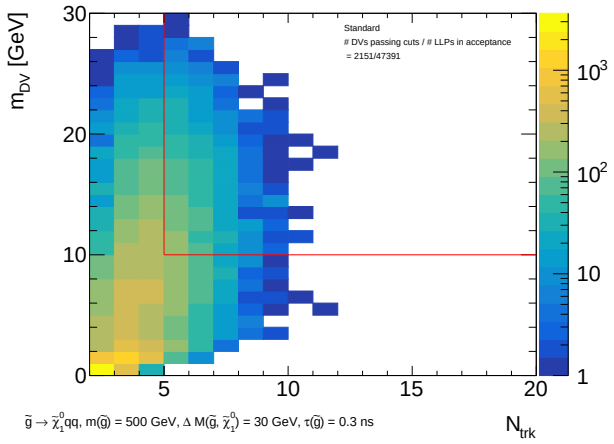

(a) Standard DV, $\tau_{\tilde{g}} = 0.3$ ns

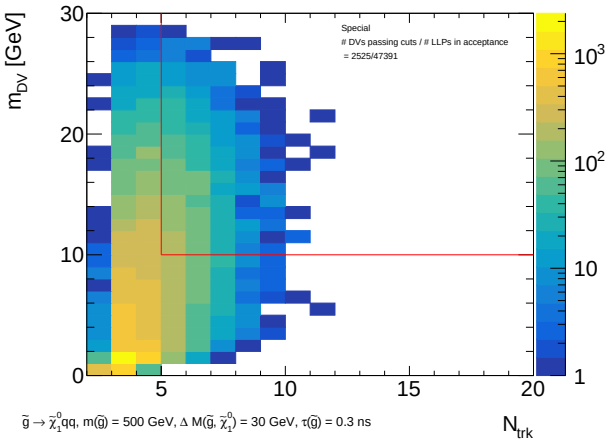

(b) Special DV, $\tau_{\tilde{g}} = 0.3$ ns

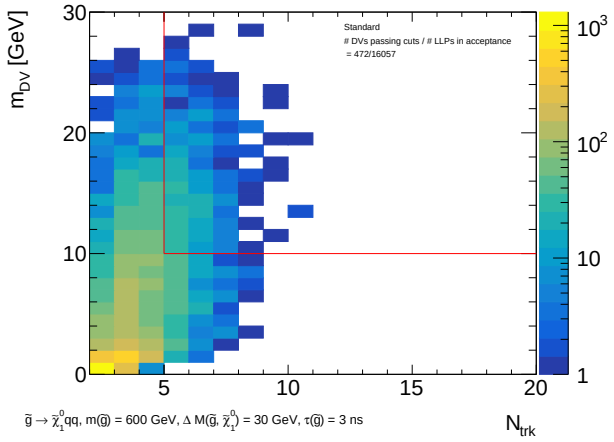

(c) Standard DV, $\tau_{\tilde{g}} = 3$ ns

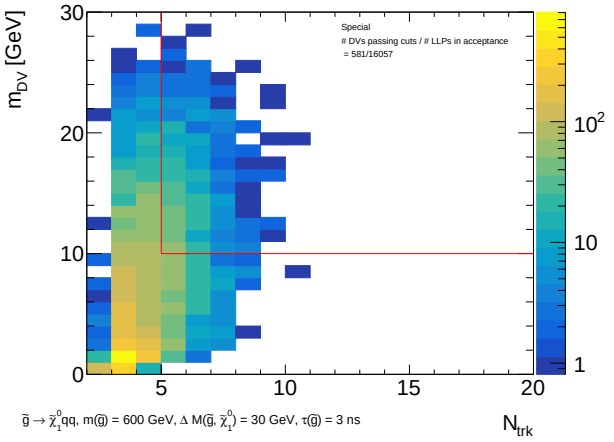

(d) Special DV, $\tau_{\tilde{g}} = 3$ ns

Figure 6.13: Number of tracks and invariant mass of the signal DVs reconstructed by the standard method (left) and special method (right). The gluino signal events with $m_{\tilde{\chi}_1^0} = 500$ GeV and $\Delta M(\tilde{g}, \tilde{\chi}_1^0) = 30$ GeV are used. "DV passing the cut" shows the number of DVs that meet the cuts shown in the red line.

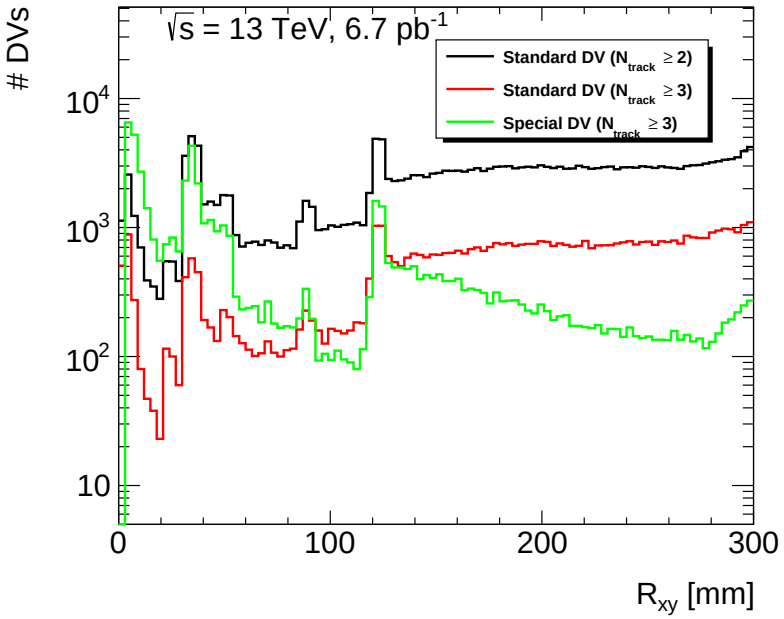

Figure 6.14: Radial position of the DVs reconstructed by the standard and special reconstruction methods using one run.

Chapter 7

Event selection

This chapter describes the definition of the signal region (SR). The selection criteria are discussed based on the properties of signal and background events.

The data flow of the ATLAS standard analyses and this analysis are shown in Figures 7.1 and 7.2. In the first stage, collision events of interest are selected by triggers. In the standard case, secondly, the standard object reconstructions are performed using the triggered data and stored in the specific data format, called Analysis Object Data (AOD). In the case of this analysis which needs some particular reconstructions for LLP search, the derived raw data (DRAW) filter is applied to skim the data before the object reconstruction. The standard and special object reconstructions are done using these limited number of events that pass the DRAW filter. Further skimming, called derivation, is applied to the AOD with both the standard and this analysis cases, producing the derived AOD (DAOD), including only the information used for each analysis. Finally, offline event- and object-level selections are performed using DAOD.

7.1 Trigger and filter

The size of the collision data is reduced with several steps as described in Section 3.2.5. The following sections explain the details of each step of this analysis.

7.1.1 DRAW filter

This analysis uses a specific data format (`DRAW_RPVLL`) because it uses non-standard objects based on low-level detector and reconstruction information. In order to save the disk space for `DRAW_RPVLL`, only a subset of events that satisfy some specific triggers or filters are made available. This skimming is mainly based on the trigger, but offline object requirements are also added to keep the event rate low. Each analysis has its own combination of trigger and offline filter. The rate of the `DRAW_RPVLL` is kept below 30 Hz on average, while keeping full RAW information for the skimmed events. Table 7.1 is the list of the $E_{\mathrm{T}}^{\mathrm{miss}}$ triggers included in the `DRAW_RPVLL` dataset. The name of the HLT algorithm corresponds to the ones mentioned in Section 3.2.5. As an offline filter for further reduction, the topo cluster-based $E_{\mathrm{T}}^{\mathrm{miss}}$

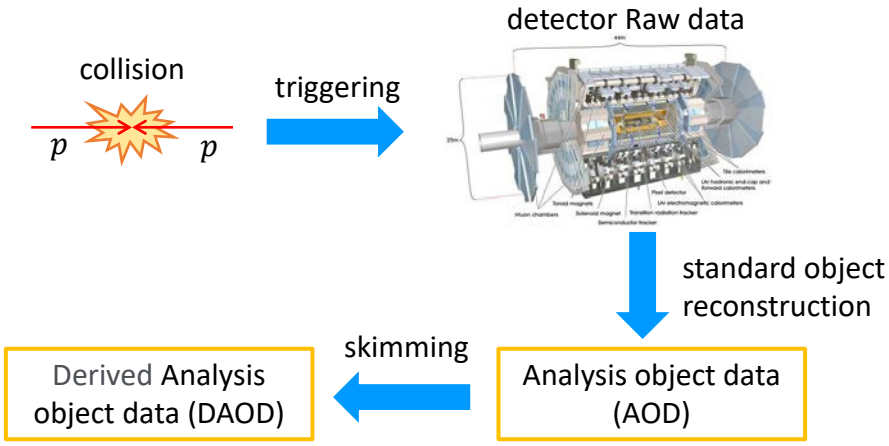

Figure 7.1: Schematic view of data flow in ATLAS standard analysis.

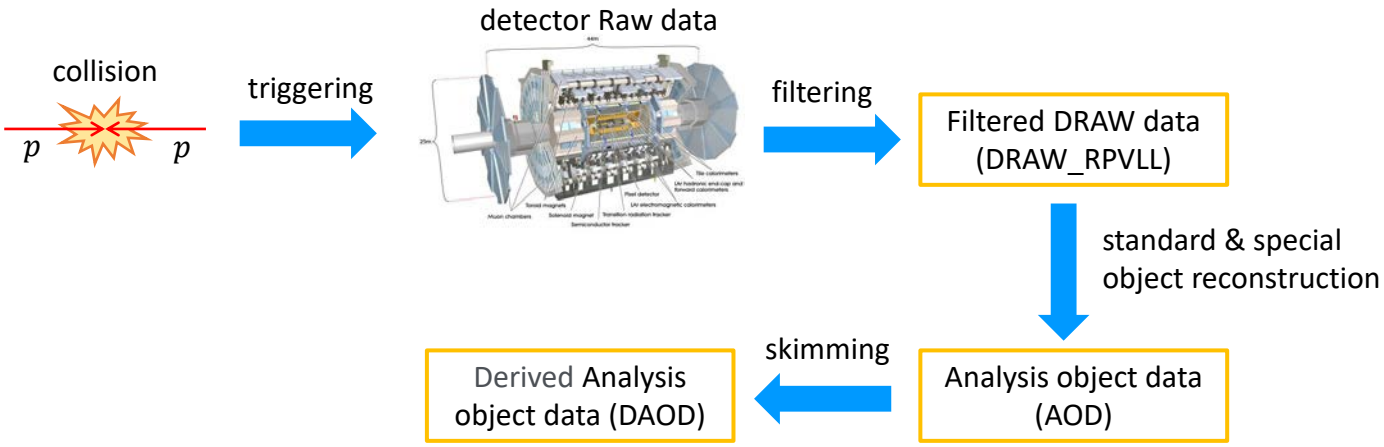

Figure 7.2: Schematic view of data flow in this analysis.

Table 7.1: Trigger selection list. For items with multiple HLT thresholds listed, any combination of thresholds is included. For example, the first row contains `HLT_xe90_L1XE50`, `HLT_xe90_L1XE55`, `HLT_xe90_L1XE60`, `HLT_xe100_L1XE50`, `HLT_xe100_L1XE55`, `HLT_xe100_L1XE60`, `HLT_xe120_L1XE50`, `HLT_xe120_L1XE55`, and `HLT_xe120_L1XE60`. The used algorithm is described in Section 3.2.6.

Trigger name	HLT algorithm and threshold [GeV]	L1 threshold [GeV]
`HLT_xeXX_L1XEZZ`	`cell` 90, 100, 120	50, 55, 60
`HLT_xeXX_tc_lcw_L1XEZZ`	`tc_lcw` 90, 100, 120	50, 55, 60
`HLT_xeXX_mht_L1XEZZ`	`mht` 90, 100, 110, 120	50, 55, 60
`HLT_xeXX_mht_L1XEZZ`	`mht` 130	50
`HLT_xeXX_mht_L1XEZZ_AND_xeYY_L1XEZZ`	`cell` 110 and `mht` 65, 70, 75, 80	50, 55
`HLT_xeXX_mht_L1XEZZ_AND_xeYY_L1XEZZ`	`cell` 120 and `mht` 80	60
`HLT_xeXX_pufit_L1XEZZ`	`pufit` 110	50, 55, 60
`HLT_xeXX_pufit_L1XEZZ`	`pufit` 120	60, 70
`HLT_xeXX_pufit_xeYY_L1XEZZ`	`pufit` 110 and `cell` 70	50
`HLT_xeXX_pufit_xeYY_L1XEZZ`	`pufit` 110 and `cell` 65	55
`HLT_xeXX_pufit_xeYY_L1XEZZ`	`pufit` 100 and `cell` 75	60
`HLT_xeXX_pufit_xeYY_L1XEZZ`	`pufit` 110 and `cell` 65	60

larger than 180 GeV, is applied. The use of topo cluster-based $E_{\mathrm{T}}^{\mathrm{miss}}$ is motivated because it is a simpler variable that is not significantly affected throughout data-taking than the offline $E_{\mathrm{T}}^{\mathrm{miss}}$.

7.1.2 SUSY15 filter

The analysis data samples after DRAW filtering contain not only the events used in this analysis but also those for other analyses, passing triggers other than $E_{\mathrm{T}}^{\mathrm{miss}}$. For further data reduction and special reconstruction, a more specific derivation, called `DAOD_SUSY15`, is applied. It skims the data by selecting the events passing any triggers used in the ATLAS long-lived SUSY searches. Events passing at least one of the lowest unprescaled $E_{\mathrm{T}}^{\mathrm{miss}}$ triggers are selected. Events triggered by some other triggers, such as single muon or photon, are also made available. Moreover, some additional reconstruction algorithms, such as special displaced vertex reconstruction described in 6.2, are carried out in this stage.

7.2 Event cleaning

As described in Section 4.1, data quality information is summarized in GRL. The data flagged as bad are not used for this analysis. In addition, the events that might be affected by the following detector problems are also rejected:

- Noise burst in the Liquid argon calorimeter
- Corruption of the Tile calorimeter data
- Recovery from the single event upset in SCT

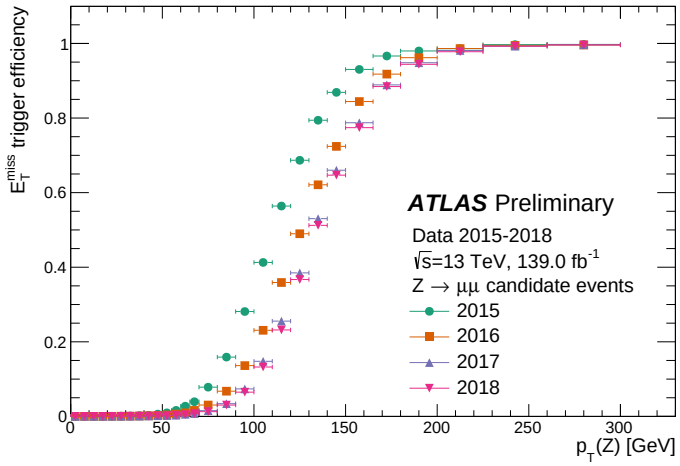

Figure 7.3: $E_{\mathrm{T}}^{\mathrm{miss}}$ trigger efficiency of each year measured by $Z \to \mu\mu$ events [47]. The trigger efficiency when $p_{\mathrm{T}}(Z) = 250$ GeV is approximately 100%, but not when $p_{\mathrm{T}}(Z) = 150$ GeV.

7.3 PV selection

In order to suppress the effects of pileups on the $E_{\mathrm{T}}^{\mathrm{miss}}$ calculation, the events are required to have at least one PV with two or more associated tracks, and z position $|z_{\mathrm{PV}}| < 200$ mm.

7.4 Offline $E_{\mathrm{T}}^{\mathrm{miss}}$ selection

In addition to the $E_{\mathrm{T}}^{\mathrm{miss}}$ trigger and filter, the $E_{\mathrm{T}}^{\mathrm{miss}}$ calculated offline based on Equation 5.8 is used for event selection. Since the offline $E_{\mathrm{T}}^{\mathrm{miss}}$ includes the objects not based on the calorimeter (i.e. muons and soft terms), the resolution is better than the topo-cluster based $E_{\mathrm{T}}^{\mathrm{miss}}$. In this analysis, events are required to have an offline $E_{\mathrm{T}}^{\mathrm{miss}}$ larger than 150 GeV. Figure 7.3 shows the $E_{\mathrm{T}}^{\mathrm{miss}}$ trigger efficiency measured using the $Z \to \mu\mu$ events. Since muons are not included in the $E_{\mathrm{T}}^{\mathrm{miss}}$ calculation at the triggers, the p_{T} of the reconstructed Z boson can be used as a proxy for $E_{\mathrm{T}}^{\mathrm{miss}}$. The previous ATLAS analysis using DVs and $E_{\mathrm{T}}^{\mathrm{miss}}$ [86] required the offline $E_{\mathrm{T}}^{\mathrm{miss}} > 250$ GeV, which is almost on the plateau region of the $E_{\mathrm{T}}^{\mathrm{miss}}$ efficiency curve. In this analysis. this threshold is decreased to 150 GeV so that it becomes more sensitive to the cases with small mass splitting between $\tilde{\chi}_2^0$ and $\tilde{\chi}_1^0$, which tend to have small $E_{\mathrm{T}}^{\mathrm{miss}}$. However, this threshold is in the middle of the turn-on curve, and the trigger performance of the data and MC are not validated to be the same in this region. The uncertainty of signal selection efficiency by the $E_{\mathrm{T}}^{\mathrm{miss}}$ trigger performance is discussed in Section 9.2.

7.5 Non-collision background veto

When a large $E_{\mathrm{T}}^{\mathrm{miss}}$ is required, the effect of non-collision background (NCB), such as detector noises or secondary particles from noncolliding protons, becomes significant. The dominant NCB source in this analysis is the beam-induced background due to proton losses upstream of the collision point. Secondary

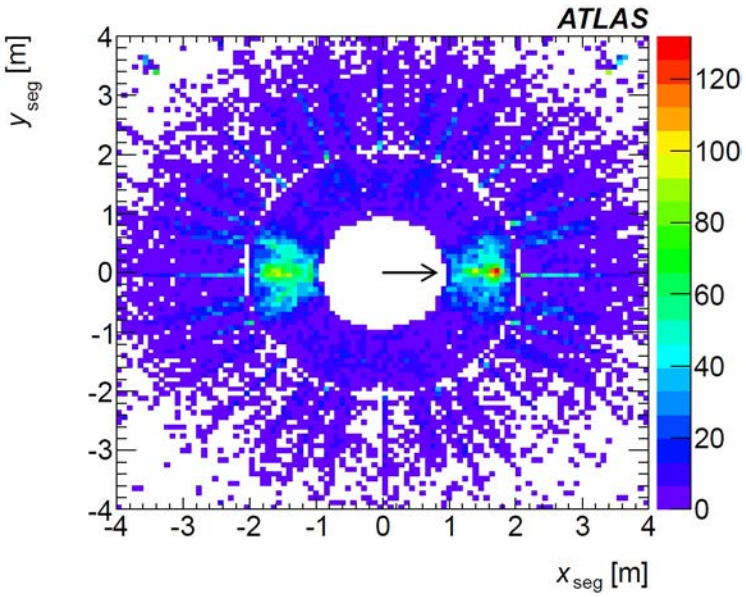

Figure 7.4: x-y position of the muon segments in the CSC and the inner MDT endcaps [87]. The segments parallel to the beam line that are likely to be NCB-induced are pointed by an arrow.

muons induced by these proton losses can reach the ATLAS detector. Figure 7.4 shows the x-y position of the muon segment in the CSC and the inner MDT in the NCB-enriched events. Two peaks at $\phi = 0, \pm\pi$ show that the NCB is spread in a horizontal axis, which is mainly due to the magnet around the collision point. The energy deposits of the secondary muons can be reconstructed as fake jets in the calorimeter, resulting in a fake $E_{\mathrm{T}}^{\mathrm{miss}}$.

Since event selection includes the requirement for PV, NCB does not satisfy the selection itself. However, NCB may affects this analysis if it is overlapping with the collision events. To discriminate these signal-like events with NCB-induced large $E_{\mathrm{T}}^{\mathrm{miss}}$, two level of NCB vetos are used in this analysis. First, if any jet in the event meets any of the following criteria (*SuperLooseBadLLP* cleaning [88]), the event is rejected:

- $(f_{\mathrm{max}} > 0.99)$ and (jet $|\eta| < 2$)
- $(E_{\mathrm{neg}} > 60$ GeV$)$
- $(f_{\mathrm{HEC}} > 0.5)$ and $(|f_{\mathrm{Q}}^{\mathrm{HEC}}| > 0.5)$ and $(\langle Q \rangle > 0.8)$
- $(f_{\mathrm{EM}} > 0.95)$ and $(f_{Q}^{\mathrm{LAr}} > 0.8)$ and (jet $|\eta| < 2.8$) and $(\langle Q \rangle > 0.8)$

where the variables used are:

- f_{max}: Maximum energy fraction in any single calorimeter layer
- E_{neg}: Sum of all cells in the jet with negative energy
- f_{HEC}: Ratio of the energy in the HEC calorimeter to the total energy of the jet

- $f_{\mathrm{Q}}^{\mathrm{HEC}}$: Fraction of the energy in the HEC cells of the jet with poor signal shape quality
- $\langle Q \rangle$: Energy-squared weighted average of the pulse quality of the cells in the jet
- f_{Q}^{LAr}: Fraction of the energy in the LAr cells with poor signal shape quality in the jet
- f_{EM}: Ratio of the energy in the electromagnetic calorimeter to the total energy of the jet

This cleaning is done with event-level because such bad jets may affects the whole event.

However, the *SuperLooseBadLLP* jet cleaning alone is not sufficient to remove NCB. As the second step of NCB veto, a stricter selection is applied to the leading jet. The events whose leading jet satisfies at least one of the following criteria are rejected:

- $f_{\mathrm{max}} > 0.8$
- $f_{\mathrm{EM}} > 0.96$
- $f_{\mathrm{ch}}/f_{\mathrm{max}} < 0.1$

where f_{ch} is the fraction of the scalar sum of track p_{T} in the jet and jet p_{T}, respectively. Figures 7.5 show the correlation between the $E_{\mathrm{T}}^{\mathrm{miss}}$ direction ϕ and those variables. The events passing the trigger, $E_{\mathrm{T}}^{\mathrm{miss}}$ filter, event cleaning, PV conditions, and offline $E_{\mathrm{T}}^{\mathrm{miss}}$ selection described in the previous sections of this chapter are included. Peaks in ϕ are prominent when the f_{max} or f_{EM} is large, and when $f_{\mathrm{ch}}/f_{\mathrm{max}}$ is small. Figure 7.6 shows the azimuthal $E_{\mathrm{T}}^{\mathrm{miss}}$ angle distribution before and after the NCB veto described above. The peaks around $\phi = 0, \pm\pi$ seen before the NCB veto, which seems to be induced by the NCB, almost disappeared.

7.6 Dead Tile module veto

Even after applying the NCB veto, some spikes are visible in the $E_{\mathrm{T}}^{\mathrm{miss}}$ ϕ distribution, as seen in Figure 7.6. They are caused by issues with the modules on the Tile calorimeter. Those modules are called dead Tile modules. When there is a deal Tile module on the jet direction, the jet energy would be measured to be smaller than the true energy, resulting in a fake $E_{\mathrm{T}}^{\mathrm{miss}}$. Figure 7.7 shows an example that di-jet event has a fake $E_{\mathrm{T}}^{\mathrm{miss}}$ caused by a dead Tile module. To avoid these events with pathologically mismeasured $E_{\mathrm{T}}^{\mathrm{miss}}$, event is vetoed if any jet with $p_{\mathrm{T}} > 50$ GeV and $\Delta\phi(E_{\mathrm{T}}^{\mathrm{miss}}, \text{jet}) < 0.3$ is on the dead Tile modules listed in Table 7.2. Figure 7.8 shows the ϕ in $E_{\mathrm{T}}^{\mathrm{miss}}$ of the events passing $E_{\mathrm{T}}^{\mathrm{miss}}$ selection, PV selection, and strict NCB veto with and without dead tile module veto. The spikes corresponding to the dead tile modules listed in Table 7.2 have been removed by this veto.

A set of events that satisfies the above selections, i.e., the $E_{\mathrm{T}}^{\mathrm{miss}}$ conditions, PV selection, NCB veto, and dead Tile module veto, is defined as "$E_{\mathrm{T}}^{\mathrm{miss}}$-triggered region (MTR)."

7.7 DV selection

This analysis targets the DV $O(1)$-$O(100)$ mm away from the collision point. This section describes the selection of DVs applied to reduce background events. As explained in Chapter 6, this analysis uses the

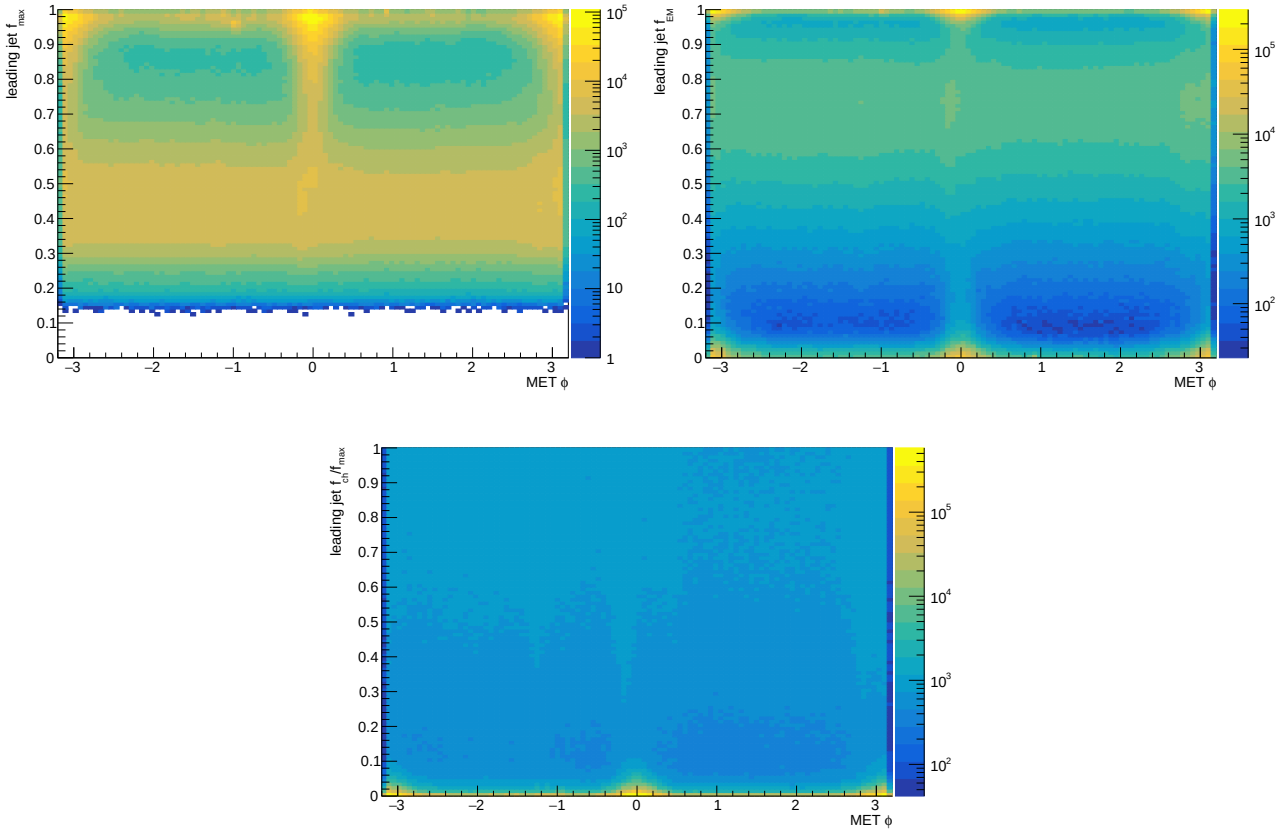

Figure 7.5: Correlation between the $E_{\mathrm{T}}^{\mathrm{miss}}$ ϕ and the leading jet f_{max} (top left), f_{EM} (top right), and $f_{\mathrm{ch}}/f_{\mathrm{max}}$ (bottom). The events are required to pass the trigger, $E_{\mathrm{T}}^{\mathrm{miss}}$ filter, event cleaning, PV conditions, and offline $E_{\mathrm{T}}^{\mathrm{miss}}$ selection.

Table 7.2: Location of dead modules on the Tile calorimeter [89].

Year	Run	dead module region
2016	302053-311481	$0.0 < \eta < 0.9$, $-1.33 < \phi < -1.13$
2016	306988-311481	$-0.9 < \eta < 0.0$, $0.34 < \phi < 0.54$
2017	325713-340453	$-0.9 < \eta < 0.0$, $-0.25 < \phi < -0.05$
2017	325713-340453	$0.8 < \eta < 1.7$, $0.14 < \phi < 0.34$
2018	350310-352514	$0.0 < \eta < 0.9$, $2.7 < \phi < 3.0$
2018	355261-364292	$0.0 < \eta < 0.9$, $\lvert\phi\rvert > 3.0$

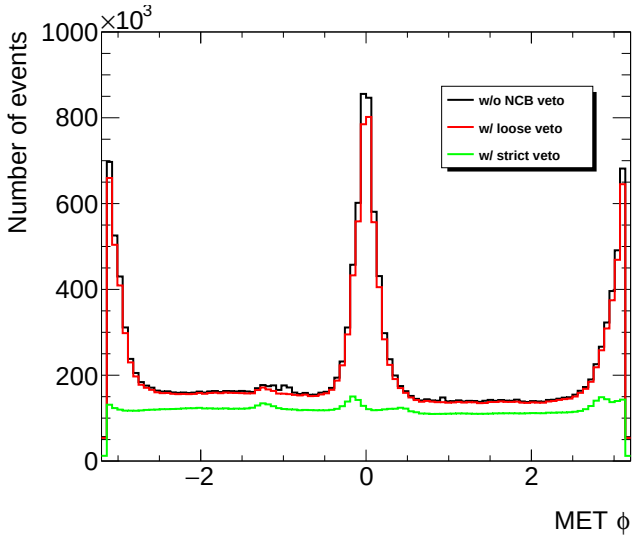

Figure 7.6: The ϕ distribution of the $E_{\mathrm{T}}^{\mathrm{miss}}$ in events passing $E_{\mathrm{T}}^{\mathrm{miss}}$ and PV selection criteria. The black line shows the case without any NCB veto, the red line shows the case after applying *SuperLooseBadLLP* jet veto, and the green line shows the case after applying *SuperLooseBadLLP* jet veto and the selection to the leading jet.

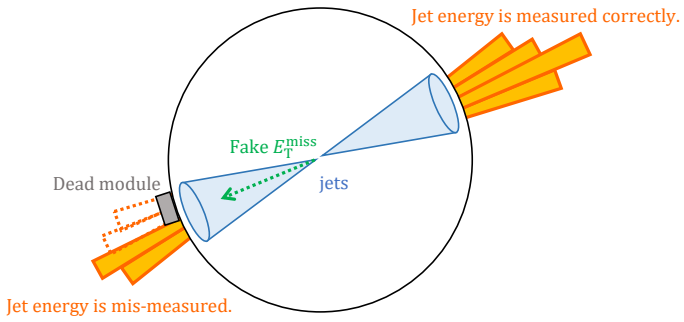

Figure 7.7: Fake $E_{\mathrm{T}}^{\mathrm{miss}}$ caused by a dead Tile module in a di-jet event. The energy of the jet on the left-hand side is measured smaller than the true energy due to a dead Tilde module, and it causes the mismeasurement of the $E_{\mathrm{T}}^{\mathrm{miss}}$.

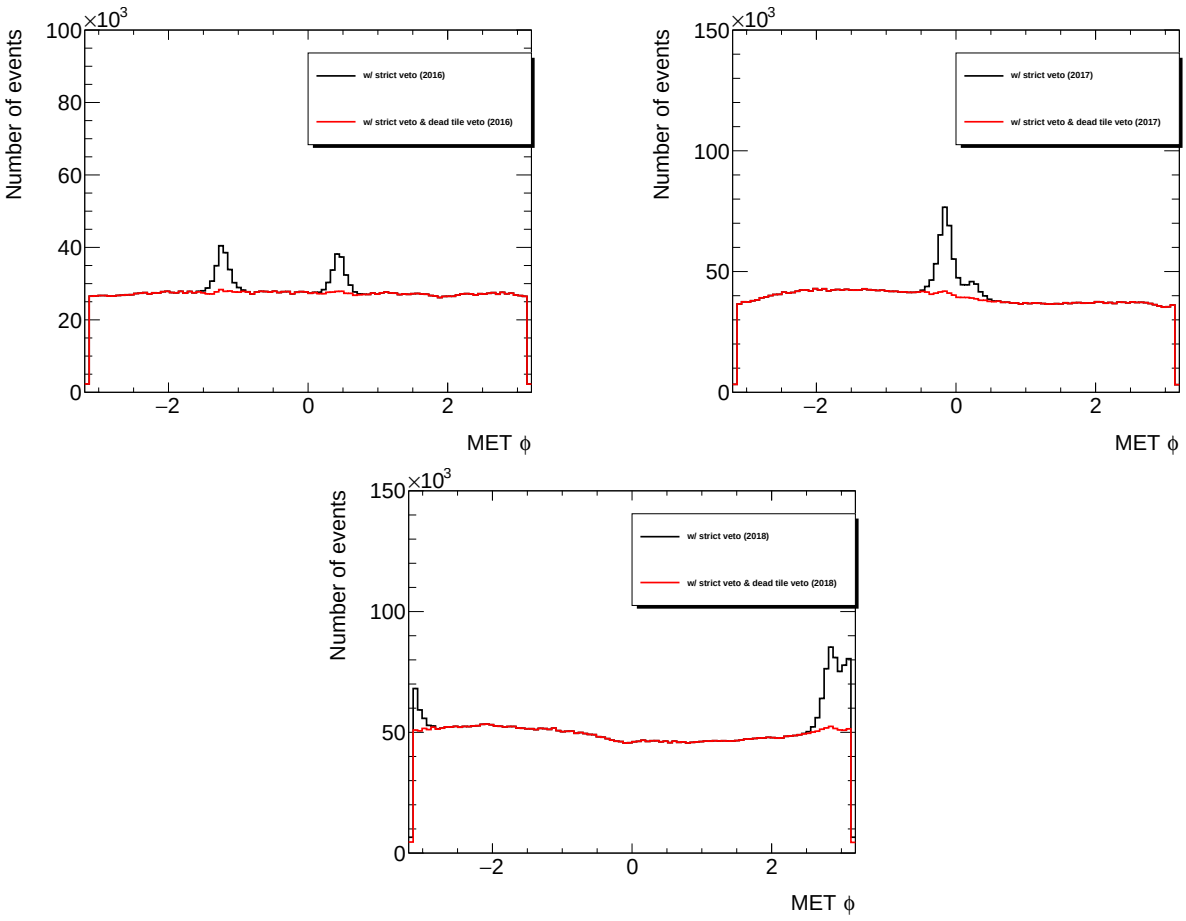

Figure 7.8: The $E_{\mathrm{T}}^{\mathrm{miss}}$ ϕ distribution in 2016 (upper left), 2017 (upper right), and 2018 (bottom). The black line shows the events passing $E_{\mathrm{T}}^{\mathrm{miss}}$ and PV selection and strict NCB veto, and the red line shows the case when dead tile module veto is additionally applied. The reason for the asymmetry between the $E_{\mathrm{T}}^{\mathrm{miss}}\phi > 0$ and $E_{\mathrm{T}}^{\mathrm{miss}}\phi < 0$ after the dead tile module veto is because the beam position was shifted in y-direction in the Run 2 operation.

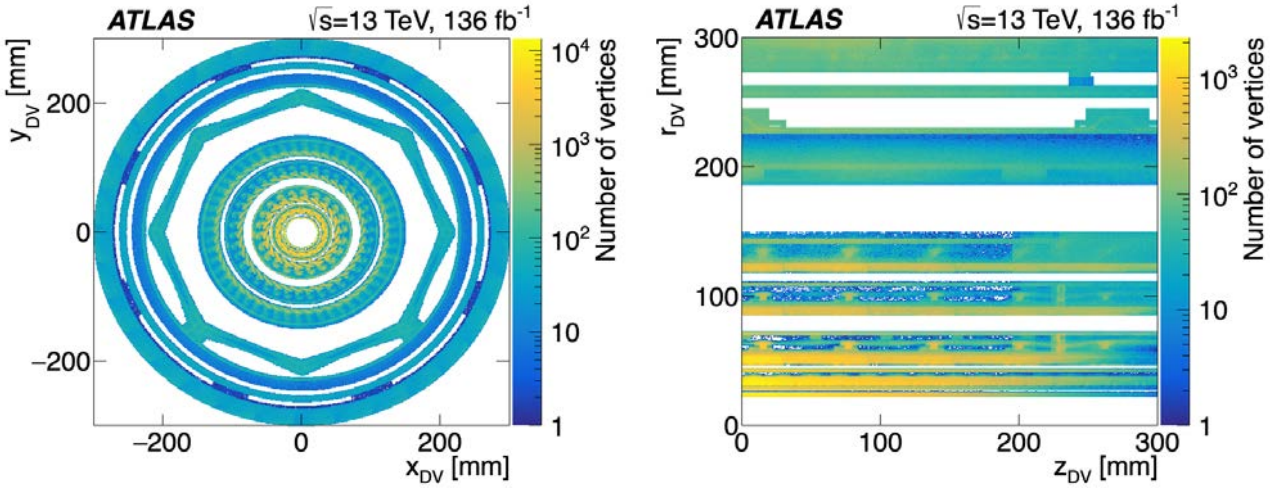

Figure 7.9: Position of the known detector materials and reconstructed low-mass standard DVs in the (a) x-y plane and (b) r-z plane [90]. The colored regions are defined as "inside material" and DVs in these regions are vetoed.

DV reconstructed by the special DV reconstruction method because it is expected to have high selection efficiency for the target signal.

7.7.1 Baseline DV selection

The DV position must be in the fiducial volume defined as $R_{xy} = \sqrt{x_{\mathrm{DV}}^2 + y_{\mathrm{DV}}^2} < 300$ mm and $|z_{\mathrm{DV}}| < 300$ mm, where x_{DV}, y_{DV} and z_{DV} represent the position of the DV. The range $R_{xy} < 300$ mm and $|z_{\mathrm{DV}}| < 300$ mm roughly correspond to the region inside the first SCT barrel layer and inside the first Pixel layer (i.e. IBL) coverage, respectively. In addition, a DV must be separated at least 4 mm in the $x - y$ plane from the primary vertex. This reduces the background events containing long-lived SM particles, such as heavy-flavor hadrons.

In the detector material region, SM particles produce many DVs with high track multiplicity due to hadronic interaction. In order to reject such background DVs, DVs reconstructed inside the detector material region are rejected. The three-dimensional material maps, as shown in Figure 7.9, defining which detector regions should be voted, comprises two sections: the inner section ($R_{xy} < 150$ mm) and the outer section ($R_{xy} > 150$ mm). In the inner section, the material map is constructed by mapping out the low-mass standard DVs that do not originate from K_s^0 decay. In the outer section, an initial map is constructed based on the known detector geometry, with certain regions not seen in the data being removed and regions seen in the data and not seen in the initial map being added. This material map occupies 48% of the fiducial volume. Removing the DVs in the material map is defined as "loose material map veto." Moreover, the "strict material map veto" is applied. It takes into account the uncertainties of the DV position. The DV is removed if the material region is within 1σ uncertainty of the DV position.

Tracks from photon conversions can enhance the production of the SM background DVs. In order to

suppress potential background with the tracks from photon conversions and to make the photon-triggered region, defined in Section 8.2.1 and used in the background estimate, more comparable to the MTR, DV is vetoed if the ΔR between its PV-DV vector and any photons with $p_{\mathrm{T}} > 60$ GeV ($\Delta R_{\gamma,\mathrm{DV}}$) is smaller than 0.1. The effect of this veto is negligible on the signal selection efficiency is negligible.

7.7.2 DV-track selection

The reconstructed DVs contain a large number of non-signal-like tracks. In order to remove them while keeping the signal selection efficiency high, several track-level selections are applied to the tracks in the DVs after the baseline DV selection. The criteria are determined from the variables of tracks that belong to the DVs that pass all baseline selections and have at least four tracks and 5 GeV invariant mass of several signal samples and $Z \to \nu\bar{\nu}$ background samples. Since track features may be different depending on the DV position, the variables are compared for each DV radial position: inside the IBL ($R_{xy} < 34$ mm), inside the Pixel (34 mm $< R_{xy} <$ 150 mm) and outside the Pixel ($R_{xy} > 150$ mm).

- **Upstream hit veto**: All tracks that have hit within R_{xy} are removed because if the track really comes from the particle decay at the DV position, it must not have the hits inner than the DV position.
- **Track p_{T}**: Figure 7.10 shows track p_{T}. The tracks in the signal and background events have a similar distribution, but tracks with p_{T} smaller than around 1.1 GeV are more in the background. Tracks with p_{T} smaller than 1.1 GeV are removed to reduce those background tracks.
- **Track d_0 significance**: Figure 7.11 shows d_0 significance ($S_{d_0} = |d_0|/\sigma(d_0)$) of the tracks. The distribution has a peak around 0 for background events, while it is a flatter distribution for signal tracks. Tracks with S_{d_0} smaller than 5 are decided to be removed.
- **Tracks with small angle and d_0 significance**: The angle $\alpha(\mathrm{track}, \mathrm{PV} - \mathrm{DV})$ is defined as the angle between the track and the PV-DV vector, as described in Figure 7.12(a). The angle $\alpha_{\mathrm{min}}(\mathrm{track}, \mathrm{PV} - \mathrm{DV})$ is the minimum $\alpha(\mathrm{track}, \mathrm{PV} - \mathrm{DV})$ for all PVs including the hard scatter and pileups, as described in Figure 7.12(b). Figures 7.13 and 7.14 show the correlation between $\alpha_{\mathrm{min}}(\mathrm{track}, \mathrm{PV} - \mathrm{DV})$ and S_{d_0} of the signal and background, respectively. Most background tracks are gathered around (0,0). They are expected to originate from one of the PVs. Tracks with $\alpha_{\mathrm{min}}(\mathrm{track}, \mathrm{PV} - \mathrm{DV}) < 0.15$ and $S_{d_0} < 60$ of the DV inside the IBL, minimal $\alpha_{\mathrm{min}}(\mathrm{track}, \mathrm{PV} - \mathrm{DV}) < 0.15$ and $S_{d_0} < 70$ of the DV inside the Pixel are decided to be removed.
- **Backwards-going tracks**: Figure 7.15 shows the $\Delta\phi$ between the tracks and PV-DV vector direction ($\Delta\phi_{\mathrm{PV-DV}}$). Inside the IBL, signal and background tracks are both distributed in a wide range, but only background tracks have a small peak of around 2.2. $\Delta\phi_{\mathrm{PV-DV}} < 1.75$ for DVs inside the IBL is applied to remove background-like back-to-back tracks. Only background tracks have a large $\Delta\phi_{\mathrm{PV-DV}}$ inside and outside the Pixel. $\Delta\phi_{\mathrm{PV-DV}} < 1$ for DVs inside and outside the Pixel is applied to remove them.

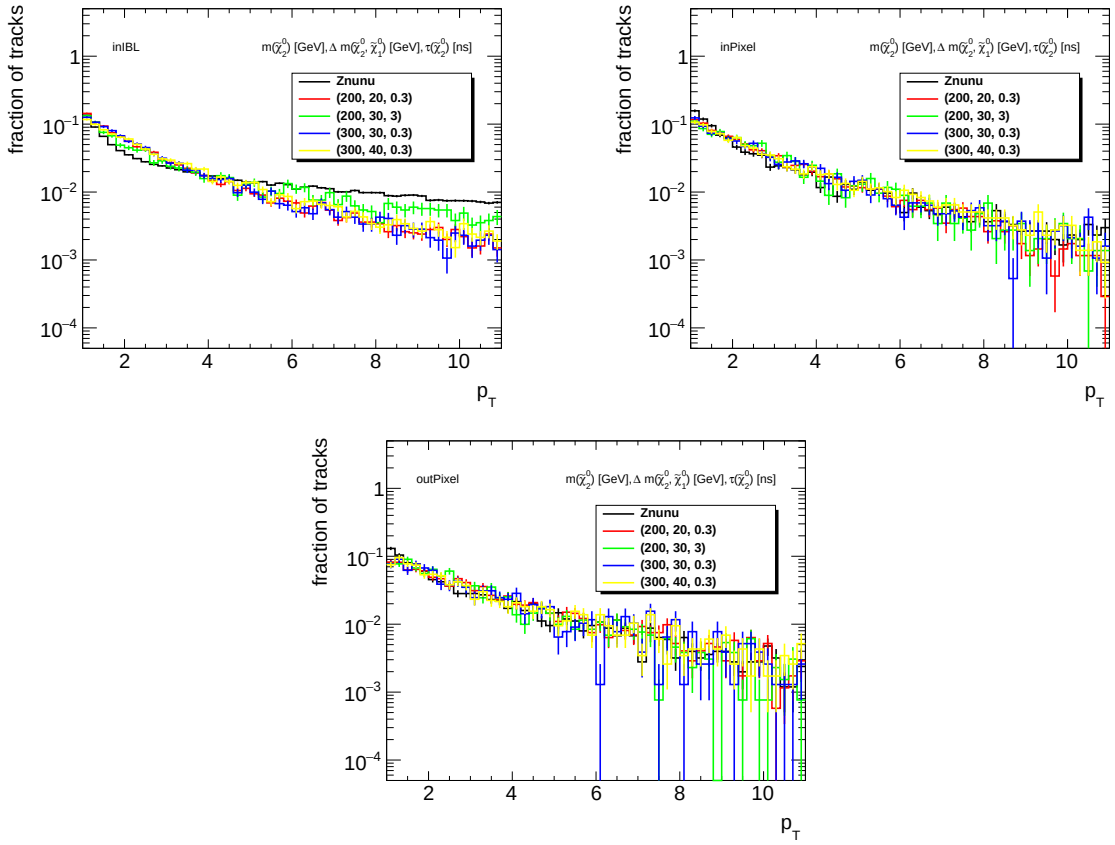

Figure 7.10: p_{T} of track in DVs inside the IBL (top left), inside the Pixel (top right), and outside the Pixel (bottom).

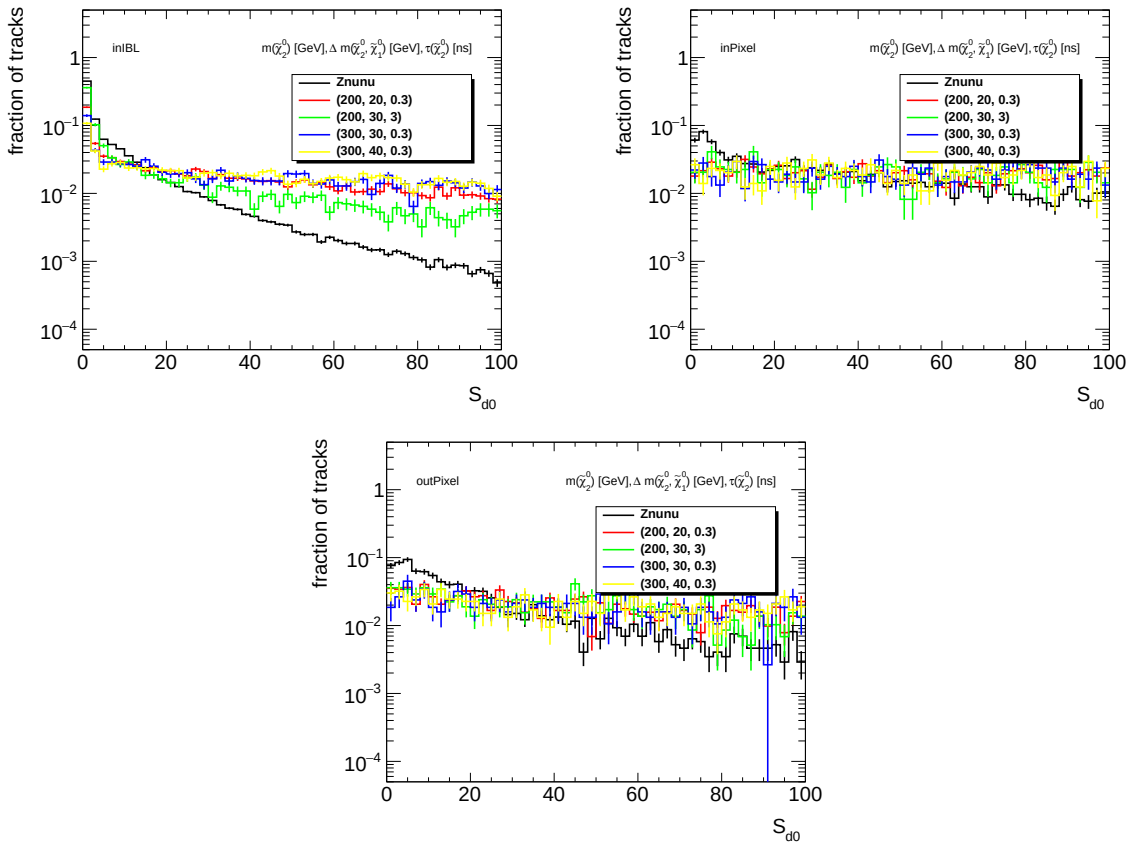

Figure 7.11: S_{d_0} of track in DVs inside the IBL (top left), inside the Pixel (top right), and outside the Pixel (bottom).

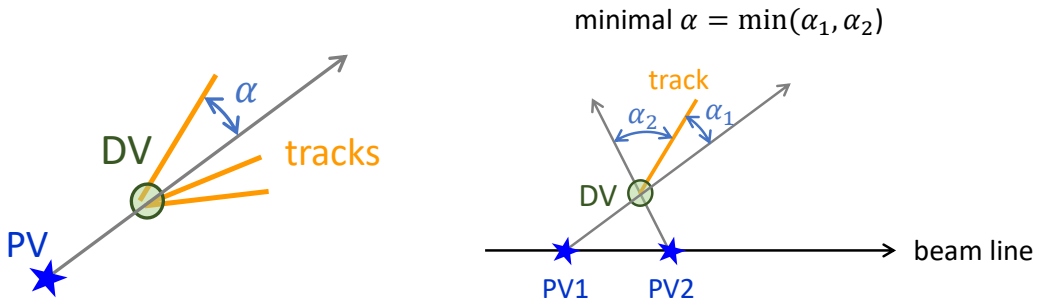

(a) **(b)**

Figure 7.12: Definition of (a) $\alpha(\text{track}, \text{PV} - \text{DV})$ and (b) $\alpha_{\min}(\text{track}, \text{PV} - \text{DV})$ for a track when there are two PVs.

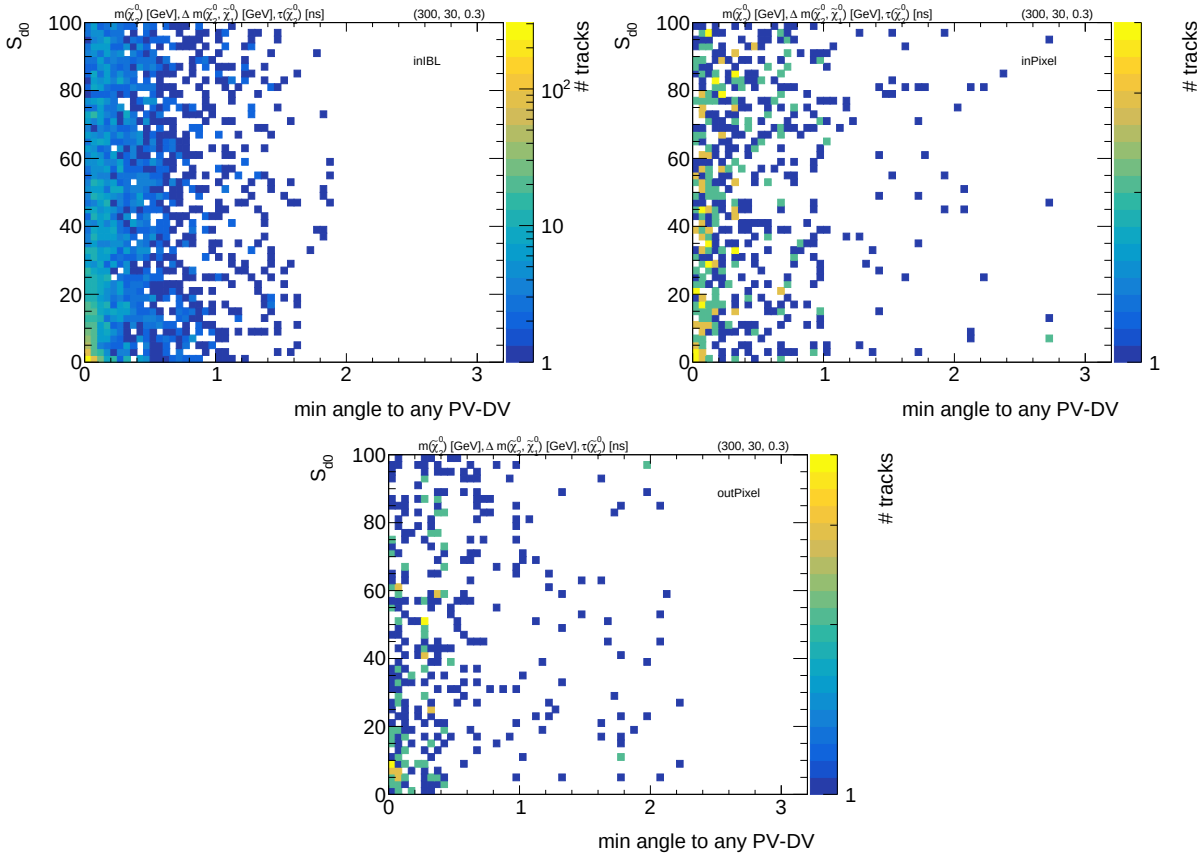

Figure 7.13: $\alpha_{\min}(\text{track}, \text{PV} - \text{DV})$ and S_{d_0} of tracks in DVs inside the IBL (top left), inside the Pixel (top right) and outside the Pixel (bottom) of signal MC ($m_{\tilde{\chi}_2^0} = 200$ GeV, $\Delta m(m_{\tilde{\chi}_2^0}, m_{\tilde{\chi}_1^0}) = 30$ GeV, $\tau_{\tilde{\chi}_2^0} = 0.3$ ns).

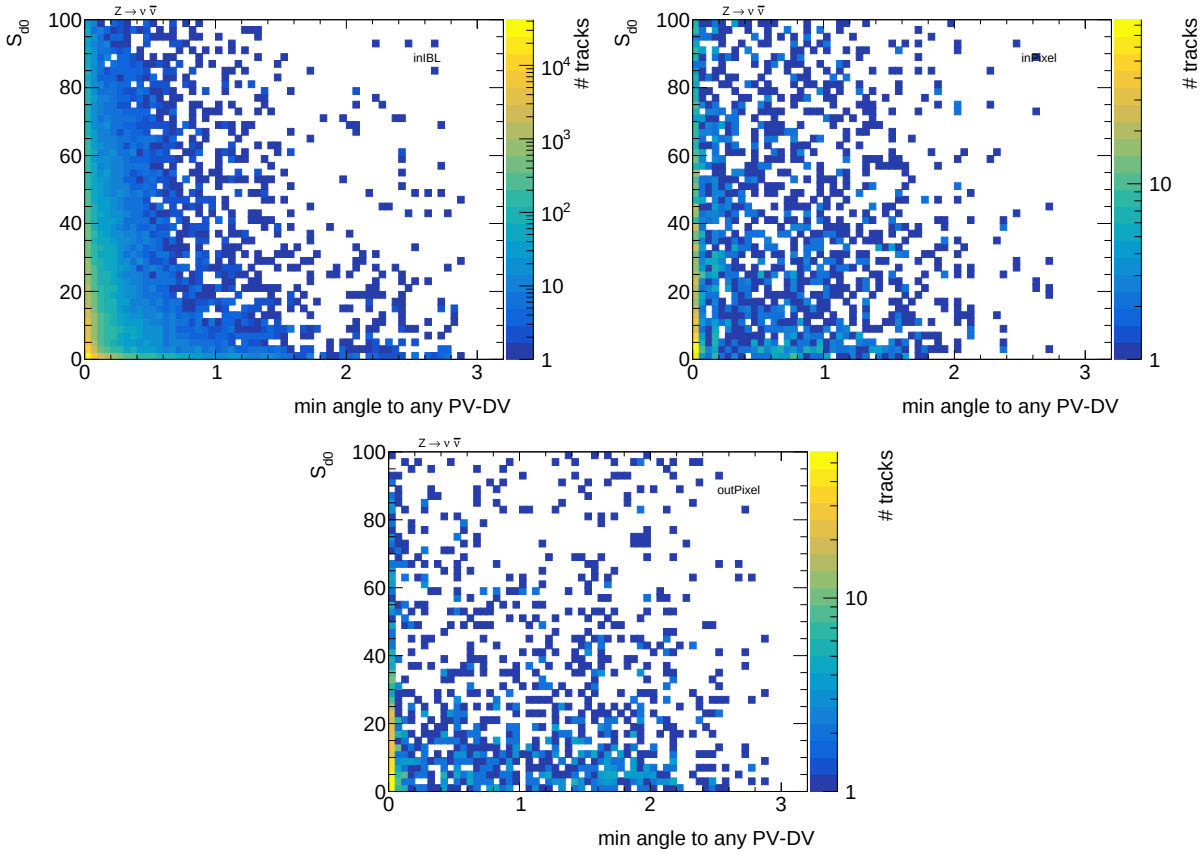

Figure 7.14: $\alpha_{\min}(\text{track}, \text{PV} - \text{DV})$ and S_{d_0} of tracks in DVs inside the IBL (top left), inside the Pixel (top right), and outside the Pixel (bottom) of $Z \to \nu\bar{\nu}$ background MC.

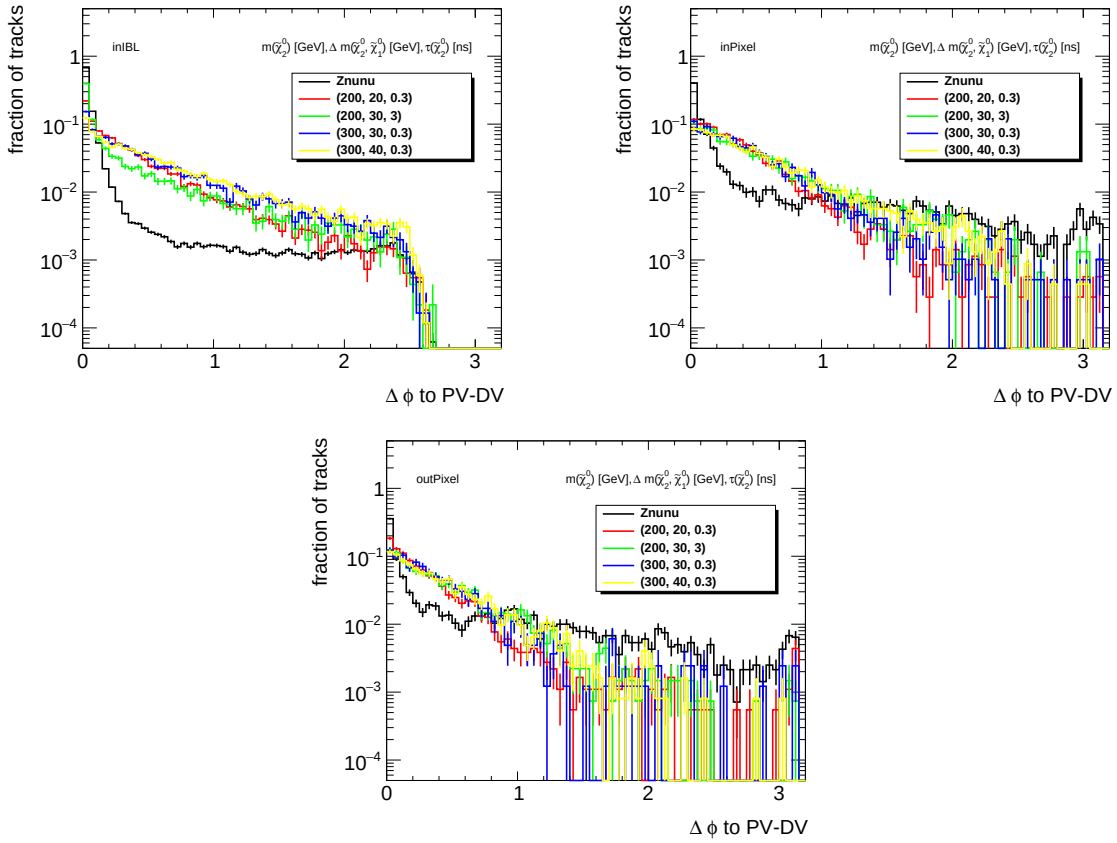

Figure 7.15: $\Delta\phi$ between track and PV-DV vector direction of DVs inside the IBL (top left), inside the Pixel (top right), and outside the Pixel (bottom).

Table 7.3: Summary of the DV-track selection.

Region	inside the IBL	inside the Pixel	outside the Pixel
Upstream hit veto	tracks are rejected if they have any hits within the DV radii		
Track p_{T} [GeV]	> 1.1		
Track S_{d_0}	> 5		
$\alpha_{\min}(\mathrm{track}, \mathrm{PV} - \mathrm{DV})$	> 0.15 if $S_{d_0} < 60$	> 0.15 if $S_{d_0} < 70$	-
$\Delta\phi_{\mathrm{PV-DV}}$	< 1.75	< 1	< 1

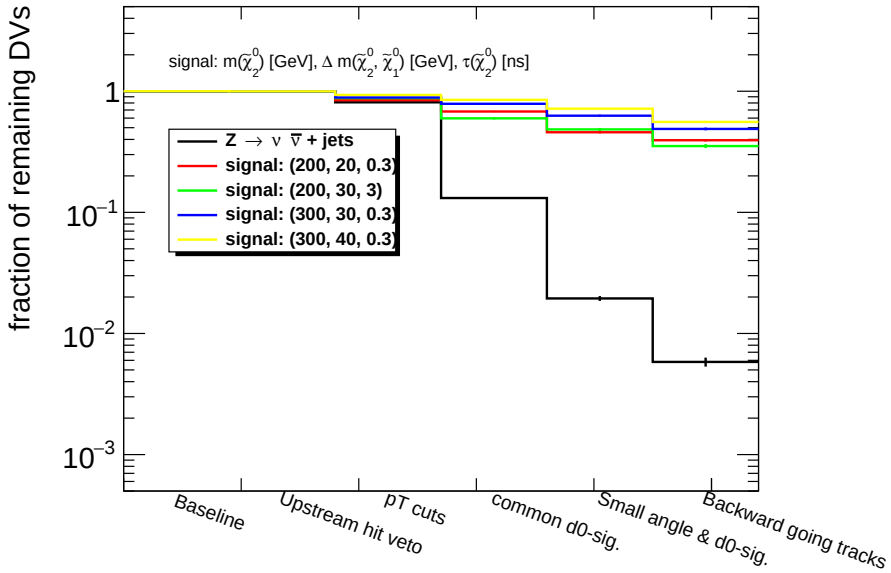

Figure 7.16: Cutflow showing how the fraction of DVs with at least four tracks and larger than 5 GeV invariant mass of several signal and a background MC samples change by applying DV-track selection.

Table 7.3 summarizes DV-track selection criteria. Figure 7.16 shows the effect of this DV-track selection on the signals and $Z \to \nu\bar{\nu}$ backgrounds.

7.7.3 Signal DV selection

After DV track-level selection, track multiplicity (N_{tracks}), the number of two-track seeds (N_{seeds}), and all DV variables that are calculated from the 4-vector of the tracks are re-calculated. The invariant mass of the DV (m_{DV}) is calculated from the four-vector of tracks, assuming that the particle has a charged pion mass. Regarding N_{seeds}, if both tracks constructing the seed pass the DV track-level selection, the seed is counted.

If the tracks with the highest p_{T} ($p_{\mathrm{T}}{}^{\mathrm{max}}$) account for more than 90% of the scalar sum p_{T} of all DV tracks ($\Sigma|\boldsymbol{p}_{\mathrm{T}}|$), the DV is rejected. It is because such tracks tend to have extremely high p_{T}, which are likely to be caused by mis-measurement. In addition, if the maximum $\Delta\eta$ between the four-vector of a target track and sum of four-vector of tracks other than the target track in the DV ($\max(\Delta\eta(p_{\mathrm{trk}}, p_{\mathrm{tot}} -$

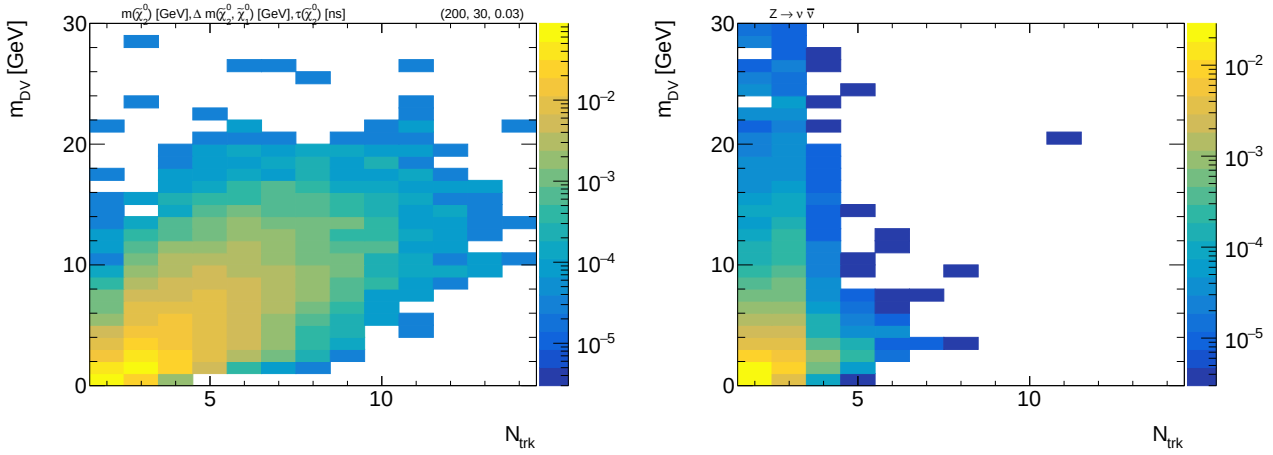

Figure 7.17: Distribution of N_{tracks} and m_{DV} after track cleaning for a bino-wino signal (left) and $Z \to \nu\bar{\nu}$ background (right) events. The number of events is not normalized and is simply number of events in the MC samples.

p_{trk})) is larger than 3.5, the DV is rejected. It removes high-mass background DVs caused by a randomly crossed track.

Figure 7.17 shows the two-dimensional distribution of N_{tracks} and m_{DV} for the signal and $Z \to \nu\bar{\nu}$ background MC. The background DV rarely has large values for both N_{tracks} and m_{DV}. As the final discriminant, DVs are required to satisfy "$N_{\text{tracks}} \geq 5$ and $m_{\text{DV}} > 10$ GeV." In addition, requirements for N_{seeds} depending on the N_{tracks} are applied. As shown in Figure 7.18, there is a strong correlation between N_{tracks} and N_{seeds} for signal events. Signal DVs have peaks at ${}_{N_{\text{tracks}}}C_2$, where any pair of DV tracks form two-track seeds. Therefore, DVs are required to satisfy "$N_{\text{seeds}} \geq {}_{N_{\text{tracks}}}C_2 - 1$." DVs satisfying all baseline and signal selection criteria are referred to as "signal-like DV." To avoid the overlap with another signal region, events with two or more DVs satisfying the following "softer DV" selections are removed:

- $N_{\text{tracks}} \geq 4$
- $m_{\text{DV}} > 1.5$ GeV
- $N_{\text{seeds}} \geq N_{\text{tracks}}$
- $|\eta_{\text{PV-DV}}| < 2.5$ ($\eta_{\text{PV-DV}}$: η direction w.r.t the PV position)
- Jet-DV matching: Has at least one jet with ΔR w.r.t PV-DV direction ($\Delta R_{\text{jet,DV}}$) smaller than 0.4

7.8 Signal selection efficiency

Figure 7.19 shows the signal selection efficiency of each selection for several representative models. The final selection efficiency for various bino-wino models is shown in Figure 7.20. The selection efficiency tends to be higher when the mass of $\tilde{\chi}_1^0$ is high because a high-mass $\tilde{\chi}_1^0$ creates a large $E_{\text{T}}^{\text{miss}}$. The efficiency decreases as the lifetime of $\tilde{\chi}_2^0$ increases because of the increase in the probability that it passes through

Table 7.4: Definitions of the signal regions.

Event Selection:	
$E_{\mathrm{T}}^{\mathrm{miss}}$ trigger	Pass the lowest unprescaled $E_{\mathrm{T}}^{\mathrm{miss}}$ trigger (requirement from DRAW filter)
$E_{\mathrm{T}}^{\mathrm{miss}}$ filter	Topo cluster-based $E_{\mathrm{T}}^{\mathrm{miss}} > 180$ GeV (requirement from DRAW filter)
Event cleaning	Pass Good Runs List
	Reject bad/corrupted events
Primary vertex	At least one PV, with two or more tracks and $\lvert z_{\mathrm{PV}}\rvert < 200$ mm
Offline $E_{\mathrm{T}}^{\mathrm{miss}}$	Offline calibrated $E_{\mathrm{T}}^{\mathrm{miss}} > 150$ GeV
NCB veto	Reject events if any jet fails the *SuperLooseBadLLP* jet cleaning
	Reject events where the leading jet satisfies
	$f_{\mathrm{max}} > 0.8$, $f_{\mathrm{EM}} > 0.96$, or $f_{\mathrm{ch}}/f_{\mathrm{max}} < 0.1$
Dead Tile module veto	Reject events if any jet satisfies
	$p_{\mathrm{T}} > 50$ GeV and $\Delta\phi(E_{\mathrm{T}}^{\mathrm{miss}}, \mathrm{jet}) < 0.3$ on the dead Tile modules listed in Table 7.2
Signal-like DV	Has at least one DV satisfying baseline and signal selection
Softer DV veto	Reject events with two or more DV satisfying baseline and softer selection
Baseline DV selection:	
Fiducial volume	$\lvert R_{xy}\rvert < 300$ mm, $\lvert z_{\mathrm{DV}}\rvert < 300$ mm
Displacement	> 4 mm from PVs in radial position
Material veto	Pass strict material map veto
Photon veto	$\Delta R_{\gamma,\mathrm{DV}} > 0.1$
Signal DV selection:	
Scalar p_{T} sum	${p_{\mathrm{T}}}^{\mathrm{max}}/\Sigma\lvert\boldsymbol{p}_{\mathrm{T}}\rvert < 0.9$
Max $\Delta\eta$ between tracks	$\max(\Delta\eta(p_{\mathrm{trk}}, p_{\mathrm{tot}} - p_{\mathrm{trk}})) < 3.5$
Track multiplicity	$N_{\mathrm{tracks}} \geq 5$
Invariant mass	$m_{\mathrm{DV}} > 10$ GeV
Number of two-track seeds	$N_{\mathrm{seeds}} \geq {}_{N_{\mathrm{tracks}}}C_2 - 1$
Softer DV selection:	
Scalar p_{T} sum	${p_{\mathrm{T}}}^{\mathrm{max}}/\Sigma\lvert\boldsymbol{p}_{\mathrm{T}}\rvert < 0.9$
Direction	$\lvert\eta_{\mathrm{PV-DV}}\rvert < 2.5$
Jet-DV matching	$\Delta R_{\mathrm{jet,DV}} < 0.4$
Track multiplicity	$N_{\mathrm{tracks}} \geq 4$
Invariant mass	$m_{\mathrm{DV}} > 1.5$ GeV
Number of two-track seeds	$N_{\mathrm{seeds}} \geq N_{\mathrm{tracks}}$

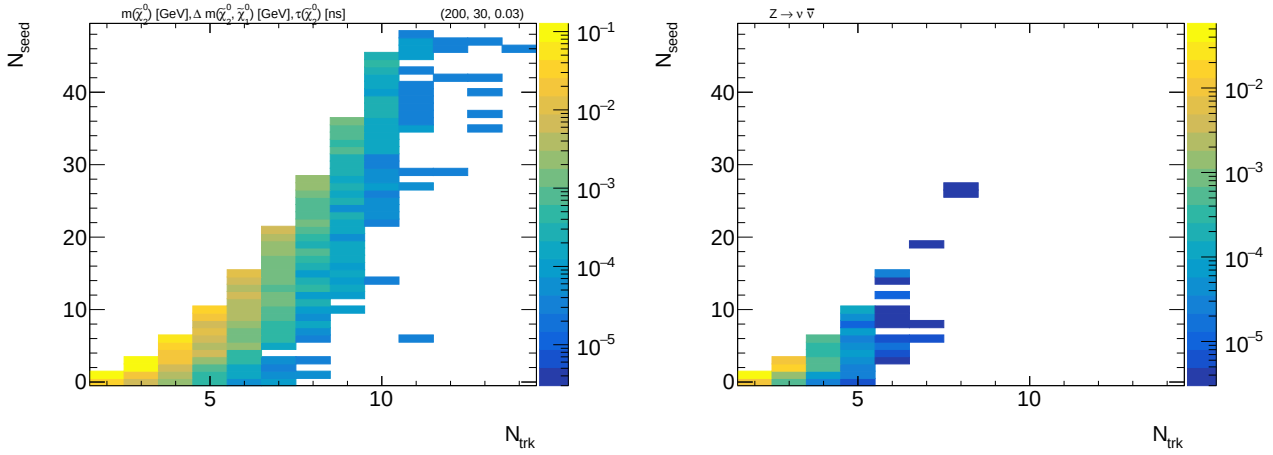

Figure 7.18: Distribution of N_{tracks} and N_{seeds} after track cleaning for a bino-wino signal (left) and $Z \to \nu\bar{\nu}$ background (right) events. The number of events is not normalized and is simply number of events in the MC samples.

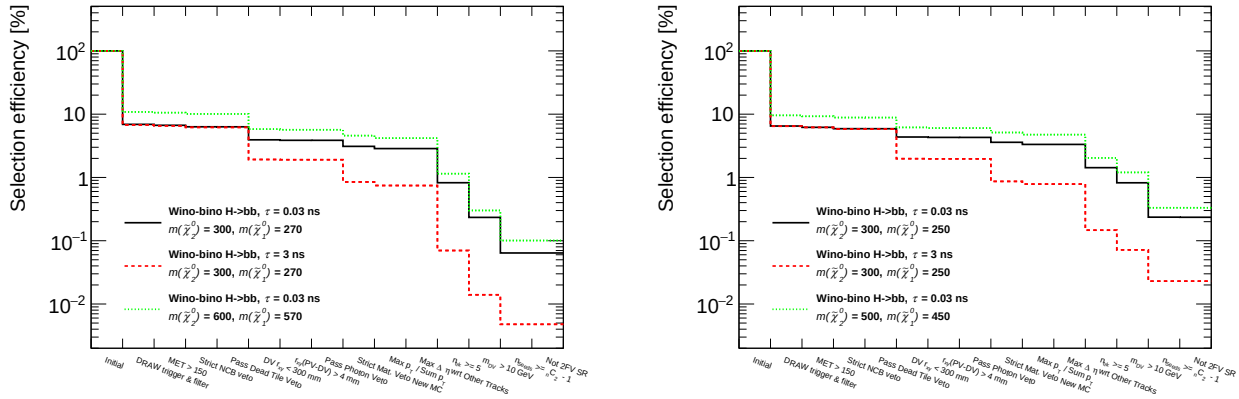

Figure 7.19: Selection efficiency of representative signal models.

the ID before decaying. In addition, even if it decays within the ID, the farther away from the center the track reconstruction efficiency decreases, then the vertex selection efficiency also decreases.

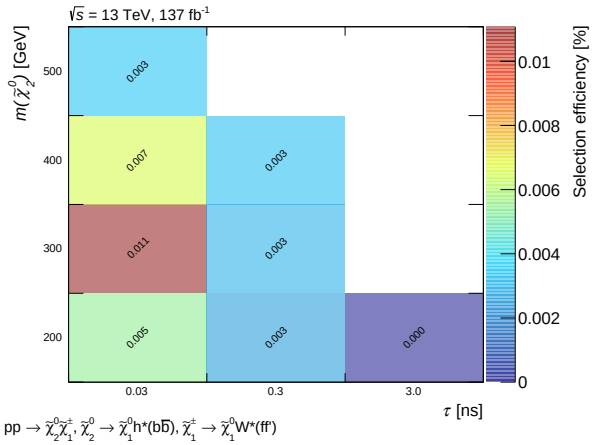

(a) $\Delta M(\tilde{\chi}_2^0, \tilde{\chi}_1^0) = 20$ GeV

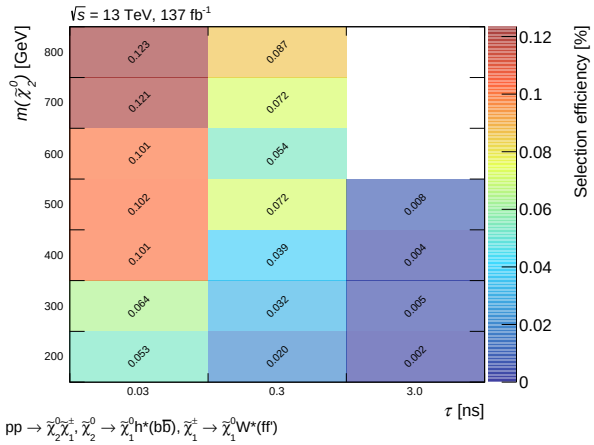

(b) $\Delta M(\tilde{\chi}_2^0, \tilde{\chi}_1^0) = 30$ GeV

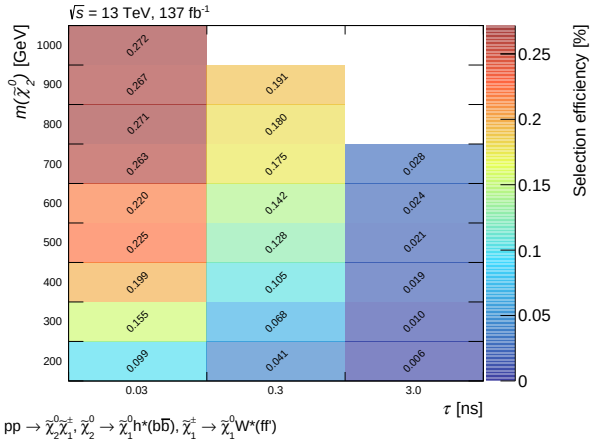

(c) $\Delta M(\tilde{\chi}_2^0, \tilde{\chi}_1^0) = 40$ GeV

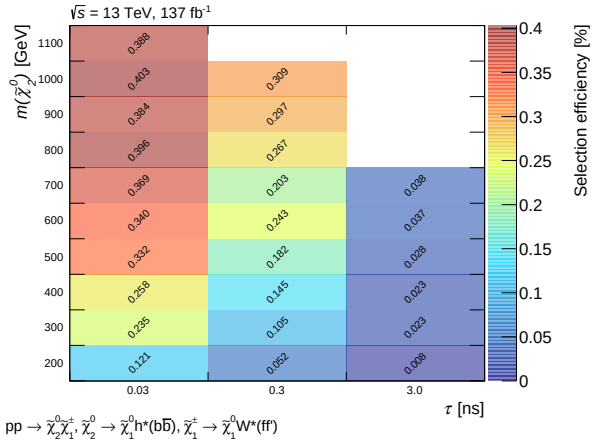

(d) $\Delta M(\tilde{\chi}_2^0, \tilde{\chi}_1^0) = 50$ Gev

Figure 7.20: Selection efficiency for bino-wino signal models as a function of $\tilde{\chi}_2^0$ mass and lifetime with (a) $\Delta M(\tilde{\chi}_2^0, \tilde{\chi}_1^0) = 20$ GeV, (b) $\Delta M(\tilde{\chi}_2^0, \tilde{\chi}_1^0) = 30$ GeV, (c) $\Delta M(\tilde{\chi}_2^0, \tilde{\chi}_1^0) = 40$ GeV, and (d) $\Delta M(\tilde{\chi}_2^0, \tilde{\chi}_1^0) = 50$ GeV. Bins with no MC samples are shown as blank.

Chapter 8

Background estimation

This chapter describes the background components of DV and the background estimation procedure. The categorization of the background components of DVs and their characteristics are discussed in the first part of this chapter. The latter part describes estimating the number of background events in the SR. The estimation method is then validated using several validation regions (VRs).

8.1 Background component

There is no heavy long-lived particle in the SM. However, SM particles can produce DVs with a high track multiplicity and invariant mass from algorithmic and experimental effects. Figure 8.1 shows the dominant background DV sources. The definition of each category is described as follows:

- Hadronic interaction and the SM LLP decay (HI)

  The first one is the hadronic interaction. SM particles interact hadronically with the nuclei of the detector material or gas. DVs with high track multiplicity can be reconstructed if several charged particles are produced in the interaction.

  The second one is the decay of a meta-stable SM particle. Several meta-stable SM particles, such as K^0_Ss, Λ^0s, and b-hadrons, decay to multiple particles after flying an observable distance. Such decay points are reconstructed as DVs with typically low mass.

  All of the constituent tracks in those DVs initially originated from the same particle. In this thesis, such DVs are classified in this category.

- Accidental crossing (AX)

  The masses of DVs made by hadronic interactions or long-lived SM particle decays are usually low. When an unrelated track accidentally intersects with such a low-mass DV with a large angle, it is reconstructed as a single high-mass DV.

- Merged vertices (MV)

  When two or more long-lived SM particles decay near each other and create vertices, those vertices can be merged into a single DV. Such DVs can have high track multiplicity and high mass.

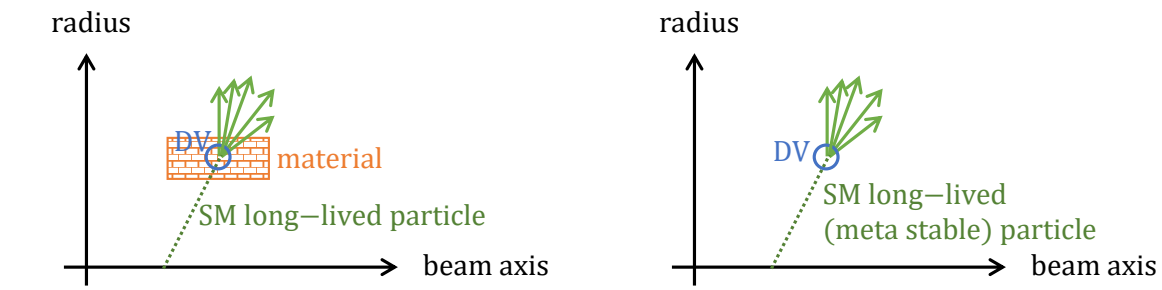

(a) hadronic interaction (left) and the SM LLP decay (right) (HI)

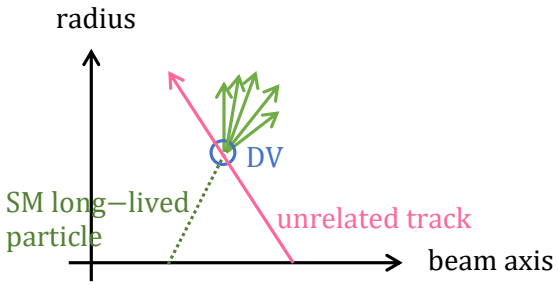

(b) Accidental crossing (AX)

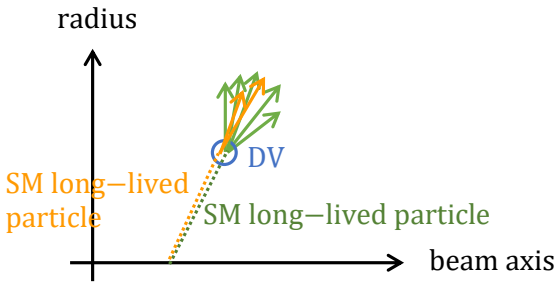

(c) Merged vertices (MV)

Figure 8.1: Classification of the background sources. (a) Hadronic interaction and the SM LLP decay (HI). (b) Accidental crossing (AX). (c) Merged vertices (MV).

Figures 8.2 show the mass distributions of background DVs with four and more than four tracks in each category. All DV selections are applied except for the N_{tracks} and m_{DV} conditions. $Z \to \nu\bar{\nu}$ MC samples are used to categorize background sources. HI DVs with a high track multiplicity are easily reconstructed, but the mass peak is around 2 GeV, and a tiny fraction of them have an invariant mass greater than 10 GeV. AX and MV will likely have lower track multiplicity and a higher invariant mass than HI.

Figure 8.3 shows the mass distributions of the DVs of each category inside the material region, meaning that the DV fails the strict material map veto. The fraction of the HI is more significant than that of the outside material region because of the hadronic interaction with the detector material. As the number of HI DVs increases, the AX and MV DVs also increase.

On the other hand, DVs that fail the seed condition have a different component, as shown in Figure 8.4. Unlike DVs, which satisfy the seed condition, AX and MV are easily reconstructed.

8.2 Background estimation strategy

Since the modeling of the vertexing in the MC is not well validated, the SM background remaining in the SR is estimated by the data in this analysis. Several kinds of physics objects are expected to be correlated with the presence of a DV. For example, the existence of a DV is significantly correlated with the existence of a jet because if there is a DV, the track density around it is high, and then a jet is reconstructed from

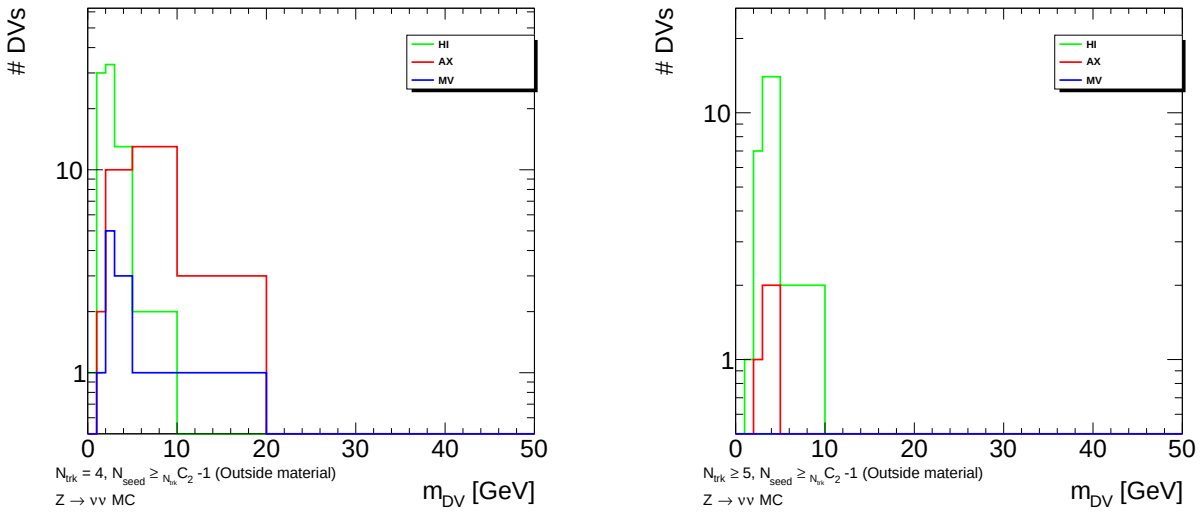

Figure 8.2: The mass distributions of DVs outside material region with four tracks (left) and more than four tracks (right) from three background sources. All DV selections are applied except the N_{tracks} and m_{DV} conditions. $Z \to \nu\bar{\nu}$ MC samples are used.

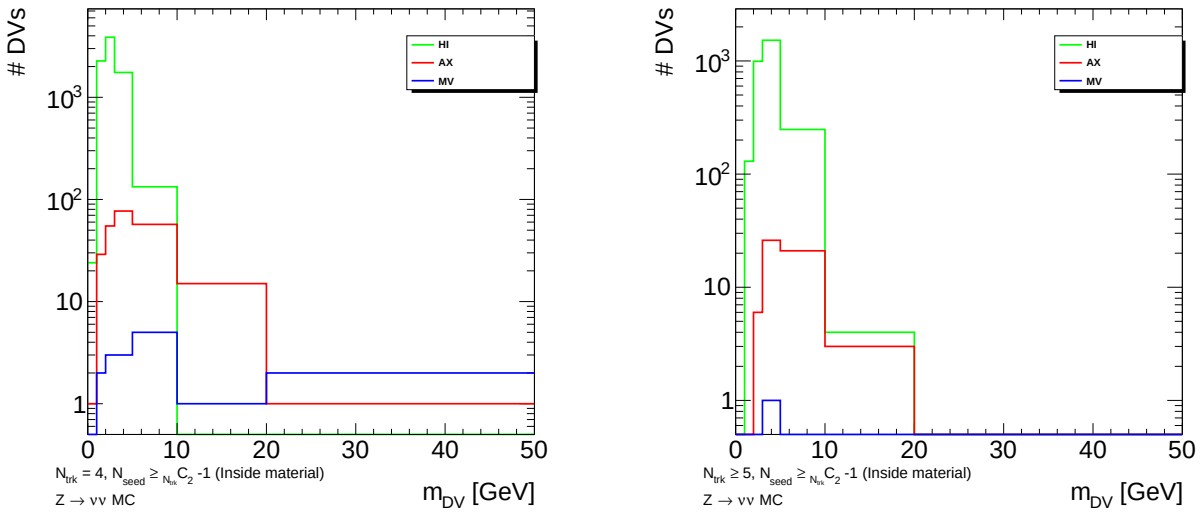

Figure 8.3: The mass distributions of DVs inside the material region with four tracks (left) and more than four tracks (right) from three background sources. The DV must fail the strict material map veto and pass other selections, except for applying the N_{tracks} and m_{DV} selections. $Z \to \nu\bar{\nu}$ MC samples are used.

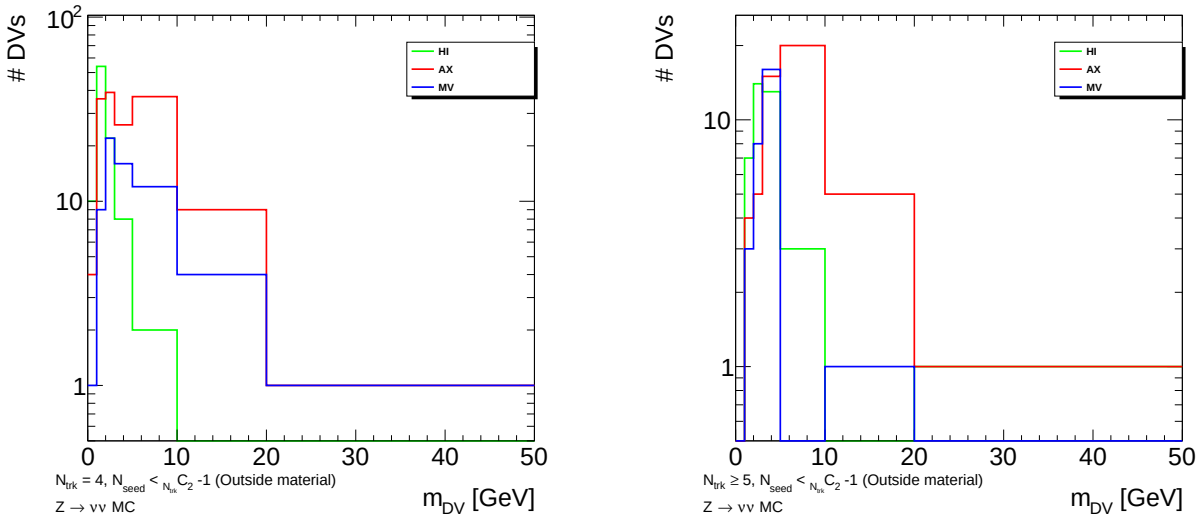

Figure 8.4: The mass distributions of DVs that fail the seed condition with four tracks (left) and more than four tracks (right) from three background sources. The DV must fail the seed condition and pass other selections, except for applying the N_{tracks} and m_{DV} conditions. $Z \to \nu\bar{\nu}$ MC samples are used.

its energy deposits, as illustrated in Figure 8.5. Several previous ATLAS analyses that use the standard DVs [91, 92] adopt background estimate methods using "jet-DV probability" based on this correlation. This analysis uses a similar method.

8.2.1 Variables correlated with DVs

To avoid seeing the events in the SR included in the MTR, a separate region orthogonal to the MTR is used to investigate the correlations between the special DVs and other physics objects. The "photon-triggered region (PTR)," is designed to be orthogonal and have a similar event topology to the MTR. The definition is as follows:

- Events passing a single photon trigger with $p_{\text{T}} > 140$ GeV.
- Events that do not meet $E_{\text{T}}^{\text{miss}}$ trigger, $E_{\text{T}}^{\text{miss}}$ filter, or offline $E_{\text{T}}^{\text{miss}}$ requirements used for MTR.
- Events that pass the event cleaning and PV requirements.
- Events passing the strict NCB veto.
- Events passing the dead tile module veto.

A single photon trigger is used because the events triggered by a single photon and $E_{\text{T}}^{\text{miss}}$ have a similar topology except for the difference of photon and $E_{\text{T}}^{\text{miss}}$, and they have large statistics and tiny contamination of signal events.

First, the correlation between DV and other objects is investigated using the PTR. Figure 8.6 shows the fraction of DV in the PTR as a function of various event-level variables. It includes the total number of tracks associated with any PV ($N_{\text{tracks}}^{\text{event}}$) per event (a), the sum of p_{T} of all tracks associated with any

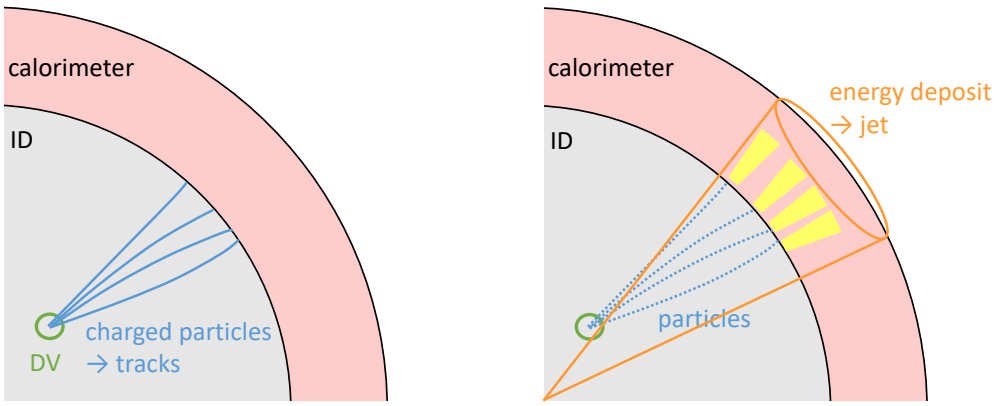

Figure 8.5: Correlation between DV and jet.

PVs ($p_{\mathrm{T}}^{2,\mathrm{event}}$) per event (b), the number of calo jets ($N_{\mathrm{calojet}}^{\mathrm{event}}$) reconstructed per event (c), the number of track jets ($N_{\mathrm{trackjet}}^{\mathrm{event}}$) reconstructed per event (d) and the number of b-tagged calo jets ($N_{\text{b-tagged jet}}^{\mathrm{event}}$) reconstructed per event (e). $N_{\mathrm{tracks}}^{\mathrm{event}}$ is strongly correlated with the presence of DV. It is reasonable that the larger the number of tracks in an event, the more likely they will intersect each other by chance, creating a signal-like high-track-multiplicity background DV. The $p_{\mathrm{T}}^{2,\mathrm{event}}$ is also correlated with the presence of DV, but it is smaller than the one between $N_{\mathrm{tracks}}^{\mathrm{event}}$ and the presence of a DV. Moreover, the presence of jets is correlated with the presence of a DV. When comparing the track jet and the calo jet, the calo jet has a more evident correlation. This difference is likely because only jets with tracks originating from PVs can be reconstructed as track jets. In other words, if the jet originates from a neutral hadron or b-hadron, whose lifetime is of the order of picoseconds, it will not be reconstructed as a track jet. Among the calo jet, the b-tagged jet is significantly correlated with the presence of DV. b-hadrons have a lifetime on the order of picoseconds, and they travel a visible length before decaying, giving a group of displaced tracks that can be reconstructed as a low-mass DV. In addition, a signal-like high-mass DV can be formed if a random track intersects a b-hadron.

Next, distributions of these variables are compared between the PTR and MTR. Figure 8.7 shows the event-level variables of PTR and MTR. Both PTR and MTR have a broad peak around 300 in the distributions for the number of tracks associated with any PVs, but the MTR has a slightly more significant fraction of events with more than 500 tracks than the PTR. The distributions for the sum of p_{T} of tracks associated with any PV are also similar but have a slight deviation in the large $p_{\mathrm{T}}^{2,\mathrm{event}}$ region.

The PTR and MTR have similar distributions for the number of track jets, with slight deviations in the regions less than two and larger than around ten. In contrast, the MTR tends to have more calo jets than the PTR. Since the $E_{\mathrm{T}}^{\mathrm{miss}}$ used for triggers are calculated using only the energy deposits on the calorimeter, it is expected that events in the MTR would have calorimeter activity larger than that of

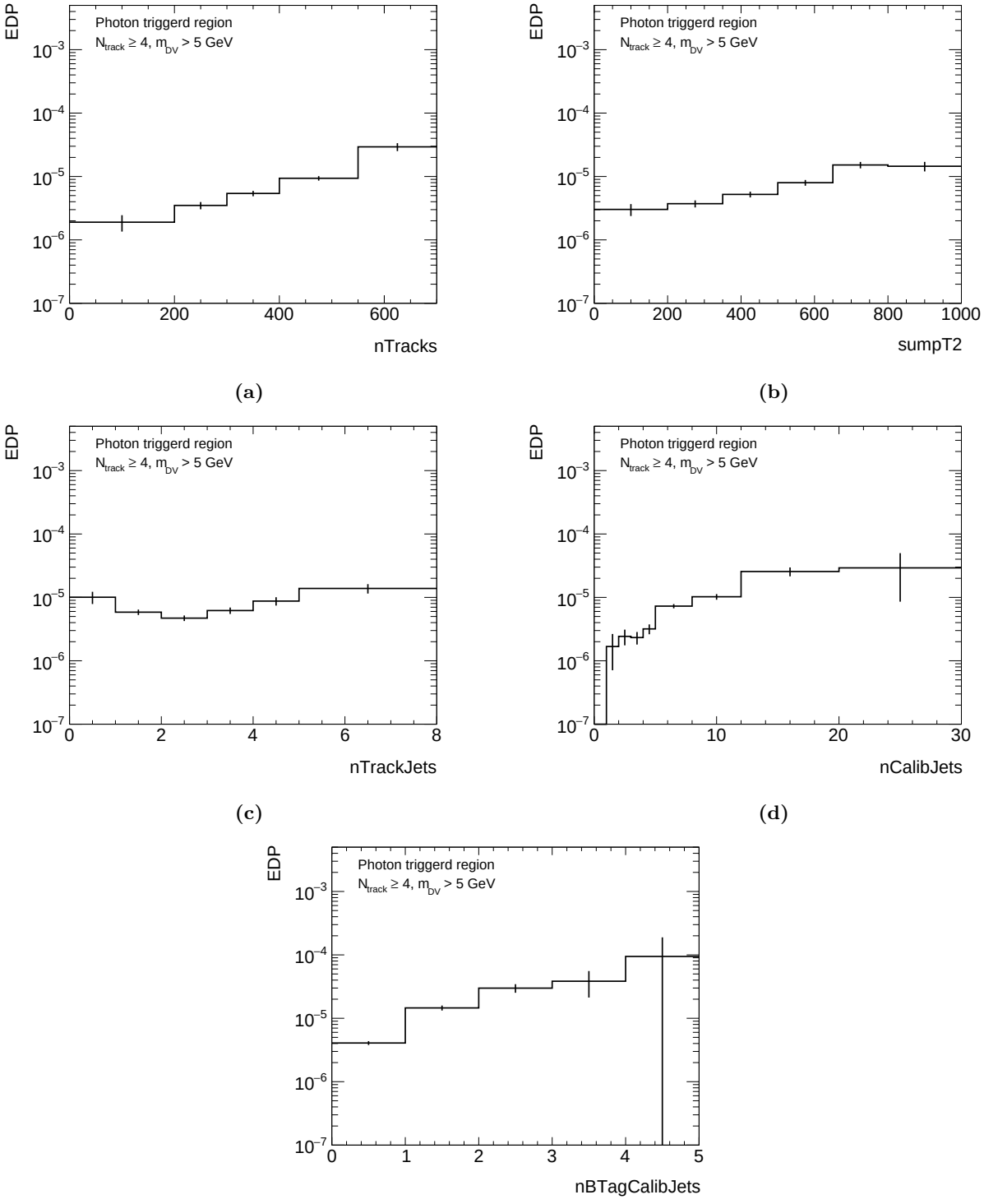

Figure 8.6: Fraction of the events in the PTR with a DV passing all DV selection except that $N_{\text{tracks}} \geq 4$ and $m_{\text{DV}} > 10$ GeV. (Style must be updated.)

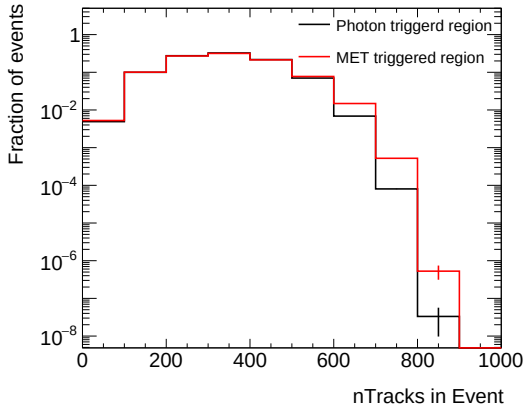

(a) $N_{\text{tracks}}^{\text{event}}$

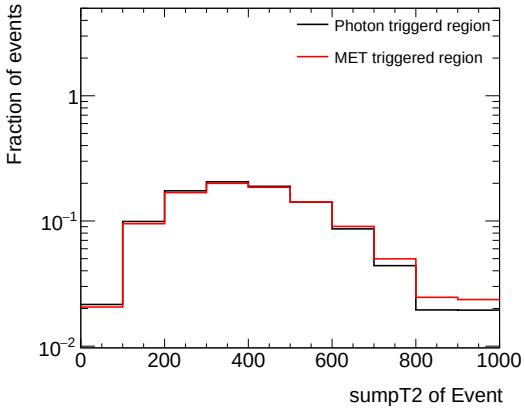

(b) $p_{\text{T}}^{2,\text{event}}$

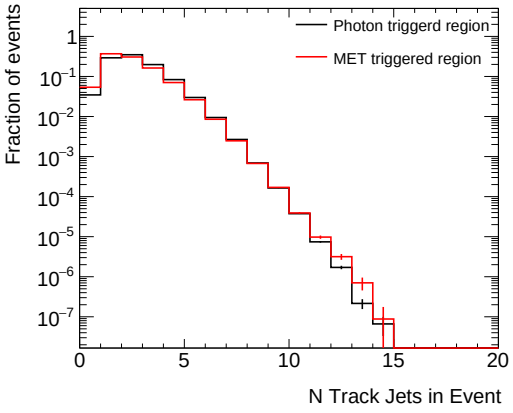

(c) $N_{\text{calojet}}^{\text{event}}$

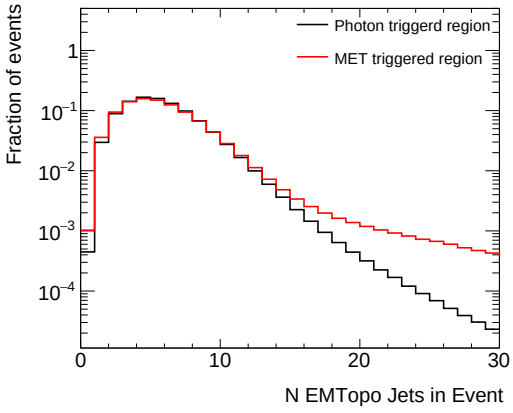

(d) $N_{\text{trackjet}}^{\text{event}}$

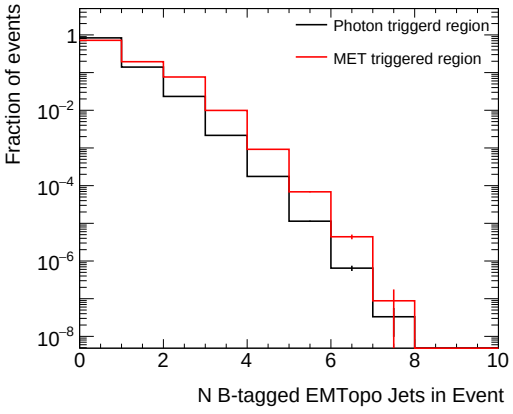

(e) $N_{\text{b-tagged jet}}^{\text{event}}$

Figure 8.7: Comparison of event-level variables between the PTR and MTR.

the PTR. Moreover, the distribution for the number of b-tagged calo jets differs significantly between the PTR and MTR. The background estimation must especially consider the difference in the number of b-tagged calo jets because, as mentioned above, the b-hadron is also easily reconstructed as a DV.

8.2.2 Background estimation procedure

As shown in Section 8.2.1, several event-level variables correlate with a DV's presence. This analysis uses an "event-DV probability" for background estimation, assuming that DVs in the PTR and MTR have an exact correlation with those variables.

Calculation of event-DV probability

The event-DV probability, the probability that the event has a DV, is used to estimate the number of background events in the SR. It is parameterized by the event-level variables (e.g., the number of tracks and jets). From the observation in Section 8.2.1, $N^{\text{event}}_{\text{tracks}}$ and $N^{\text{event}}_{\text{b-tagged jet}}$, which have an obvious correlation with the presence of DV and whose distributions are different between PTR and MTR, are used to construct an event-DV probability in this analysis. The event-DV probability of event i can be calculated using the events in the PTR:

$$\text{Prob}_i(\text{DV} \mid \text{event}) = \frac{\text{Number of DVs in the PTR with the same } N^{\text{event}}_{\text{tracks}} \text{ and } N^{\text{event}}_{\text{b-tagged jet}}}{\text{Total number of events in the PTR with the same } N^{\text{event}}_{\text{tracks}} \text{ and } N^{\text{event}}_{\text{b-tagged jet}}}. \quad (8.1)$$

In practice, the events in the PTR with $N^{\text{event}}_{\text{tracks}}$ and $N^{\text{event}}_{\text{b-tagged jet}}$ in the same bin are used instead of the ones with exactly the same $N^{\text{event}}_{\text{tracks}}$ and $N^{\text{event}}_{\text{b-tagged jet}}$, as shown below. Figure 8.8 is an example of calculating an event-DV probability for the DV with $N_{\text{tracks}} \geq 4$ and $m_{\text{DV}} > 5$ GeV. The total number of events in the PTR and the number of DVs in the PTR are each binned by $N^{\text{event}}_{\text{tracks}}$ and $N^{\text{event}}_{\text{b-tagged jet}}$, and the event-DV probability is calculated by taking their ratio.

Application of event-DV probability

All the events in the MTR are assigned a weight (Prob (DV | event)$_i$) equal to the corresponding event-DV probability. The number of events in the SR is estimated by summing up the number of events in the MTR ($N^{\text{MTR}}_{\text{event}}$) with a weight of event-DV probability:

$$N^{\text{est}}_{\text{Bkg}} = \sum_{i=0}^{N^{\text{MTR}}_{\text{event}}} \text{Prob}(\text{DV} \mid \text{event}_i). \quad (8.2)$$

The event-DV probability can be applied this way to estimate the number of events with a DV because the probability that an event has two or more DVs is negligible.

However, the statistics of the DVs satisfying the signal DV selections in the PTR are too insufficient to calculate the event-DV probability. Therefore, the estimation uses DVs in the PTR with a looser N_{tracks} and m_{DV} condition. The "extended" DV selections are defined as the baseline and signal DV selections

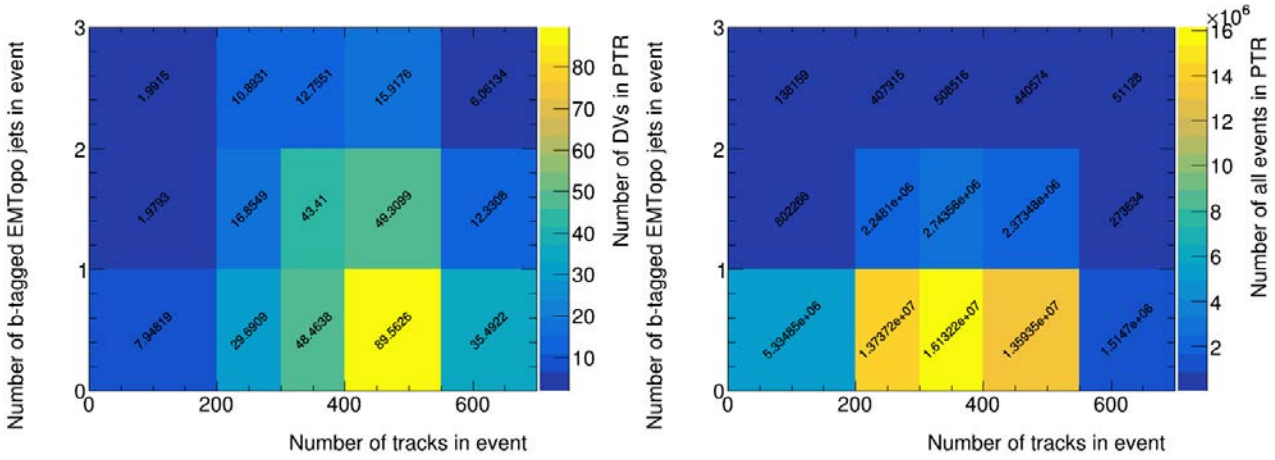

(a) Number of DVs in the PTR, binned by $N^{\text{event}}_{\text{tracks}}$ and $N^{\text{event}}_{\text{b-tagged jet}}$.

(b) Number of events in the PTR binned by $N^{\text{event}}_{\text{tracks}}$ and $N^{\text{event}}_{\text{b-tagged jet}}$.

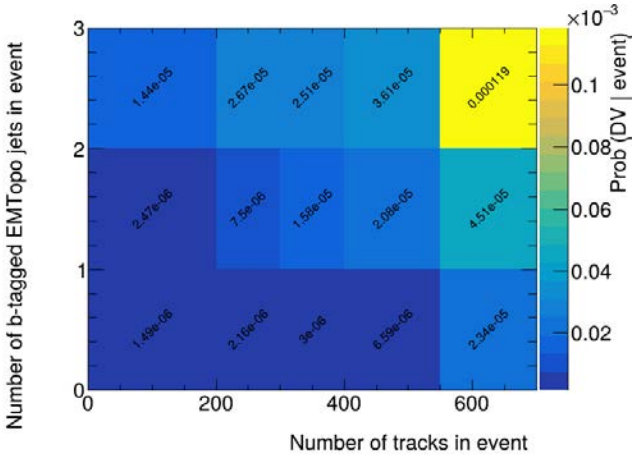

(c) Event-DV probability.

Figure 8.8: Example of calculating an event-DV probability. The event-DV probability(c) is calculated by dividing (a) by (b).

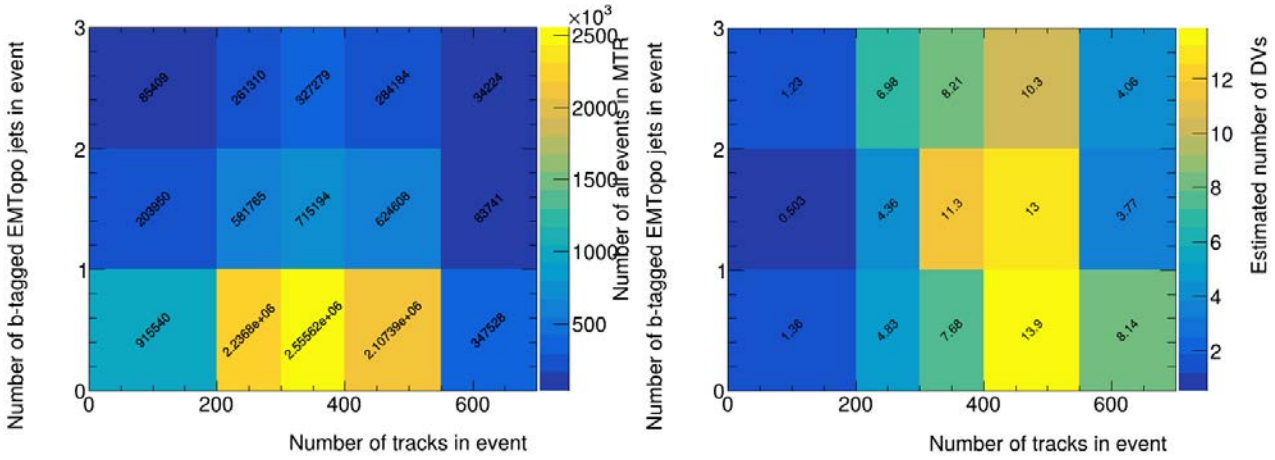

(a) Total number of events in the MTR binned by $N_{\text{tracks}}^{\text{event}}$ and $N_{\text{b-tagged jet}}^{\text{event}}$.

(b) Estimated number of DVs that pass the extended DV selections in the MTR.

Figure 8.9: Application of the event-DV probability. (b) is obtained by multiplying (a) and the event-DV probability shown in Figure 8.8(c). The number of events in the SR is then estimated by scaling down (b) with f-factor shown in Equation 8.4.

except that the track multiplicity requirement is loosed to $N_{\text{tracks}} \geq 4$ and the invariant mass requirement is loosened to $m_{\text{DV}} > 5$ GeV. Equation 8.2 is then modified to the following formula:

$$N_{\text{Bkg}}^{\text{est}} = f \cdot \sum_{i=0}^{N_{\text{event}}^{\text{MTR}}} \text{Prob}_{\text{extended}}(\text{DV} \mid \text{event}_i), \tag{8.3}$$

where $\text{Prob}_{\text{extended}}(\text{DV} \mid \text{event})$ is the event-DV probability for the DVs that pass the extended selections, and f is the ratio of the number of DVs that pass the signal DV selections divided by the number of DVs that pass the extended DV selections in the PTR:

$$f = \frac{N_{\text{DV}}(N_{\text{tracks}} \geq 5, m_{\text{DV}} > 10 \text{ GeV})}{N_{\text{DV}}(N_{\text{tracks}} \geq 4, m_{\text{DV}} > 5 \text{ GeV})} \text{ in the PTR.} \tag{8.4}$$

The factor f is obtained as $3.11/382.66 = 0.00813$ for the signal region. The numerator and denominator are not integers because the pileup reweighting is applied to them, as described in Section 8.3.

Figure 8.9 shows an example of applying the event-DV probability. By multiplying the event-DV probability shown in 8.8(c) and the total number of events in the MTR shown in 8.9(a), the expected number of DVs passing the extended DV selections in the MTR, which can be well approximated to the number of events with DVs that pass the extended DV selections, is obtained as in Figure 8.9(b). The expected number of background events in the SR is obtained by multiplying f-factor to Figure 8.9 and taking a sum of all bins.

8.3 Uncertainty of background estimation

Three sources of uncertainty in the background estimation are considered.

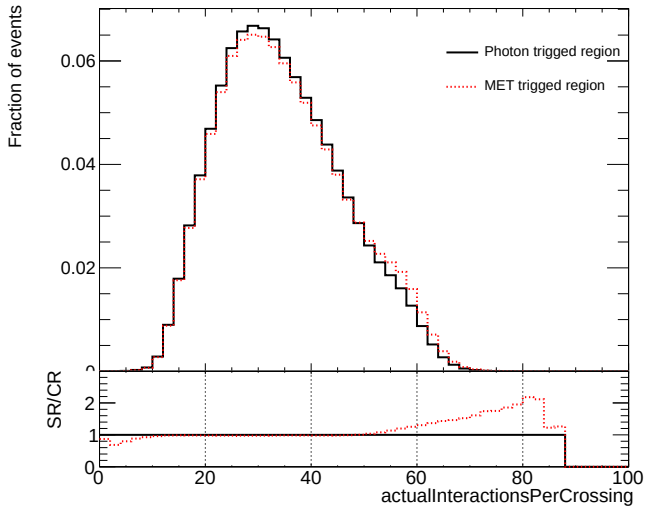

Figure 8.10: Pileup distributions in the PTR and MTR.

First, the effect of the statistical uncertainty of the number of DVs in the PTR on the background estimation is considered. It considers the statistical uncertainty on the number of DVs used to calculate the event-DV probability and the f-factor. A toy-based pseudo-experiment with 10000 events is performed. The number of DVs in the PTR that pass the extended DV selections varies bin-by-bin of event-DV probability within its statistical uncertainty. In each toy event, each bin's entry (number of DVs) randomly varies based on the Poisson distribution, with the original entry as the mean. For example, if a bin's original entry is three, the new entry's value would be randomly assigned from the Poisson distribution with a mean of three. A new event-DV probability is calculated using the histogram with these new numbers of DVs. In the same toy event, the varied f-factor is also calculated. The numbers of DVs that pass the extended and signal DV selections vary based on the Poisson distribution, with the original numbers of DVs as the mean. Using the new numbers of DVs, a new f is calculated. The number of events in the SR is recalculated using this new event-DV probability and the new f. This procedure is repeated using 10,000 toy events, and the standard deviation of the estimated number of events in the SR is assigned as an uncertainty. It is obtained as 57%.

Second, the uncertainty that comes from the difference in the pileup distribution between the PTR and MTR is considered. Figure 8.10 shows these regions' normalized pileup distribution and ratio. The difference is significant in the region with a pileup larger than around 60. This difference is due to the degradation of the $E_{\mathrm{T}}^{\mathrm{miss}}$ trigger performance under high pileup conditions. The track density increases as the pileup increases, and the background DV is more likely to be reconstructed. In order to take into account this difference, the event weights that match the the pileup distribution of the PTR to the MTR are applied to the PTR events. The event-DV probability and f are recalculated with the weighted events, and the number of events in the SR is estimated using the new event-DV probability and f. Applying the pileup reweighting, the estimated number of events in the SR changes from 0.797 to 0.809, which is a 1.5% increase. The estimated value after pileup reweighting is used as the nominal value and the difference from the value before reweighting is considered the pileup uncertainty.

Table 8.1: Estimated number of background events in the SR. 'PTR statistics' uncertainty is calculated by propagating the statistical uncertainty of the DVs in the PTR to the final estimation. 'Pileup' uncertainty is calculated by taking the difference of the estimation with and without pileup reweighting that matches the pileup distribution of the PTR to the MTR. 'Non-closure' uncertainty is calculated from the ratios of the observation divided by the estimate in the validation regions.

Region	Estimate	Uncertainties			
		PTR statistics	Pileup	Non-closure	Total
SR	0.81 ± 0.49	57%	2%	22%	61%

As a result of the validation, non-closures between the estimation and observation are seen in several validation regions. The non-closure uncertainty is therefore defined by taking these ratios and obtained as 22%. Section 8.4 describes setting the non-closure uncertainty.

The estimated number of background events in the SR and its uncertainty are shown in Table 8.1.

8.4 Validation

The validity of the background estimation is confirmed using three types of VRs:

- Inside material region
- Seed multiplicity sideband region
- Track multiplicity and invariant mass sideband region

8.4.1 Inside material region

The number of events with a DV inside material is estimated using the same method. In this validation region, DVs are required to pass the final DV selection except that they fail the strict material map veto. Not only this "inside material true VR", the sideband DVs in terms of the N_{tracks} or m_{DV} are also used for validation. The definition of the small subsets of inside material VR is shown in Figure 8.11. Event-DV probabilities are calculated in each track and mass window using the DVs reconstructed inside the material in the PTR. The number of events in the MTR with a DV inside material with each track and invariant mass is estimated. The observed and estimated numbers of DVs in these VRs are shown in Figure 8.12.

The observation and estimate in the VRs with m_{DV} larger than 10 GeV are consistent within 1σ of the uncertainties. The method tends to overestimate in the VRs with m_{DV} lower than 10 GeV. The largest discrepancy between the estimate and observation is seen in VRVeryLowMass, which is 16%.

8.4.2 Low number of seed region

The number of events with a DV with lower N_{seeds} is estimated using the same method. In this VR, DVs are required to pass the final DV selection except that they fail the N_{seeds} requirements and have a lower

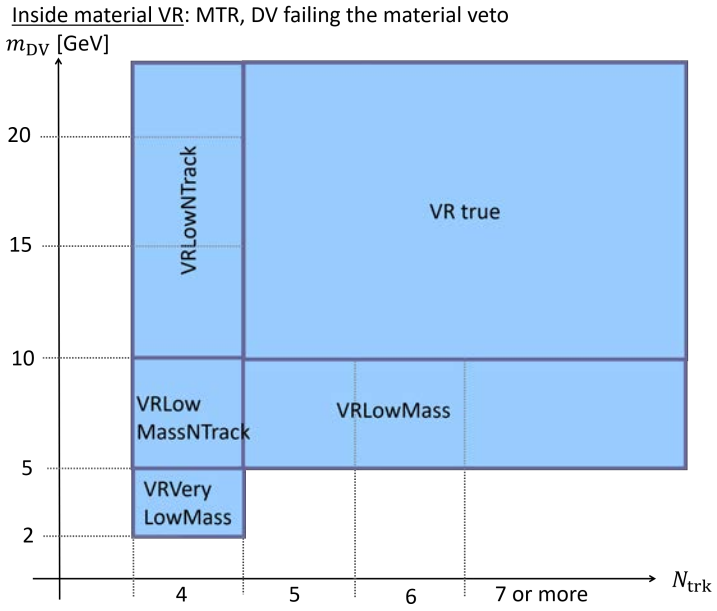

Figure 8.11: Binning of the inside material validation region.

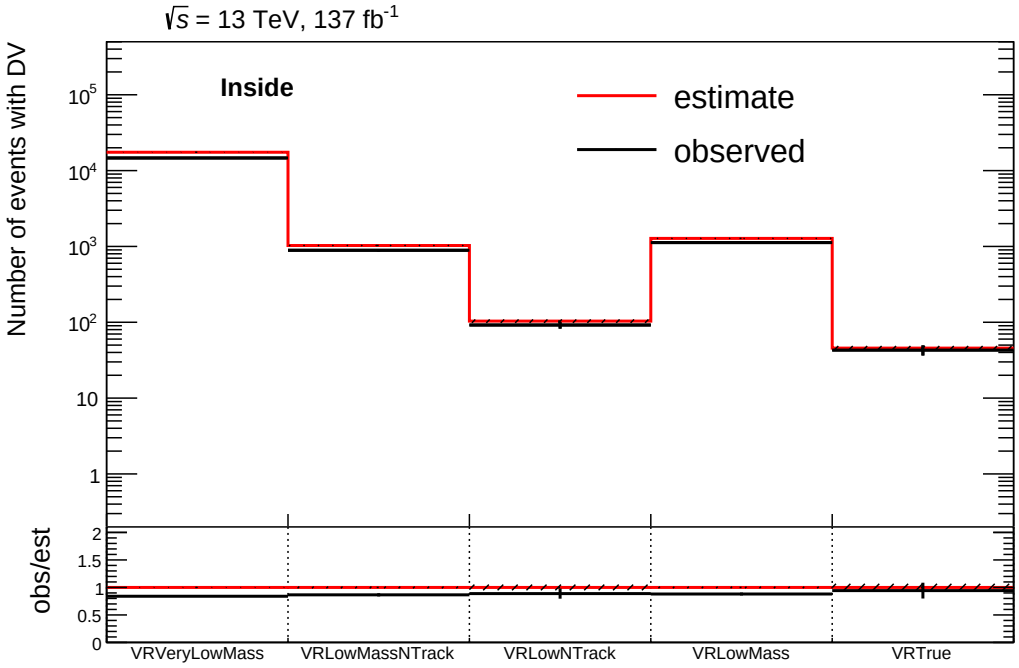

Figure 8.12: Estimated and observed number of DVs in the inside material region. The error bar includes the PTR statistic and the pileup uncertainties.

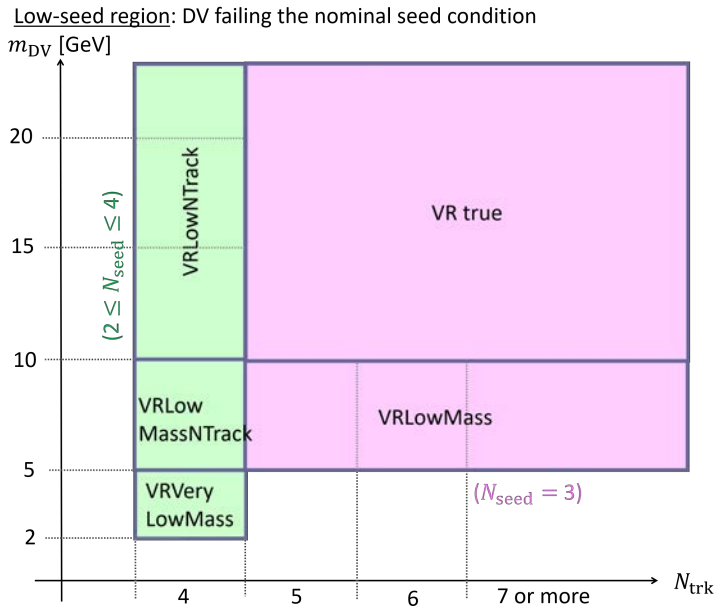

Figure 8.13: Definition of the SR and the low track multiplicity/low mass validation region.

number of N_{seeds}. Like the inside material VR, the low number of seed true VR, as well as its sideband regions, are used for validation. Figure 8.13 shows the definition of the subsets of the low number of seed VR and N_{seeds} condition in each region. The observed and estimated numbers of DVs in these VRs are shown in Figure 8.14.

The observation is consistent with the estimate within 1σ of the uncertainty, except that VRVeryLowMass has a 13% overestimate. The observed and estimated numbers of DVs in these VRs are shown in Figure 8.14.

8.4.3 Low track multiplicity/low mass region

The number of events with a DV with lower track multiplicities and invariant mass is estimated using the same methods. To avoid potential signal contamination, only VRVeryLowMass, the region with four tracks and a mass of 2-5 GeV, is used. Figure 8.15 shows the definition of the SR and the low track multiplicity/ low mass VR. Figure 8.16 shows the estimation for the VR and SR and the observed number of DVs in the VR.

The estimation method underestimates the number of backgrounds by 22%. As a result of validation, observation and estimation are consistent within the uncertainty in most regions. However, some VRs have a discrepancy larger than 1σ of uncertainty that has already been considered. Among those VRs, the largest relative error is seen in the low-track multiplicity and invariant mass VR. This 22% relative error is added as a non-closure uncertainty.

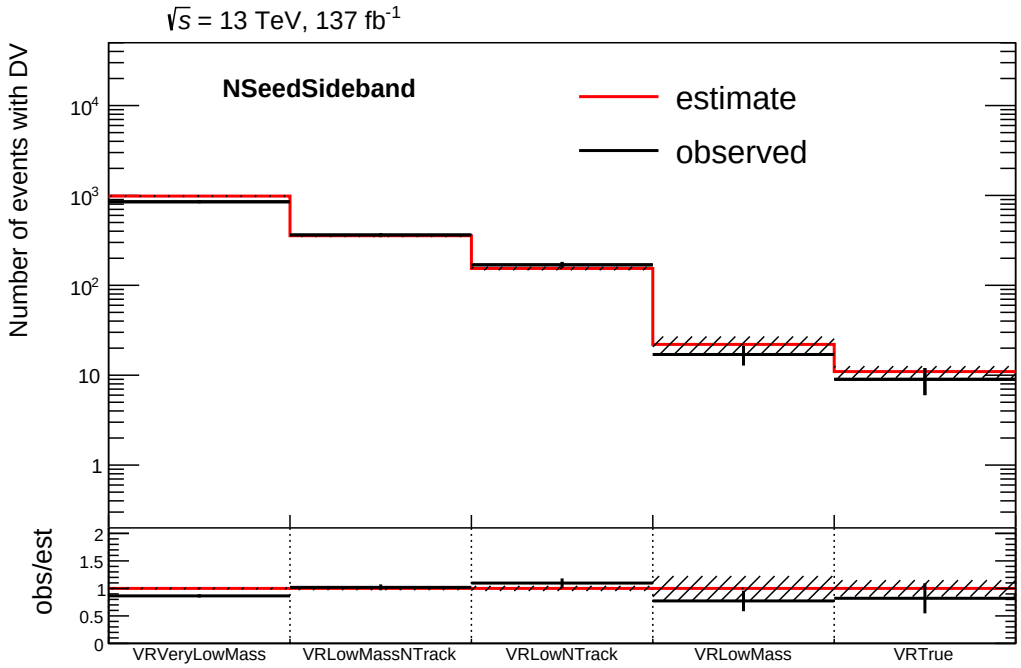

Figure 8.14: Estimated and observed number of DVs in the n-seed sideband region. The error bar includes the PTR statistic and the pileup uncertainties.

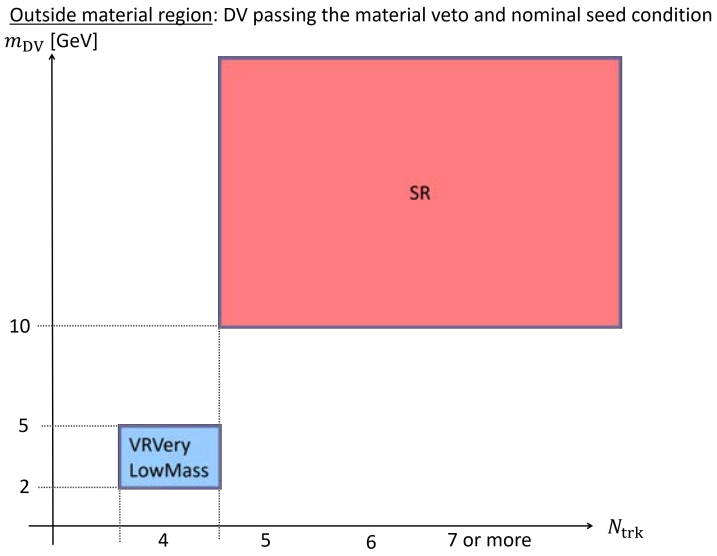

Figure 8.15: Definition of the SR and the low track multiplicity/low mass validation region.

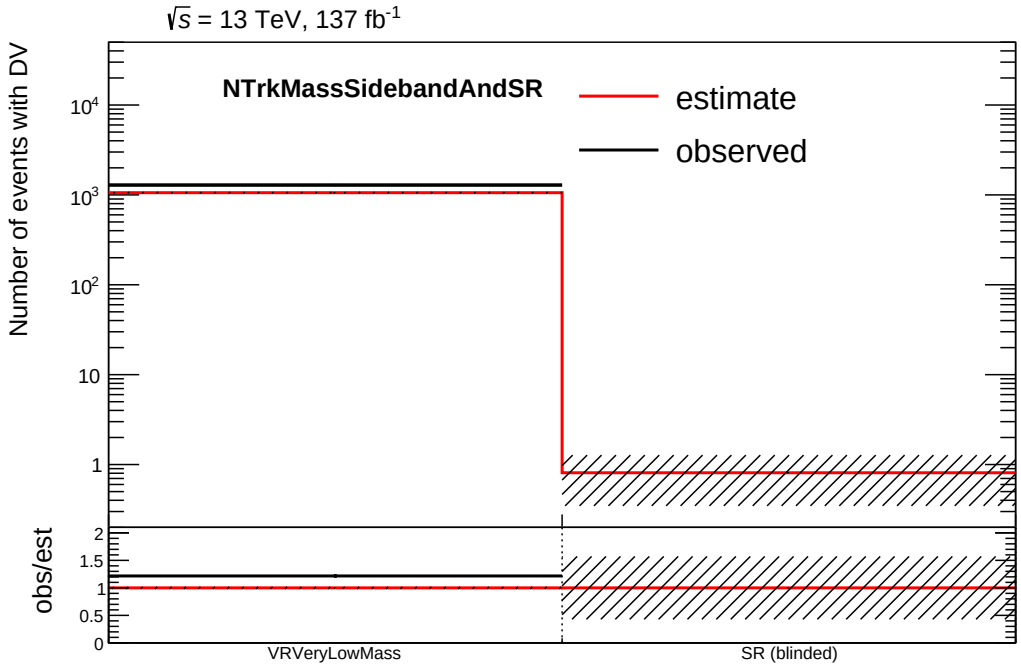

Figure 8.16: Estimated number of DVs in the SR and n-track/mass sideband region, and observed number of DVs in the n-track/mass sideband region. The error bar includes the PTR statistic and the pileup uncertainties.

Chapter 9

Systematic uncertainties

The systematic uncertainties on the expected number of background events are discussed in Section 8.3. This chapter discusses the systematic uncertainties on the expected number of signal events. Signal MC samples are used to interpret the results. Therefore, it is necessary to quantify differences between simulated signal events and actual data that may impact the signal selection efficiency. These systematic uncertainties of the signal events are included in the fitting in the statistical analysis as nuisance parameters.

9.1 Uncertainties on tracking efficiency

The dominant uncertainty comes from the uncertainty on the track reconstruction efficiency by the large radius tracking in data and MC. The uncertainty on the track reconstruction efficiency by the standard tracking is evaluated as approximately 1.8% [93], while the uncertainty on the track reconstruction efficiency by the large radius tracking has not been studied well. The uncertainty of the signal yields, which comes from the uncertainty on the track reconstruction efficiency by the large radius tracking, is estimated as follows:

1. Calculate the ratio of the reconstructed DVs originating from the decay of the K^0_S meson in data and MC. Using this ratio, calculate the probability that a track is not reconstructed (i.e., the uncertainty on the track reconstruction efficiency) in data.

2. Remove tracks from the DV randomly in the signal event based on the above probability. This procedure is named "track-killing". Then, recalculate the expected signal yields after track-killing. The difference in the signal yield before and after track-killing in DVs is defined as the systematic uncertainty from the uncertainty of the track reconstruction efficiency.

First, the decay $K^0_S \to \pi^+\pi^-$ is used to estimate the uncertainty of the track reconstruction efficiency. Since K^0_S meson has 90 ps of lifetime, its decay is reconstructed as a DV with two tracks with opposite charges. The inefficiency of reconstructing K^0_S ($1-\epsilon_{K_S}$, where ϵ_{K_S} is the reconstruction efficiency of K^0_S) is expressed as a function of the inefficiency in tracking ($1-\epsilon_{\rm trk}$) as follows:

$$1-\epsilon_{K_S} = 2\cdot(1-\epsilon_{\rm trk}) - (1-\epsilon_{\rm trk})^2 \Rightarrow 1-\epsilon_{\rm trk} = 1-\sqrt{\epsilon_{K_S}}. \tag{9.1}$$

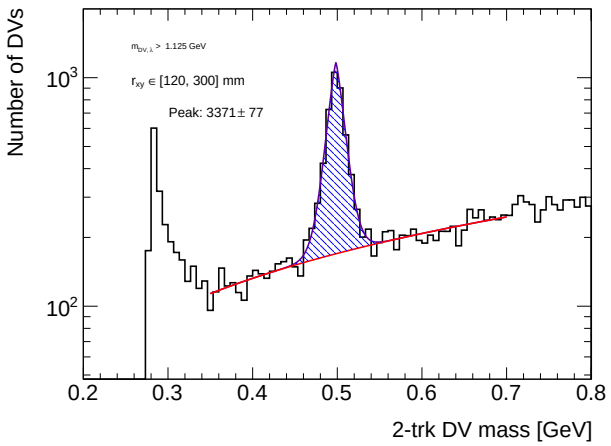

Figure 9.1: Mass distribution of K_S^0 candidates in the outermost radial region (120 mm $< R_{xy} <$ 300 mm) observed in data. The mass distribution is fitted by an asymmetric Gaussian (purple) plus liner (red) function. The integral of the asymmetric Gaussian function in the mass range from 0.4 to 0.6 GeV is shown.

A deviation of this inefficiency in the data/MC ratio is considered as the uncertainty of the track reconstruction efficiency on the MC samples.

The data taken in four runs from 2016, three from 2017, and three from 2018, corresponding to 2.8 fb^{-1} in total, are used for this study. The MC samples are $Z \to \nu\bar{\nu}$ + jets. Events that pass the MTR conditions are used. Those events are weighted to match the pileup distribution to the one in the MTR with the full dataset, shown in Figure 5.6. The DVs of the K_S^0 candidate are selected by requiring them to pass all baseline DV selections and have exactly two tracks with opposite charges. Figure 9.2(a) shows the number of reconstructed K_S^0 candidate's DVs in each radial position. In each radial bin, the mass distribution of K_S^0 candidate's DVs selected above is fitted by an asymmetric Gaussian plus quadratic function or asymmetric Gaussian plus linear function. The fitted asymmetric Gaussian function is integrated in the range of 0.4 GeV $< m_{\rm DV} <$ 0.6 GeV and defined as the number of K_S^0, which is shown in Figure 9.1. This radial bin is defined based on the material distribution of ID. The DVs with small radii are reconstructed from the tracks reconstructed by the standard tracking, whose uncertainty is well-evaluated. Therefore, the K_S^0 yields in the MC events are normalized to data using the region with $R_{xy} <$ 22 mm.

An uncertainty per track is calculated from the uncertainty obtained from Equation 9.1 and 1.8% uncertainty from the standard tracking, adding them with quadrature as a conservative estimate. Figure 9.2(b) shows the obtained tracking uncertainty.

Next, this tracking uncertainty is propagated to the expected signal yields in the SR using a track-killing method. Tracks in the reconstructed DVs in the simulated signal events are randomly removed with a probability equal to the obtained per-track uncertainty shown in Figure 9.2(b). The properties of each DV ($N_{\rm tracks}$, $m_{\rm DV}$, $N_{\rm seeds}$, and $\max(\Delta\eta(p_{\rm trk}, p_{\rm tot} - p_{\rm trk}))$) are recalculated using the remaining tracks, and the signal yield in the SR after track-killing is obtained. This track-killing procedure is repeated 100 times for each signal grid. The average of the expected signal yields by these track-killed samples is calculated, and the difference from the one without track-killing is added to the signal uncertainty. The uncertainty on the signal yields is calculated signal grid by signal grid, which is obtained up to 17%.

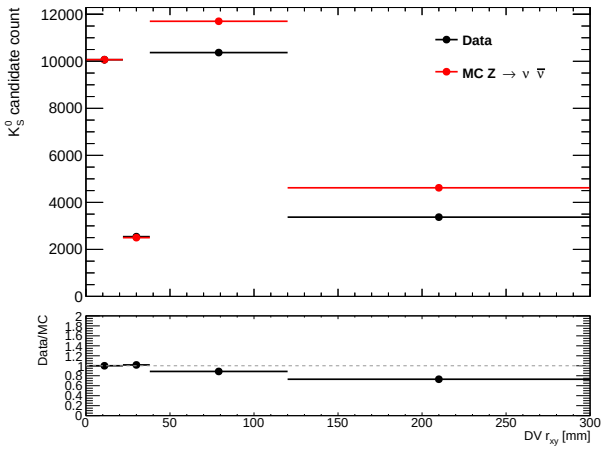

(a) The number of K^0_S candidates.

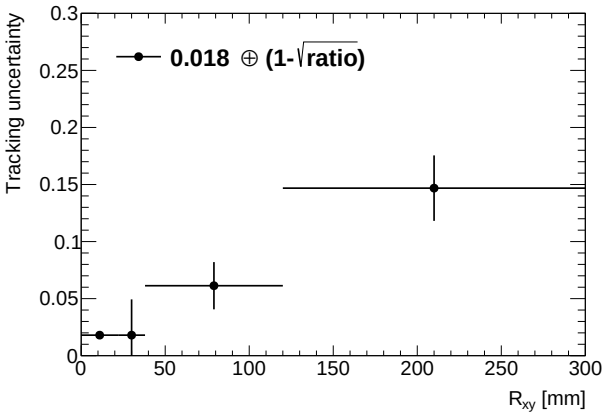

(b) Tracking uncertainty.

Figure 9.2: (a)The number of reconstructed K^0_S candidates in each radial region in data and MC. The MC is normalized to data using the first radial bin. (b)Tracking uncertainty in each DV radial region.

Figure 9.3 shows the uncertainty for several signal grids. The larger uncertainty is obtained for the grids with longer $\tilde{\chi}^0_2$ lifetime. In addition, the uncertainty tends to be more significant when the mass splitting between $\tilde{\chi}^0_2$ and $\tilde{\chi}^0_1$ is smaller because when the mass splitting is small, the reconstructed DVs have lower track multiplicity and invariant mass, which is significantly affected by the removal of a single track.

9.2 Uncertainties on $E_{\mathrm{T}}^{\mathrm{miss}}$ trigger efficiency

This analysis uses an offline $E_{\mathrm{T}}^{\mathrm{miss}}$ selection of 150 GeV, which is lower than the plateau of the $E_{\mathrm{T}}^{\mathrm{miss}}$ efficiency curve where the trigger performance is well validated. Therefore, the performance of the lowest unpresecaled triggers for data and MC is compared. If there is a significant difference in trigger performance between data and MC, we consider applying a scaling factor.

A method called tag-and-prob is used to measure the $E_{\mathrm{T}}^{\mathrm{miss}}$ trigger efficiency. The events with a muon are selected using highly efficient muon triggers. Then it is checked if these "tag" events pass the $E_{\mathrm{T}}^{\mathrm{miss}}$ trigger or not, which is called "probe." The efficiency is measured as a function of $E_{\mathrm{T}}^{\mathrm{miss}}$ without muons, referred to as $E_{\mathrm{T}}^{\text{miss, mu-subtracted}}$, in order to imitate the $E_{\mathrm{T}}^{\mathrm{miss}}$ used in triggers, which does not include muons in the $E_{\mathrm{T}}^{\mathrm{miss}}$ calculation. The shape of the $E_{\mathrm{T}}^{\mathrm{miss}}$ trigger efficiency curve is compared between data and $Z \to \mu\mu$ + jets MC samples. As a result, the discrepancy in the $E_{\mathrm{T}}^{\mathrm{miss}}$ trigger efficiency in the region with $E_{\mathrm{T}}^{\text{miss, mu-subtracted}}$ larger than 150 GeV between the data and MC is up to 2%, whose effect on the uncertainty in the number of signal events is insignificant compared to other uncertainties. Figure 9.4 shows the $E_{\mathrm{T}}^{\mathrm{miss}}$ trigger efficiency in each data-taking period (2016 A-D1, 2016 D4-[1)], 2017, and 2018). Therefore, no scaling to the MC is applied.

The $E_{\mathrm{T}}^{\mathrm{miss}}$ trigger efficiency in the data and in the signal MC samples is also compared. Since signal

[1)] The data-taking period for each year is further divided into several periods, and the used triggers differed depending on the period.

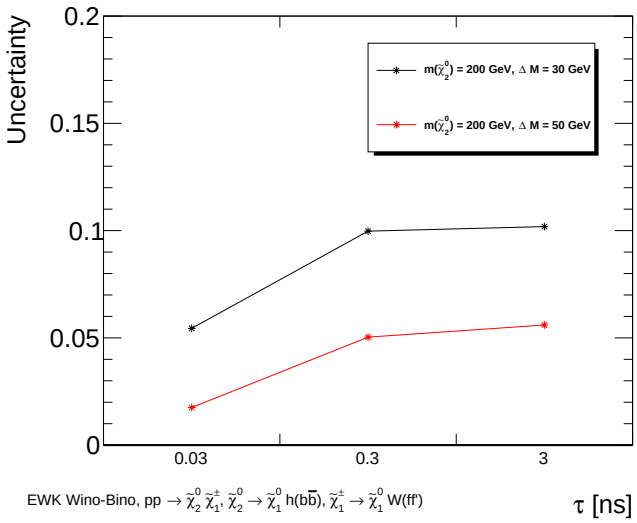

Figure 9.3: Uncertainty on the signal yields of the bino-wino signal model with several $\tilde{\chi}_2^0$ lifetime and mass splitting between $\tilde{\chi}_2^0$ and $\tilde{\chi}_1^0$ with a fixed $\tilde{\chi}_2^0$ mass of 200 GeV.

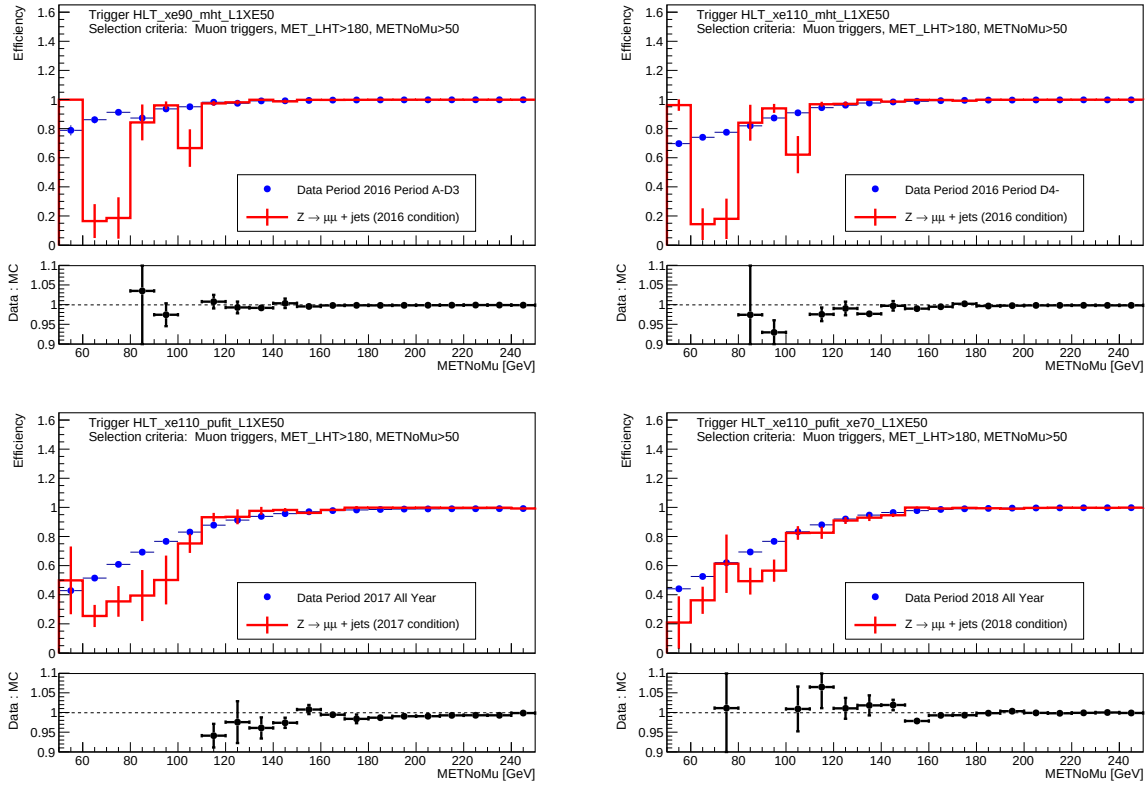

Figure 9.4: $E_{\mathrm{T}}^{\mathrm{miss}}$ trigger efficiency as a function of $E_{\mathrm{T}}^{\mathrm{miss,\ mu\text{-}subtracted}}$ in data and $Z \to \mu\mu$ MC. The trigger which is unplescaled throughout each period is used.

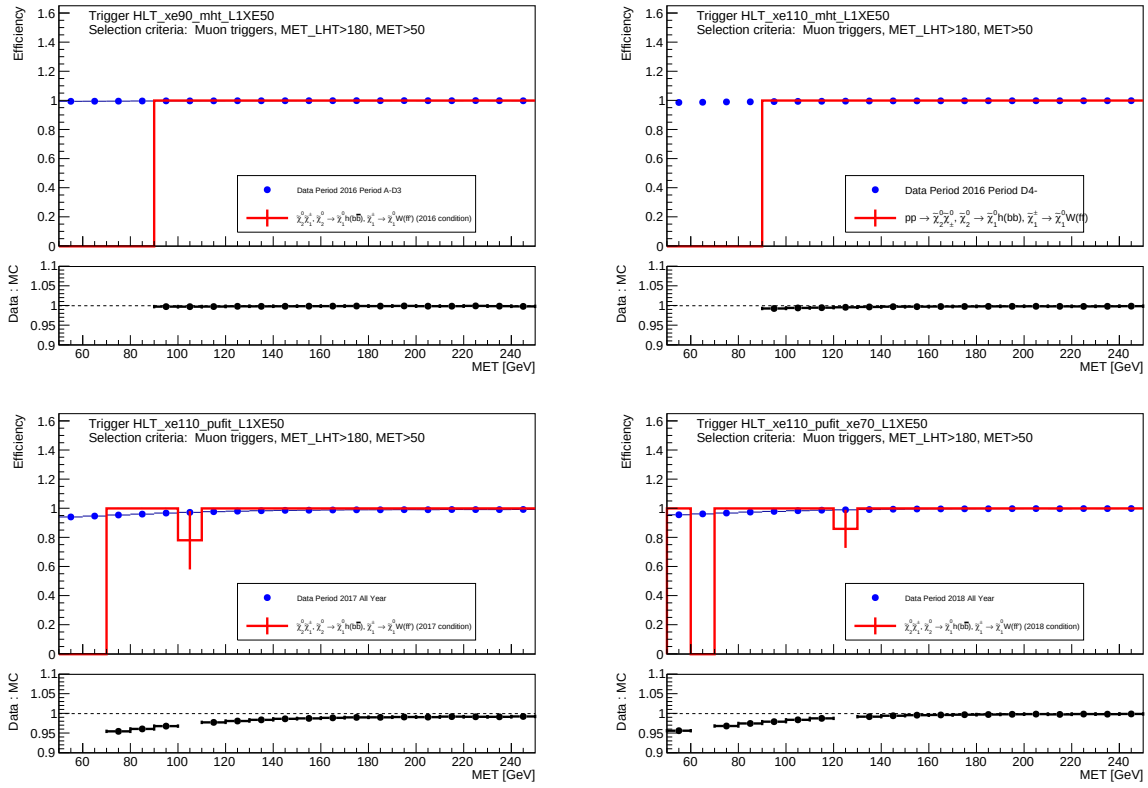

Figure 9.5: $E_{\mathrm{T}}^{\mathrm{miss}}$ trigger efficiency as a function of $E_{\mathrm{T}}^{\mathrm{miss}}$ in data and bino-wino signal MC with $m_{\tilde{\chi}_2^0} = 200$ GeV and $\Delta M(\tilde{\chi}_2^0, \tilde{\chi}_1^0) = 20$ GeV. The MC samples with $\tau_{\tilde{\chi}_2^0} = 0.03$ ns, 0.3 ns, and 3 ns are merged. The trigger which is unplescaled throughout each period is used.

events are not muon-specific events, we still use muon triggers as a reference but do not measure the efficiency curves as a function of $E_{\mathrm{T}}^{\mathrm{miss,\ mu\text{-}subtracted}}$ but instead $E_{\mathrm{T}}^{\mathrm{miss}}$. A good agreement between the data and signal MC is observed in the region with $E_{\mathrm{T}}^{\mathrm{miss}} > 150$ GeV. Figure 9.5 is an example of comparing the data and signal MC.

From the above studies, the uncertainty from the difference in the $E_{\mathrm{T}}^{\mathrm{miss}}$ trigger efficiency between data and MC is confirmed to be negligible compared to other systematic uncertainties.

9.3 Uncertainty on offline $E_{\mathrm{T}}^{\mathrm{miss}}$

The uncertainty from the difference of the offline $E_{\mathrm{T}}^{\mathrm{miss}}$ resolution between data and simulated events is considered. The major components of the $E_{\mathrm{T}}^{\mathrm{miss}}$ are the jet and soft terms. Four uncertainties on these terms are thus evaluated - JES, JER, the scale of the $E_{\mathrm{T}}^{\mathrm{miss}}$ soft term, and the resolution of the $E_{\mathrm{T}}^{\mathrm{miss}}$ soft term. The expected signal yields are recalculated by changing each component within the uncertainty, and the difference from the nominal yields is assigned as the uncertainty. They are obtained as less than 10%.

Table 9.1: Summary of the systematic uncertainties in the predicted number of signal events.

Source of uncertainty	Relative uncertainty [%]
Tracking efficiency	2 – 17
Offline $E_{\mathrm{T}}^{\mathrm{miss}}$ resolution	< 10
PDF choice and strong coupling	< 10
factorization and renormalization scales	< 8
Integrated luminosity	0.84

9.4 Luminosity

The uncertainty of the integrated luminosity of 2016-2018 is measured as 0.84% [26]. This is taken as an overall uncertainty on the luminosity-normalized signal yield.

9.5 Theoretical uncertainties

Cross sections and their uncertainties for wino-like $\tilde{\chi}_2^0\tilde{\chi}_1^\pm$ pair production model was calculated at NNLO+NLL by the LHC SUSY Cross Sections Working Group [22].

The uncertainties on the signal yields due to uncertainties in the signal selection efficiency from PDF selection, factorization scale, renormalization scale, and strong-coupling constants are also considered. They are evaluated by varying the parameters given in the generation of the signal MC samples. The uncertainties of the PDF choice are estimated using other PDFs. The uncertainty of the choice of the strong coupling constant is evaluated by changing the value within its uncertainty. The uncertainties from the factorization and renormalization scales are evaluated by changing these parameters by 0.5 to 2 around the nominal values. The difference from the nominal number of expected signal yields in each signal grid is applied as systematic uncertainty. The uncertainty from the PDF choice and strong coupling constant are up to 10%, and the one from the factorization and renormalization scales are up to 8%.

Table 9.1 summarizes the systematic uncertainties on the number of signal events considered.

Chapter 10

Results

After the number of background events in the SR is estimated and its validity is confirmed as described in Chapter 8, the SR is *unblinded*, i.e. the number of observed events in the SR is checked. In this chapter, the expected number of signal events and the observed number of events in the SR are shown.

10.1 Expected signal events

Figure 10.1 shows the expected signal yields after applying all the selection criteria as a function of $\tilde{\chi}_2^0$ mass and lifetime. The mass splitting between $\tilde{\chi}_2^0$ and $\tilde{\chi}_1^0$ is set to 20, 30, 40, and 50 GeV.

10.2 Observed events

Three events were observed in the SR, while the expected number of background events is 0.81 ± 0.49, as shown in Section 8.2. Figure 10.2 shows the distribution of N_{tracks} and m_{DV} of the DV observed in the MTR.

All events in the SR have a DV with five tracks located inside the beam pipe. The information of each observed event is shown in Tables 10.1, 10.2, and 10.3. The "prompt" jet mean that it is considered to originate from the hard scatter PV based on the jet vertex tagger. The origins of these events are discussed in more detail in Section 11.2.2.

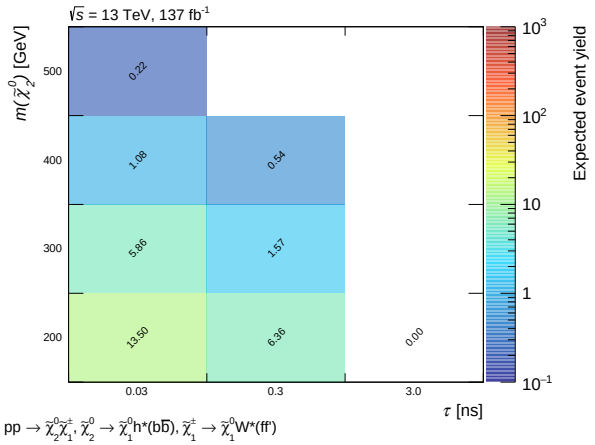

(a) $\Delta M(\tilde{\chi}_2^0, \tilde{\chi}_1^0) = 20$ GeV

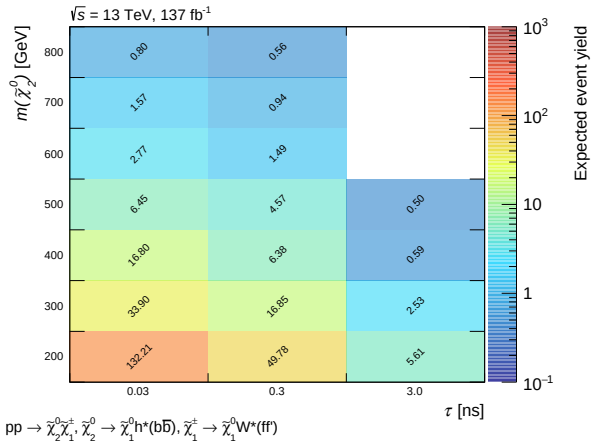

(b) $\Delta M(\tilde{\chi}_2^0, \tilde{\chi}_1^0) = 30$ GeV

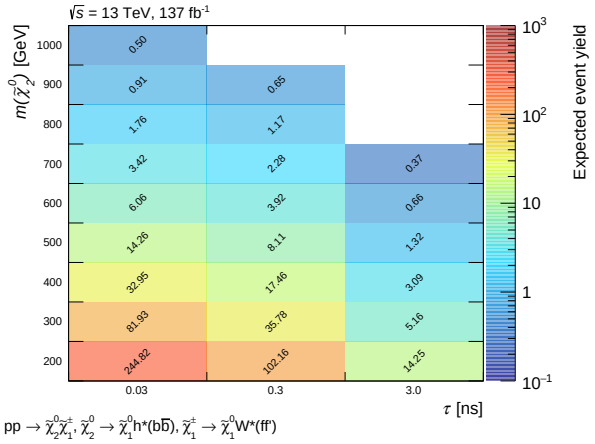

(c) $\Delta M(\tilde{\chi}_2^0, \tilde{\chi}_1^0) = 40$ GeV

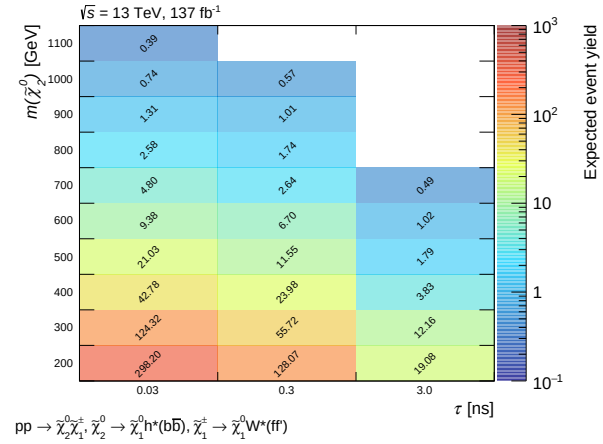

(d) $\Delta M(\tilde{\chi}_2^0, \tilde{\chi}_1^0) = 50$ GeV

Figure 10.1: Expected Bino-Wino signal yields in the case with (a) $\Delta M(\tilde{\chi}_2^0, \tilde{\chi}_1^0) = 20$ GeV, (b) $\Delta M(\tilde{\chi}_2^0, \tilde{\chi}_1^0) = 30$ GeV, (c) $\Delta M(\tilde{\chi}_2^0, \tilde{\chi}_1^0) = 40$ GeV, and (d) $\Delta M(\tilde{\chi}_2^0, \tilde{\chi}_1^0) = 50$ GeV. Bins with no MC samples are shown as blank.

Table 10.1: Information of the SR event #1.

Event property
$E_{\mathrm{T}}^{\mathrm{miss}}$: 169.7 GeV
$E_{\mathrm{T}}^{\mathrm{miss}}$ ϕ: 2.54
Number of pileups: 32
Number of PVs: 14
Number of jets: 4
Jet property (p_{T}, η, ϕ, b-tagged, prompt)
Jet 1: 199.5 GeV, -1.04, -0.63, true, true
Jet 2: 132.2 GeV, -1.58, 0.95, false, true
Jet 3: 63.5 GeV, -0.34, -2.24, true, true
Jet 4: 26.9 GeV, -0.51, -0.45, false, true
Lepton property (p_{T}, η, ϕ)
- Muon 1: (71.8 GeV, -1.25, -2.87)
DV property
$(x_{\mathrm{DV}}, y_{\mathrm{DV}}, z_{\mathrm{DV}}) = (-9.72, -12.10, -22.43)$ mm
$\eta_{\mathrm{PV-DV}}, \phi_{\mathrm{PV-DV}} = (-0.31, -2.26)$
N_{tracks}: 5
m_{DV}: 14.1 GeV
N_{seeds}: 9
DV-track property (p_{T}, η, ϕ, charge)
Track 1: (2.6, -0.16, -2.16, 1)
Track 2: (6.3, -0.32, -2.15, -1)
Track 3: (1.9, -0.37, -2.06, 1)
Track 4: (22.7, -0.36, $-2,35$, -1)
Track 5: (1.2, 1.41, -3.07, 1)
2-track seed position (x, y, z) mm
Seed 1: $(-9.77, -12.18, -22.50)$
Seed 2: $(-10.04, -12.62, -22.57)$
Seed 3: $(-9.96, -12.46, -22.56)$
Seed 4: $(-9.65, -11.98, -22.38)$
Seed 5: $(-9.62, -11.96, -22.39)$
Seed 6: $(-9.76, -12.09, -22.39)$
Seed 7: $(-9.15, -11.26, -22.34)$
Seed 8: $(-9.32, -11.27, -21.99)$
Seed 9: $(-9.19, -11.28, -22.18)$

Table 10.2: Information of the SR event #2.

Event property
$E_{\mathrm{T}}^{\mathrm{miss}}$: 196.8 GeV
$E_{\mathrm{T}}^{\mathrm{miss}}$ ϕ: -1.56
Number of pileups: 33
Number of PVs: 20
Number of jets: 6
Jet property (p_{T}, η, ϕ, b-tagged, prompt)
Jet 1: 154.1 GeV, -0.29, 1.99, true, true
Jet 2: 111.8 GeV, -0.50, 0.86, false, true
Jet 3: $88,2$ GeV, -0.05, 1.64, false, true
Jet 4: 48.5 GeV, 1.60, -2.91, false, true
Jet 5: 31.6 GeV, -1.41, 0.71, false, false
Jet 6: 27.7 GeV, -1.01, -0.09, false, false
Lepton property (p_{T}, η, ϕ)
- Muon 1: (104.6 GeV, 0.18, -1.23)
DV property
(x_{DV}, y_{DV}, z_{DV}) = (5.63, -0.00, -59.06) mm
$\eta_{\mathrm{PV-DV}}, \phi_{\mathrm{PV-DV}}$ = (0.58, 0.14)
N_{tracks}: 5
m_{DV}: 14.5 GeV
N_{seeds}: 9
DV-track property (p_{T}, η, ϕ, charge)
Track 1: (1.2, 0.51, 0.31, -1)
Track 2: (1.4, 0.47, 0.54, 1)
Track 3: (1.6, 0.50, -0.46, -1)
Track 4: (4.0, 1.79, -1.12, -1)
Track 5: (1.4, -1.30, 0.77, -1)
2-track seed position (x, y, z) mm
Seed 1: (5.33, -0.16, -59.42)
Seed 2: (5.34, -0.15, -59.32)
Seed 3: (5.34, -0.15, -59.41)
Seed 4: (5.33, 0.22, -58.88)
Seed 5: (5.50, 0.21, -58.85)
Seed 6: (5.50, 0.29, -59.02)
Seed 7: ((5.94, -0.33, -58.58)
Seed 8: (6.36, 0.19, -58.76)
Seed 9: (6.41, 0.40, -58.92)

Table 10.3: Information of the SR event #3.

Event property
$E_{\mathrm{T}}^{\mathrm{miss}}$: 199.9 GeV
$E_{\mathrm{T}}^{\mathrm{miss}}$ ϕ: -1.35
Number of pileups: 40
Number of PVs: 21
Number of jets: 6
Jet property (p_{T}, η, ϕ, b-tagged, prompt)
Jet 1: 224.0 GeV, 0.16, 2.35, false, true
Jet 2: 165.9 GeV, -0.22, 2.52, false, true
Jet 3: 136.5 GeV, 0.10, -0.56, false, true
Jet 4: 93.1 GeV, -1.18, 0.79, false, true
Jet 5: 24.9 GeV, 2.05, -0.88, false, true
Jet 6: 21.5 GeV, 2.45, -0.46, false, true
DV property
$(x_{\mathrm{DV}}, y_{\mathrm{DV}}, z_{\mathrm{DV}}) = (3.88, -2.29, -41.57)$ mm
$\eta_{\mathrm{PV-DV}}, \phi_{\mathrm{PV-DV}} = (-0.42, -0.32)$
N_{tracks}: 5
m_{DV}: 12.0 GeV
N_{seeds}: 9
DV-track property (p_{T}, η, ϕ, charge)
Track 1: (1.6, 0.20, -0.08, 1)
Track 2: (2.7, 0.29, -0.18, 1)
Track 3: (1.7, 0.28, -0.04, 1)
Track 4: $(7.3, 0.43, -0,50, -1)$
Track 5: (2.3, -1.25, 0.90, 1)
2-track seed position (x, y, z) mm
Seed 1: (4.03, -2.35, -41.60)
Seed 2: (3.86, -2.32, -41.62)
Seed 3: (4.10, -2.36, -41.50)
Seed 4: (4.08, -2.35, -41.53)
Seed 5: (4.03, -2.33, -41.53)
Seed 6: (3.73, -2.16, -41.63)
Seed 7: (3.69, -2.24, -41.58)
Seed 8: (3.69, -2.26, -41.54)
Seed 9: (3.67, -2.27, -41.56)

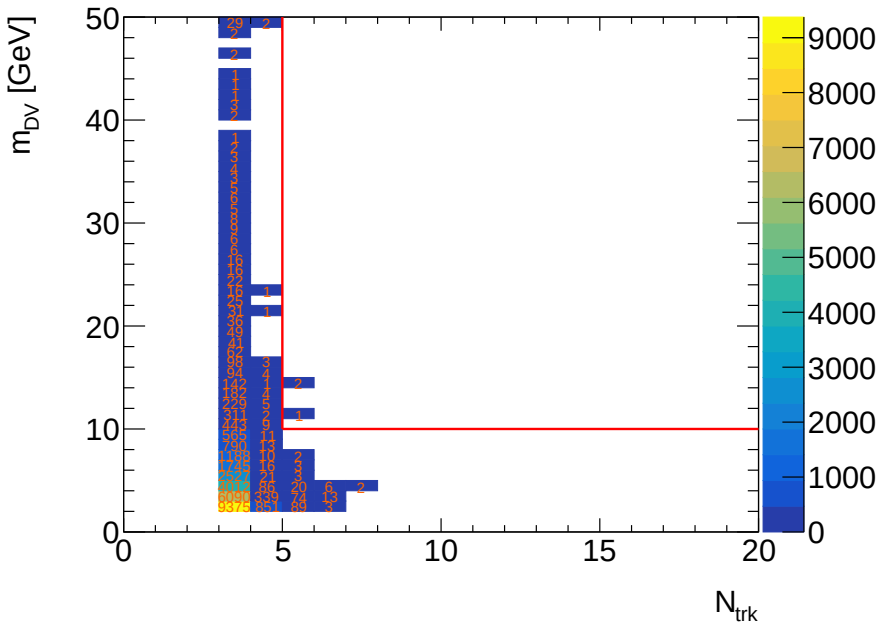

Figure 10.2: Two-dimensional distribution of N_{tracks} and m_{DV} of the DV observed in the MTR. All the baseline DV selection and signal DV selection except for N_{tracks} and m_{DV} conditions are applied. DVs with $N_{\text{tracks}} < 3$ or $m_{\text{DV}} < 2$ GeV are not shown. The upper right region of the two red lines corresponds to the SR.

Chapter 11

Interpretation and discussion

In this chapter, the results are interpreted. The statistical analysis method for the interpretation is described first, and then the results of the interpretation to the bino-wino model is shown. Investigations on the observed events in the SR are also provided.

11.1 Statistical analysis

Interpretation of the results is done using statistical analysis. It uses a hypothesis test, which quantifies the disagreement between the observation and estimation under an assumption based on a specific signal model. The likelihood function L quantifies the likelihood that the observation supports the hypothesis with a signal strength μ. It is formed as the products of the Poisson probability distribution functions for all SR bins:

$$L(\text{data}|\mu, \boldsymbol{\theta}) = \prod_{i=1}^{N_{\text{bin}}} \frac{(\mu s_i + b_i)^{n_i}}{n_i!} e^{-(\mu s_i + b_i)} \times C_{\text{syst}}(\boldsymbol{\theta}), \tag{11.1}$$

where n_i is the observed events in each SR bin i and N_{bin} is the number of SR bins. $\mu s_i + b_i$ is the expected number of events in bin i, where s_i and b_i are the expected number of signal and background events, respectively. The systematic uncertainties are parameterized by a set of nuisance parameters, referred to as $\boldsymbol{\theta}$, which constrains the fit. $C_{\text{syst}}(\boldsymbol{\theta})$ is the probability distribution function of nuisance parameters. We need to estimate both μ and $\boldsymbol{\theta}$, but the post-fit values of $\boldsymbol{\theta}$ are not of interest. To achieve this, we consider to "profile out" the nuisance parameters, which allows to use the same one-dimensional interval for the parameter of interest, independent of nuisance parameters [94]. The profile likelihood is obtained by replacing $\boldsymbol{\theta}$ with $\hat{\hat{\boldsymbol{\theta}}}$, which maximizes L under a specified μ (conditional maximum likelihood estimator).

The profile likelihood ratio with a specified value of μ is defined as [95]:

$$\lambda(\mu) = \frac{L(\mu, \hat{\hat{\boldsymbol{\theta}}})}{L(\hat{\mu}, \hat{\boldsymbol{\theta}})}, \tag{11.2}$$

where $\hat{\mu}$ and $\hat{\boldsymbol{\theta}}$ are the unconditional maximum likelihood estimators of μ and $\boldsymbol{\theta}$, respectively. Figure 11.1 is an illustration showing the relationship between $L(\hat{\mu}, \hat{\boldsymbol{\theta}})$ and $L(\hat{\mu}, \hat{\boldsymbol{\theta}})$. From Equation 11.2, $\lambda(\mu)$ always

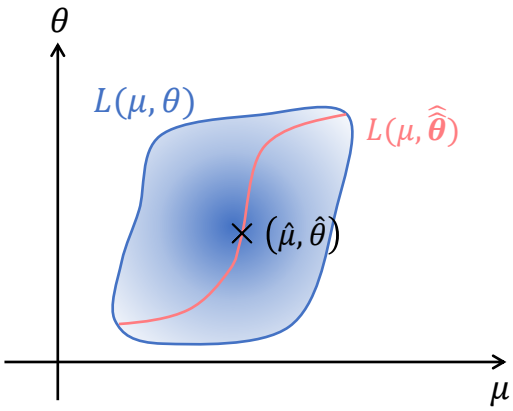

Figure 11.1: Illustration of $L(\mu,\theta)$ and $L(\mu,\hat{\hat{\theta}})$. The blue shade shows two-dimensional $L(\mu,\theta)$. It takes the maximum at $(\hat{\mu},\hat{\theta})$, and its contour is bounded by a certain confidence level. The red line shows $L(\mu,\hat{\hat{\theta}})$.

meets $0 \leq \lambda(\mu) \leq 1$, and $\lambda(\mu)$ close to 1 implies good agreement between the data and the specified value of μ.

Usually, the test statistics $\tilde{q}_\mu$ is used instead of $\lambda(\mu)$. It is defined as:

$$\tilde{q}_\mu = \begin{cases} -2\ln\frac{L(\mu,\hat{\hat{\boldsymbol{\theta}}}(\mu))}{L(0,\hat{\hat{\boldsymbol{\theta}}}(0))} & (\hat{\mu} < 0), \\ -2\ln\frac{L(\mu,\hat{\hat{\boldsymbol{\theta}}}(\mu))}{L(\hat{\mu},\hat{\boldsymbol{\theta}})} & (\hat{\mu} \geq 0). \end{cases} \tag{11.3}$$

It is defined to ensure that the signal process has $\mu \geq 0$. A higher value of $\tilde{q}_\mu$ means that the data and μ are less compatible. The level of agreement between the data and specified μ is quantified with p-value:

$$p_\mu = \int_{\tilde{q}_{\mu,\mathrm{obs}}}^{\infty} f(\tilde{q}_\mu|\mu)d\tilde{q}_\mu, \tag{11.4}$$

where $\hat{q}_{\mu,\mathrm{obs}}$ is the value of the observed test statistic. Here, $f(\tilde{q}_\mu|\mu)$ is the probability density function of the test statistics with specified μ, which is obtained by using asymptotic formulae [95] or a pseudo-experiment. In this thesis, the former method is used. Figure 11.2 shows the illustration of p_μ.

When the observed number of events exceeds the expected number of background events, the level of disagreement between the data and the hypothesis without any new physics ($\mu = 0$) is quantified. The test statistics with $\mu = 0$ is obtained from Equation 11.4:

$$q_0 = \begin{cases} -2\ln\lambda(0) & (\hat{\mu} \geq 0), \\ 0 & (\hat{\mu} < 0), \end{cases} \tag{11.5}$$

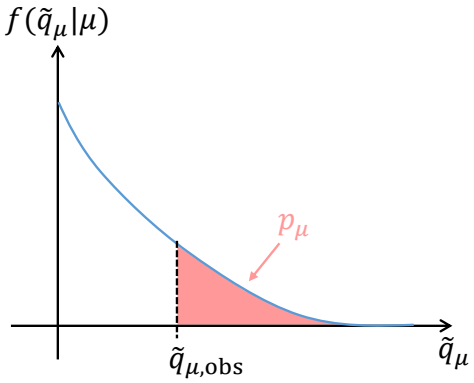

Figure 11.2: Illustration of p_μ.

where $\lambda(0)$ is the profile likelihood ratio with $\mu = 0$. The p-value with $\mu = 0$ is then calculated as:

$$p_0 = \int_{q_0,\mathrm{obs}}^{\infty} f(q_0|0)dq_0. \tag{11.6}$$

If $p_0 < 0.0027$ which corresponds to 3σ standard deviation, an evidence of a new physics can be claimed. A discovery can be claimed if $p_0 < 6 \times 10^{-7}$ which corresponds to 5σ standard deviation.

If no significant excess from the background prediction is observed, an upper limit is set to the signal strength assuming that it is too small to make an excess. In the case of upper limit setting, the test statistics is defined as:

$$\tilde{q}_\mu = \begin{cases} -2\ln\frac{L(\mu,\hat{\hat{\boldsymbol{\theta}}})}{L(0,\hat{\hat{\boldsymbol{\theta}}})} & (\hat{\mu} < 0, \mu \geq 0), \\ -2\ln\frac{L(\mu,\hat{\hat{\boldsymbol{\theta}}})}{L(\hat{\mu},\hat{\boldsymbol{\theta}})} & (0 \leq \hat{\mu} \leq \mu), \\ 0 & (0 \leq \mu < \hat{\mu}). \end{cases} \tag{11.7}$$

Figure 11.3 is the illustration of $\tilde{q}_\mu$. $\tilde{q}_\mu$ is set to 0 for $\hat{\mu} > \mu$ because when an upper limit is set, data with $\hat{\mu} > \mu$ are not regarded as representing less compatibility with μ than the observed data, and therefore this is not considered part of the rejection region of the test.

The CL_s method [96] sets the observed exclusion limit using p-values. CL_s is defined as:

$$\mathrm{CL}_s = \frac{p_{s+b}}{1 - p_b}, \tag{11.8}$$

where p_b is the for background-only hypothesis ($\mu = 0$), and p_{s+b} is the p-value for signal plus background hypothesis. If CL_s is less than 0.05 for a specific μ, its signal hypothesis is excluded with a 95% confidence level. An expected exclusion limit is set, assuming that there is no excess from the background-only hypothesis. It is calculated by replacing the $\tilde{q}_{\mu,\mathrm{obs}}$ in Equation 11.4 to the median $\tilde{q}_\mu$ expected with data distributed when $\mu = 0$.

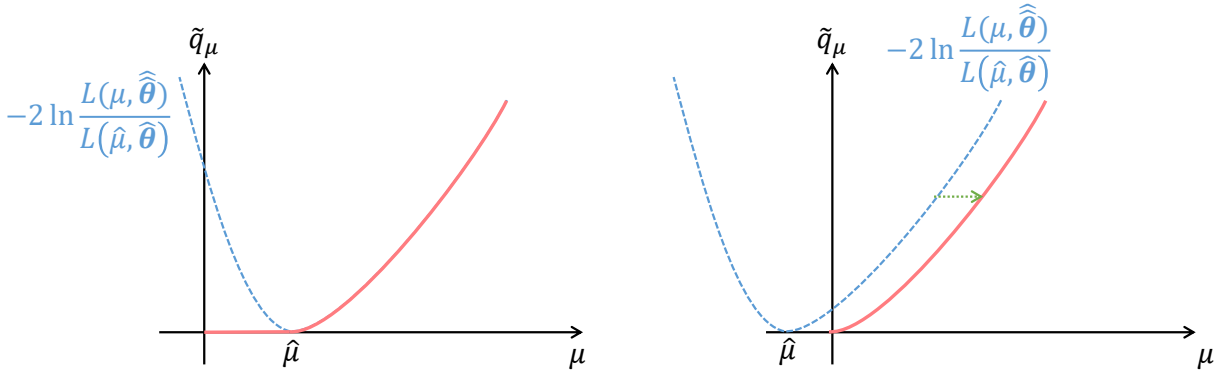

(a) $\hat{\mu} \geq 0$ **(b)** $\hat{\mu} < 0$

Figure 11.3: Illustration of $\tilde{q}_\mu$ (a) when $\hat{\mu} \geq 0$ and (b) when $\hat{\mu} < 0$.

11.2 Interpretation on bino-wino model

The results are interpreted to bino-wino signal model.

11.2.1 Limit setting

The fit is made using the pyhf package [97, 98]. The p_0 is calculated as 0.06, corresponding to 1.59σ standard deviation from the background expectation. An upper limit on the cross-section of the target signal model and the exclusion limit of the parameter space with a certain confidence level is set.

The 95% confidence level upper limit on the cross-section for $\tilde{\chi}_1^\pm\tilde{\chi}_2^0$ production in the bino-wino model is calculated. Figure 11.4 is the cross-section upper limit as a function of the mass and lifetime of $\tilde{\chi}_2^0$ when the mass splitting between $\tilde{\chi}_2^0$ and $\tilde{\chi}_1^0$ is 50 GeV. The higher the signal selection efficiency, the smaller cross-section upper limit is obtained. Since the signals with a longer lifetime have lower selection efficiency, only the larger cross-sections have been excluded for those models. The loss of the signal selection efficiency for the models with a long lifetime is caused by the low track reconstruction efficiency due to lack of the number of hits when the LLP decay position is far from the collision point. In addition, the cross-section upper limit becomes slightly smaller as the $\tilde{\chi}_2^0$ mass increases. This is because as the mass of $\tilde{\chi}_1^0$ in the final state increases, the event is more likely to have a large $E_{\mathrm{T}}^{\mathrm{miss}}$. If we assume the theoretical expectation of the cross-section of the $\tilde{\chi}_1^\pm\tilde{\chi}_2^0$ pair production shown in Figure 2.14, the parameter spaces under the black line are excluded.

The 95% confidence level exclusion limit on the $\tilde{\chi}_2^0$ mass as a function of $\tilde{\chi}_2^0$ lifetime with fixed mass splittings is shown in Figure 11.5. In any mass-splitting case, the more strict excluded region is obtained for a shorter lifetime, as the signal selection efficiency is higher for a shorter lifetime case. In the case when the mass splitting is 50 GeV, the excluded $\tilde{\chi}_2^0/\tilde{\chi}_1^\pm$ mass reaches up to around 650 GeV when the $\tilde{\chi}_2^0$ lifetime is 0.03 ns, and around 300 GeV when the $\tilde{\chi}_2^0$ lifetime is 3 ns. For the case with smaller mass

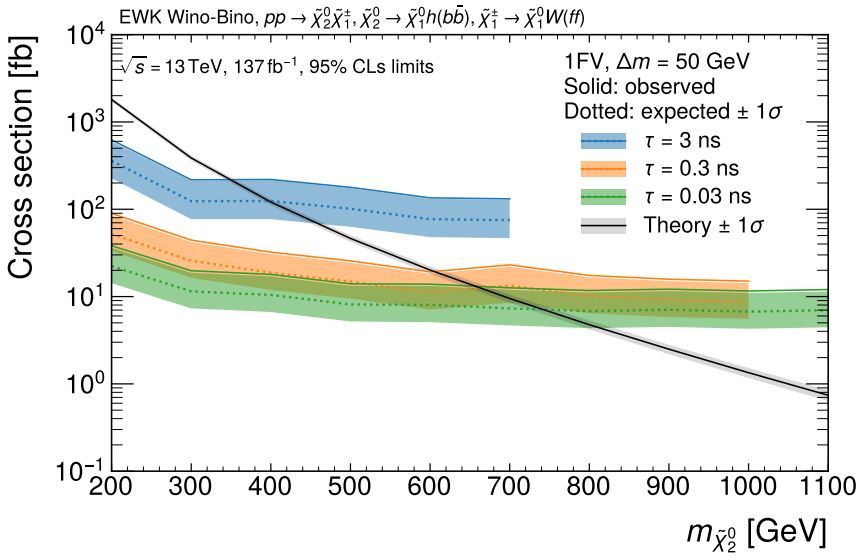

Figure 11.4: The upper limit on the cross-section for $\tilde{\chi}_1^\pm\tilde{\chi}_2^0$ production in bino-wino model as a function of $m_{\tilde{\chi}_2^0}$ with various fixed $\tau_{\tilde{\chi}_2^0}$ when $\Delta M(\tilde{\chi}_2^0, \tilde{\chi}_1^0) = 50$ GeV. The solid lines show the observed limit, and dashed lines and bands show the expected limit with $\pm 1\sigma$. The black line and band show the theoretical expectation and its uncertainty of the cross-section of the $\tilde{\chi}_1^\pm\tilde{\chi}_2^0$ pair production. The limits for $\tau_{\tilde{\chi}_2^0} = 0.3$ ns and $\tau_{\tilde{\chi}_2^0} = 3$ ns are cut off at $m_{\tilde{\chi}_2^0} = 1000$ GeV and $m_{\tilde{\chi}_2^0} = 700$ GeV respectively due to the absence of corresponding MC samples.

splitting, the exclusion limit weakens due to the loss of signal selection efficiency, resulting in the $\tilde{\chi}_2^0$ decay being less likely to produce a vertex that passes the track multiplicity and mass requirements.

Figure 11.6 shows the 95% confidence level exclusion limit on the $\tilde{\chi}_1^0$ mass as a function of ΔM lifetime with fixed lifetimes and the parameter region where the observed DM relic density is well explained drawn based on Figure 2.7. The region left side of the red line are excluded from the observed result if we assume the SUSY cross-section prediction. When $\tilde{\chi}_2^0$ lifetime is 0.03 ns, the $\tilde{\chi}_1^0$ DM in bino-wino co-annihilation model is excluded up to approximately 500 GeV. When the $\tilde{\chi}_2^0$ lifetime is 0.3 ns, only the region where $\tilde{\chi}_1^0$ mass is around 300 GeV is excluded. On the other hand, no $\tilde{\chi}_1^0$ DM mass could be excluded when the $\tilde{\chi}_2^0$ lifetime is 3 ns. Thus, this result provides some constraints on the mass of $\tilde{\chi}_1^0$ as a DM, but we would say that we are just beginning to explore interesting regions in this model from a DM perspective and there is still plenty of room for this search.

This is the first analysis that uses the special DV reconstruction method described in Section 6.2 in the ATLAS experiment. Furthermore, this is the first result that gives the limit on the bino-wino model with long-lived $\tilde{\chi}_2^0$ decaying via off-shell Higgs boson in the LHC experiments.

11.2.2 Discussion on observed events

In this analysis, not a significant but a mild excess was observed. Although the origin of this mild excess can not be solved at this stage, this section further investigates the events observed in the SR. Figure 11.7 shows their event displays with DV, jets, $E_{\mathrm{T}}^{\mathrm{miss}}$, and leptons, and the ones with tracks and seeds in

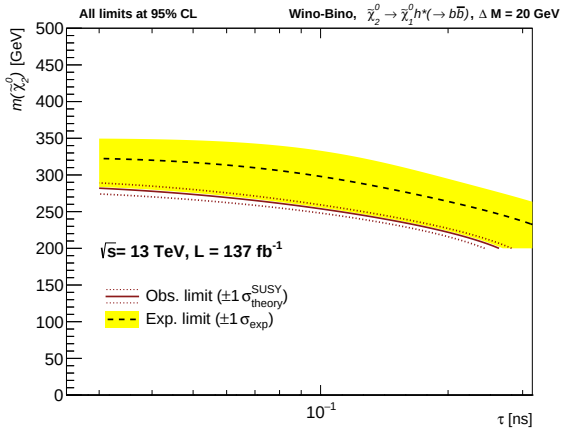

(a) $\Delta M(\tilde{\chi}_2^0, \tilde{\chi}_1^0) = 30$ GeV

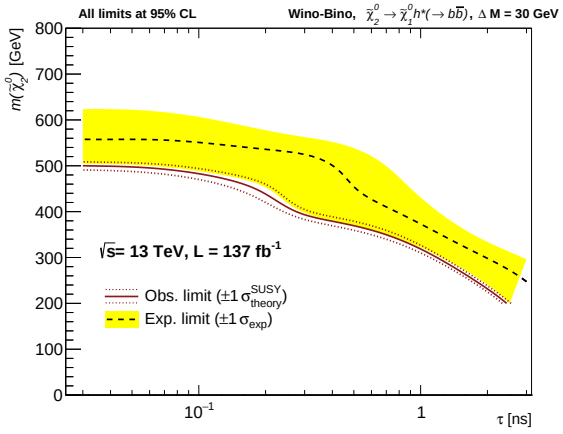

(b) $\Delta M(\tilde{\chi}_2^0, \tilde{\chi}_1^0) = 30$ GeV

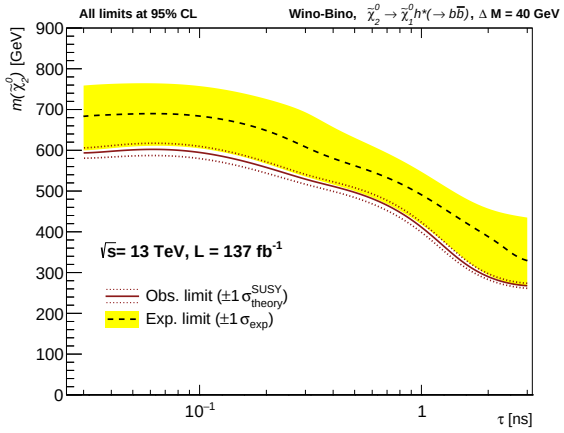

(c) $\Delta M(\tilde{\chi}_2^0, \tilde{\chi}_1^0) = 40$ GeV

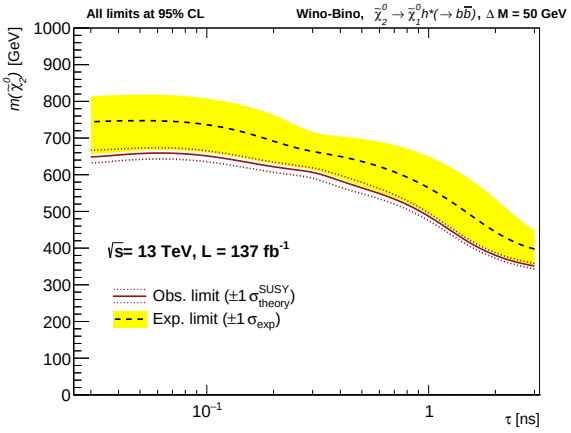

(d) $\Delta M(\tilde{\chi}_2^0, \tilde{\chi}_1^0) = 50$ GeV

Figure 11.5: 95% confidence level (CL) observed and expected exclusion limits in $\tau_{\tilde{\chi}_2^0}$ vs. $m_{\tilde{\chi}_2^0}$ plane for bino-wino model with various fixed $\Delta M(\tilde{\chi}_2^0, \tilde{\chi}_1^0)$. The region bellow the red line is excluded by the observation. The observed limit is lower than the expected limit because of a mild excess.

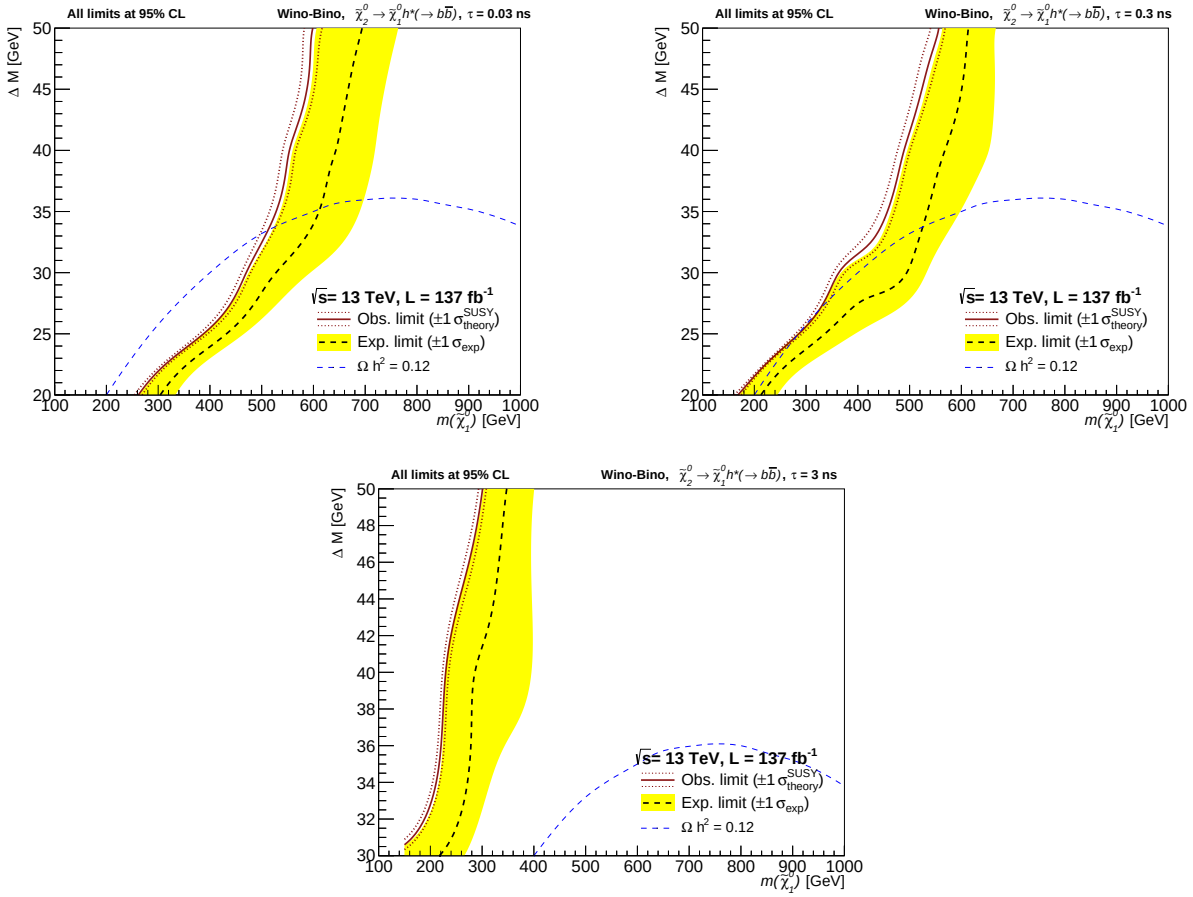

Figure 11.6: The observed and expected exclusion limits in $m_{\tilde{\chi}_1^0}$ vs. ΔM plane for bino-wino model with various fixed $m_{\tilde{\chi}_2^0}$. The region left side of the red line is excluded by the observation. The blue dashed showing the region where the observed DM relic is well explained is drawn by eyeballing the line in Figure 2.7.

Table 11.1: Parameters and expected yields of the signal events used to compare with the observed events.

$m_{\tilde{\chi}_2^0}$ [GeV], ΔM [GeV], $\tau_{\tilde{\chi}_2^0}$ [ns]	Expected signal yields
(600, 30, 0.03)	2.77
(600, 30, 0.3)	1.49
(300, 30, 2)	2.53
(800, 50, 0.03)	2.58
(700, 50, 0.3)	2.64

the DV.

Looking at Table 10.1 and Figure 11.7, among the tracks in the DV in Event#1, all tracks except #5 have similar directions to a prompt b-tagged jet, and the track #5 intersects with a large angle to others. It is likely to be a background event with a DV in which an accidental track intersected with a b-hadron. However, since the DVs of signal events may also have a similar characteristics, it impossible to determine whether event #1 is a signal or a background event. Events #2 and #3 do not have any particular characteristics that make them seem like signal or background events.

The physics objects other than DVs are also compared with other regions. Figure 11.8 compares the event quantities related to the $E_{\mathrm{T}}^{\mathrm{miss}}$ or jets between the events observed in the whole MTR, VRVeryLow-Mass, and SR. The events observed in the SR have fairly typical $E_{\mathrm{T}}^{\mathrm{miss}}$ and jet characteristics in the MTR. Therefore, nothing is significantly inconsistent in considering this mild excess as a statistical fluctuation in background events.

On the other hand, if we assume that this mild excess is of signal origin, the model whose estimated yield is around two events is likely to be preferred. Several bino-wino model parameters which would yield similar number of events are picked up, and the distributions of $E_{\mathrm{T}}^{\mathrm{miss}}$ and DV variables of SR events are compared. Table 11.1 lists the picked-up signal MC samples. Figure 11.9 shows the distributions of $E_{\mathrm{T}}^{\mathrm{miss}}$, DV track multiplicity (N_{tracks}), DV invariant mass (m_{DV}), and DV radial position (R_{xy}) in the data and signal MC samples in the SR. The peak of the $E_{\mathrm{T}}^{\mathrm{miss}}$ distribution of the signal events tends to be slightly higher than the observed three events in the data. The DVs in all observed events in the data have exactly five tracks, and all picked-up signal samples are most likely to have five tracks as well. Additionally, the $m_{\mathrm{DV}}$of the observed events is slightly higher than the peak of the m_{DV}distribution of any signal samples. Both data and signal samples tend to have a mass close to the threshold (10 GeV). N_{tracks} and m_{DV} have similar distributions for any signal model currently under consideration. In contrast, the shape of R_{xy} distribution changes depending on the $\tilde{\chi}_2^0$ lifetime. The R_{xy} distribution of the observed events in data is more similar to that of signal models with shorter than longer lifetimes.

11.3 Possible future improvements

The LHC Run 3 operation has started in July 2022, and is planned to continue by 2025 or later. In Run 3, in addition to the increase in statistics of the collected data, there are many possible improvements that achieve the better sensitivity in the DV search.

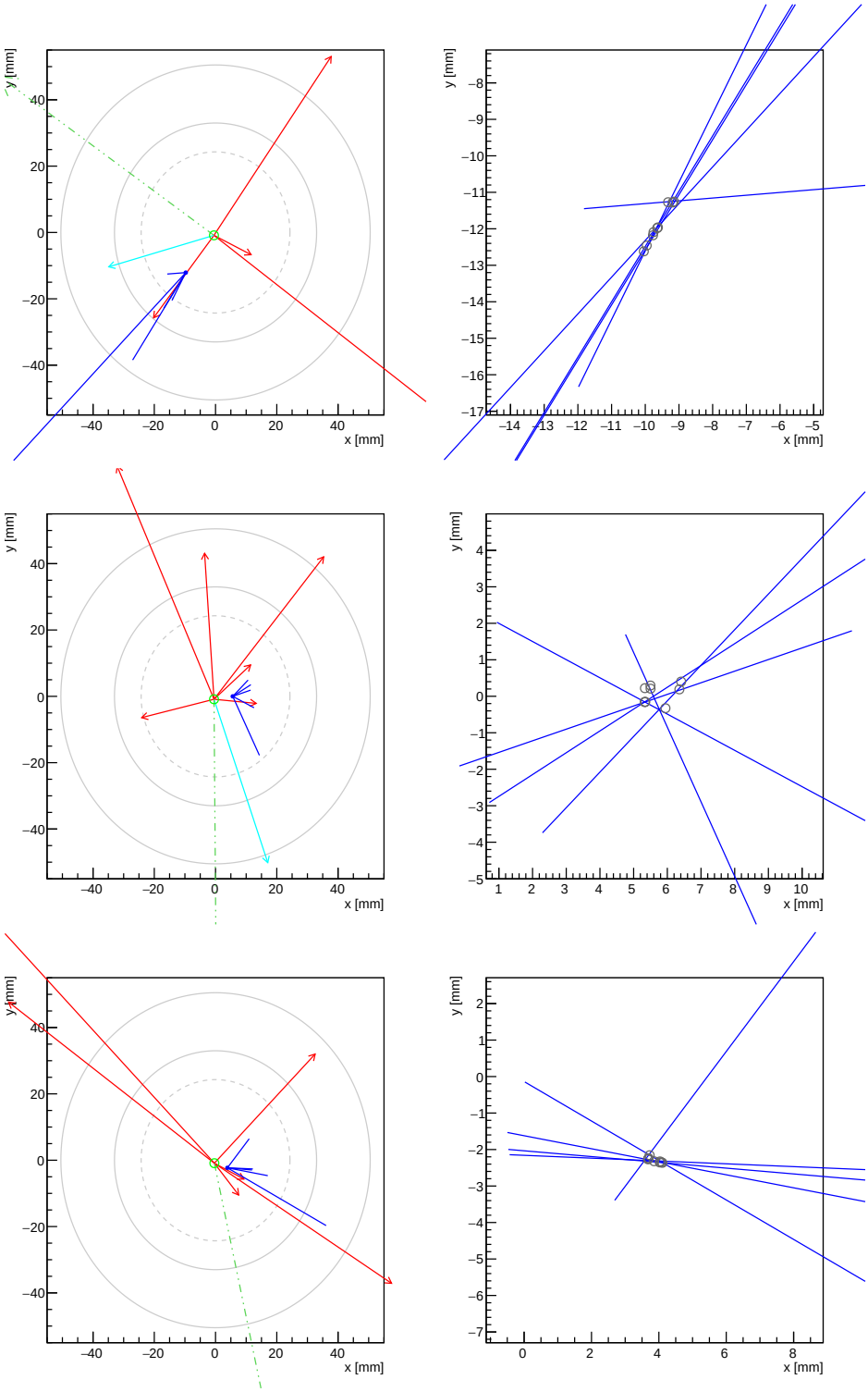

Figure 11.7: Object distribution (left) and track/seed distribution (right) in the x-y plane of the observed three events (top, middle, bottom). The blue lines show the tracks belonging to the DV. In the left figures, red, green, and cyan lines show jets, $E_{\mathrm{T}}^{\mathrm{miss}}$, and muons, respectively. The line length is proportional to the object's p_{T}. The gray dashed and solid circles are the beam pipe and Pixel layers. In the right figures, the positions of the DV seeds are shown in dark-gray points.

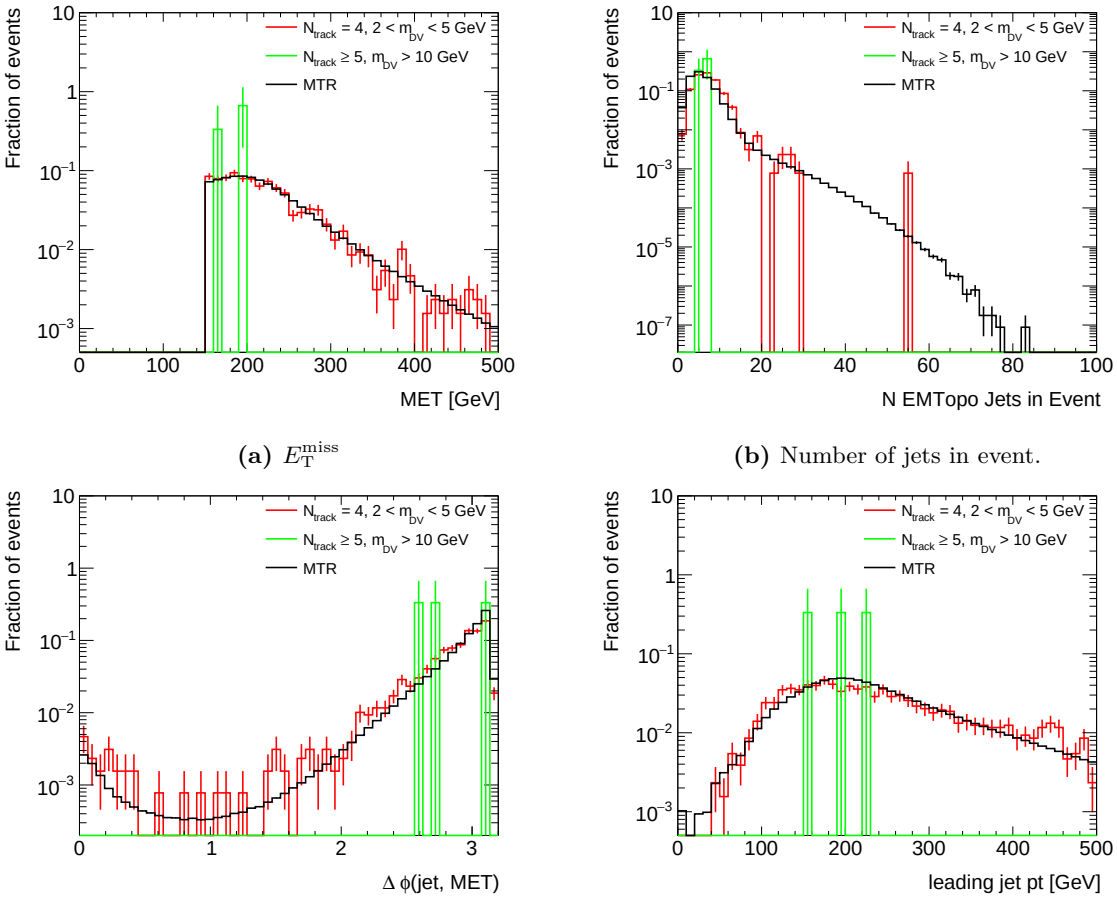

(a) $E_{\mathrm{T}}^{\mathrm{miss}}$

(b) Number of jets in event.

(c) $\Delta\phi$ between $E_{\mathrm{T}}^{\mathrm{miss}}$ and the leading jet.

(d) Leading jet p_{T}.

Figure 11.8: Event level quantities in the observed three events (green) comparing with all events in the MTR (black) and events in the VRVeryLowMass (red).

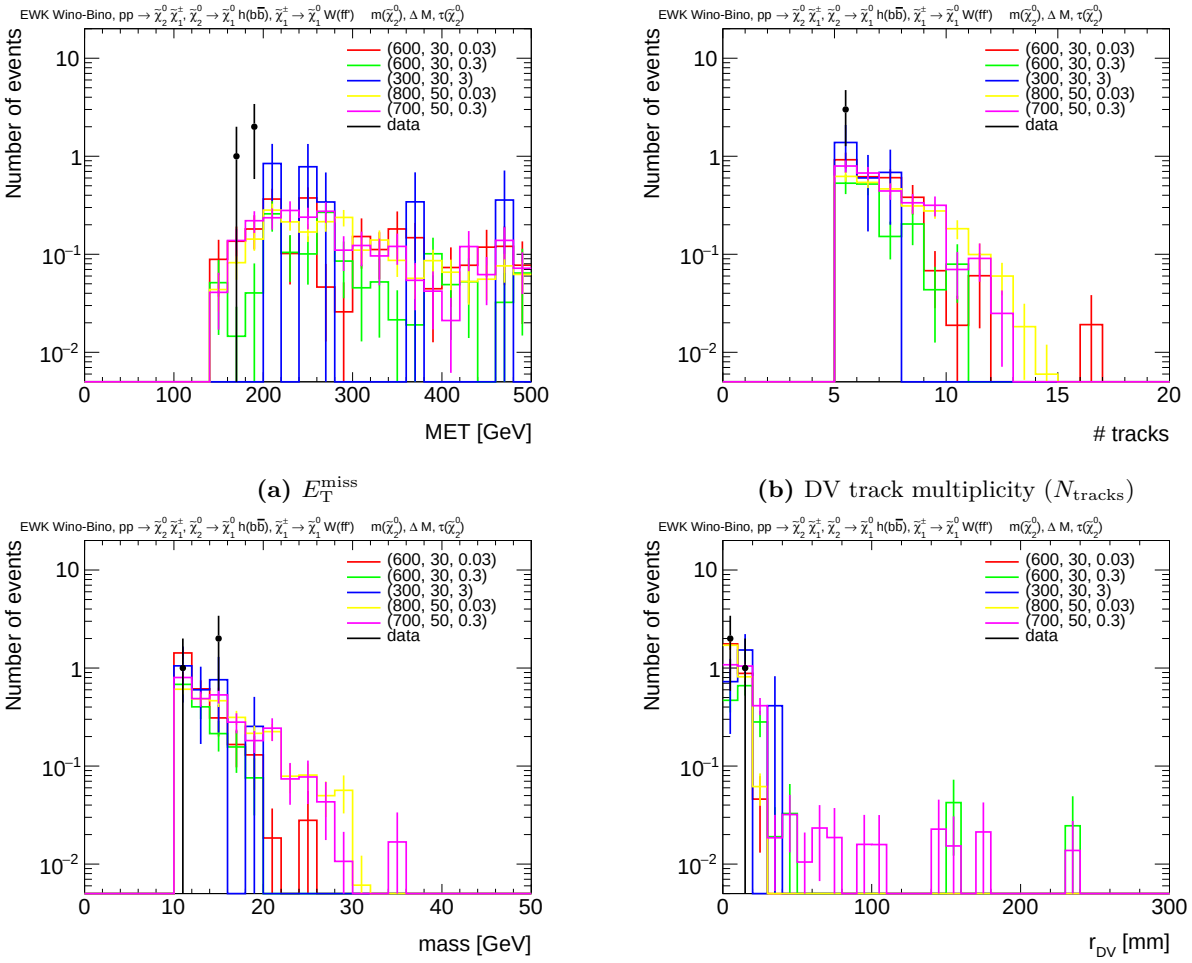

(a) $E_{\mathrm{T}}^{\mathrm{miss}}$

(b) DV track multiplicity (N_{tracks})

(c) DV invariant mass (m_{DV})

(d) DV radial position (R_{xy})

Figure 11.9: $E_{\mathrm{T}}^{\mathrm{miss}}$ and DV variables of the data and various signal samples in the SR.

Updated large radius tracking

An updated large radius tracking algorithm has been used since the beginning of Run 3 [99]. This improvement suppresses the reconstruction of fake tracks from incorrect combinations of hits significantly, enabling the large radius tracking to be run on the whole dataset. Therefore, we can eliminate the restrictions on available data from the `DRAW_RPVLL` filter and use more data. The fewer fake tracks will reduce the background DVs with a fake track as well. The search presented in this thesis uses a DV-track selection to suppress signal-like background DVs which has a non-negligible effects on the signal DVs too. This selection can be loosened when using the updated large radius tracking, which potentially increases the signal selection efficiency.

Use of DV trigger

A new HLT trigger targeting DV search has been implemented in Run 3 [100]. The trigger makes use of hits not associated with the standard tracks after the fast tracking scan at the trigger stage. It triggers the events that pass the $E_{\mathrm{T}}^{\mathrm{miss}}$ or jet triggers with a jet containing a large number of non-associated hits outer layers of the ID and few on the inner layers which indicates the existence of the DVs that are not reconstructed. A BDT using the fraction of hits in the ID layers is used to distinguish the signal and background events. Since a small mass splitting between $\tilde{\chi}_2^0$ and $\tilde{\chi}_1^0$ is preferred in bino-wino model, the efficiency that the event passes $E_{\mathrm{T}}^{\mathrm{miss}}$ trigger is typically low, The use of new DV trigger may remove the current strict $E_{\mathrm{T}}^{\mathrm{miss}}$ requirement and increase the signal selection efficiency.

Improvements on the special DV analysis

The search presented in this thesis is the first analysis which uses the special DV, and there is still room for improvements. The special DV reconstruction method, especially the two-track seed merging step that is currently cut-based, could still be significantly improved. The current merging step judges whether the two seed to be merged using only a few variables, such as the seed positions, track p_{T}, and the angles between tracks. The performance of this method could be improved by using more track and seed information. Furthermore, instead of deciding whether to merge each pair of seeds one by one, as is currently done, it may be possible to perform the seed clustering from all reconstructed seeds as inputs using machine learning that can handle a variable number of inputs. The analysis procedure can be also improved. One idea is the use of the variables specific to the special DV in the DV selection. Although the special DV method achieves to reconstruct "fuzzy" instead point-like LLP decays including b-hadrons, no variable is used to indicate whether the DV is likely to contain b-hadrons. For example, the BDT score used in the two-track seed forming step can be used in the DV selection step too. Also, the variables that quantify the distribution of tracks or two-track seeds in the DV, such as the deviation of the positions of the seed vertices in the DV, may become a good discriminant that effectively separates the signal DVs without b-hadrons, the signal DVs with b-hadrons, and the background DVs.

Chapter 12

Conclusion

This thesis presents a search for a long-lived SUSY particle using data from 2016 to 2018 using the ATLAS detector. The bino-wino co-annihilation model, one of the SUSY models motivated by DM, is searched. In this model, $\tilde{\chi}_2^0$ can be long-lived due to heavy higgsino mass and small mass splitting between $\tilde{\chi}_2^0$ and $\tilde{\chi}_1^0$. This thesis focuses on the case where $\tilde{\chi}_2^0$ has a lifetime of $O(0.01)$-$O(1)$ ns, and its decay includes a b-quark pair.

If such $\tilde{\chi}_2^0$ is produced in the LHC, it leaves a secondary vertex away from the pp collision point, called displaced vertex (DV), in the final state. The ATLAS group has a standard algorithm to reconstruct DVs, but it cannot reconstruct DVs with enough track multiplicity when the decay includes b-quarks and the decay products are soft. Therefore, a new special algorithm has been developed for the decay of the ling-lived $\tilde{\chi}_2^0$ in the bino-wino model. In this method, candidates of the signal track pairs are efficiently selected using multi-variable analysis, and two-track seed vertices are reconstructed using those track pairs. Multi-track vertices are reconstructed by merging the two-track seed vertices based on some clustering conditions but without fitting. Using this special method, the probability that the DVs from the target signal events have a high track multiplicity and high mass becomes several times larger than that of the standard method. In addition to developing the DV reconstruction algorithm, a new analysis method using this special DV has been established. The signal region (SR) requires the $E_{\mathrm{T}}^{\mathrm{miss}}$ trigger and the offline $E_{\mathrm{T}}^{\mathrm{miss}}$ greater than 150 GeV and at least one reconstructed DV in the ATLAS inner detector. Even though no heavy long-lived particle exists in the SM, they can create DVs with high track multiplicity and invariant mass from the experimental effects. Since the special DV method reconstructs more background DVs than the ATLAS standard method in for the sake of a high signal selection efficiency, strict conditions are imposed not only on the characteristics of the DV but also on the tracks within the DV, which suppresses background events. As the signal DV selection, the DVs are required to have at least five tracks and invariant mass greater than 5 GeV.

A simple data-driven background estimation method using the correlation between DV and other objects is established. It estimates 0.81 ± 0.49 background events in the SR. Three events are observed in the SR, equivalent to 1.59σ excess from the estimated number of background events. The result is interpreted in the context of the bino-wino co-annihilation model. The mass of $\tilde{\chi}_2^0/\tilde{\chi}_1^{\pm}$ in the bino-wino model is excluded up to around 650 GeV for the case with $\tau = 0.03$ ns and $\Delta M = 50$ GeV at 95%

confidence level. This is the first result of the LHC experiments for the bino-wino model where $\tilde{\chi}_2^0$ is a long-lived particle. It far exceeds the current limit set by the LEP II experiments.

Although this search did not find an evidence of new physics model, it constrains them and leaves room for the physics this thesis focuses on. This result motivates further searches in Run 3, which began in July 2022. Not only the statistics of the collected data in Run 3 increases, but several new techniques to benefit the DV analysis have been developed, such as the updates on large radius tracking and the implementation of the DV trigger. This is the first search that uses a special DV reconstruction, and there is still a lot of room for improvement in both reconstruction algorithms and analysis methods, which could significantly increase the signal sensitivity.

Acknowledgments

There are so many people without whom I could not complete this thesis. I apologize for not being able to list all of them.

First, I would like to express my sincere appreciation to my supervisor, Professor Osamu Jinnouchi. Through my seven and a half years in Jinnouchi Lab, I obtained a wide range of knowledge, skills, and experience. I really appreciate that he took the time to discuss my study with me, give me a lot of feedback and ideas, and review my thesis despite his super busy schedule. Thanks to him, I was able to keep pursuing the topic I wanted to tackle halfway through.

I would like to show my gratitude to the SUSY DV team. I am thrilled to have been working in such an incredible team. If I hadn't participated with you, I wouldn't have enjoyed my study so much. In particular to Christian Ohm and Simone Pagan Griso, the former SUSY DV analysis conveners, thank you for all your follow-ups as I worked on the DV analysis. Also, in particular, Evan Carlson, David Rousso, and Benjamin John Rosser, the DV+MET analysis contacts, thank you for leading the team and working with me on so many parts of the analysis.

I would like to express my gratitude to Hideyuki Oide, the former assistant professor of Jinnouchi Lab. and LLP analysis expert. He gave me a starting point to begin this topic and various knowledge. I would also like to thank him for his follow-up comments at the SUSY DV group meetings, as well as for his many suggestions and technical support on my topic.

I would like to show my gratitude to Kazuki Todome, the assistant professor and the great senior member of Jinnouchi Lab. He often had discussions with me and gave me many suggestions. In addition, he encouraged me and gave me advice when I could not make progress as planned.

I would like to thank Yohei Yamaguchi, the former assistant professor of Tokyo Tech ATLAS group. I appreciate that he attended the ATLAS analysis meeting in Tokyo Tech and had discussions on my topic every week.

I would like to thank the ATLAS Pixel detector team for working with me on the Pixel DQ and Pixel timing analysis. In particular to Yosuke Takubo and Soshi Tsuno, thank you for supervising my qualification task and meny technical support on it, as well as follow-ups when I stayed at CERN.

I would like to thank Professor Masahiro Kuze, my sub-supervisor, for his interesting lectures and discussions, as well as occasional comments and advice on my study.

I would like to thank the members of Jinnochi Lab, who are very fun and made my lab. life enjoyable. Especially to Arisa Kubota, who was the same year student as me in Jinnouchi Lab. We have been helping and enjoying each other since we were undergraduate students.

This work was supported by JSPS KAKENHI Grant Number 202113788.

Lastly, I would like to thank my family. It is thanks to their supports that I was able to concentrate on my study and live a comfortable life.

Bibliography

[1] Sheldon L. Glashow. Partial-symmetries of weak interactions. *Nuclear Physics*, 22(4):579–588, 1961.

[2] Steven Weinberg. A model of leptons. *Phys. Rev. Lett.*, 19:1264–1266, Nov 1967.

[3] Abdus Salam. Weak and Electromagnetic Interactions. *Conf. Proc. C*, 680519:367–377, 1968.

[4] Murray Gell-Mann. A Schematic Model of Baryons and Mesons. *Phys. Lett.*, 8:214–215, 1964.

[5] Georges Aad et al. Observation of a new particle in the search for the Standard Model Higgs boson with the ATLAS detector at the LHC. *Phys. Lett. B*, 716:1–29, 2012.

[6] Serguei Chatrchyan et al. Observation of a New Boson at a Mass of 125 GeV with the CMS Experiment at the LHC. *Phys. Lett. B*, 716:30–61, 2012.

[7] F. Zwicky. On the Masses of Nebulae and of Clusters of Nebulae. *Astrophys. J.*, 86:217–246, 1937.

[8] V C Rubin and W K Ford, Jr. Rotation of the andromeda nebula from a spectroscopic survey of emission regions. *Astrophys. J. 159: 379-403(Feb 1970).*, 1 1970.

[9] Vera C. Rubin, W. Kent Ford, and Norbert Thonnard. Rotational properties of 21 sc galaxies with a large range of luminosities and radii, from ngc 4605 /r = 4kpc/ to ugc 2885 /r = 122 kpc/. *The Astrophysical Journal*, 238:471–487, 1980.

[10] Richard Massey, Thomas Kitching, and Johan Richard. The dark matter of gravitational lensing. *Rept. Prog. Phys.*, 73:086901, 2010.

[11] Douglas Clowe, Maruš a Bradač, Anthony H. Gonzalez, Maxim Markevitch, Scott W. Randall, Christine Jones, and Dennis Zaritsky. A direct empirical proof of the existence of dark matter. *The Astrophysical Journal*, 648(2):L109–L113, 2006.

[12] N. Aghanim et al. Planck 2018 results. VI. Cosmological parameters. *Astron. Astrophys.*, 641:A6, 2020.

[13] Krzysztof Rolbiecki and Kazuki Sakurai. Long-lived bino and wino in supersymmetry with heavy scalars and higgsinos. *Journal of High Energy Physics*, 2015(11), 2015.

[14] Natsumi Nagata, Hidetoshi Otono, and Satoshi Shirai. Probing bino-wino coannihilation at the LHC. *Journal of High Energy Physics*, 2015(10), 2015.

[15] Andrew Purcell. Go on a particle quest at the first CERN webfest. Le premier webfest du CERN se lance à la conquête des particules. (35/2012):10, 2012.

[16] A. D. Martin, W. J. Stirling, R. S. Thorne, and G. Watt. Parton distributions for the LHC. *The European Physical Journal C*, 63(2):189–285, 2009.

[17] Stephen P. Martin. A Supersymmetry primer. *Adv. Ser. Direct. High Energy Phys.*, 18:1–98, 1998.

[18] Glennys R. Farrar and Pierre Fayet. Phenomenology of the Production, Decay, and Detection of New Hadronic States Associated with Supersymmetry. *Phys. Lett. B*, 76:575–579, 1978.

[19] A. Arbey, M. Boudaud, F. Mahmoudi, and G. Robbins. Robustness of dark matter constraints and interplay with collider searches for new physics. *Journal of High Energy Physics*, 2017(11), 2017.

[20] https://lepsusy.web.cern.ch/lepsusy/www/inoslowdmsummer02/charginolowdm_pub.html.

[21] Georges Aad et al. Search for chargino–neutralino pair production in final states with three leptons and missing transverse momentum in $\sqrt{s} = 13$ TeV pp collisions with the ATLAS detector. *Eur. Phys. J. C*, 81(12):1118, 2021.

[22] Lhc susy cross section working group. https://twiki.cern.ch/twiki/bin/view/LHCPhysics/SUSYCrossSections#Cross_sections_for_various_s_AN1.

[23] Lyndon Evans and Philip Bryant. LHC Machine. *JINST*, 3:S08001, 2008.

[24] G Aad et al. The ATLAS Experiment at the CERN Large Hadron Collider. *JINST*, 3:S08003, 2008.

[25] Ewa Lopienska. The CERN accelerator complex, layout in 2022. Complexe des accélérateurs du CERN en janvier 2022. 2022. General Photo.

[26] G. Aad et al. Luminosity determination in *pp* collisions at $\sqrt{s} = 13$ TeV using the ATLAS detector at the LHC. *Eur. Phys. J. C*, 83(10):982, 2023.

[27] R. Bruce, N. Fuster-Martínez, A. Mereghetti, D. Mirarchi, and S. Redaelli. Review of LHC Run 2 Machine Configurations. In *9th LHC Operations Evian Workshop*, pages 187–197, Geneva, Switzerland, 2019.

[28] ATLAS collaboration. Public ATLAS Luminosity Results for Run-2 of the LHC. https://twiki.cern.ch/twiki/bin/view/AtlasPublic/LuminosityPublicResultsRun2.

[29] Joao Pequenao. Computer generated image of the whole ATLAS detector. 2008.

[30] ATLAS Magnet Group. Atlas magnet system. http://atlas.web.cern.ch/Atlas/GROUPS/MUON/magfield/.

[31] Joao Pequenao. Computer generated image of the ATLAS inner detector. 2008.

[32] ATLAS Collaboration. Study of the material of the ATLAS inner detector for Run 2 of the LHC. *JINST*, 12:P12009, 2017.

[33] M Capeans, G Darbo, K Einsweiller, M Elsing, T Flick, M Garcia-Sciveres, C Gemme, H Pernegger, O Rohne, and R Vuillermet. ATLAS Insertable B-Layer Technical Design Report. Technical report, 2010.

[34] ATLAS Insertable B-Layer Technical Design Report Addendum. Technical report, 2012. Addendum to CERN-LHCC-2010-013, ATLAS-TDR-019.

[35] Azriel Rosenfeld and John L. Pfaltz. Sequential operations in digital picture processing. *J. ACM*, 13:471–494, 1966.

[36] B. Abbott et al. Production and Integration of the ATLAS Insertable B-Layer. *JINST*, 13(05):T05008, 2018.

[37] *ATLAS inner detector: Technical Design Report, 1.* Technical design report. ATLAS. CERN, Geneva, 1997.

[38] Joao Pequenao. Computer Generated image of the ATLAS calorimeter. 2008.

[39] Joao Pequenao. Computer generated image of the ATLAS Muons subsystem. 2008.

[40] Standard Model Summary Plots February 2022. Technical report, CERN, Geneva, 2022.

[41] R Achenbach et al. The ATLAS Level-1 Calorimeter Trigger. Technical report, CERN, Geneva, 2008.

[42] F Anulli et al. The level-1 trigger muon barrel system of the atlas experiment at cern. 4(04):P04010, apr 2009.

[43] Rosa Simoniello. The atlas level-1 topological processor: from design to routine usage in run-2. In *2018 IEEE Nuclear Science Symposium and Medical Imaging Conference Proceedings (NSS/MIC)*, pages 1–4, 2018.

[44] Performance of the ATLAS Trigger System in 2015. Performance of the ATLAS Trigger System in 2015. *Eur. Phys. J. C*, 77(5):317, 2017.

[45] Performance of the missing transverse momentum triggers for the ATLAS detector during run-2 data taking. *Journal of High Energy Physics*, 2020(8), aug 2020.

[46] W Lampl, S Laplace, D Lelas, P Loch, H Ma, S Menke, S Rajagopalan, D Rousseau, S Snyder, and G Unal. Calorimeter Clustering Algorithms: Description and Performance. Technical report, CERN, Geneva, 2008.

[47] Georges Aad et al. Performance of the missing transverse momentum triggers for the ATLAS detector during Run-2 data taking. *JHEP*, 08:080, 2020.

[48] T. Golling, H. S. Hayward, P. U. E. Onyisi, H. J. Stelzer, and P. Waller. The ATLAS Data Quality Defect Database System. *Eur. Phys. J. C*, 72:1960, 2012.

[49] Georges Aad et al. ATLAS data quality operations and performance for 2015–2018 data-taking. *JINST*, 15(04):P04003, 2020.

[50] Gavin P. Salam. Elements of QCD for hadron colliders. In *2009 European School of High-Energy Physics*, 11 2010.

[51] J. Alwall, R. Frederix, S. Frixione, V. Hirschi, F. Maltoni, O. Mattelaer, H. S. Shao, T. Stelzer, P. Torrielli, and M. Zaro. The automated computation of tree-level and next-to-leading order differential cross sections, and their matching to parton shower simulations. *JHEP*, 07:079, 2014.

[52] Richard D. Ball, Valerio Bertone, Stefano Carrazza, Christopher S. Deans, Luigi Del Debbio, Stefano Forte, Alberto Guffanti, Nathan P. Hartland, José I. Latorre, Juan Rojo, and Maria Ubiali. Parton distributions with lhc data. *Nuclear Physics B*, 867(2):244–289, 2013.

[53] Pierre Artoisenet, Rikkert Frederix, Olivier Mattelaer, and Robbert Rietkerk. Automatic spin-entangled decays of heavy resonances in Monte Carlo simulations. *JHEP*, 03:015, 2013.

[54] Torbjörn Sjöstrand, Stefan Ask, Jesper R. Christiansen, Richard Corke, Nishita Desai, Philip Ilten, Stephen Mrenna, Stefan Prestel, Christine O. Rasmussen, and Peter Z. Skands. An introduction to PYTHIA 8.2. *Comput. Phys. Commun.*, 191:159–177, 2015.

[55] ATLAS Pythia 8 tunes to 7 TeV data. Technical report, CERN, Geneva, 2014.

[56] Tania Robens, Tim Stefaniak, and Jonas Wittbrodt. Two-real-scalar-singlet extension of the SM: LHC phenomenology and benchmark scenarios. *Eur. Phys. J. C*, 80(2):151, 2020.

[57] Enrico Bothmann et al. Event Generation with Sherpa 2.2. *SciPost Phys.*, 7(3):034, 2019.

[58] Richard D. Ball et al. Parton distributions for the LHC Run II. *JHEP*, 04:040, 2015.

[59] The Pythia 8 A3 tune description of ATLAS minimum bias and inelastic measurements incorporating the Donnachie-Landshoff diffractive model. Technical report, CERN, Geneva, 2016.

[60] G. Aad et al. The ATLAS Simulation Infrastructure. *Eur. Phys. J. C*, 70:823–874, 2010.

[61] S. Agostinelli et al. Geant4—a simulation toolkit. *Nuclear Instruments and Methods in Physics Research Section A: Accelerators, Spectrometers, Detectors and Associated Equipment*, 506(3):250–303, 2003.

[62] Andreas Salzburger and on behalf of the ATLAS Collaboration. Optimisation of the atlas track reconstruction software for run-2. *Journal of Physics: Conference Series*, 664(7):072042, dec 2015.

[63] T Cornelissen, M Elsing, I Gavrilenko, W Liebig, E Moyse, and A Salzburger. The new atlas track reconstruction (newt). *Journal of Physics: Conference Series*, 119(3):032014, jul 2008.

[64] R. Frühwirth. Application of kalman filtering to track and vertex fitting. *Nuclear Instruments and Methods in Physics Research Section A: Accelerators, Spectrometers, Detectors and Associated Equipment*, 262(2):444–450, 1987.

[65] Performance of the reconstruction of large impact parameter tracks in the ATLAS inner detector. Technical report, CERN, Geneva, 2017.

[66] Federico Meloni. Primary vertex reconstruction with the ATLAS detector. *JINST*, 11(12):C12060, 2016.

[67] S Boutle, D Casper, B Hooberman, K Grimm, B Gui, G Lee, J Maurer, A Morley, S Pagan Griso, B Petersen, K Prokofiev, L Shan, D Shope, A Wharton, B Whitmore, M Zhang, and on behalf of the ATLAS Collaboration. Primary vertex reconstruction at the atlas experiment. *Journal of Physics: Conference Series*, 898(4):042056, oct 2017.

[68] Matteo Cacciari, Gavin P. Salam, and Gregory Soyez. The anti-k_t jet clustering algorithm. *JHEP*, 04:063, 2008.

[69] M. Aaboud et al. Jet energy scale measurements and their systematic uncertainties in proton-proton collisions at $\sqrt{s} = 13$ TeV with the ATLAS detector. *Phys. Rev. D*, 96(7):072002, 2017.

[70] Jet energy scale and resolution measured in proton-proton collisions at tev with the atlas detector. https://atlas.web.cern.ch/Atlas/GROUPS/PHYSICS/PAPERS/JETM-2018-05/.

[71] Matteo Cacciari and Gavin P. Salam. Pileup subtraction using jet areas. *Phys. Lett. B*, 659:119–126, 2008.

[72] Tagging and suppression of pileup jets with the ATLAS detector. Technical report, CERN, Geneva, 2014.

[73] Forward Jet Vertex Tagging: A new technique for the identification and rejection of forward pileup jets. Technical report, CERN, Geneva, 2015.

[74] Commissioning of the ATLAS high-performance b-tagging algorithms in the 7 TeV collision data. Technical report, CERN, Geneva, 2011.

[75] G Piacquadio and C Weiser. A new inclusive secondary vertex algorithm for b-jet tagging in atlas. 119(3):032032, jul 2008.

[76] Optimisation and performance studies of the ATLAS b-tagging algorithms for the 2017-18 LHC run. Technical report, CERN, Geneva, 2017.

[77] Georges Aad et al. Topological cell clustering in the ATLAS calorimeters and its performance in LHC Run 1. *Eur. Phys. J. C*, 77:490, 2017.

[78] E. Hines. Performance of Particle Identification with the ATLAS Transition Radiation Tracker. In *Meeting of the APS Division of Particles and Fields*, 9 2011.

[79] Morad Aaboud et al. Electron reconstruction and identification in the ATLAS experiment using the 2015 and 2016 LHC proton-proton collision data at $\sqrt{s} = 13$ TeV. *Eur. Phys. J. C*, 79(8):639, 2019.

[80] Georges Aad et al. Electron and photon performance measurements with the ATLAS detector using the 2015–2017 LHC proton-proton collision data. *JINST*, 14(12):P12006, 2019.

[81] Muon reconstruction and identification efficiency in ATLAS using the full Run 2 *pp* collision data set at $\sqrt{s} = 13$ TeV. *Eur. Phys. J., C*, 81:578, 2021. 64 pages in total, author list starting page 42, auxiliary material starting at page 59, 34 figures, 3 tables. All figures including auxiliary figures are available at https://atlas.web.cern.ch/Atlas/GROUPS/PHYSICS/PAPERS/MUON-2018-03/.

[82] Performance of vertex reconstruction algorithms for detection of new long-lived particle decays within the ATLAS inner detector. Technical report, CERN, Geneva, 2019.

[83] V Kostyukhin. VKalVrt - package for vertex reconstruction in ATLAS. Technical report, CERN, Geneva, 2003. revised version number 1 submitted on 2003-09-24 11:10:53.

[84] S.R. Das. On a new approach for finding all the modified cut-sets in an incompatibility graph. *IEEE Transactions on Computers*, C-22(2):187–193, 1973.

[85] Andreas Hoecker et al. TMVA - Toolkit for Multivariate Data Analysis, 2007.

[86] Morad Aaboud et al. Search for long-lived, massive particles in events with displaced vertices and missing transverse momentum in $\sqrt{s} = 13$ TeV *pp* collisions with the ATLAS detector. *Phys. Rev. D*, 97(5):052012, 2018.

[87] Georges Aad et al. Characterisation and mitigation of beam-induced backgrounds observed in the ATLAS detector during the 2011 proton-proton run. *JINST*, 8:P07004, 2013.

[88] Selection of jets produced in 13TeV proton-proton collisions with the ATLAS detector. Technical report, CERN, Geneva, 2015.

[89] Emma Sian Kuwertz et al. ATLAS Data Quality Operations and Performance during Run 2. Technical report, CERN, Geneva, 2019.

[90] Georges Aad et al. Search for long-lived, massive particles in events with a displaced vertex and a muon with large impact parameter in *pp* collisions at $\sqrt{s} = 13$ TeV with the ATLAS detector. *Phys. Rev. D*, 102(3):032006, 2020.

[91] Search for long-lived, massive particles in events with displaced vertices and multiple jets in pp collisions at $\sqrt{s} = 13$ TeV with the ATLAS detector. 2022.

[92] Georges Aad et al. Search for exotic decays of the Higgs boson into long-lived particles in *pp* collisions at $\sqrt{s} = 13$ TeV using displaced vertices in the ATLAS inner detector. *JHEP*, 11:229, 2021.

[93] Early Inner Detector Tracking Performance in the 2015 data at $\sqrt{s} = 13$ TeV. 2015.

[94] Robert D. Cousins. Lectures on Statistics in Theory: Prelude to Statistics in Practice. 7 2018.

[95] Glen Cowan, Kyle Cranmer, Eilam Gross, and Ofer Vitells. Asymptotic formulae for likelihood-based tests of new physics. *Eur. Phys. J. C*, 71:1554, 2011. [Erratum: Eur.Phys.J.C 73, 2501 (2013)].

[96] Alexander L. Read. Presentation of search results: The CL_s technique. *J. Phys. G*, 28:2693–2704, 2002.

[97] Matthew Feickert, Lukas Heinrich, and Giordon Stark. pyhf: a pure-Python statistical fitting library with tensors and automatic differentiation. *PoS*, ICHEP2022:245, 11 2022.

[98] Lukas Heinrich, Matthew Feickert, and Giordon Stark. pyhf: v0.7.6. https://github.com/scikit-hep/pyhf/releases/tag/v0.7.6.

[99] Georges Aad et al. Performance of the reconstruction of large impact parameter tracks in the inner detector of ATLAS. *Eur. Phys. J. C*, 83(11):1081, 2023.

[100] Georges Aad et al. The ATLAS Trigger System for LHC Run 3 and Trigger performance in 2022. *JINST*, 19:P06029, 2024.

List of Figures

2.1 Elementary particles in the SM [15]. Graviton is not included in the SM. 4
2.2 One-loop correction to the m_H from a fermion f. 6
2.3 One-loop correction to the m_H from a scalar particle S. 7
2.4 DM relic density depending on the LSP type [19]. 'Mixed' means the case where DM is composed of any combination of bino, higgsiono, and wino. 10
2.5 Mass spectrum of gauginos in bino-wino co-annihilation scenario. 11
2.6 Contributions to the co-annihilation of dark matter $\tilde{\chi}_1^0$ LSPs with slightly heavier $\tilde{\chi}_2^0$ and $\tilde{\chi}_1^\pm$. 11
2.7 The relation between the DM relic density (blue dashed line) and bino mass ($M_{\tilde{B}^0}$) and mass difference between bino and wino ($M_{\tilde{W}^0} - M_{\tilde{B}^0}$) [14]. The black and red lines show the decay length of $\tilde{W}^0$ with fixed μ and $\tan\beta$. Equation 2.23 is an approximation of the formula used to calculate these decay lengths. 12
2.8 Diagrams contributing to $\tilde{W}^\pm \to f'\bar{f}\ \tilde{B}^0$. The coupling is proportional to $g/|\mu|$. 13
2.9 Diagrams contributing to $\tilde{W}^0 \to f\bar{f}\ \tilde{B}^0$. The coupling of $\tilde{W}^0$–$\tilde{B}^0$–h^* is proportional to $m_f/|\mu|$ and the coupling of $\tilde{W}^0$–$\tilde{B}^0$–Z^* is proportional to $g/|\mu|^2$. While Higgs mediated decay needs a $\tilde{h}^0$-$\tilde{W}^0$ or $\tilde{h}^0$-$\tilde{B}^0$ mixing, Z boson mediated decay needs both $\tilde{h}^0$-$\tilde{W}^0$ mixing and $\tilde{h}^0$-$\tilde{B}^0$ mixing. 13
2.10 The decay width of $\tilde{\chi}_2^0$ as a function of μ with $\Delta M = 20$, 50 GeV and $\tan\beta = 2$, 10. The black line, red line, and blue lines show the total, Higgs boson mediated, and Z-boson mediated decay width. The range between around the green and pink lines corresponds the lifetime where the decay would occur in the ATLAS inner detector. The structure of the ATLAS detector is described in Chapter 3. 14
2.11 Current exclusion limits obtained for the WZ-mediated models in the bino-wino co-annihilation scenario by the ATLAS Experiment [21]. 15
2.12 Diagram of the pair production of electrowikinos $\tilde{\chi}_2^0\tilde{\chi}_1^\pm$ decaying to $\tilde{\chi}_1^0$ via off-shell W-boson and Higgs boson. The off-shell Higgs decays into any pair of fermions with a mass less than itself. In the case of ΔM of a few tens of GeV, which is the target of this thesis, the dominant decay mode is the b-quark pair. 16
2.13 Topology of the signal event with an ISR jet. 16
2.14 Production cross-section of SUSY particles [22]. The cross section of the signal event is calculated based on the pink line. 17

3.1 Accelerator complex at CERN [25]. . . . 19
3.2 The integrated and peak luminosity (top), the β^* and beam crossing angle (middle), and the bunch luminosity and the number of bunches (bottom) during Run 2 [27]. . . . 20
3.3 The number of pp interactions per bunch crossing in 2015-2018 [28]. . . . 21
3.4 Overview of the ATLAS detector [29]. It consists of the inner detector, calorimeters, muon detector, and magnet system. . . . 22
3.5 ATLAS coordinate system. . . . 23
3.6 Illustration of the ATLAS magnet system [30]. The inner cylinder shows the solenoid, and the outer rings show the toroids. . . . 23
3.7 Particle trajectories. (a)Charged particles passing through the inner detector. (b)Muon passing through the toroidal magnet region. . . . 24
3.8 Cut-away view of the inner detector [31]. . . . 25
3.9 R-z cross-sectional view of the inner detector. The upper part shows 1/4 of the inner detector, and the bottom shows a zoomed view of the Pixel detector [32]. . . . 25
3.10 ToT. It becomes larger proportional to the signal pulse height. . . . 27
3.11 Pixel cluster. The red shade shows the magnitude of charge collected by each pixel. The average pixel position weighted by the collected charge shown by a star is assumed to be the position where the charged particle passes. . . . 27
3.12 Cut-away view of the ATLAS calorimeter [38]. The electromagnetic calorimeter, which measures electron and photon energies, is located inside, and the hadron calorimeter, which measures quark and gluon jet energies, is located outside. . . . 29
3.13 Cut-away view of the ATLAS muon detector [39]. The barrel region consists of MDT and RPC, and the endcap region consists of CSC and TGC. . . . 29
3.14 Predicted and measured cross-sections of the SM processes in pp collision in the LHC [40]. Each line shows a theoretical prediction of the cross-section of each process, and each point shows the measurement by ATLAS. . . . 30
3.15 The ATLAS trigger system [44]. The L1 trigger is formed by the Central Trigger Processor (CTP), which receives input from the calorimeter and muon detectors. The events that pass the L1 trigger are then buffered in the Readout System (ROS) and processed by the HLT. The events that pass the HLT are transferred to the data storage. . . . 31
3.16 Rates of various HLTs as a function of $\langle\mu\rangle$ in each year [47]. . . . 33

4.1 Fraction of data flagged as bad in each sub-detector [49]. . . . 35
4.2 Total integrated luminosity delivered by the LHC ('LHC delivered'), recorded by ATLAS ('ATLAS recorded') and available for physics analyses ('Good for physics') in 2015-2018 [28]. The integrated luminosity of "Good for physics" is 139 fb^{-1} in this figure but has been re-calculated as 140 fb^{-1} [26]. . . . 36
4.3 Schematics of the event generation process. . . . 37
4.4 Theoretical calculation of the branching ratio of Higgs boson with various mass [56]. . . . 37
4.5 Feynman diagram (left) and event topology (right) of $Z \to \nu\bar{\nu}$ + jets event. . . . 38

5.1 Relation between the objects. Objects in boxes on the right are used in the signal region selection. Events are not required to have jets, but events with jets satisfying certain criteria are excluded. Furthermore, events are not required to have photons, but DVs are required to be away from photons. 41
5.2 Schematic of the track parameters at the perigee (P). 42
5.3 Schematic figure of track finding procedure. (a)Track seeds are build from three consecutive space-points. (b)The road window is set by the direction of the seed. (c)The hits in the window are judged to be added by a combinatorial Kalman filter. (d)Reconstructed track candidates. 44
5.4 Simple example of the ambiguity solving process, illustrated in the SCT barre region [63]. Track candidates **a**, **b**, and **c** have been reconstructed at the stage of the track finding but have several shared hits (ambiguous hits). In this example, a module hit representing measurements on both sides of an SCT module obtains a relatively higher score than two sensor hits representing single measurements only on one side of the module. Hits in an overlapping region for track **b** receive particularly a high score, while holes on tracks give a penalty to the track score. 45
5.5 Track reconstruction efficiency with and without large radius tracking (LRT) as a function of the LLP decay radius (r_{decay}) for signal MC sample ($m_{\tilde{\chi}_2^0} = 200$ GeV, $\Delta M(\tilde{\chi}_2^0, \tilde{\chi}_1^0) = 30$ GeV, $\tau_{\tilde{\chi}_2^0} = 3$ ns). The r_{decay} shown here is target range of the LLP decay of this search, which corresponds to inside the innermost SCT layer. 45
5.6 Hard scatter vertex and pileup vertices. 46
5.7 (a) Fractional JES systematic uncertainty as a function of jet p_{T} [70]. The green line labeled 'EM+JES' is the JES uncertainty for the jets used in this analysis. (b) Relative JER as a function of jet p_{T} [69]. 48

6.1 Schematics of the hit pattern consistency used for secondary vertices [82]. (a) A vertex is reconstructed between B-Layer and Layer-1. The tracks must not have any hits on the IBL nor B-Layer, the layers inner than the radial vertex position, and must have a hit on the Layer-1, the closest layer outside the vertex position. (b) A vertex is reconstructed close to and inside B-Layer. The tracks must not have any hits on the IBL but are allowed to have a hit on the B-Layer and must have a hit on the Layer-1. 53
6.2 Sketch of the $\tilde{\chi}_2^0$ decay in the target event. $\tilde{\chi}_2^0$ decays to $\tilde{\chi}_1^0$ and a pair of b-quarks, forming b-hadrons. B-hadrons decay into lighter hadrons and leptons after flying a few mm. . . . 55
6.3 The number of reconstructed particles originating from $\tilde{\chi}_2^0$ and the invariant mass reconstructed by all the reconstructed particles originating from $\tilde{\chi}_2^0$. Only the events with at least two reconstructed events are included in the left figure. 55
6.4 Schematic diagram of two-track seed vertex reconstruction in the special method. 57
6.5 The way of multi-track vertex reconstruction in the special method. 58
6.6 Definitions of variables $\sum {p_{\text{T}}}^{\text{prim}}$, $\sum {p_{\text{T}}}^{\text{sub}}$, and ϕ_{max}, which are used for seed merging. . . 59

6.7 Correlation between the primary seeds and substitute seeds inside the beam pipe in the signal MC (left) and data (right). The bino-wino signal sample with $m_{\tilde{\chi}_2^0} = 200$ GeV, $\Delta M(\tilde{\chi}_2^0, \tilde{\chi}_1^0) = 30$ GeV, $\tau_{\tilde{\chi}_2^0} = 0.03$ ns is used. The pairs of primary and substitute seeds above the red line are not merged. 59
6.8 DV reconstruction efficiency of standard (black) and special (red) DV method as a function of the LLP decay position. The signal events in the bino-wino model with $m_{\tilde{\chi}_2^0} = 200$ GeV and $\tau_{\tilde{\chi}_2^0} = 3$ ns are used. Reconstructed DVs are required to have at least three tracks here because special DVs with only two tracks have been removed. 61
6.9 Comparison of a signal DV reconstructed by the standard (left) and the special method (right) in the same event. The origin is the signal LLP decay point. Gray lines and red lines show the tracks associated and not associated with the DV, respectively. The blue point in the left figure is the DV reconstructed by the standard method. In the right figure, black points show the two-track seed vertices belonging to the DV, and the blue circle is five times the size of the DV reconstructed by the special method, where the size is defined as the standard deviation of the two-track seed positions included in it. 62
6.10 Number of tracks and invariant mass of the signal DVs reconstructed by the standard method (left) and special method (right). Only the tracks originating from the LLP are counted. The bino-wino signal events with $m_{\tilde{\chi}_2^0} = 200$ GeV and $\Delta M(\tilde{\chi}_2^0, \tilde{\chi}_1^0) = 30$ GeV are used. "DV passing the cut" shows the number of DVs that meet the cuts shown in the red line. 63
6.11 Number of tracks and invariant mass of the signal DVs reconstructed by the standard method (left) and special method (right). The bino-wino signal events with $m_{\tilde{\chi}_2^0} = 200$ GeV and $\Delta M(\tilde{\chi}_2^0, \tilde{\chi}_1^0) = 50$ GeV are used. "DV passing the cut" shows the number of DVs that meet the cuts shown in the red line. 64
6.12 Feynman diagram of pair production of $\tilde{g}$ decaying to the $\tilde{\chi}_1^0$ and light quarks (q). In this case, $\tilde{g}$ becomes long-lived. 65
6.13 Number of tracks and invariant mass of the signal DVs reconstructed by the standard method (left) and special method (right). The gluino signal events with $m_{\tilde{\chi}_1^0} = 500$ GeV and $\Delta M(\tilde{g}, \tilde{\chi}_1^0) = 30$ GeV are used. "DV passing the cut" shows the number of DVs that meet the cuts shown in the red line. 66
6.14 Radial position of the DVs reconstructed by the standard and special reconstruction methods using one run. 67

7.1 Schematic view of data flow in ATLAS standard analysis. 69
7.2 Schematic view of data flow in this analysis. 69
7.3 $E_{\mathrm{T}}^{\mathrm{miss}}$ trigger efficiency of each year measured by $Z \to \mu\mu$ events [47]. The trigger efficiency when $p_{\mathrm{T}}(Z) = 250$ GeV is approximately 100%, but not when $p_{\mathrm{T}}(Z) = 150$ GeV. 71
7.4 x-y position of the muon segments in the CSC and the inner MDT endcaps [87]. The segments parallel to the beam line that are likely to be NCB-induced are pointed by an arrow. 72

7.5 Correlation between the $E_{\mathrm{T}}^{\mathrm{miss}}$ ϕ and the leading jet f_{max} (top left), f_{EM} (top right), and $f_{\mathrm{ch}}/f_{\mathrm{max}}$ (bottom). The events are required to pass the trigger, $E_{\mathrm{T}}^{\mathrm{miss}}$ filter, event cleaning, PV conditions, and offline $E_{\mathrm{T}}^{\mathrm{miss}}$ selection. 74
7.6 The ϕ distribution of the $E_{\mathrm{T}}^{\mathrm{miss}}$ in events passing $E_{\mathrm{T}}^{\mathrm{miss}}$ and PV selection criteria. The black line shows the case without any NCB veto, the red line shows the case after applying *SuperLooseBadLLP* jet veto, and the green line shows the case after applying *SuperLooseBadLLP* jet veto and the selection to the leading jet. 75
7.7 Fake $E_{\mathrm{T}}^{\mathrm{miss}}$ caused by a dead Tile module in a di-jet event. The energy of the jet on the left-hand side is measured smaller than the true energy due to a dead Tilde module, and it causes the mismeasurement of the $E_{\mathrm{T}}^{\mathrm{miss}}$. 75
7.8 The $E_{\mathrm{T}}^{\mathrm{miss}}$ ϕ distribution in 2016 (upper left), 2017 (upper right), and 2018 (bottom). The black line shows the events passing $E_{\mathrm{T}}^{\mathrm{miss}}$ and PV selection and strict NCB veto, and the red line shows the case when dead tile module veto is additionally applied. The reason for the asymmetry between the $E_{\mathrm{T}}^{\mathrm{miss}}\phi > 0$ and $E_{\mathrm{T}}^{\mathrm{miss}}\phi < 0$ after the dead tile module veto is because the beam position was shifted in y-direction in the Run 2 operation. 76
7.9 Position of the known detector materials and reconstructed low-mass standard DVs in the (a) x-y plane and (b) r-z plane [90]. The colored regions are defined as "inside material" and DVs in these regions are vetoed. 77
7.10 p_{T} of track in DVs inside the IBL (top left), inside the Pixel (top right), and outside the Pixel (bottom). 79
7.11 S_{d_0} of track in DVs inside the IBL (top left), inside the Pixel (top right), and outside the Pixel (bottom). 80
7.12 Definition of (a) $\alpha(\mathrm{track}, \mathrm{PV} - \mathrm{DV})$ and (b) $\alpha_{\mathrm{min}}(\mathrm{track}, \mathrm{PV} - \mathrm{DV})$ for a track when there are two PVs. 80
7.13 $\alpha_{\mathrm{min}}(\mathrm{track}, \mathrm{PV} - \mathrm{DV})$ and S_{d_0} of tracks in DVs inside the IBL (top left), inside the Pixel (top right) and outside the Pixel (bottom) of signal MC ($m_{\tilde{\chi}_2^0}$ = 200 GeV, $\Delta m(m_{\tilde{\chi}_2^0}, m_{\tilde{\chi}_1^0})$ = 30 GeV, $\tau_{\tilde{\chi}_2^0}$ = 0.3 ns). 81
7.14 $\alpha_{\mathrm{min}}(\mathrm{track}, \mathrm{PV} - \mathrm{DV})$ and S_{d_0} of tracks in DVs inside the IBL (top left), inside the Pixel (top right), and outside the Pixel (bottom) of $Z \to \nu\bar{\nu}$ background MC. 82
7.15 $\Delta\phi$ between track and PV-DV vector direction of DVs inside the IBL (top left), inside the Pixel (top right), and outside the Pixel (bottom). 83
7.16 Cutflow showing how the fraction of DVs with at least four tracks and larger than 5 GeV invariant mass of several signal and a background MC samples change by applying DV-track selection. 84
7.17 Distribution of N_{tracks} and m_{DV} after track cleaning for a bino-wino signal (left) and $Z \to \nu\bar{\nu}$ background (right) events. The number of events is not normalized and is simply number of events in the MC samples. 85
7.18 Distribution of N_{tracks} and N_{seeds} after track cleaning for a bino-wino signal (left) and $Z \to \nu\bar{\nu}$ background (right) events. The number of events is not normalized and is simply number of events in the MC samples. 87

7.19 Selection efficiency of representative signal models. 87
7.20 Selection efficiency for bino-wino signal models as a function of $\tilde{\chi}_2^0$ mass and lifetime with (a) $\Delta M(\tilde{\chi}_2^0, \tilde{\chi}_1^0) = 20$ GeV, (b) $\Delta M(\tilde{\chi}_2^0, \tilde{\chi}_1^0) = 30$ GeV, (c) $\Delta M(\tilde{\chi}_2^0, \tilde{\chi}_1^0) = 40$ GeV, and (d) $\Delta M(\tilde{\chi}_2^0, \tilde{\chi}_1^0) = 50$ GeV. Bins with no MC samples are shown as blank. 88

8.1 Classification of the background sources. (a) Hadronic interaction and the SM LLP decay (HI). (b) Accidental crossing (AX). (c) Merged vertices (MV). 90
8.2 The mass distributions of DVs outside material region with four tracks (left) and more than four tracks (right) from three background sources. All DV selections are applied except the N_{tracks} and m_{DV} conditions. $Z \to \nu\bar{\nu}$ MC samples are used. 91
8.3 The mass distributions of DVs inside the material region with four tracks (left) and more than four tracks (right) from three background sources. The DV must fail the strict material map veto and pass other selections, except for applying the N_{tracks} and m_{DV} selections. $Z \to \nu\bar{\nu}$ MC samples are used. 91
8.4 The mass distributions of DVs that fail the seed condition with four tracks (left) and more than four tracks (right) from three background sources. The DV must fail the seed condition and pass other selections, except for applying the N_{tracks} and m_{DV} conditions. $Z \to \nu\bar{\nu}$ MC samples are used. 92
8.5 Correlation between DV and jet. 93
8.6 Fraction of the events in the PTR with a DV passing all DV selection except that $N_{\text{tracks}} \geq 4$ and $m_{\text{DV}} > 10$ GeV. (Style must be updated.) 94
8.7 Comparison of event-level variables between the PTR and MTR. 95
8.8 Example of calculating an event-DV probability. The event-DV probability(c) is calculated by dividing (a) by (b). 97
8.9 Application of the event-DV probability. (b) is obtained by multiplying (a) and the event-DV probability shown in Figure 8.8(c). The number of events in the SR is then estimated by scaling down (b) with f-factor shown in Equation 8.4. 98
8.10 Pileup distributions in the PTR and MTR. 99
8.11 Binning of the inside material validation region. 101
8.12 Estimated and observed number of DVs in the inside material region. The error bar includes the PTR statistic and the pileup uncertainties. 101
8.13 Definition of the SR and the low track multiplicity/low mass validation region. 102
8.14 Estimated and observed number of DVs in the n-seed sideband region. The error bar includes the PTR statistic and the pileup uncertainties. 103
8.15 Definition of the SR and the low track multiplicity/low mass validation region. 103
8.16 Estimated number of DVs in the SR and n-track/mass sideband region, and observed number of DVs in the n-track/mass sideband region. The error bar includes the PTR statistic and the pileup uncertainties. 104

9.1 Mass distribution of K_S^0 candidates in the outermost radial region (120 mm $< R_{xy} <$ 300 mm) observed in data. The mass distribution is fitted by an asymmetric Gaussian (purple) plus liner (red) function. The integral of the asymmetric Gaussian function in the mass range from 0.4 to 0.6 GeV is shown. 106
9.2 (a)The number of reconstructed K_S^0 candidates in each radial region in data and MC. The MC is normalized to data using the first radial bin. (b)Tracking uncertainty in each DV radial region. 107
9.3 Uncertainty on the signal yields of the bino-wino signal model with several $\tilde{\chi}_2^0$ lifetime and mass splitting between $\tilde{\chi}_2^0$ and $\tilde{\chi}_1^0$ with a fixed $\tilde{\chi}_2^0$ mass of 200 GeV. 108
9.4 $E_{\mathrm{T}}^{\mathrm{miss}}$ trigger efficiency as a function of $E_{\mathrm{T}}^{\mathrm{miss,\ mu\text{-}subtracted}}$ in data and $Z \to \mu\mu$ MC. The trigger which is unplescaled throughout each period is used. 108
9.5 $E_{\mathrm{T}}^{\mathrm{miss}}$ trigger efficiency as a function of $E_{\mathrm{T}}^{\mathrm{miss}}$ in data and bino-wino signal MC with $m_{\tilde{\chi}_2^0} =$ 200 GeV and $\Delta M(\tilde{\chi}_2^0, \tilde{\chi}_1^0) = 20$ GeV. The MC samples with $\tau_{\tilde{\chi}_2^0} = 0.03$ ns, 0.3 ns, and 3 ns are merged. The trigger which is unplescaled throughout each period is used. 109

10.1 Expected Bino-Wino signal yields in the case with (a) $\Delta M(\tilde{\chi}_2^0, \tilde{\chi}_1^0) = 20$ GeV, (b) $\Delta M(\tilde{\chi}_2^0, \tilde{\chi}_1^0)$ = 30 GeV, (c) $\Delta M(\tilde{\chi}_2^0, \tilde{\chi}_1^0) = 40$ GeV, and (d) $\Delta M(\tilde{\chi}_2^0, \tilde{\chi}_1^0) = 50$ GeV. Bins with no MC samples are shown as blank. 112
10.2 Two-dimensional distribution of N_{tracks} and m_{DV} of the DV observed in the MTR. All the baseline DV selection and signal DV selection except for N_{tracks} and m_{DV} conditions are applied. DVs with $N_{\mathrm{tracks}} < 3$ or $m_{\mathrm{DV}} < 2$ GeV are not shown. The upper right region of the two red lines corresponds to the SR. 116

11.1 Illustration of $L(\mu, \theta)$ and $L(\mu, \hat{\hat{\theta}})$. The blue shade shows two-dimensional $L(\mu, \theta)$. It takes the maximum at $(\hat{\mu}, \hat{\theta})$, and its contour is bounded by a certain confidence level. The red line shows $L(\mu, \hat{\hat{\theta}})$. 118
11.2 Illustration of p_μ. 119
11.3 Illustration of $\tilde{q}_\mu$ (a) when $\hat{\mu} \geq 0$ and (b) when $\hat{\mu} < 0$. 120
11.4 The upper limit on the cross-section for $\tilde{\chi}_1^\pm \tilde{\chi}_2^0$ production in bino-wino model as a function of $m_{\tilde{\chi}_2^0}$ with various fixed $\tau_{\tilde{\chi}_2^0}$ when $\Delta M(\tilde{\chi}_2^0, \tilde{\chi}_1^0) = 50$ GeV. The solid lines show the observed limit, and dashed lines and bands show the expected limit with $\pm 1\sigma$. The black line and band show the theoretical expectation and its uncertainty of the cross-section of the $\tilde{\chi}_1^\pm \tilde{\chi}_2^0$ pair production. The limits for $\tau_{\tilde{\chi}_2^0} = 0.3$ ns and $\tau_{\tilde{\chi}_2^0} = 3$ ns are cut off at $m_{\tilde{\chi}_2^0} = 1000$ GeV and $m_{\tilde{\chi}_2^0} = 700$ GeV respectively due to the absence of corresponding MC samples. 121
11.5 95% confidence level (CL) observed and expected exclusion limits in $\tau_{\tilde{\chi}_2^0}$ vs. $m_{\tilde{\chi}_2^0}$ plane for bino-wino model with various fixed $\Delta M(\tilde{\chi}_2^0, \tilde{\chi}_1^0)$. The region bellow the red line is excluded by the observation. The observed limit is lower than the expected limit because of a mild excess. 122

11.6 The observed and expected exclusion limits in $m_{\tilde{\chi}_1^0}$ vs. ΔM plane for bino-wino model with various fixed $m_{\tilde{\chi}_2^0}$. The region left side of the red line is excluded by the observation. The blue dashed showing the region where the observed DM relic is well explained is drawn by eyeballing the line in Figure 2.7. 123
11.7 Object distribution (left) and track/seed distribution (right) in the x-y plane of the observed three events (top, middle, bottom). The blue lines show the tracks belonging to the DV. In the left figures, red, green, and cyan lines show jets, $E_{\mathrm{T}}^{\mathrm{miss}}$, and muons, respectively. The line length is proportional to the object's p_{T}. The gray dashed and solid circles are the beam pipe and Pixel layers. In the right figures, the positions of the DV seeds are shown in dark-gray points. 125
11.8 Event level quantities in the observed three events (green) comparing with all events in the MTR (black) and events in the VRVeryLowMass (red). 126
11.9 $E_{\mathrm{T}}^{\mathrm{miss}}$ and DV variables of the data and various signal samples in the SR. 127

List of Tables

2.1 Fermions, Higgs bosons, and their super partners of the MSSM [17]. 8
2.2 Gauge bosons and their super partners of the MSSM [17]. 8

3.1 LHC design parameters [23]. 18
3.2 The LHC operational parameters in each year of Run 2 [26]. These values are representative of the best LHC performance during the normal operation period. 21
3.3 Layout of the Pixel detector [34, 36]. 26
3.4 Layout of the SCT [37]. 27

4.1 Summary of the integrated luminosity and uncertainties assessed as good for physics. [26]. Data taken in 2015 are not used for this analysis as mentioned later. 34

5.1 Usage of each object in this analysis. 40
5.2 Description of the track parameters. 41
5.3 Track selections used for the standard tracking and large radius tracking [65]. 44

6.1 Dataset information used for training to develop the special DV reconstruction method. The sample labeled as "signal-long / signal-middle / signal-short" and "background" are used to learn the characteristics of track pairs of the signal events with long / middle / short lifetime and background events. 56
6.2 Variables used to classify the signal-like tarck pairs and random-like track pairs. The superscript indicates the index of the track (1 or 2). The first seven variables are for tracks #1 and #2, there are 18 variables in total. 57

7.1 Trigger selection list. For items with multiple HLT thresholds listed, any combination of thresholds is included. For example, the first row contains `HLT_xe90_L1XE50`, `HLT_xe90_L1XE55`, `HLT_xe90_L1XE60`, `HLT_xe100_L1XE50`, `HLT_xe100_L1XE55`, `HLT_xe100_L1XE60`, `HLT_xe120_L1XE50`, `HLT_xe120_L1XE55`, and `HLT_xe120_L1XE60`. The used algorithm is described in Section 3.2.6. 70
7.2 Location of dead modules on the Tile calorimeter [89]. 74
7.3 Summary of the DV-track selection. 84
7.4 Definitions of the signal regions. 86

8.1 Estimated number of background events in the SR. 'PTR statistics' uncertainty is calculated by propagating the statistical uncertainty of the DVs in the PTR to the final estimation. 'Pileup' uncertainty is calculated by taking the difference of the estimation with and without pileup reweighting that matches the pileup distribution of the PTR to the MTR. 'Non-closure' uncertainty is calculated from the ratios of the observation divided by the estimate in the validation regions. 100

9.1 Summary of the systematic uncertainties in the predicted number of signal events. 110

10.1 Information of the SR event #1. 113
10.2 Information of the SR event #2. 114
10.3 Information of the SR event #3. 115

11.1 Parameters and expected yields of the signal events used to compare with the observed events. 124